

**Magnetic domain walls
in ultrathin films:
Contribution of the
Dzyaloshinsky-Moriya interaction**

Von der Fakultät für Mathematik, Informatik und Naturwissenschaften
der Rheinisch-Westfälischen Technischen Hochschule Aachen
zur Erlangung des akademischen Grades eines Doktors der Naturwissenschaften
genehmigte Dissertation

vorgelegt von

Diplom-Physiker
Marcus Heide

aus Düsseldorf

Berichter: Universitätsprofessor Dr. Stefan Blügel
Universitätsprofessor Dr. Peter H. Dederichs

Tag der mündlichen Prüfung: 28. Feb. 2006

Diese Dissertation ist auf den Internetseiten der Hochschulbibliothek online verfügbar.

This thesis was written at the institute
Theorie 1, Institut für Festkörperforschung (IFF), Forschungszentrum Jülich.

It is available online at the internet pages of the library of
RWTH Aachen university.

Abstract

In this theoretical thesis the structure of magnetic domain walls is explained by an interplay of spin stiffness, anisotropy energy and Dzyaloshinsky-Moriya interaction. The wall structures are discussed within a micromagnetic model and the corresponding model parameters are obtained ab initio by electronic-structure calculations.

The inclusion of the Dzyaloshinsky-Moriya interaction in these investigations is a new aspect. This interaction arises only in certain crystal symmetries, it is of particular importance in the studied ultrathin magnetic films deposited on non-magnetic surfaces. The Dzyaloshinsky-Moriya interaction leads to unusual domain-wall structures that can be classified in several distinct phases. The ab-initio calculations are done with the FLAPW method that relies on density functional theory. Within this method a perturbative approach is developed, that allows to estimate the effect of spin-orbit coupling on spin spirals with large spatial periods and thus allows to estimate the strength of the Dzyaloshinsky-Moriya interaction. The theory is applied to the system Fe/W(110), i.e. to the W(110)-surface covered with one respectively two atomic layers of Fe. The domain-wall widths are calculated and compared with experimental data. Furthermore, a new explanation is given for the experimentally observed phenomenon, that the domain walls in the Fe double-layer are preferably oriented along the $[\bar{1}\bar{1}0]$ -direction.

Contents

| | | |
|----------|--|-----------|
| 1 | Introduction | 4 |
| 2 | Density functional theory | 8 |
| 2.1 | Theorem of Hohenberg and Kohn | 9 |
| 2.2 | Kohn-Sham equation | 9 |
| 2.3 | Local density approximation | 12 |
| 2.4 | Total energy | 13 |
| 2.5 | Relativistic Kohn-Sham equation | 14 |
| 2.5.1 | Spin-orbit coupling | 14 |
| 3 | Solving the Kohn-Sham equation, the FLAPW method | 16 |
| 3.1 | The selfconsistency cycle | 16 |
| 3.2 | Calculating the total energy | 17 |
| 3.3 | Solving the secular equation | 18 |
| 3.3.1 | Core states | 18 |
| 3.3.2 | Valence states | 19 |
| 3.4 | LAPW basis functions | 19 |
| 3.4.1 | LAPW basis in film geometry | 21 |
| 3.4.2 | Representation of density and potential | 23 |
| 3.5 | Calculating the density | 23 |
| 3.6 | Calculating the potential | 24 |
| 3.7 | Magnetic calculations | 25 |
| 3.7.1 | LAPW basis functions | 26 |
| 3.7.2 | Constrained magnetic moments | 27 |
| 3.7.3 | Generalized Bloch theorem | 27 |
| 3.8 | Relativistic effects in the valence band | 29 |
| 3.9 | Spin-orbit coupling in helical spin spirals | 31 |
| 3.9.1 | Local force theorem | 31 |
| 3.9.2 | Second variation | 32 |
| 3.9.3 | Diagonalizing the sparse matrix $H_0 + H_{so}$ | 34 |
| 4 | Magnetic interactions | 35 |
| 4.1 | Exchange interactions | 35 |
| 4.1.1 | Dzyaloshinsky-Moriya interaction | 36 |
| 4.2 | Magnetostatic interactions | 37 |
| 4.3 | Domain structure | 38 |

| | | |
|----------|--|------------|
| 5 | Domain walls | 39 |
| 5.1 | Some definitions | 39 |
| 5.2 | Micromagnetic model | 40 |
| 5.2.1 | Ansatz | 41 |
| 5.2.2 | Symmetry considerations to the \mathbf{D} -vector | 43 |
| 5.2.3 | Analytic solution for $\mathbf{D}=0$ | 44 |
| 5.2.4 | Influence of the Dzyaloshinsky-Moriya term | 45 |
| 5.3 | Effects of the discrete lattice structure | 54 |
| 5.3.1 | The case $\mathbf{D}=0$ | 55 |
| 5.3.2 | Influence of the Dzyaloshinsky-Moriya term | 56 |
| 5.4 | Extension of the models | 57 |
| 6 | The system Fe/W(110) | 59 |
| 6.1 | Structure | 59 |
| 6.2 | Experimental observations | 60 |
| 6.3 | Magnetostatic dipolar interactions | 62 |
| 6.4 | Effective exchange interactions | 65 |
| 6.4.1 | Spin stiffness | 65 |
| 6.4.2 | Hopping parameters | 65 |
| 6.5 | Magnetocrystalline anisotropy in the ferromagnetic domains | 67 |
| 6.6 | Dzyaloshinsky-Moriya interaction in the DL domain walls | 68 |
| 6.7 | Modeling the domain-wall structure | 69 |
| 6.7.1 | Domain magnetization | 69 |
| 6.7.2 | Micromagnetic model for the broad DL walls | 70 |
| 6.7.3 | Micromagnetic and discrete model for the narrow ML walls | 72 |
| 6.8 | Summary | 74 |
| 7 | Summary | 76 |
| A | Applying GGA to non-collinear magnetism | 78 |
| B | SOC matrix elements described with the LAPW basis | 83 |
| C | Local force theorem | 86 |
| D | Perturbation theory for the sum of eigenvalues | 89 |
| E | Relations between real- and spin-space symmetries | 94 |
| F | Details concerning the domain wall models | 97 |
| F.1 | Derivation of the micromagnetic model | 97 |
| F.2 | Optimizing the magnetization numerically | 98 |
| F.3 | Period length of the rotating ground state | 101 |
| F.4 | Phase transitions of the micromagnetic ground state | 103 |
| F.5 | DM interaction in the discrete model | 106 |
| G | Calculation of the ML exchange parameters | 109 |
| H | Computational details | 118 |
| | Bibliography | 123 |

Chapter 1

Introduction

This thesis deals with the structure of magnetic domain walls. Even though the corresponding basic micromagnetic equations were derived and solved already 70 years ago by Landau and Lifshitz [57], the topic gave rise to numerous vivid discussions throughout the decades. Nowadays, when the information density of magnetic data-storage media steadily increases and spintronic devices come in sight, a good understanding of the magnetic domain boundaries is of increasing technological relevance.

The internal structure of the magnetic domain walls is determined by a competition of spin stiffness and anisotropy energy. In the simplest case, both quantities can be regarded as local and the magnetization changes only in the spatial direction r normal to the wall. In a simple model, both quantities are local and the magnetization direction depends only on the distance perpendicular to the wall. It is often sufficient to approximate the energy E of a wall in-between two oppositely magnetized domains by

$$E[\vartheta(r)] = \int_{-\infty}^{+\infty} dr \left(\underbrace{A \left(\frac{d}{dr} \vartheta(r) \right)^2}_{\text{spin stiffness}} + \underbrace{K \cos^2(\vartheta(r))}_{\text{anisotropy energy}} \right) \quad \text{with} \quad \begin{cases} \vartheta(r) \xrightarrow{r \searrow -\infty} 0 \\ \vartheta(r) \xrightarrow{r \nearrow +\infty} \pi \end{cases} \quad (1.1)$$

where the angle $\vartheta(r)$ characterizes the magnetization direction. The wall structure (depending on the system-specific model parameters A, K) is given by the variation of $E[\vartheta]$, a straightforward analytical solution of this *Landau-Lifshitz equation* was for the first time presented in [57]. However, in many cases it is necessary to extend the model beyond the basic ansatz (1.1).

First extensions take into account a variety of crystal symmetries. This includes different structures of the anisotropy term and allows for non-collinear alignments of two adjacent (ferromagnetic) domains [e.g. 62].

The problem gets more involved when the long-ranged nature of the magnetostatic interactions is taken into account. In this case, the shape and size of the magnetic sample can have considerable influence on the wall structure. An ordinary magnetic film of finite thickness already shows very complex magnetic wall structures. In 1955 Néel realized that the rotation axis of the magnetization depends on the film thickness [75]. Later on, improved micromagnetic methods [e.g. 10, 48, 88] allowed for more detailed investigations of the magnetic films. It was discovered, that the correct treatment of the magnetostatic stray fields can lead to wall structures that break the symmetry of the energy functional: The local wall structure is not necessarily symmetric with respect to the two adjacent domains [e.g. 44, 56, 87, 92], furthermore a stable two-dimensional superstructure (called cross tie) can evolve [e.g. 42, 43, 70]. A resulting phase diagram is given in [86].

Further wall structures result from other constrictions (besides the reduced film thickness) [e.g. 19,47].

The previously mentioned models rely on system-dependent parameters. These parameters can be fitted to experimental results. But, from this ansatz one does not gain much insight in the electronic origins of the described effects and it requires a lot of data to obtain the model parameters and to confirm the applicability of the model ansatz simultaneously. It is very desirable to describe the systems by *ab-initio*¹ calculations. A breakthrough for this approach and, thus, for the theoretical description of solids, was the development of the density functional theory. Starting 40 years ago with the famous works of Kohn, Hohenberg and Sham [41,52], by now the density functional theory and the resulting Kohn-Sham formalism are well established and represent a very powerful tool for the calculation of the electronic and magnetic structure of real solids, the approximations involved keep a good balance between accuracy and computational effort.

In some recent calculations simple domain walls are treated entirely *ab initio* [e.g. 73,91,102]. But the systems presented in this thesis (i.e. domain walls in thin magnetic films deposited on surfaces) are too complex for this approach, even with present algorithms and computing facilities. Therefore, a multiscale approach is followed here: The values of the model parameters are obtained from parameter-free electronic-structure calculations (i.e. on atomic scales) and inserted in the previously mentioned (mesoscopic) models. Thus, the domain wall properties are calculated without adjustable parameters, but the simple models are not abandoned. The unavoidable use of the simplified micromagnetic models for the description of large systems does not need to be regarded as a drawback to the parameter-free approach, since these simplifications are very useful to illustrate the main effects.

For many years the theoretically predicted details of the the wall structures could hardly be confirmed (or disproved) experimentally. But, the experimental techniques have strongly progressed since the pioneering work of Landau and Lifshitz and by now the magnetic imaging of surface films has achieved almost atomic resolution. The early experiments were restricted to the superstructures (cross ties) at the surfaces, but more than 40 years ago it was already possible to determine the rotation axis of the magnetization by Bitter powder patterns [e.g. 69] and Lorentz electron microscopy reached a spatial resolution sufficient to image the gradual change of the magnetization direction in walls of various systems [e.g. 37,38]. For about three decades Lorentz microscopy remained the most accurate experimental technique for the imaging of surface domain walls, especially in scanning transmission mode [e.g. 101]. Other electron microscopy techniques do not provide the same spatial resolution of magnetic structures, but a resolution of 20 nm is also obtained with spin-polarized scanning electron microscopy (i.e. SEMPA) [2,67].

In the last 15 years spin-polarized scanning tunneling microscopy (spin-polarized STM) [e.g. 13,100] and magnetic force microscopy [e.g. 8,39,84] have evolved into very powerful tools for the analysis of magnetic nanostructures on surfaces. By now, these techniques allow to resolve magnetic structures on the nanometer length-scale. This provides an insight into a class of magnetic systems that previously were subject to hardly revisable theories.

¹The term *ab initio* means that the ansatz does not contain any adjustable parameters. In the context of solid state physics the term usually denotes calculations that determine the electronic structure (and resulting observables) from the positions and charges of the nuclei by applying the Schrödinger or Dirac equation to the interacting electron system.

This thesis presents theoretical investigations of domain walls, including micromagnetic models as well as ab-initio calculations of the model parameters. As mentioned previously, this approach bridges between an atomistic and a mesoscopic micromagnetic description.

The focus is laid on the Dzyaloshinsky-Moriya interaction [29, 71]. This interaction is a consequence of spin-orbit coupling and arises in spin structures where the symmetry between right-handed and left-handed spin alignment is broken by the crystal field. In the case of spin spirals (i.e. curling magnetic structures) it can be viewed as a linear approximation to the helicity-dependent energy term.

The former micromagnetic investigations that included the Dzyaloshinsky-Moriya term mainly focussed on vortex structures [e.g. 15–17]. The influence of this term on domain walls (i.e. on systems with the boundary conditions of Eqn. (1.1)) is only fragmentary discussed in literature [e.g. 18, 46, 93], but in detail studied within this thesis.

The extension of the micromagnetic energy functional by a local Dzyaloshinsky-Moriya term increases the complexity of the problem remarkably. Even for very simple crystal structures and under the neglect of long-ranged magnetostatic interactions, the magnetization rotates on a complicated 3-dimensional path in spin-space and the domain walls can be described by a rich phase diagram.

In order to obtain the domain-wall model parameters (i.e. spin-stiffness constant, anisotropy-energy tensor, Dzyaloshinsky vector) by ab-initio calculations, the FLAPW method (based on density functional theory) is employed. It is not straightforward to include the Dzyaloshinsky-Moriya interaction in the currently established ab-initio methods. Recently, this has been done for some quantum-chemistry problems [96]. For the description of the domain walls, however, the relevant length scales impose a formidable problem as the spatial rotation of the magnetization is very small. Even with modern massively parallelized supercomputers a sophisticated perturbative approach is indispensable.

The theoretical concepts are applied for a detailed investigation of the domain-wall structures of atomically thin Fe films on the non-magnetic W(110)-surface. This system is chosen since its magnetic structure is well known from recent STM experiments [e.g. 81, 83], this allows a detailed comparison between theory and experiment.

The system nicely illustrates the significance of the various effects in a sample that is scaled down to the atomic size: The magnetostatic stray field is essential for the explanation of the domain-wall structure in thick Fe films, but irrelevant in films of one or two atomic layers. On the other hand, spin-orbit coupling plays a particular important role in these ultrathin films where the low surface symmetry is crucial in the local environment of all magnetic atoms. This causes a large Dzyaloshinsky-Moriya interaction and a large magnetocrystalline anisotropy. The latter leads to very narrow domain walls (this might even make the micromagnetic ansatz questionable).

This thesis is structured in three parts:

In the Chapters 2 and 3 the methods and the underlying theory of the electronic structure calculations are described. In Chapter 2 the basic ideas of density functional theory and the Kohn-Sham formalism are illustrated. In Chapter 3 details of the computational method are described. The LAPW basis set is introduced. Then, the (by now well established) treatments of spin-orbit coupling and non-collinear magnetism are sketched. Special attention is paid to a new methodical tool that is developed within this thesis, namely to a perturbative approach that allows to calculate the effect of spin-orbit coupling in spin spirals with large spatial periods. With this approach, the Dzyaloshinsky-Moriya interaction can be estimated for a variety of systems for which this quantity previously was hardly accessible by ab-initio calculations.

The Chapters 4 and 5 deal with the model descriptions of magnetic structures, in par-

ticular those of domain walls. The main focus is laid on the influence of the Dzyaloshinsky-Moriya interaction. Chapter 4 briefly discusses the atomistic models that are relevant in the Chapters 5 and 6. In Chapter 5 the domain walls are described with a micromagnetic as well as with a discrete Heisenberg-like model. The inclusion of the Dzyaloshinsky-Moriya interaction gives rise to a variety of phase transitions. Within a simple micromagnetic model the resulting phase diagrams are systematically studied, to our knowledge for the first time.

Finally, in Chapter 6 the previously developed theories and methods are applied to a real system, namely an ultrathin Fe film (of one and two atomic layers respectively) covering the W(110)-surface. The parameters of the models are obtained from ab-initio calculations and the results are compared with experimental data. In the interpretation of the results, the Dzyaloshinsky-Moriya interaction plays a key role again.

Chapter 2

Density functional theory

In this chapter the *density functional theory (DFT)* for electronic structures is described. DFT presents a powerful method for the calculation of the total energy and other observables of a many-electron systems.

The theory is derived from the N -body Schrödinger equation¹

$$\mathcal{H}\Psi = E\Psi \quad (2.1)$$

$$\text{with } \mathcal{H} = \sum_{\nu=1}^N \left(\hat{\mathbf{p}}_{\nu}^2 + \sum_{\substack{\nu'=1 \\ \nu' \neq \nu}}^N \frac{1}{|\mathbf{r}_{\nu} - \mathbf{r}_{\nu'}|} + V_{\text{ext}}(\mathbf{r}_{\nu}) \right), \quad \Psi = \Psi(\mathbf{r}_1, \mathbf{r}_2, \dots, \mathbf{r}_N).$$

In the solid systems that are discussed within this thesis, Ψ represents an (antisymmetric) N -electron wavefunction and the *external potential* V_{ext} is the Coulomb potential of the atomic nuclei. Thus, the electronic structure is analyzed for fixed nuclear positions (i.e. in the Born-Oppenheimer approximation). Further external electromagnetic fields are not considered.

The N -particle problem (2.1) is extremely complex, a (numerically) exact solution is feasible only for very small systems. The DFT reduces the complexity of the equations drastically, since here the basic quantity is not the N -body wavefunction $\Psi(\mathbf{r}_1, \mathbf{r}_2, \dots, \mathbf{r}_N)$ but the corresponding electron density $n(\mathbf{r})$:

$$n(\mathbf{r}) = \int d^3\mathbf{r}_1 d^3\mathbf{r}_2 \dots d^3\mathbf{r}_N \Psi(\mathbf{r}_1, \mathbf{r}_2, \dots, \mathbf{r}_N)^{\dagger} \sum_{\nu=1}^N \delta(\mathbf{r} - \mathbf{r}_{\nu}) \Psi(\mathbf{r}_1, \mathbf{r}_2, \dots, \mathbf{r}_N). \quad (2.2)$$

The remarkable consequence of the theorem of Hohenberg and Kohn (cf. Chapter 2.1) is, that the density n (i.e. a function $\mathbb{R}^3 \rightarrow \mathbb{R}$) contains the same information as the wavefunction Ψ (i.e. a function $\mathbb{R}^{3N} \rightarrow \mathbb{C}$), provided that Ψ is the ground-state solution of a Schrödinger equation. Thus, it is in principle possible to calculate all ground-state observables without determining Ψ explicitly.

In the actual calculations it is necessary to introduce an auxiliary function Ψ_{KS} that has the form of a wavefunction of N *non-interacting* fermions (cf. Chapter 2.2). Such a wavefunction can be represented by N functions $\mathbb{R}^3 \rightarrow \mathbb{C}$:

$$\Psi_{\text{KS}} = \hat{S}^{(-)} \prod_{\nu=1}^N \psi_{\nu}(\mathbf{r}_{\nu}) = \frac{1}{\sqrt{N!}} \det(\psi_{\nu}(\mathbf{r}_{\nu'}))_{\nu, \nu'}, \quad \int d^3\mathbf{r} \psi_{\nu'}(\mathbf{r})^{\dagger} \psi_{\nu}(\mathbf{r}) = \delta_{\nu, \nu'}$$

where $\hat{S}^{(-)}$ denotes the antisymmetrizer operator. The set $\{\psi_{\nu}(\mathbf{r})\}$ of auxiliary single-particle wavefunctions is much easier to handle than the many-body wavefunction $\Psi(\{\mathbf{r}_{\nu}\})$.

¹Atomic Rydberg units are used throughout this thesis. Exeptions are stated explicitly.

When the electron spin is taken into account, the wavefunction Ψ is a two-component spinor and the DFT works with the electron density n (Eqn. (2.2)) and the three-component magnetization density \mathbf{m} :

$$\mathbf{m}(\mathbf{r}) = \int d^3\mathbf{r}_1 d^3\mathbf{r}_2 \dots d^3\mathbf{r}_N \Psi(\mathbf{r}_1, \mathbf{r}_2, \dots, \mathbf{r}_N)^\dagger \boldsymbol{\sigma} \sum_{\nu=1}^N \delta(\mathbf{r} - \mathbf{r}_\nu) \Psi(\mathbf{r}_1, \mathbf{r}_2, \dots, \mathbf{r}_N) \quad (2.3)$$

where $\boldsymbol{\sigma} = (\sigma_x, \sigma_y, \sigma_z)^\dagger$ is a real-space vector of Pauli matrices.

2.1 Theorem of Hohenberg and Kohn

The theorem of Hohenberg and Kohn can be written in the following form:

- 1) The ground-state many-body wavefunction Ψ is uniquely determined by the ground-state densities $\{n, \mathbf{m}\}$ (i.e., two different ground-state eigenfunctions Ψ of the Schrödinger equation (2.1) for two (different or identical) external potentials V_{ext} represent different densities $\{n, \mathbf{m}\}$).
- 2.1) For every potential V_{ext} there exists a functional $E_{\text{tot}}[\tilde{n}, \tilde{\mathbf{m}}]$ that is minimal (and equal to the ground-state energy E_0) if the variational densities $\{\tilde{n}, \tilde{\mathbf{m}}\}$ coincide with the ground-state densities $\{n, \mathbf{m}\}$ of Eqn. (2.1):

$$\{\tilde{n}, \tilde{\mathbf{m}}\} \in \mathcal{N} \quad \Rightarrow \quad E_{\text{tot}}[\tilde{n}, \tilde{\mathbf{m}}] \geq E_{\text{tot}}[n, \mathbf{m}] = E_0. \quad (2.4)$$

Here \mathcal{N} denotes the space of *N-representable densities*. These are densities with $\int d^3\mathbf{r} n(\mathbf{r}) = N$ that are obtained from any antisymmetric *N*-body wavefunction.

- 2.2) The contribution of the potential energy can be separated from the total energy:

$$E_{\text{tot}}[n, \mathbf{m}] = E_{\text{uni}}[n, \mathbf{m}] + \int d^3\mathbf{r} V_{\text{ext}}(\mathbf{r}) n(\mathbf{r}) \quad (2.5)$$

where the *universal functional* $E_{\text{uni}}[n, \mathbf{m}]$ depends on the densities but not explicitly on the potential V_{ext} .

These propositions are exact. Proposition 1) implies that the densities $\{n, \mathbf{m}\}$ contain all information of the ground state that is described by Ψ . Therefore, any observable O is a functional of the densities, i.e. $O[n, \mathbf{m}]$. If this functional is known, the observable can be calculated without determining the wavefunction Ψ explicitly. Proposition 2) indicates how the ground-state densities $\{n, \mathbf{m}\}$ can be calculated if the functional E_{uni} is known. Approximations for this functional are discussed in Chapters 2.2 and 2.3.

In the original work of Hohenberg and Kohn [41], the theorem is formulated in a slightly different way. Important developments of the theory are the allowance of a degenerate ground state [51], the inclusion of the electron spin and the magnetization density \mathbf{m} [98] and the extension of the set of trial densities $\{\tilde{n}, \tilde{\mathbf{m}}\}$ in (2.4) to all *N*-representable densities [60].

2.2 Kohn-Sham equation

The theorem, that is presented in the previous chapter, is exact. But, the energy functional $E_{\text{tot}}[n, \mathbf{m}]$ is not known explicitly. Kohn and Sham introduced some approximations [52], that allow to determine the ground-state densities $\{n, \mathbf{m}\}$ from the variation of E_{tot} (cf. Eqns. (2.4), (2.5)). Although these approximations seem quite plausible, a

rigid justification for them is not simple and is omitted here. For detailed explanations cf. e.g. [33].

The energy functional (2.5) can be written as

$$E_{\text{tot}}[n, \mathbf{m}] = E_{\text{kin}}[n, \mathbf{m}] + E_{\text{ee}}[n, \mathbf{m}] + E_{\text{ei}}[n]$$

with

$$\begin{aligned} E_{\text{kin}}[n, \mathbf{m}] &= \sum_{\nu} \langle \Psi | \hat{\mathbf{p}}_{\nu}^2 | \Psi \rangle \\ E_{\text{ee}}[n, \mathbf{m}] &= E_{\text{H}}[n] + E_{\widetilde{\text{xc}}}[n, \mathbf{m}] = \int d^3\mathbf{r} d^3\mathbf{r}' \frac{n(\mathbf{r})n(\mathbf{r}')}{|\mathbf{r} - \mathbf{r}'|} + E_{\widetilde{\text{xc}}}[n, \mathbf{m}] \\ E_{\text{ei}}[n] &= \int d^3\mathbf{r} V_{\text{ext}}(\mathbf{r}) n(\mathbf{r}) . \end{aligned}$$

$E_{\widetilde{\text{xc}}}$ denotes all electron-electron interactions that are not included in the Hartree term E_{H} (i.e. exchange and correlation). The functional $E_{\text{kin}}[n, \mathbf{m}] + E_{\widetilde{\text{xc}}}[n, \mathbf{m}]$ is not explicitly known. It is dominated by the kinetic energy E_{kin} . It is not straightforward to calculate the kinetic energy from the densities without knowing the wavefunction. In the following it is illustrated how this problem is solved by introducing an auxiliary wavefunction Ψ_{KS} .

The auxiliary function Ψ_{KS} has the form of a N -body wavefunction of *non-interacting* fermions:

$$\Psi_{\text{KS}}(\mathbf{r}_1, \mathbf{r}_2, \dots, \mathbf{r}_N) = \frac{1}{\sqrt{N!}} \det \left(\psi_{\nu}(\mathbf{r}_{\nu'}) \right)_{\nu, \nu'} \quad \text{with} \quad \int d^3\mathbf{r} \psi_{\nu'}(\mathbf{r})^{\dagger} \psi_{\nu}(\mathbf{r}) = \delta_{\nu, \nu'} . \quad (2.6)$$

With Eqns. (2.2), (2.3) Ψ_{KS} leads to the densities

$$n(\mathbf{r}) = \sum_{\nu=1}^N \psi_{\nu}(\mathbf{r})^{\dagger} \psi_{\nu}(\mathbf{r}) \quad , \quad \mathbf{m}(\mathbf{r}) = \sum_{\nu=1}^N \psi_{\nu}(\mathbf{r})^{\dagger} \boldsymbol{\sigma} \psi_{\nu}(\mathbf{r}) . \quad (2.7)$$

The basic ideas of the Kohn-Sham formalism are:

- 1) The set of trial densities in the variation of E_{tot} (cf. Eqn. (2.4)) is restricted to the densities that can be represented as in Eqn. (2.7).
- 2) The major part of the kinetic energy is approximated by the kinetic energy of the auxiliary function:

$$E_{\text{kin}}[n, \mathbf{m}] = \sum_{\nu=1}^N \langle \Psi_{\text{KS}} | \hat{\mathbf{p}}_{\nu}^2 | \Psi_{\text{KS}} \rangle + E_{\text{kin}}^{(1)}[n, \mathbf{m}] = \sum_{\nu=1}^N \int d^3\mathbf{r} \psi_{\nu}(\mathbf{r})^{\dagger} \hat{\mathbf{p}}^2 \psi_{\nu}(\mathbf{r}) + E_{\text{kin}}^{(1)}[n, \mathbf{m}] .$$

The correction term $E_{\text{kin}}^{(1)}$ is well approximated by a simple expression (i.e. by a local function, cf. Chapter 2.3).

With the abbreviations

$$V_{\text{H}}(\mathbf{r}) = 2 \int d^3\mathbf{r}' \frac{n(\mathbf{r}')}{|\mathbf{r} - \mathbf{r}'|}$$

for the *Hartree potential* and

$$E_{\text{xc}}[n, \mathbf{m}] = E_{\widetilde{\text{xc}}}[n, \mathbf{m}] + E_{\text{kin}}^{(1)}[n, \mathbf{m}] = E_{\widetilde{\text{xc}}}[n, \mathbf{m}] + \left(E_{\text{kin}}[n, \mathbf{m}] - \sum_{\nu=1}^N \langle \Psi_{\text{KS}} | \hat{\mathbf{p}}_{\nu}^2 | \Psi_{\text{KS}} \rangle \right)$$

for the *exchange-correlation energy* the ground-state energy-functional (2.5) can be written as

$$E_{\text{tot}}[\{\psi_\nu\}_\nu] = \int d^3\mathbf{r} \left(\sum_{\nu=1}^N \psi_\nu(\mathbf{r})^\dagger \hat{\mathbf{p}}^2 \psi_\nu(\mathbf{r}) + \left(\frac{1}{2} V_{\text{H}}(\mathbf{r}) + V_{\text{ext}}(\mathbf{r}) \right) n(\mathbf{r}) \right) + E_{\text{xc}}[n, \mathbf{m}] \quad (2.8)$$

$$\text{with } n(\mathbf{r}) = n(\{\psi_\nu(\mathbf{r})\}_\nu) \quad , \quad \mathbf{m}(\mathbf{r}) = \mathbf{m}(\{\psi_\nu(\mathbf{r})\}_\nu) \quad , \quad V_{\text{H}}(\mathbf{r}) = V_{\text{H}}[\mathbf{r}, n] .$$

The only approximation entering (2.8) is the restriction of the space \mathcal{N} of N -representable trial densities to the densities that are represented by N non-interacting fermions (Eqn. (2.7)). But, the functional $E_{\text{xc}}[n, \mathbf{m}]$ is not known. The advantage of the formulation (2.8) is, that the major part of the kinetic energy is expressed explicitly, therefore the errors introduced by an approximation to E_{xc} are relatively small.

Astonishingly, $E_{\text{xc}}[n, \mathbf{m}]$ can be approximated well by a functional of the form

$$E_{\text{xc}}[n, \mathbf{m}] \approx \int d^3\mathbf{r} f_{\text{xc}}(n(\mathbf{r}), \mathbf{m}(\mathbf{r}))$$

where f_{xc} is a function of n, \mathbf{m} (i.e. local in real-space). This *local density approximation (LDA)* is used to approximate all many-body effects beyond the Hartree term. It is further described in Chapter 2.3.

The next step is to find the orthonormal wavefunctions $\{\psi_\nu(\mathbf{r})\}_{\nu \in [1, N]}$ that minimize the functional E_{xc} described in (2.8).

With the Lagrange multipliers $\{\epsilon_\nu\}_\nu$, that are introduced in order to constrain the normalization of the wavefunctions, the functional F to be minimized is

$$F[\{\psi_\nu\}_\nu] = E_{\text{tot}}[\{\psi_\nu\}_\nu] - \sum_\nu \epsilon_\nu \int d^3\mathbf{r} \psi_\nu(\mathbf{r})^\dagger \psi_\nu(\mathbf{r}) .$$

The variation of F leads to $4N$ Euler-Lagrange equations, since the up- and down-components of $\psi_\nu(\mathbf{r}) = \begin{pmatrix} \uparrow_\nu(\mathbf{r}) \\ \downarrow_\nu(\mathbf{r}) \end{pmatrix}$ both have a real and an imaginary part. But it is sufficient to calculate the variations with respect to the up- and down-components because

$$\left. \begin{aligned} \frac{\delta F}{\delta \text{Re } \uparrow_\nu} &= \frac{\delta F}{\delta \uparrow_\nu} + \frac{\delta F}{\delta \uparrow_\nu^*} \stackrel{!}{=} 0 \\ \frac{\delta F}{\delta \text{Im } \uparrow_\nu} &= i \frac{\delta F}{\delta \uparrow_\nu} - i \frac{\delta F}{\delta \uparrow_\nu^*} \stackrel{!}{=} 0 \end{aligned} \right\} \Rightarrow \frac{\delta F}{\delta \uparrow_\nu^*} = 0 .$$

This leads to the differential equations

$$\begin{aligned} \frac{\delta F}{\delta \uparrow_\nu^*} &= \left(\hat{\mathbf{p}}^2 + V_{\text{H}} + V_{\text{ext}} + \frac{\delta E_{\text{xc}}}{\delta n} + \frac{\delta E_{\text{xc}}}{\delta m_z} - \epsilon_\nu \right) \uparrow_\nu + \left(\frac{\delta E_{\text{xc}}}{\delta m_x} - i \frac{\delta E_{\text{xc}}}{\delta m_y} \right) \downarrow_\nu , \\ \frac{\delta F}{\delta \downarrow_\nu^*} &= \left(\hat{\mathbf{p}}^2 + V_{\text{H}} + V_{\text{ext}} + \frac{\delta E_{\text{xc}}}{\delta n} - \frac{\delta E_{\text{xc}}}{\delta m_z} - \epsilon_\nu \right) \downarrow_\nu + \left(\frac{\delta E_{\text{xc}}}{\delta m_x} + i \frac{\delta E_{\text{xc}}}{\delta m_y} \right) \uparrow_\nu . \end{aligned} \quad (2.9)$$

Note that the prefactor $\frac{1}{2}$ of V_{H} appears in the functional F but not in the expression for $\frac{\delta F}{\delta \uparrow_\nu^*}$ since both factors of $n(\mathbf{r}) n(\mathbf{r}')$ depend on \uparrow_ν^* .

Within the LDA the variations of E_{xc} get a simple structure. In Chapter 2.3 it is shown that

$$\frac{\delta E_{\text{xc}}}{\delta \uparrow_\nu^*} = V_{\text{xc}}^{(\uparrow, \uparrow)}(n, \mathbf{m}) \uparrow_\nu + V_{\text{xc}}^{(\uparrow, \downarrow)}(n, \mathbf{m}) \downarrow_\nu \quad , \quad \frac{\delta E_{\text{xc}}}{\delta \downarrow_\nu^*} = V_{\text{xc}}^{(\downarrow, \uparrow)}(n, \mathbf{m}) \uparrow_\nu + V_{\text{xc}}^{(\downarrow, \downarrow)}(n, \mathbf{m}) \downarrow_\nu$$

where $V_{\text{xc}}^{(\uparrow,\uparrow)}$, $V_{\text{xc}}^{(\uparrow,\downarrow)}$, $V_{\text{xc}}^{(\downarrow,\uparrow)}$, $V_{\text{xc}}^{(\downarrow,\downarrow)}$ are functions of $n(\mathbf{r})$, $\mathbf{m}(\mathbf{r})$, i.e. in real-space they depend only locally on the densities. This allows to express the variations of E_{xc} in the form of a local potential, i.e. an *exchange-correlation potential* matrix

$$\mathbf{V}_{\text{xc}}(\mathbf{r}) = \mathbf{V}_{\text{xc}}(n(\mathbf{r}), \mathbf{m}(\mathbf{r})) = \begin{pmatrix} V_{\text{xc}}^{(\uparrow,\uparrow)}(n, \mathbf{m}) & V_{\text{xc}}^{(\uparrow,\downarrow)}(n, \mathbf{m}) \\ V_{\text{xc}}^{(\downarrow,\uparrow)}(n, \mathbf{m}) & V_{\text{xc}}^{(\downarrow,\downarrow)}(n, \mathbf{m}) \end{pmatrix} \quad (2.10)$$

that can *in practice* be calculated from the densities. Inserted in (2.9) the matrix \mathbf{V}_{xc} has the form of a density-dependent potential, the Euler-Lagrange equations (2.9) can be written as

$$\mathcal{H}[n, \mathbf{m}] \psi_\nu = \epsilon_\nu \psi_\nu \quad \text{with} \quad \mathcal{H}[n, \mathbf{m}] = \hat{\mathbf{p}}^2 + (V_{\text{H}}[n] + V_{\text{ext}}) \mathbb{1} + \mathbf{V}_{\text{xc}}[n, \mathbf{m}]. \quad (2.11)$$

This equation is called *Kohn-Sham equation*. It has a formal analogy to a single-particle Schrödinger equation with an *effective potential* $V_{\text{eff}} = (V_{\text{H}} + V_{\text{ext}}) \mathbb{1} + \mathbf{V}_{\text{xc}}$. The Hamiltonian \mathcal{H} depends on the densities, thus the selfconsistent solution for $\{\psi_\nu\}_\nu$, V_{H} , \mathbf{V}_{xc} has to be calculated iteratively.

The sought-after solution of (2.11) is the one given by the set of orthonormal trial functions $\{\psi_\nu\}_{\nu \in [1, N]}$ that minimizes E_{tot} . Of course, these functions are eigenfunctions of the Hamiltonian $\mathcal{H}[n, \mathbf{m}]$ in selfconsistency. In practice, it is assumed that E_{tot} is minimized by the set of eigenfunctions of \mathcal{H} with the N lowest eigenvalues $\{\epsilon_\nu\}_\nu$. Thus, a *Fermi energy* ϵ_{F} is introduced for the auxiliary single-particle wavefunctions $\{\psi_\nu\}_\nu$ and the densities (2.7) are calculated from the N single-particle eigenfunctions of \mathcal{H} with $\epsilon_\nu < \epsilon_{\text{F}}$. The total electronic energy E_{tot} , however, needs to be calculated from Eqn. (2.8).

2.3 Local density approximation

All electron-electron interactions beyond the Hartree term $\int d^3\mathbf{r} \frac{1}{2} V_{\text{H}}(\mathbf{r}) n(\mathbf{r})$ are represented by the exchange-correlation energy functional $E_{\text{xc}}[n, \mathbf{m}]$.

As already mentioned in Chapter 2.2, E_{xc} is in many cases successfully approximated by the local density approximation

$$E_{\text{xc}}[n, \mathbf{m}] \approx \int d^3\mathbf{r} f_{\text{lda}}(n(\mathbf{r}), |\mathbf{m}(\mathbf{r})|). \quad (2.12)$$

In real space the integrand f_{lda} is a function of the densities, thus it depends only on their local values. From symmetry reasons, it is obvious that it cannot depend on the direction of \mathbf{m} . f_{lda} is an universal function that can be applied to a wide class of systems. It is derived for the homogeneous electron gas and is exact in the limit of spatial constant densities $\{n, \mathbf{m}\}$. A widely used approximation of f_{lda} is obtained by a RPA [72, 98]. The most accurate approximations are obtained with quantum Monte Carlo calculations of the homogeneous electron gas [e.g. 22].

For the case of spatially rapidly varying densities the approximation (2.12) needs to be improved. For *collinear* magnetization densities (i.e. $\mathbf{m}(\mathbf{r}) = m(\mathbf{r}) \mathbf{e}_m$, $\mathbf{e}_m = \text{const}$) approximations of the form

$$E_{\text{xc}}[n, m] \approx \int d^3\mathbf{r} f_{\text{gga}}(n(\mathbf{r}), |\nabla n(\mathbf{r})|, |m(\mathbf{r})|, |\nabla m(\mathbf{r})|)$$

have been constructed [e.g. 79, 80]. These approximation is called *generalized gradient approximation* (GGA). Simple generalizations of the known GGA functionals to non-collinear

situations are discussed in Appendix A.1.

According to Eqns. (2.9) the variations of E_{xc} can be written as

$$\begin{pmatrix} \frac{\delta E_{xc}}{\delta \uparrow_\nu^*} \\ \frac{\delta E_{xc}}{\delta \downarrow_\nu^*} \end{pmatrix} = \begin{pmatrix} \frac{\delta E_{xc}}{\delta n} + \frac{\delta E_{xc}}{\delta m_z} & \frac{\delta E_{xc}}{\delta m_x} - i \frac{\delta E_{xc}}{\delta m_y} \\ \frac{\delta E_{xc}}{\delta m_x} + i \frac{\delta E_{xc}}{\delta m_y} & \frac{\delta E_{xc}}{\delta n} - \frac{\delta E_{xc}}{\delta m_z} \end{pmatrix} \begin{pmatrix} \uparrow_\nu \\ \downarrow_\nu \end{pmatrix}.$$

Within the local density approximation (2.12) the last equation simplifies to

$$\begin{pmatrix} \frac{\delta E_{xc}}{\delta \uparrow_\nu^*} \\ \frac{\delta E_{xc}}{\delta \downarrow_\nu^*} \end{pmatrix} = \begin{pmatrix} \frac{\partial f_{lda}}{\partial n} + \frac{\partial f_{lda}}{\partial m_z} & \frac{\partial f_{lda}}{\partial m_x} - i \frac{\partial f_{lda}}{\partial m_y} \\ \frac{\partial f_{lda}}{\partial m_x} + i \frac{\partial f_{lda}}{\partial m_y} & \frac{\partial f_{lda}}{\partial n} - \frac{\partial f_{lda}}{\partial m_z} \end{pmatrix} \begin{pmatrix} \uparrow_\nu \\ \downarrow_\nu \end{pmatrix} = \mathbf{V}_{xc} \psi_\nu$$

$$\text{with } \mathbf{V}_{xc}(n, \mathbf{m}) = V_{xc} \mathbb{1} + \mathbf{B}_{xc} \cdot \boldsymbol{\sigma} \quad , \quad V_{xc}(n, \mathbf{m}) = \frac{\partial f_{lda}}{\partial n} \quad , \quad \mathbf{B}_{xc}(n, \mathbf{m}) = \frac{\partial f_{lda}}{\partial |\mathbf{m}|} \frac{\mathbf{m}}{|\mathbf{m}|}.$$

Thus, within LDA the exchange-correlation potential V_{xc} has the structure (2.10).

The derivation of an exchange-correlation potential for GGA functionals is shown in Appendix A.1.

2.4 Total energy

The electronic energy E_{tot} is given by the functional (2.8). With (2.11) this can be rewritten as

$$\begin{aligned} E_{tot} &= \int d^3\mathbf{r} \left(\sum_{\nu=1}^N \psi_\nu^\dagger \hat{\mathbf{p}}^2 \psi_\nu + \left(\frac{1}{2}V_H + V_{ext}\right) n \right) + E_{xc} \\ &= \sum_{\nu=1}^N \int d^3\mathbf{r} \psi_\nu^\dagger \left(\hat{\mathbf{p}}^2 + \left(\frac{1}{2}V_H + V_{ext}\right) \mathbb{1} \right) \psi_\nu + E_{xc} \\ &= \sum_{\nu=1}^N \left(\epsilon_\nu - \int d^3\mathbf{r} \psi_\nu^\dagger \left(\frac{1}{2}V_H \mathbb{1} + \mathbf{V}_{xc} \right) \psi_\nu \right) + E_{xc} \\ &= \sum_{\nu=1}^N \epsilon_\nu - \underbrace{\int d^3\mathbf{r} \left(\left(\frac{1}{2}V_H + V_{xc}\right) n + \mathbf{B}_{xc} \cdot \mathbf{m} \right)}_{= E_{dc}} + E_{xc}. \end{aligned} \quad (2.13)$$

E_{dc} is called *double-counting term* in analogy of the double-counting term $\int d^3\mathbf{r} \frac{1}{2}V_H n$ of the Hartree method. In the actual calculations the double-counting term can be expressed in a slightly different way for better numerical accuracy (cf. Chapter 3.2).

The formulation $E_{tot} = \sum_\nu \epsilon_\nu + E_{dc}$ can be clarifying since one often has some intuitive picture about the behaviour of the single-particle energies $\{\epsilon_\nu\}_\nu$. For small changes in the external potential V_{ext} it is justified to neglect the changes in E_{dc} (cf. local force theorem, Chapter 3.9.1 and Appendix C).

The energy E that is relevant for the analysis of an entire chemical, structural and magnetic configuration is the sum of the electronic energy E_{tot} and the energy E_{ii} due to the Coulomb interaction between the atomic nuclei:

$$E = E_{tot} + E_{ii}.$$

With $\mathbf{R}^{(\mu)}$ and $Z^{(\mu)}$ denoting position and atomic number of the μ th nucleus and M denoting the number of atoms one gets

$$E_{\text{ii}} = \sum_{\substack{\mu, \mu' \in \{1, M\} \\ \mu \neq \mu'}} \frac{Z^{(\mu)} Z^{(\mu')}}{|\mathbf{R}^{(\mu)} - \mathbf{R}^{(\mu')}|}.$$

2.5 Relativistic Kohn-Sham equation

The formalism of the previous chapters can be generalized to relativistic systems. A generalization of the theorem of Hohenberg and Kohn to QED states that the ground state is a unique functional of the relativistic four-currents $j^\mu(\mathbf{r}) = \psi(\mathbf{r})^\dagger \gamma^0 \gamma^\mu \psi(\mathbf{r})$ [85]. In analogy to the non-relativistic case the total energy is decomposed in the sum of single particle kinetic energies, the Hartree term and the exchange-correlation term E_{xc} . Of course in the relativistic theory the kinetic energies are calculated from the Dirac equation. In solids with no external magnetic field one can use the charge and spin densities n , \mathbf{m} to approximate the four-currents and to construct a local approximation for the exchange-correlation energy functional $E_{\text{xc}}[n, \mathbf{m}] \approx \int d^3\mathbf{r} f_{\text{xc}}(n(\mathbf{r}), \mathbf{m}(\mathbf{r}))$ [34, 65]. The charge and spin densities are much easier to handle than the four-currents, in the “standard” representation (cf. e.g. [59]) that is used throughout this thesis they are defined as

$$n(\mathbf{r}) = \sum_\nu \begin{pmatrix} \varphi_\nu(\mathbf{r}) \\ \chi_\nu(\mathbf{r}) \end{pmatrix}^\dagger \begin{pmatrix} \varphi_\nu(\mathbf{r}) \\ \chi_\nu(\mathbf{r}) \end{pmatrix}, \quad \mathbf{m}(\mathbf{r}) = \sum_\nu \begin{pmatrix} \varphi_\nu(\mathbf{r}) \\ \chi_\nu(\mathbf{r}) \end{pmatrix}^\dagger \begin{pmatrix} \boldsymbol{\sigma} & 0 \\ 0 & \boldsymbol{\sigma} \end{pmatrix} \begin{pmatrix} \varphi_\nu(\mathbf{r}) \\ \chi_\nu(\mathbf{r}) \end{pmatrix}.$$

The total energy in absence of an external magnetic field becomes

$$\begin{aligned} E_{\text{tot}} = \int d^3\mathbf{r} \left(\sum_\nu \begin{pmatrix} \varphi_\nu(\mathbf{r}) \\ \chi_\nu(\mathbf{r}) \end{pmatrix}^\dagger \begin{pmatrix} +\frac{1}{2}c^2 \mathbb{1} & c \boldsymbol{\sigma} \cdot \hat{\mathbf{p}} \\ c \boldsymbol{\sigma} \cdot \hat{\mathbf{p}} & -\frac{1}{2}c^2 \mathbb{1} \end{pmatrix} \begin{pmatrix} \varphi_\nu(\mathbf{r}) \\ \chi_\nu(\mathbf{r}) \end{pmatrix} \right. \\ \left. + \left(\frac{1}{2}V_{\text{H}}(\mathbf{r}) + V_{\text{ext}}(\mathbf{r}) \right) n(\mathbf{r}) \right. \\ \left. + f_{\text{xc}}(n(\mathbf{r}), \mathbf{m}(\mathbf{r})) \right). \end{aligned}$$

With this ansatz for E_{tot} the variation of the total energy with respect to the normalized wavefunctions can be done the same way as in the non-relativistic case. It leads to the *Kohn-Sham Dirac equation*

$$\begin{aligned} \left(c \boldsymbol{\sigma} \cdot \hat{\mathbf{p}} \begin{pmatrix} 0 & \mathbb{1} \\ \mathbb{1} & 0 \end{pmatrix} + \frac{1}{2}c^2 \begin{pmatrix} +\mathbb{1} & 0 \\ 0 & -\mathbb{1} \end{pmatrix} + (V_{\text{eff}} + \boldsymbol{\sigma} \cdot \mathbf{B}_{\text{xc}}) \begin{pmatrix} \mathbb{1} & 0 \\ 0 & \mathbb{1} \end{pmatrix} \right) \begin{pmatrix} \varphi_\nu \\ \chi_\nu \end{pmatrix} \\ = (\epsilon_\nu + \frac{1}{2}c^2) \begin{pmatrix} \varphi_\nu \\ \chi_\nu \end{pmatrix}. \end{aligned} \tag{2.14}$$

Here the eigenenergies ϵ_ν are given with respect to the rest-mass energy $\frac{1}{2}c^2$ and $V_{\text{eff}} = V_{\text{H}} + V_{\text{ext}} + V_{\text{xc}}$ denotes the effective potential. The exchange-correlation potential V_{xc} , \mathbf{B}_{xc} is defined in analogy to the non-relativistic case.

2.5.1 Spin-orbit coupling

In this thesis Eqn. (2.14) is not solved exactly, but the Kohn-Sham equation (2.11) is extended by some relativistic corrections that are deduced from (2.14). These approximations are further described in Chapter 3.8. In this chapter the spin-orbit coupling (SOC)

operator is deduced from the well-known $\frac{1}{c^2}$ -expansion of the Dirac equation (2.14) (cf. e.g. [9]):

$$\begin{aligned}
\mathcal{H}_{\text{rel}} \phi_\nu &= \epsilon_\nu \phi_\nu \quad \text{where} \quad \varphi_\nu = \left(1 - \frac{1}{2c^2} \hat{\mathbf{p}}^2\right) \phi_\nu + \mathcal{O}(c^{-4}) \\
\chi_\nu &= \left(\frac{1}{c} (\boldsymbol{\sigma} \cdot \hat{\mathbf{p}}) + \frac{1}{c^3} \left(-\frac{1}{2} \hat{\mathbf{p}}^2 + V - \epsilon_\nu\right) (\boldsymbol{\sigma} \cdot \hat{\mathbf{p}})\right) \phi_\nu + \mathcal{O}(c^{-5}) \\
\mathcal{H}_{\text{rel}} &= \hat{\mathbf{p}}^2 + V \\
&\quad + \frac{1}{c^2} \left(-\hat{\mathbf{p}}^4 + \frac{1}{2} (\nabla^2 V) + \boldsymbol{\sigma} \cdot ((\nabla V_{\text{eff}}) \times \hat{\mathbf{p}})\right) + \frac{1}{c^2} \mathbf{B} \\
&\quad + \mathcal{O}(c^{-4}) \\
V &= V_{\text{eff}} \mathbb{1} + \boldsymbol{\sigma} \cdot \mathbf{B}_{\text{xc}} = (V_{\text{H}} + V_{\text{ext}} + V_{\text{xc}}) \mathbb{1} + \boldsymbol{\sigma} \cdot \mathbf{B}_{\text{xc}} .
\end{aligned}$$

The term \mathbf{B} is a (2×2) -matrix, whose elements contain products of the form $(\frac{d}{dr_s} B_{s'}) \hat{p}_{s''}$ and $B_s \hat{p}_{s'} \hat{p}_{s''}$. Usually $\frac{1}{c^2} \mathbf{B}$ can be neglected as \mathbf{B}_{xc} and $\nabla \cdot \mathbf{B}_{\text{xc}}$ are very small compared to ∇V_{H} close to the atom core where the momentum is high.

The terms that couple real- and spin-space are dominated by the SOC operator

$$\mathcal{H}_{\text{so}} = \frac{1}{c^2} \boldsymbol{\sigma} \cdot ((\nabla V_{\text{eff}}) \times \hat{\mathbf{p}}) . \quad (2.15)$$

In the region where the potential gradient is large (i.e. close to the atom core) the potential can be approximated well by its spherically symmetric average (i.e. $V_{\text{eff}}(\mathbf{r}) \approx \tilde{V}_{\text{eff}}(r)$, $r = |\mathbf{r} - \mathbf{R}|$ where \mathbf{R} denotes the position of the nucleus). Then Eqn. (2.15) can be simplified by using

$$(\nabla V_{\text{eff}}) \times \hat{\mathbf{p}} \approx \left(\frac{d}{dr} \tilde{V}_{\text{eff}}\right) \mathbf{r} \times \hat{\mathbf{p}} = \left(\frac{d}{dr} \tilde{V}_{\text{eff}}\right) \hat{\mathbf{L}} .$$

The spin-orbit coupling operator gets the form

$$\mathcal{H}_{\text{so}} = v(r) \boldsymbol{\sigma} \cdot \hat{\mathbf{L}} \quad (2.16)$$

where $v(r)$ is a spherically symmetric function that decays fast for increasing distance r from the nucleus.

Chapter 3

Solving the Kohn-Sham equation, the FLAPW method

This chapter gives an introduction on the computational method that is used in this thesis to solve the Kohn-Sham equation (2.11) selfconsistently. Most attention is paid to the parts of the method one has to be aware of when performing the actual calculations.

The calculations were performed with the *full-potential linearized augmented plane wave (FLAPW) method* implemented in the FLEUR code [36]. A good introduction to the computational method can be found in [94], details of the implementation are well described in [54].

For simplicity the methods are first explained for a spinless Kohn-Sham equation

$$\left(\hat{\mathbf{p}}^2 + V_{\text{H}}[n] + V_{\text{ext}} + V_{\text{xc}}(n) \right) \psi_{\nu} = \epsilon_{\nu} \psi_{\nu} . \quad (3.1)$$

The generalization to the magnetic case is discussed thereupon.

3.1 The selfconsistency cycle

Eqn. (3.1) is solved iteratively with the following selfconsistency cycle:

- Starting from an input density $n_N^{(\text{in})}$ the density-dependent potential $V_{\text{H}}[n_N^{(\text{in})}] + V_{\text{xc}}(n_N^{(\text{in})})$ is calculated.
- The eigenstates of the Kohn-Sham equation (3.1) are determined for the potential $V = V_{\text{H}}[n_N^{(\text{in})}] + V_{\text{ext}} + V_{\text{xc}}(n_N^{(\text{in})})$.

Since only periodic crystals are considered, the Bloch theorem is applied. The Brillouin zone is sampled by a finite mesh of Bloch vectors $\{\mathbf{k}\}$. For each of these \mathbf{k} -points the secular equation

$$\mathcal{H} \psi_{\mathbf{k},\nu} = (\hat{\mathbf{p}}^2 + V) \psi_{\mathbf{k},\nu} = \epsilon_{\mathbf{k},\nu} \psi_{\mathbf{k},\nu}$$

is solved in the subspace that restricts $\{e^{-i\mathbf{k}\cdot\mathbf{r}} \psi_{\mathbf{k},\nu}\}_{\nu}$ to lattice-periodic functions.

- The Fermi energy and the occupation numbers $w_{\mathbf{k},\nu}$ of the Kohn-Sham states $\{\psi_{\mathbf{k},\nu}\}$ are determined. Of course, all states from all \mathbf{k} -points have to be considered when the Fermi energy is calculated.

- The output density $n_N^{(\text{out})}$ is determined by summing over all occupied states of all \mathbf{k} -points:

$$n_N^{(\text{out})} = \sum_{\mathbf{k}, \nu} w_{\mathbf{k}, \nu} \psi_{\mathbf{k}, \nu}^\dagger \psi_{\mathbf{k}, \nu} .$$

- A new input density $n_{N+1}^{(\text{in})}$ for the next iteration is calculated by mixing of $n_N^{(\text{in})}$ and $n_N^{(\text{out})}$. In most cases, the selfconsistency cycle does not converge if the output density $n_N^{(\text{out})}$ is used directly as new input density $n_{N+1}^{(\text{in})}$. In the *simple mixing* scheme the new input density is obtained by

$$n_{N+1}^{(\text{in})} = (1 - \alpha) n_N^{(\text{in})} + \alpha n_N^{(\text{out})} .$$

Typically, the damping factor is $\alpha < 0.1$. In [27] it is shown that the selfconsistency cycle always converges for sufficiently small α . The speed of the convergence can be improved with more sophisticated mixing schemes. The schemes used in this thesis are described e.g. in [11].

3.2 Calculating the total energy

The total electronic energy E_{tot} is given by the functional (2.8). If selfconsistency is achieved, it can be calculated by Eqn. (2.13). In the actual calculations, however, the density n is never exactly converged. Therefore, the density $n^{(\text{in})}$ that is used to construct the potential V_{eff} in the Kohn-Sham equation (2.11) differs from the density $n^{(\text{out})}$ that is constructed from the solutions $\{\psi_\nu\}$ of (2.11):

$$\left(\hat{\mathbf{p}}^2 + \underbrace{V_{\text{H}}[n^{(\text{in})}] + V_{\text{ext}} + V_{\text{xc}}[n^{(\text{in})}]}_{V_{\text{eff}}[n^{(\text{in})}]} \right) \psi_\nu = \epsilon_\nu \psi_\nu \quad , \quad n^{(\text{in})} \neq n^{(\text{out})} = \sum_\nu \psi_\nu^\dagger \psi_\nu .$$

In order to minimize the error, the total energy E_{tot} should be calculated by inserting only one density in the energy functional (2.8). This has to be $n^{(\text{out})}$: The evaluation of the kinetic energy term $\sum_\nu \psi_\nu^\dagger \hat{\mathbf{p}}^2 \psi_\nu$ requires the knowledge of the wavefunctions, but the wavefunctions are not known for $n^{(\text{in})}$ since the latter is obtained from the density-mixing process. Thus, the total electronic energy is calculated with (2.8):

$$E_{\text{tot}}[n^{(\text{out})}] = \int d^3\mathbf{r} \left(\sum_\nu \psi_\nu^\dagger \hat{\mathbf{p}}^2 \psi_\nu + n^{(\text{out})} V_{\text{ext}} \right) + E_{\text{H}}[n^{(\text{out})}] + E_{\text{xc}}[n^{(\text{out})}] .$$

For numerical reasons, it is not convenient to evaluate the kinetic-energy term directly. The derivatives can be avoided since the wavefunctions $\{\psi_\nu\}$ are solutions of the Kohn-Sham equation (2.11):

$$(\hat{\mathbf{p}}^2 + V_{\text{eff}}[n^{(\text{in})}]) \psi_\nu = \epsilon_\nu \psi_\nu \quad \Rightarrow \quad \sum_\nu \psi_\nu^\dagger \hat{\mathbf{p}}^2 \psi_\nu = \sum_\nu \psi_\nu^\dagger (\epsilon_\nu - V_{\text{eff}}[n^{(\text{in})}]) \psi_\nu .$$

The last expression allows to simplify $E_{\text{tot}}[n^{(\text{out})}]$:

$$E_{\text{tot}}[n^{(\text{out})}] = \sum_\nu \epsilon_\nu + \int d^3\mathbf{r} n^{(\text{out})} \left(-V_{\text{H}}[n^{(\text{in})}] - V_{\text{xc}}[n^{(\text{in})}] \right) + E_{\text{H}}[n^{(\text{out})}] + E_{\text{xc}}[n^{(\text{out})}] . \quad (3.2)$$

The right-hand side of (3.2) can be interpreted as a functional \tilde{E} that depends on $n^{(\text{out})}$, $n^{(\text{in})}$, $\{\epsilon_\nu\}$:

$$\tilde{E}[n_1, n_2, \{\epsilon_\nu\}] = E_{\text{tot}}[n_1] \Big|_{n^{(\text{in})}=n_2}.$$

For a reasonably well converged charge density one can write

$$n^{(\text{out})} = n^{(\text{in})} + \delta n \quad \text{with} \quad \|\delta n\| \ll \|n^{(\text{in})}\|$$

and $E_{\text{tot}}[n^{(\text{out})}]$ can be approximated by

$$E_{\text{tot}}[n^{(\text{out})}] = \tilde{E}[n^{(\text{out})}, n^{(\text{in})}, \{\epsilon_\nu\}] \approx \\ \tilde{E}[n^{(\text{in})}, n^{(\text{in})}, \{\epsilon_\nu\}] + \int d^3\mathbf{r} (\delta n) \left. \frac{\delta \tilde{E}[\tilde{n}, n^{(\text{in})}, \{\epsilon_\nu\}]}{\delta \tilde{n}} \right|_{\tilde{n}=n^{(\text{in})}} + \mathcal{O}((\delta n)^2).$$

The second term in the last expression vanishes since

$$\left. \frac{\delta \tilde{E}[\tilde{n}, n^{(\text{in})}, \{\epsilon_\nu\}]}{\delta \tilde{n}} \right|_{\tilde{n}=n^{(\text{in})}} = -V_{\text{H}}[n^{(\text{in})}] - V_{\text{xc}}[n^{(\text{in})}] + \left(\underbrace{\frac{\delta E_{\text{H}}[\tilde{n}]}{\delta \tilde{n}}}_{V_{\text{H}}[\tilde{n}]} + \underbrace{\frac{\delta E_{\text{xc}}[\tilde{n}]}{\delta \tilde{n}}}_{V_{\text{xc}}[\tilde{n}]} \right) \Big|_{\tilde{n}=n^{(\text{in})}} = 0.$$

Therefore, the expression

$$E_{\text{tot}}[n^{(\text{out})}] \approx \tilde{E}[n^{(\text{in})}, n^{(\text{in})}, \{\epsilon_\nu\}] = \\ \sum_{\nu} \epsilon_{\nu} - \int d^3\mathbf{r} n^{(\text{in})} \left(\frac{1}{2} V_{\text{H}}[n^{(\text{in})}] + V_{\text{xc}}[n^{(\text{in})}] \right) + E_{\text{xc}}[n^{(\text{in})}] \quad (3.3)$$

is a good approximation for (3.2) if the density is well converged. Note, that (3.3) has the same structure as (2.13).

Expression (3.2) is slightly more accurate, but Expression (3.3) is easier to implement in the computer code since it avoids the calculation of the potential from the output-density. In the code used in this thesis E_{tot} is calculated with (3.3).

3.3 Solving the secular equation

In each loop of the selfconsistency cycle the secular problem of the Kohn-Sham Hamiltonian has to be solved. This is done differently for the core and valence states.

3.3.1 Core states

For the core states the relativistic effects are strong. Therefore, the Kohn-Sham Dirac equation (2.14) is used and the states are represented by four-spinors.

The core states are localized very close to the nuclei. Therefore, for the calculation of core states the atoms can be treated as isolated atoms. Within a certain distance (i.e. R_{MT} , see below) from the respective nucleus the potential is replaced by its spherical average, beyond this distance it is neglected. This simplifies the solution of the Dirac equation significantly.

3.3.2 Valence states

The valence states are expanded in LAPW functions (cf. Chapter 3.4). They are called basis functions for the valence states, although they do not really form a basis of the Hilbert space: These basis functions are linear independent but not orthogonal. Furthermore, the number of basis functions is finite.

The set of basis functions depends on the Bloch vector \mathbf{k} . For a fixed \mathbf{k} -point the basis functions can be labeled with (\mathbf{G}, \mathbf{k}) . In this Chapter 3.3 the index \mathbf{k} is dropped for simplicity, $\{|\mathbf{G}\rangle\}_{\mathbf{G}}$ denotes the set of basis functions.

The ν th eigenstate of \mathcal{H} expanded in this basis functions has the form $|\psi_\nu\rangle = \sum_{\mathbf{G}} c_{\nu,\mathbf{G}} |\mathbf{G}\rangle$ and the eigenvalue equation has the form

$$\mathcal{H} \sum_{\mathbf{G}} c_{\nu,\mathbf{G}} |\mathbf{G}\rangle = \epsilon_\nu \sum_{\mathbf{G}} c_{\nu,\mathbf{G}} |\mathbf{G}\rangle \quad \Rightarrow \quad \sum_{\mathbf{G}'} \langle \mathbf{G}' | \mathcal{H} | \mathbf{G} \rangle c_{\nu,\mathbf{G}} = \epsilon_\nu \sum_{\mathbf{G}} \langle \mathbf{G}' | \mathbf{G} \rangle c_{\nu,\mathbf{G}} .$$

In the actual calculations a finite basis set has to be used, therefore the exact eigenvalue equation is approximately represented by the matrix equation

$$(H - \epsilon_\nu S) \mathbf{c}_\nu = 0 \quad \text{where} \quad H_{\mathbf{G}',\mathbf{G}} = \langle \mathbf{G}' | \mathcal{H} | \mathbf{G} \rangle \quad , \quad S_{\mathbf{G}',\mathbf{G}} = \langle \mathbf{G}' | \mathbf{G} \rangle . \quad (3.4)$$

The (hermitian) matrices H and S are called Hamiltonian matrix and overlap matrix respectively. The overlap matrix is positive definite. This becomes clear as it can be written as $S = T T^\dagger$ where T denotes the transformation matrix from the (linear independent) LAPWs to an orthogonal basis set. In a standard secular equation the overlap matrix is the unit matrix, an equation of the form (3.4) is called *generalized eigenvalue problem*. The transformation of this generalized eigenvalue problem to an equivalent eigenvalue problem of a hermitian matrix of same rank can be found in numerical text books [e.g. 104].

One should keep in mind that the solution of (3.4) has better numerical stability when the off-diagonal elements of S are small.

Usually the diagonalization of the Hamiltonian is the most time consuming part of the calculations, it scales cubic with the number of basis functions $\{\mathbf{G}\}$.

3.4 LAPW basis functions

This chapter introduces the basis set that is used to expand the solutions of the Kohn-Sham equation in the valence band. The right choice of the basis set is very critical in these kind of calculations. It is already mentioned in the previous chapter that the diagonalization of the Hamiltonian matrix is the most time consuming part in the calculations. Therefore it is very important to keep the number of basis functions small, but they need to be able to describe the lower eigenstates of \mathcal{H} properly. Furthermore for numerical reasons one has to be careful not to choose functions with a large overlap.

Plane waves form a particular simple basis set that is already suggested by the Bloch theorem. Plane waves are orthogonal, can easily be transformed from real to momentum space and can be described by simple formulas. Unfortunately wavefunctions and charge density vary very rapidly near the atomic nuclei, therefore a very large number of plane waves is needed in order to describe the electronic structure properly. A common way to circumvent this problem is the use of *pseudopotentials*. These potentials replace the effective potential of the atom nuclei and the core electrons by a relatively smooth function. They are constructed in such a way that outside a certain core-radius the corresponding wavefunctions mimic the valence electron wave functions of the all-electron system. The construction of the pseudopotentials is not trivial, besides the nuclear and Hartree potential

they have to simulate all relevant exchange and correlation effects. For many applications it is sufficient to work with pseudopotentials that have been constructed once for each chemical element and to represent the wavefunctions with plane waves.

In this thesis a different basis set is used that allows a better description of the wavefunctions near the nucleus. The investigated magnetic properties are relatively small changes to the charge density and the energies. Therefore the pseudopotential approach might not be accurate enough. In particular the spin-orbit coupling is preferably treated with an all-electron potential since it originates mainly from the region close to the nucleus where the potential gradient is high.

In the calculations presented in this thesis the wavefunctions are represented in *linearized augmented plane waves (LAPWs)*. This is a numerically very efficient and still handable basis set that is first proposed in [3]. Here the real-space is divided in several regions: In the transition region between the atoms the basis functions are simple plane waves (i.e. solutions of the Schrödinger equation with constant potential), whereas in spheres around each nucleus they are constructed from the solutions of the Schrödinger equation with spherical potential. The regions around the nuclei are called the *muffin-tin spheres* of the atoms while the remaining space is called the *interstitial region* (cf. Fig. 3.1).

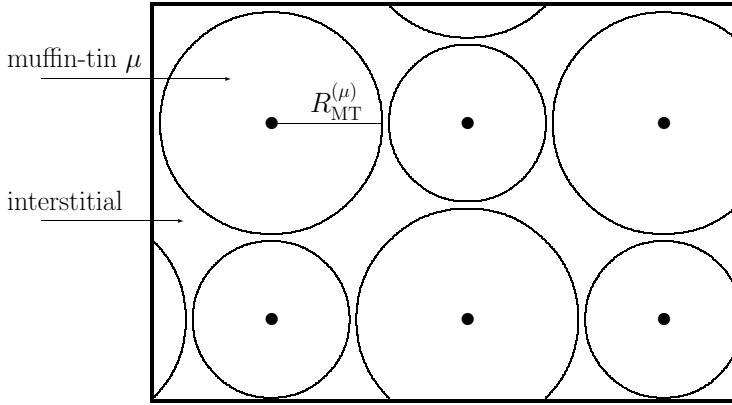


Figure 3.1: Division of the space in non-overlapping spheres and interstitial region. The muffin-tin sphere μ is centered in $\mathbf{R}^{(\mu)}$ at the nucleus of atom μ and has the *muffin-tin radius* $R_{\text{MT}}^{(\mu)}$.

For simplicity one can work with a local coordinate frame for each muffin-tin sphere, with $\mathbf{R}^{(\mu)}$ denoting the center of the μ th sphere the vector \mathbf{r} can be expressed in polar coordinates with the notation $\mathbf{r} - \mathbf{R}^{(\mu)} = r^{(\mu)} (\sin \vartheta^{(\mu)} \cos \varphi^{(\mu)} \mathbf{e}_x + \sin \vartheta^{(\mu)} \sin \varphi^{(\mu)} \mathbf{e}_y + \cos \vartheta^{(\mu)} \mathbf{e}_z)$. Then the LAPW basis function that corresponds to the wave vector \mathbf{K} in the interstitial region can be written as

$$\phi_{\mathbf{K}}(\mathbf{r}) = \begin{cases} \exp(i \mathbf{K} \cdot \mathbf{r}) & \text{interstitial region} \\ \sum_{\ell, m} Y_{\ell, m}(\vartheta^{(\mu)}, \varphi^{(\mu)}) \left(A_{\mathbf{K}, \ell, m}^{(\mu)} u_{\ell}^{(\mu)}(r^{(\mu)}) + B_{\mathbf{K}, \ell, m}^{(\mu)} \dot{u}_{\ell}^{(\mu)}(r^{(\mu)}) \right) & \text{muffin-tin sphere } \mu \end{cases} \quad (3.5)$$

Here $Y_{\ell, m}$ denote the angular dependent spherical harmonics and $u_{\ell}^{(\mu)}, \dot{u}_{\ell}^{(\mu)}$ are radial dependent functions whose construction will be described below. The coefficients $A_{\mathbf{K}, \ell, m}^{(\mu)}, B_{\mathbf{K}, \ell, m}^{(\mu)}$ are usually referred as the *muffin-tin A- and B-coefficients*. They are determined by the matching conditions that $\phi_{\mathbf{K}}(\mathbf{r})$ and $\nabla_{\mathbf{r}} \phi_{\mathbf{K}}(\mathbf{r})$ must be continuous at the muffin-tin sphere boundary.

As it is known from standard quantum-mechanics text-books, the solutions of the Schrödinger equation with a radial symmetric potential $V(r)$ can be written in the form

$Y_{\ell,m}(\vartheta, \varphi) \tilde{u}_\ell(\epsilon, r)$ where \tilde{u}_ℓ denotes the solution of the radial Schrödinger equation

$$\left(-\frac{d^2}{dr^2} - \frac{2}{r} \frac{d}{dr} + \frac{\ell(\ell+1)}{r^2} + V(r) - \epsilon \right) \tilde{u}_\ell(\epsilon, r) = 0. \quad (3.6)$$

For each ϵ this equation has one solution $\tilde{u}_\ell(\epsilon, r)$ that is regular at $r=0$, provided that the potential is reasonable. In the APW method (already suggested by Slater in 1937 [95]) the regular solutions \tilde{u} of Eqn. (3.6) are used as the radial functions u in Eqn. (3.5), whereas B is kept zero. In order to represent the same eigenstate in all regions in space the function \tilde{u} has to be constructed when ϵ is set to the band energy. This imposes some problems as the band energies are different for each eigenstate and have to be determined in the selfconsistency cycle. The introduction of the term $B_{\ell,m} \dot{u}_\ell$ in the basis functions allows to construct the radial functions u_ℓ, \dot{u}_ℓ from approximate band energies ϵ_ℓ . \dot{u} can be regarded as the linear term in the Taylor expansion of \tilde{u} around the approximate band energy:

$$\tilde{u}_\ell(\epsilon, r) = \underbrace{\tilde{u}_\ell(\epsilon_\ell, r)}_{u_\ell(r)} + (\epsilon - \epsilon_\ell) \underbrace{\frac{d}{d\epsilon} \tilde{u}_\ell(\epsilon, r) \Big|_{\epsilon=\epsilon_\ell}}_{\dot{u}_\ell(r)} + \mathcal{O}((\epsilon - \epsilon_\ell)^2).$$

Differentiating Eqn. (3.6) with respect to ϵ leads to a conditional equation for $\dot{u}_\ell(r) = \frac{d}{d\epsilon} \tilde{u}_\ell(\epsilon, r) \Big|_{\epsilon=\epsilon_\ell}$:

$$\left(-\frac{d^2}{dr^2} - \frac{2}{r} \frac{d}{dr} + \frac{\ell(\ell+1)}{r^2} + V(r) - \epsilon_\ell \right) \underbrace{\frac{d}{d\epsilon} \tilde{u}_\ell(\epsilon, r) \Big|_{\epsilon=\epsilon_\ell}}_{\dot{u}_\ell(r)} - \underbrace{\tilde{u}_\ell(\epsilon, r) \Big|_{\epsilon=\epsilon_\ell}}_{u_\ell(r)} = 0.$$

The ϵ_ℓ are called *energy parameters*. They are determined during the selfconsistency cycle from the average band energies but (in contrast to the use of plain APW basis functions) it is usually sufficient to describe all valence electrons with one $\epsilon_\ell^{(\mu)}$ for each μ, ℓ .

Note that the energy parameters, radial functions and A- and B-coefficients need to be calculated for each loop of the selfconsistency cycle since the potential changes.

Despite the fact that the basis functions are constructed under some assumptions of the potential (constant in interstitial and spherical in muffin tins) they form a very good basis in the sense that relatively few basis functions are needed to describe the solutions of the Hamiltonian. Unfortunately the LAPWs are not orthogonal, this has to be taken into account when diagonalizing the Hamiltonian (cf. Chapter 3.3).

3.4.1 LAPW basis in film geometry

The LAPW basis set as presented in the previous chapter is periodic in real-space. If one wants to describe surfaces instead of (infinite) bulk systems one has to use supercells in which the surfaces are far enough separated to minimize the interaction between them. This implies the use of a very large unit cell and therefore of a very big number of basis functions. In order to reduce this problems an extension of the LAPW basis set is introduced in [53]. It allows to calculate a film without the use of supercells. The film is periodic and infinite in two dimensions but truly finite in the third dimension. Within the film the basis functions are constructed as described in the previous chapter, but additionally to the muffin tins and interstitial two *vacuum regions* are introduced. They begin on both sides of the film and extend infinitely in the direction normal to the film plane (cf. Fig. 3.2). In this regions the basis functions are constructed from the solutions of a Schrödinger equation with asymptotically decaying potential.

One should note that in this setup the Bloch theorem can be applied only in the two dimensions with translational symmetry. X_z and \mathbf{X}_{\parallel} shall denote the component normal to the film plane and the 2-dimensional in-plane vector respectively. According to the 2-dimensional Bloch theorem the wavefunctions can be written as

$$\psi_{\mathbf{k}_{\parallel}}(\mathbf{r}) = \exp(i\mathbf{k}_{\parallel} \cdot \mathbf{r}_{\parallel}) \sum_{\mathbf{G}_{\parallel}} c_{\mathbf{k}_{\parallel}, \mathbf{G}_{\parallel}}(r_z) \exp(i\mathbf{G}_{\parallel} \cdot \mathbf{r}_{\parallel})$$

where the sum runs over all \mathbf{G}_{\parallel} -vectors that are commensurate in the 2-dimensional unit cell and thus describes a lattice periodic function. The functions $c_{\mathbf{k}_{\parallel}, \mathbf{G}_{\parallel}}(r_z)$ do not possess any periodicity, but in the interstitial region they are expanded in plane waves as well. These plane waves are commensurate in an interval that is a bit larger than the interstitial region (cf. Fig. 3.2), this way the wavefunctions have full variational freedom in the interstitial region.

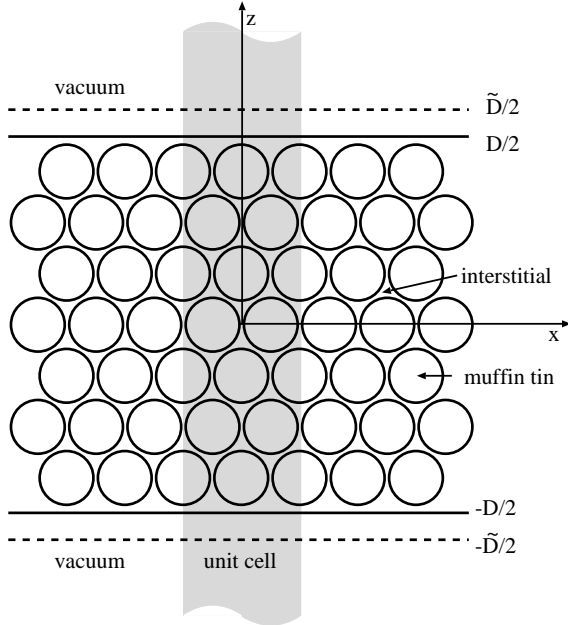


Figure 3.2: Division of the space in film calculations. In the (x, y) -plane the crystal has the usual translational symmetry, whereas in z -direction the unit cell is infinitely extended. The plane waves that describe the wavefunctions in the interstitial region have the periodicity \tilde{D} in z -direction but for $|r_z| > \frac{1}{2}D$ the basis consists of the vacuum functions that decay as z approaches infinity. The basis functions in the muffin tins are identical as in the previously described bulk case.

In the film geometry the basis functions can be labeled by the plane wave vectors \mathbf{K} like in the bulk geometry. But now $\mathbf{K} = \mathbf{k}_{\parallel} + \mathbf{G}_{\parallel} + G_z \mathbf{e}_z = (k_x + G_x) \mathbf{e}_x + (k_y + G_y) \mathbf{e}_y + G_z \mathbf{e}_z$:

$$\phi_{\mathbf{K}}(\mathbf{r}) = \begin{cases} \exp(i\mathbf{K} \cdot \mathbf{r}) & \text{interstitial} \\ & \text{region} \\ \sum_{\ell, m} Y_{\ell, m}(\vartheta^{(\mu)}, \varphi^{(\mu)}) \left(A_{\mathbf{K}, \ell, m}^{(\mu)} u_{\ell}^{(\mu)}(r^{(\mu)}) + \right. \\ \quad \left. B_{\mathbf{K}, \ell, m}^{(\mu)} \dot{u}_{\ell}^{(\mu)}(r^{(\mu)}) \right) & \text{muffin-tin} \\ & \text{sphere } \mu \\ \exp(i\mathbf{K}_{\parallel} \cdot \mathbf{r}_{\parallel}) \left(A_{\text{vac}, \mathbf{K}_{\parallel}}^{(\eta)} u_{\text{vac}, \mathbf{K}_{\parallel}}^{(\eta)}(r_z) + \right. \\ \quad \left. B_{\text{vac}, \mathbf{K}_{\parallel}}^{(\eta)} \dot{u}_{\text{vac}, \mathbf{K}_{\parallel}}^{(\eta)}(r_z) \right) & \text{vacuum} \\ & \text{region } \eta \end{cases} \quad (3.7)$$

The vacuum A- and B-coefficients and u_{vac} , \dot{u}_{vac} are constructed similar to the corresponding coefficients and functions in the muffin-tin spheres. Now $V(r_z)$ denotes the potential in the vacuum region averaged in x - and y -direction and ϵ_{vac} denotes the vacuum energy-parameter. Then u_{vac} , \dot{u}_{vac} are determined by the 1-dimensional Schrödinger equation

$$\left(\mathbf{K}_{\parallel}^2 - \frac{d^2}{dr_z^2} + V(r_z) - \epsilon_{\text{vac}} \right) u_{\text{vac}}(r_z) = 0$$

and its energy derivative

$$\left(\mathbf{K}_{\parallel}^2 - \frac{d^2}{dr_z^2} + V(r_z) - \epsilon_{\text{vac}} \right) \dot{u}_{\text{vac}}(r_z) - u_{\text{vac}}(r_z) = 0 .$$

Usually it is sufficient to describe all valence electrons with one $\epsilon_{\text{vac}}^{(\eta)}$ for each vacuum region.

3.4.2 Representation of density and potential

The previously described LAPWs are used to represent the wavefunctions. The density n and the potential V are expanded and stored in a similar fashion: In the interstitial region n, V are expanded in plane waves. The vacuum regions are sampled with an equidistant grid in the direction normal to the film plane. In each of these layers n, V are expanded in 2-dimensional plane waves. Of course, the grid in the direction normal to the film plane needs to be cut at a certain distance. The muffin-tin spheres are sampled with a logarithmic radial mesh. In each of these shells n and rV are expanded in spherical harmonics. The muffin-tin potential is represented as rV since V diverges at the nuclei.

The density and the potential possess the crystal symmetries (unlike the wavefunctions at arbitrary \mathbf{k} -vectors). Therefore, one needs to store only one expansion coefficient for all plane waves (or spherical harmonics) that are equivalent due to the crystal symmetry.

A sum of equivalent plane waves is called *star*, a sum of equivalent spherical harmonics is called *lattice harmonic*.

3.5 Calculating the density

The charge density n and magnetization density \mathbf{m} are obtained by integration over one Brillouin zone:

$$\begin{aligned} n(\mathbf{r}) &= \int_{\text{BZ}} d^3\mathbf{k} \sum_{\nu} w_{\mathbf{k},\nu} \psi_{\mathbf{k},\nu}(\mathbf{r})^{\dagger} \psi_{\mathbf{k},\nu}(\mathbf{r}) , \\ \mathbf{m}(\mathbf{r}) &= \int_{\text{BZ}} d^3\mathbf{k} \sum_{\nu} w_{\mathbf{k},\nu} \psi_{\mathbf{k},\nu}(\mathbf{r})^{\dagger} \boldsymbol{\sigma} \psi_{\mathbf{k},\nu}(\mathbf{r}) . \end{aligned} \quad (3.8)$$

Of course, only the occupied states contribute to the densities. The occupation numbers are denoted with $\{w_{\mathbf{k},\nu}\}$. The states are occupied fermionically (i.e. $w_{\mathbf{k},\nu} \leq 1$), the single-particle energy $\int d\mathbf{k} \sum_{\nu} \epsilon_{\mathbf{k},\nu}$ is minimized by occupying the all states below the Fermi energy ϵ_{F} :

$$\begin{aligned} w_{\mathbf{k},\nu} &= \begin{cases} 1 & ; \epsilon_{\mathbf{k},\nu} < \epsilon_{\text{F}} \\ 0 & ; \epsilon_{\mathbf{k},\nu} > \epsilon_{\text{F}} \end{cases} , \quad \text{with } \epsilon_{\text{F}} \text{ defined by} \\ \int_{\text{unit cell}} d^3\mathbf{r} n(\mathbf{r}) &= \int_{\text{unit cell}} d^3\mathbf{r} \int_{\text{BZ}} d^3\mathbf{k} \sum_{\nu} w_{\mathbf{k},\nu} \psi_{\mathbf{k},\nu}(\mathbf{r})^{\dagger} \psi_{\mathbf{k},\nu}(\mathbf{r}) = \frac{\# \text{ electrons}}{\text{unit cell}} . \end{aligned} \quad (3.9)$$

In practice, the occupation numbers are not calculated by a step function, but smeared out around ϵ_{F} by a Fermi distribution:

$$w_{\mathbf{k},\nu} = \frac{1}{\exp\left(\frac{1}{kT} (\epsilon_{\mathbf{k},\nu} - \epsilon_{\text{F}})\right) + 1} .$$

This improves the numerical stability: In case of a sharp Fermi distribution ($kT \searrow 0$) the occupation of a state close to the Fermi energy can change from one iteration to the next, thus the densities do not converge smoothly. For $kT > 0$ two degenerate states at the Fermi energy are both half occupied.

The \mathbf{k} -integral in Eqn. (3.8) covers the first Brillouin zone. In the actual calculations, the Brillouin zone is sampled by a discrete \mathbf{k} -mesh. In the calculations presented in this thesis the integral is evaluated simply by summing over the integrands at all \mathbf{k} -points. Of course, if \mathbf{k} -points are equivalent due to the crystal symmetry then the densities need to be evaluated only at one of these \mathbf{k} -points (i.e. the \mathbf{k} -point integration can be reduced to the irreducible wedge of the first Brillouin zone).

3.6 Calculating the potential

The potential consists of the Hartree, external and exchange-correlation part (cf. Chapter 2.2):

$$V[\mathbf{r}, n(\mathbf{r})] = V_{\text{H}}[n(\mathbf{r})] + V_{\text{ext}}(\mathbf{r}) + V_{\text{xc}}(n(\mathbf{r})) .$$

The calculation of the exchange-correlation potential V_{xc} is straightforward. For the common exchange-correlation potentials explicit parameterizations in real space are known. The density n is stored as described in Chapter 3.4.2, but it does not present a numerical difficulty to transform it into real space, calculate $V_{\text{xc}}(\mathbf{r})$ and then expand V_{xc} as described in Chapter 3.4.2. Some complications, that might arise when using a GGA potential for non-collinear magnetism, are discussed in Chapter A.2.

The Hartree potential V_{H} is given by $V_{\text{H}}(\mathbf{r}) = 2 \int d^3\mathbf{r}' \frac{n(\mathbf{r}')}{|\mathbf{r}-\mathbf{r}'|}$. The numerical evaluation of V_{H} for an arbitrary periodic charge distribution $n(\mathbf{r})$ is not trivial. For slowly varying $n(\mathbf{r})$ one can make use of the fact that the Hartree potential is local in reciprocal space. This becomes clear when realizing that V_{H} is determined by the Poisson equation:

$$\left. \begin{aligned} V_{\text{H}}(\mathbf{r}) = 2 \int d^3\mathbf{r}' \frac{n(\mathbf{r}')}{|\mathbf{r}-\mathbf{r}'|} &\Rightarrow \nabla^2 V_{\text{H}}(\mathbf{r}) = -2\pi n(\mathbf{r}) \\ n(\mathbf{r}) = \sum_{\mathbf{G}} b_{\mathbf{G}} \exp(i\mathbf{G}\cdot\mathbf{r}) & \end{aligned} \right\} \Rightarrow V_{\text{H}} = 2\pi \sum_{\mathbf{G}} \frac{b_{\mathbf{G}}}{\mathbf{G}^2} \exp(i\mathbf{G}\cdot\mathbf{r}) .$$

Close to the nuclei, however, the density gradient is very high and the Fourier sum converges very slowly. Therefore, it is not feasible to calculate the Hartree potential in reciprocal space.

The numerical problem of calculating the Coulomb potential $V_{\text{ext}}+V_{\text{H}}$ (where V_{ext} is the potential of the nuclei) can be simplified by approximating the potential shape (e.g. radial symmetric potential in the muffin tins and constant potential in the interstitial region). In the *full-potential* LAPW method no shape approximations are made, the Coulomb potential is expanded as described in Chapter 3.4.2. Even though the solution of the Poisson equation does not contribute much to the total computing time, the numerical concept is rather involved. It is based on a procedure that is first described in [99].

3.7 Magnetic calculations

Neglecting \mathbf{B}_{ext} and using the definitions

$$\mathcal{H}_{\parallel} = \hat{\mathbf{p}}^2 + V_{\text{H}} + V_{\text{ext}} + V_{\text{xc}} \quad , \quad B_{\text{xc}} = |\mathbf{B}_{\text{xc}}|$$

the Kohn-Sham equation (2.11) can be written as

$$\begin{pmatrix} \mathcal{H}_{\parallel} + B_{\text{xc}} \frac{m_z}{|\mathbf{m}|} & B_{\text{xc}} \frac{m_x - i m_y}{|\mathbf{m}|} \\ B_{\text{xc}} \frac{m_x + i m_y}{|\mathbf{m}|} & \mathcal{H}_{\parallel} - B_{\text{xc}} \frac{m_z}{|\mathbf{m}|} \end{pmatrix} \begin{pmatrix} \uparrow_{\nu} \\ \downarrow_{\nu} \end{pmatrix} = \epsilon_{\nu} \begin{pmatrix} \uparrow_{\nu} \\ \downarrow_{\nu} \end{pmatrix} . \quad (3.10)$$

In non-magnetic systems ($\mathbf{m} = B_{\text{xc}} = 0$) the last equation reduces to two equivalent equations of the form

$$\mathcal{H}_{\parallel} \psi_{\nu} = \epsilon_{\nu} \psi_{\nu} .$$

The solution of these equations has been described in the last chapters. But these methods can as well be applied to the magnetic equation (3.10). In this case for each \mathbf{K} -vector two basis functions are constructed, each is zero in one component of the spinor.

Most magnetic configurations are (approximately) *collinear*, i.e. their magnetization \mathbf{m} can be described by

$$\mathbf{m}(\mathbf{r}) = m(\mathbf{r}) \mathbf{e}_{\text{m}} \quad \text{with} \quad \mathbf{e}_{\text{m}} = \text{const} .$$

The restriction to collinear configurations reduces the computational effort a lot: With an appropriate choice of the coordinate system (i.e. $\mathbf{e}_{\text{m}} \parallel \mathbf{e}_z$) the exchange-correlation potential is diagonal in spin space and Eqn. (3.10) has the form

$$\begin{pmatrix} \mathcal{H}_{\parallel} + B_{\text{xc}} & 0 \\ 0 & \mathcal{H}_{\parallel} - B_{\text{xc}} \end{pmatrix} \begin{pmatrix} \uparrow_{\nu} \\ \downarrow_{\nu} \end{pmatrix} = \epsilon_{\nu} \begin{pmatrix} \uparrow_{\nu} \\ \downarrow_{\nu} \end{pmatrix} .$$

and Hamiltonian and overlap matrix are block-diagonal. Thus, the diagonalization of the full magnetic matrix reduces to the diagonalization of two matrices of half size that correspond to the two equations

$$(\mathcal{H}_{\parallel} + B_{\text{xc}}) \uparrow_{\nu} = \epsilon_{\nu} \uparrow_{\nu} \quad , \quad (\mathcal{H}_{\parallel} - B_{\text{xc}}) \downarrow_{\nu} = \epsilon_{\nu} \downarrow_{\nu} .$$

As the computing time for matrix diagonalization scales cubic with the matrix size, one selfconsistency iteration in a non-collinear calculation takes roughly $\frac{2^3}{2} = 4$ times longer than one iteration in an equivalent collinear calculation. A further speedup can be achieved in the collinear case if the system possesses inversion symmetry: Then the Hamiltonian and overlap matrices (Eqn. (3.4)) are real symmetric and can be diagonalized about 3 times faster than complex hermitian matrices of the same size. In practice, non-collinear calculations often take even more than $3 \cdot 4 = 12$ times than collinear calculations of the same system: The allowance of non-collinearity can reduce the symmetry of the problem (in particular the time-inversion symmetry $+\mathbf{k} \leftrightarrow -\mathbf{k}$) and thus requires a larger set of \mathbf{k} -points and in some cases the a larger unit cell. Furthermore, it can require large numerical cutoffs to resolve the energy differences between several non-collinear configurations.

The treatment of non-collinear magnetism by the code used in this thesis is in detail described in [54, 55].

3.7.1 LAPW basis functions

This chapter sketches the extensions of the basis set (3.7) that are necessary in magnetic calculations. As already mentioned, in magnetic calculations for each \mathbf{K} -vector two basis functions are constructed, namely $\phi_{\mathbf{K}}^{(\uparrow)}(\mathbf{r})$ that is purely spin-up and $\phi_{\mathbf{K}}^{(\downarrow)}(\mathbf{r})$ that is purely spin-down.

In the interstitial region the basis functions are equivalent for both spins, they have the form

$$\phi_{\mathbf{K}}^{(\uparrow)}(\mathbf{r}) = \begin{pmatrix} \exp(i\mathbf{K}\cdot\mathbf{r}) \\ 0 \end{pmatrix}, \quad \phi_{\mathbf{K}}^{(\downarrow)}(\mathbf{r}) = \begin{pmatrix} 0 \\ \exp(i\mathbf{K}\cdot\mathbf{r}) \end{pmatrix}.$$

In the muffin-tin spheres the radial components $(u(r), \dot{u}(r))$ of the basis functions are constructed from the potential via Eqn. (3.6). This potential differs between spin up and spin down, therefore the sets of basis functions for spin up and spin down differ in the muffin tins.

In the case of collinear calculations the choice of the spin coordinate frame is clear. It is chosen such that the magnetization points in z -direction, thus the potential and the Hamiltonian are diagonal in spin-space. In the case of non-collinear calculations, however, the potential matrix $\mathbf{V} = (V_{\text{H}} + V_{\text{ext}}) \mathbb{1} + \mathbf{V}_{\text{xc}}$ has off-diagonal components in spin space (namely $V_{\text{xc}}^{(\downarrow, \uparrow)}, V_{\text{xc}}^{(\uparrow, \downarrow)}$). In this case a local spin coordinate frame is introduced for each muffin-tin sphere. This frame is rotated with respect to the global spin coordinate frame that is chosen for the entire unit cell:

$$\tilde{\mathbf{V}} = \mathbf{U}_{\text{MT}}^\dagger \mathbf{V} \mathbf{U}_{\text{MT}} = (V_{\text{H}} + V_{\text{ext}}) \mathbb{1} + \begin{pmatrix} \tilde{V}_{\text{xc}}^{(\uparrow, \uparrow)} & \tilde{V}_{\text{xc}}^{(\uparrow, \downarrow)} \\ \tilde{V}_{\text{xc}}^{(\downarrow, \uparrow)} & \tilde{V}_{\text{xc}}^{(\downarrow, \downarrow)} \end{pmatrix}$$

where: The tilde ($\tilde{}$) indicates the quantities in the local coordinate frame of the μ th muffin tin.

\mathbf{U}_{MT} is a spin rotation matrix that transforms from the local to the global frame. Note that \mathbf{U}_{MT} is not the same for all muffin tins but constant within each muffin-tin sphere.

The orientation of the local frame (defined by \mathbf{U}_{MT}) should be chosen such that the total magnetic moment of the muffin tin $\tilde{\mathbf{M}} = \int_{\text{MT}} d^3\mathbf{r} \tilde{\mathbf{m}}(\mathbf{r})$ points parallel to the local \tilde{z} -direction. Then $\tilde{V}_{\text{xc}}(\mathbf{r})$ in the muffin tin is dominated by its diagonal elements $\tilde{V}_{\text{xc}}^{(\uparrow, \uparrow)}(\mathbf{r}), \tilde{V}_{\text{xc}}^{(\downarrow, \downarrow)}(\mathbf{r})$. This improves the quality of the basis functions since u, \dot{u} are constructed from the diagonal elements of $\tilde{\mathbf{V}}$. The basis functions $\{\phi_{\mathbf{K}}^{(\uparrow)}, \phi_{\mathbf{K}}^{(\downarrow)}\}$ are purely spin up or spin down in the global coordinate frame. At the muffin-tin boundary the plane waves are matched to the global spin up or spin down components of

$$Y_{\ell, m} \mathbf{U}_{\text{MT}} \begin{pmatrix} u_\ell^{(\uparrow)} \\ 0 \end{pmatrix}, \quad Y_{\ell, m} \mathbf{U}_{\text{MT}} \begin{pmatrix} 0 \\ u_\ell^{(\downarrow)} \end{pmatrix}, \quad Y_{\ell, m} \mathbf{U}_{\text{MT}} \begin{pmatrix} \dot{u}_\ell^{(\uparrow)} \\ 0 \end{pmatrix}, \quad Y_{\ell, m} \mathbf{U}_{\text{MT}} \begin{pmatrix} 0 \\ \dot{u}_\ell^{(\downarrow)} \end{pmatrix}$$

with the matching coefficients

$$\left\{ A_{\mathbf{K}, \ell, m}^{(\uparrow, \uparrow)}, A_{\mathbf{K}, \ell, m}^{(\uparrow, \downarrow)}, B_{\mathbf{K}, \ell, m}^{(\uparrow, \uparrow)}, B_{\mathbf{K}, \ell, m}^{(\uparrow, \downarrow)}, A_{\mathbf{K}, \ell, m}^{(\downarrow, \uparrow)}, A_{\mathbf{K}, \ell, m}^{(\downarrow, \downarrow)}, B_{\mathbf{K}, \ell, m}^{(\downarrow, \uparrow)}, B_{\mathbf{K}, \ell, m}^{(\downarrow, \downarrow)} \right\}_{\ell, m}.$$

In the vacuum regions the functions $u_{\text{vac}}^{(\uparrow)}, u_{\text{vac}}^{(\downarrow)}, \dot{u}_{\text{vac}}^{(\uparrow)}, \dot{u}_{\text{vac}}^{(\downarrow)}$ are constructed from $V^{(\uparrow, \uparrow)}, V^{(\downarrow, \downarrow)}$ in the global spin coordinate frame.

In the computer code that is used in this thesis the off-diagonal components of $\tilde{\mathbf{V}}_{\text{xc}}$ in the

muffin tins are neglected in the Kohn-Sham equation (3.10). Thus, within each muffin-tin sphere the exchange-correlation potential is assumed to be diagonal in the local spin coordinate frame. It is believed that the error introduced by this implementation does not play an important role in the calculations presented in Chapter 6. Plots of the magnetization density $\tilde{\mathbf{m}}(\mathbf{r})$ show that the magnetization direction of the studied systems is reasonably collinear in the region around the atoms that is assigned to the muffin-tin spheres.

3.7.2 Constrained magnetic moments

With the methods presented so far it is possible to calculate the charge and magnetization densities that are local minima of the energy functional $E_{\text{tot}}[n, \mathbf{m}]$ as defined in Eqn. (2.8) under periodic boundary conditions. It is possible to introduce further constraints into this functional without violating the theorem of Hohenberg and Kohn [26]. In particular, one can constrain the average magnetization direction

$$\hat{\mathbf{M}} = \frac{\mathbf{M}}{|\mathbf{M}|} = \left(\int_{\text{muffin tin}} d^3\mathbf{r} \mathbf{m}(\mathbf{r}) \right) \left| \int_{\text{muffin tin}} d^3\mathbf{r} \mathbf{m}(\mathbf{r}) \right|^{-1}$$

of a certain muffin-tin sphere. This is equivalent with the conditions

$$\int_{\text{muffin tin}} d^3\mathbf{r} \mathbf{m}_{\tilde{x}}(\mathbf{r}) = \int_{\text{muffin tin}} d^3\mathbf{r} \mathbf{m}_{\tilde{y}}(\mathbf{r}) = 0 \quad (3.11)$$

in the local coordinate frame of the muffin tin.

The energy functional $E_{\text{tot}}[n, \mathbf{m}]$ can be extended with these constraints by introducing the Lagrange multipliers $B_{c,\tilde{x}}$, $B_{c,\tilde{y}}$:

$$F[n, m] = E_{\text{tot}}[n, \mathbf{m}] - B_{c,\tilde{x}} \int_{\text{muffin tin}} d^3\mathbf{r} \mathbf{m}_{\tilde{x}}(\mathbf{r}) - B_{c,\tilde{y}} \int_{\text{muffin tin}} d^3\mathbf{r} \mathbf{m}_{\tilde{y}}(\mathbf{r}) .$$

The variation of $F[n, m]$ is done in the same way as described in Chapter 2.2. This leads to the Kohn-Sham equation

$$\left(\mathcal{H}_{\text{II}} \mathbb{1} + B_{\text{xc}} \boldsymbol{\sigma} \cdot \frac{\mathbf{m}}{|\mathbf{m}|} + U_{\text{MT}} (\sigma_x B_{c,\tilde{x}} + \sigma_y B_{c,\tilde{y}}) U_{\text{MT}}^\dagger \right) \begin{pmatrix} \uparrow_\nu \\ \downarrow_\nu \end{pmatrix} = \epsilon_\nu \begin{pmatrix} \uparrow_\nu \\ \downarrow_\nu \end{pmatrix} . \quad (3.12)$$

The Lagrange multipliers can be interpreted as a local magnetic field that forces the magnetization in the desired direction. Therefore $\tilde{\mathbf{B}}_c = B_{c,\tilde{x}} \mathbf{e}_{\tilde{x}} + B_{c,\tilde{y}} \mathbf{e}_{\tilde{y}}$ is called *constraining field*. The explicit dependence of the constraining field on the densities n , \mathbf{m} is not known. $\tilde{\mathbf{B}}_c$ is determined during the selfconsistency cycle, the minimal solution of the functional F needs to fulfill Eqns. (3.12) and (3.11) simultaneously.

3.7.3 Generalized Bloch theorem

In a homogeneous (helical) spin spiral the magnetization is rotated by a constant angle from one chemical lattice point to the next (cf. Fig 3.3). Such a spin spiral can be characterized by the spiral vector \mathbf{q} . The direction of \mathbf{q} defines the real-space direction along which the magnetization rotates, the rotation period is given by $2\pi |\mathbf{q}|^{-1}$. With an appropriate choice of the spin coordinate system the rotation axis points in z -direction.

With this rotation axis for the magnetization of the spin spiral there holds

$$\mathbf{m}(\mathbf{r}) = |\mathbf{m}(\mathbf{r})| \begin{pmatrix} \sin \vartheta \cos \varphi \\ \sin \vartheta \sin \varphi \\ \cos \vartheta \end{pmatrix} \Rightarrow \mathbf{m}(\mathbf{r} + \mathbf{R}) = |\mathbf{m}(\mathbf{r})| \begin{pmatrix} \sin \vartheta \cos(\varphi + \mathbf{q} \cdot \mathbf{R}) \\ \sin \vartheta \sin(\varphi + \mathbf{q} \cdot \mathbf{R}) \\ \cos \vartheta \end{pmatrix} \quad (3.13)$$

where \mathbf{R} is a lattice vector of the chemical lattice.

ϑ is called *cone angle*. It describes the deviation between the magnetization direction and the rotation axis.

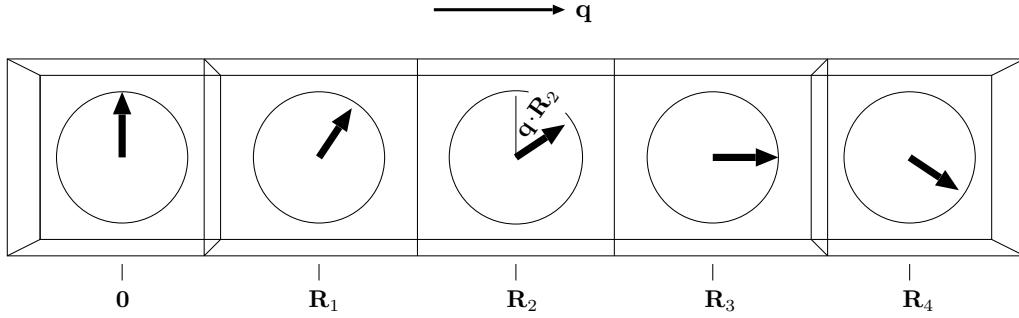


Figure 3.3: Spin spiral with $\vartheta = \frac{1}{2}\pi$. From one chemical unit cell to the next the magnetization rotates by the constant angle $\varphi_{n+1} - \varphi_n = \mathbf{q} \cdot (\mathbf{R}_{n+1} - \mathbf{R}_n)$.

In the framework of the Pauli equation with no external \mathbf{B} -field the orientation between real- and spin-space is not coupled. In this case all chemical unit cells of a spin spiral (3.13) are equivalent. This allows to calculate such systems within one chemical unit cell by applying a *generalized Bloch theorem* [89, 90]. This procedure is sketched in the following.

\mathbf{B}_{xc} is parallel to \mathbf{m} . Therefore, the condition (3.13) implies that \mathbf{B}_{xc} and the total potential \mathbf{V} perform the same rotation in spin-space. The potential \mathbf{V} and thus the Hamiltonian $\mathcal{H} = \mathcal{T}_{\text{kin}} + \mathbf{V}$ commutes with a generalized translation operator \mathcal{G} that performs a translation in real-space and a rotation in spin-space:

$$\mathcal{G}_{\mathbf{R}} \psi(\mathbf{r}) = \mathbf{U}(\mathbf{q} \cdot \mathbf{R}) \psi(\mathbf{r} - \mathbf{R}) \quad , \quad [\mathcal{G}_{\mathbf{R}}, \mathbf{V}] = [\mathcal{H}, \mathbf{V}] = 0$$

$$\text{where } \mathbf{U}(\varphi) = \begin{pmatrix} \exp(-i \frac{1}{2} \varphi) & 0 \\ 0 & \exp(+i \frac{1}{2} \varphi) \end{pmatrix} ,$$

\mathbf{R} is a lattice vector of the chemical lattice.

$\mathbf{U}(\varphi)$ is a spin rotation matrix that rotates a spinor by an angle φ around the z -axis.

In analogy to the Bloch theorem one can conclude that the eigenfunctions of \mathcal{H} can be written as

$$\psi_{\mathbf{k}, \nu}(\mathbf{r}) = \exp(i \mathbf{k} \cdot \mathbf{r}) \mathbf{U}(\mathbf{q} \cdot \mathbf{r}) \theta_{\mathbf{k}, \nu}(\mathbf{r}) = \begin{pmatrix} \exp(i(\mathbf{k} - \frac{1}{2} \mathbf{q} \cdot \mathbf{r})) \theta_{\mathbf{k}, \nu}^{(\uparrow)}(\mathbf{r}) \\ \exp(i(\mathbf{k} + \frac{1}{2} \mathbf{q} \cdot \mathbf{r})) \theta_{\mathbf{k}, \nu}^{(\downarrow)}(\mathbf{r}) \end{pmatrix} \quad (3.14)$$

$$\text{where } \theta_{\mathbf{k}, \nu}(\mathbf{r}) = \theta_{\mathbf{k}, \nu}(\mathbf{r} - \mathbf{R}) .$$

This allows to reformulate the Kohn-Sham equation $(\mathcal{T}_{\text{kin}} + \mathbf{V}) \psi_{\mathbf{k}, \nu} = \epsilon_{\mathbf{k}, \nu} \psi_{\mathbf{k}, \nu}$ as

$$\left(\mathbf{U}(\mathbf{q} \cdot \mathbf{r})^\dagger \mathcal{T}_{\text{kin}} \mathbf{U}(\mathbf{q} \cdot \mathbf{r}) + \mathbf{U}(\mathbf{q} \cdot \mathbf{r})^\dagger \mathbf{V} \mathbf{U}(\mathbf{q} \cdot \mathbf{r}) \right) \mathbf{U}(\mathbf{q} \cdot \mathbf{r})^\dagger \psi_{\mathbf{k}, \nu} = \epsilon_{\mathbf{k}, \nu} \mathbf{U}(\mathbf{q} \cdot \mathbf{r})^\dagger \psi_{\mathbf{k}, \nu}$$

and to work with the lattice-periodic potential $U(\mathbf{q}\cdot\mathbf{r})^\dagger V U(\mathbf{q}\cdot\mathbf{r})$ and the eigenfunctions $U(\mathbf{q}\cdot\mathbf{r})^\dagger \psi_{\mathbf{k},\nu}$. The functions of the form $U(\mathbf{q}\cdot\mathbf{r})^\dagger \psi_{\mathbf{k},\nu}$ can be expanded in the same basis set $\{\phi_{\mathbf{k}+\mathbf{G}}^{(\sigma)}\}_{\sigma,\mathbf{G}}$ as in the previously discussed ordinary non-collinear case. But it is recommended to construct the radial functions u, \dot{u} in the muffin tins from the diagonal elements of $U_{\text{MT}}^\dagger V U_{\text{MT}}$ (i.e. $\tilde{V}^{(\hat{i},\hat{i})}, \tilde{V}^{(\hat{l},\hat{l})}$; cf. Chapter 3.7.1) and not from the diagonal elements of $U_{\text{MT}}^\dagger U(\mathbf{q}\cdot\mathbf{r})^\dagger V U(\mathbf{q}\cdot\mathbf{r}) U_{\text{MT}}$ since the magnetization usually is approximately collinear within the muffin-tin spheres and rotates mainly in the interstitial region. Thus, the matching conditions at the muffin-tin boundaries differ from spin-spiral calculations to ordinary non-collinear calculations.

The construction of the densities and the density-dependent potential $V[n, \frac{\mathbf{m}}{|\mathbf{m}|}, |\mathbf{m}|]$ does not impose a further problem since

$$n = \sum_{\mathbf{k},\nu} \psi_{\mathbf{k},\nu}^\dagger \psi_{\mathbf{k},\nu} = \sum_{\mathbf{k},\nu} \psi_{\mathbf{k},\nu}^\dagger U(\mathbf{q}\cdot\mathbf{r}) U(\mathbf{q}\cdot\mathbf{r})^\dagger \psi_{\mathbf{k},\nu} ,$$

$$|\mathbf{m}| = \left| \sum_{\mathbf{k},\nu} \psi_{\mathbf{k},\nu}^\dagger \boldsymbol{\sigma} \psi_{\mathbf{k},\nu} \right| = \left| \sum_{\mathbf{k},\nu} \psi_{\mathbf{k},\nu}^\dagger U(\mathbf{q}\cdot\mathbf{r}) \boldsymbol{\sigma} U(\mathbf{q}\cdot\mathbf{r})^\dagger \psi_{\mathbf{k},\nu} \right| .$$

3.8 Relativistic effects in the valence band

This chapter describes relativistic corrections to the Kohn-Sham equation (2.11) that are used when calculating the valence states. These approximations are deduced from the the Kohn-Sham Dirac equation (2.14), but they work with spinors, i.e. the wavefunctions have only two independent components. This is done since a computer code that works with four-spinors is computationally very demanding.

In the following the band index ν is dropped. The abbreviations

$$A_\epsilon = -c^2 (V_{\text{eff}} + \boldsymbol{\sigma} \cdot \mathbf{B}_{\text{xc}} - c^2 - \epsilon)^{-1} - \mathbb{1} \quad , \quad V = V_{\text{eff}} + \boldsymbol{\sigma} \cdot \mathbf{B}_{\text{xc}}$$

are used.

Eqn. (2.14) represents a set of two coupled equations for φ_ν and χ_ν (i.e. for the large and small component of ψ_ν). Solving the second row of (2.14) for χ yields

$$\chi = \frac{1}{c} (A_\epsilon + \mathbb{1}) \boldsymbol{\sigma} \cdot \hat{\mathbf{p}} \varphi .$$

This expression can be inserted in the first row of (2.14):

$$\left(\boldsymbol{\sigma} \cdot \hat{\mathbf{p}} (A_\epsilon + \mathbb{1}) \boldsymbol{\sigma} \cdot \hat{\mathbf{p}} + V \right) \varphi = \epsilon \varphi .$$

With the operator identity $(\boldsymbol{\sigma} \cdot \hat{\mathbf{a}}) (\boldsymbol{\sigma} \cdot \hat{\mathbf{b}}) = \hat{\mathbf{a}} \cdot \hat{\mathbf{b}} + i \boldsymbol{\sigma} \cdot (\hat{\mathbf{a}} \times \hat{\mathbf{b}})$ the operator in the last equation can be rewritten:

$$\boldsymbol{\sigma} \cdot \hat{\mathbf{p}} (A_\epsilon + \mathbb{1}) \boldsymbol{\sigma} \cdot \hat{\mathbf{p}} + V = \hat{\mathbf{p}}^2 + V + \hat{\mathbf{p}} A_\epsilon \hat{\mathbf{p}} + i \boldsymbol{\sigma} \cdot ((\hat{\mathbf{p}} A_\epsilon) \times \hat{\mathbf{p}}) \Rightarrow$$

$$\left(\underbrace{\hat{\mathbf{p}}^2 + V}_{\mathcal{H}_0} + \underbrace{\hat{\mathbf{p}} A_\epsilon \hat{\mathbf{p}}}_{\mathcal{H}_{1,\epsilon}} + \underbrace{i \boldsymbol{\sigma} \cdot ((\hat{\mathbf{p}} A_\epsilon) \times \hat{\mathbf{p}})}_{\mathcal{H}_{\text{so},\epsilon}} \right) \varphi = \epsilon \varphi . \quad (3.15)$$

Eqn. (3.15) is equivalent to the Kohn-Sham Dirac equation (2.14). Its solutions $(\varphi, \epsilon)_\nu$ can be determined selfconsistently. In an approximate solution the band energy ϵ on the

left-hand side is fixed to an approximate value E and the resulting secular equation for φ and the eigenvalue ϵ on the right-hand side is solved [e.g. 12, 50, 64]:

$$(\mathcal{H}_0 + \mathcal{H}_{1,E} + \mathcal{H}_{\text{so},E}) \varphi_E = \epsilon_E \varphi_E . \quad (3.16)$$

For $E \approx \epsilon$ the error made in this approximation is much smaller than the error made in the Schrödinger-like equation $\mathcal{H}_0 \varphi_0 = \epsilon_0 \varphi_0$, this is obvious since

$$\mathcal{H}_{1,\epsilon} + \mathcal{H}_{\text{so},\epsilon} = \mathcal{H}_{1,E} + \mathcal{H}_{\text{so},E} + \mathcal{O}(\epsilon - E) .$$

In practice, E is obtained from the LAPW energy-parameters, usually the same value is used for the whole valence band.

A further important approximation is made when calculating the gradients ∇V : For these expressions the potential V in each muffin tin is replaced by its spherical averaged non-magnetic part:

$$\nabla V(\mathbf{r}) \approx \nabla V_{\text{eff}}(\mathbf{r}) \approx \mathbf{r} \frac{d}{dr} \tilde{V}_{\text{eff}}(r) \quad \text{with} \quad r = |\mathbf{r} - \mathbf{R}| .$$

Here \mathbf{R} denotes the position of the nucleus. Outside the muffin-tins the relativistic effects are neglected. This approximation is justified, since the contributions to the potential gradient are dominated by small regions close to the atom cores. In these regions \mathbf{B}_{xc} can be neglected and the potential is almost spherically symmetric.

At the muffin-tin boundaries φ is matched to the wavefunction spinors in the interstitial region. The small component χ can be neglected in such a distance from the atom cores. Nevertheless, inside the muffin tins the density needs to be calculated as

$$n = \sum_{\nu} \left(\varphi_{\nu}^{\dagger} \varphi_{\nu} + \chi_{\nu}^{\dagger} \chi_{\nu} \right) \neq \sum_{\nu} \left(\varphi_{\nu}^{\dagger} \varphi_{\nu} \right) .$$

In Eqn. (3.16) the term $\mathcal{H}_{\text{so},E}$ describes the *spin-orbit coupling*, i.e. the coupling between real- and spin-space. In the *scalar-relativistic approximation* this term is dropped. This is useful, if a collinear magnetization with $B_x = B_y = 0$ can be assumed. In this case the scalar-relativistic Hamiltonian $\mathcal{H}_0 + \mathcal{H}_{1,E}$ is diagonal in spin-space and the Hamiltonian is block diagonal:

$$\mathbf{B} = B_z \mathbf{e}_z \quad \Rightarrow$$

$$\begin{aligned} \mathbf{A}_{\epsilon} &= \begin{pmatrix} -\frac{V_+ - \epsilon}{V_+ - \epsilon - c^2} & 0 \\ 0 & -\frac{V_- - \epsilon}{V_- - \epsilon - c^2} \end{pmatrix} \\ &= \begin{pmatrix} -\frac{V_+ - E}{V_+ - E - c^2} & 0 \\ 0 & -\frac{V_- - E}{V_- - E - c^2} \end{pmatrix} + (\epsilon - E) \begin{pmatrix} \left(\frac{c}{V_+ - E - c^2} \right)^2 & 0 \\ 0 & \left(\frac{c}{V_- - E - c^2} \right)^2 \end{pmatrix} + \mathcal{O}((\epsilon - E)^2) \end{aligned}$$

$$\text{with} \quad V_+ = V_{\text{eff}} + B_z \quad , \quad V_- = V_{\text{eff}} - B_z .$$

The SOC operator $\mathcal{H}_{\text{so},E}$ is not generally included in the calculations. As already indicated in Chapter 2.5.1, it is approximated by a term of the form (2.16)

$$\mathcal{H}_{\text{so},E} \approx v(r) \boldsymbol{\sigma} \cdot \hat{\mathbf{L}} .$$

If the potential can be approximated by a collinear potential then $\mathcal{H}_{\text{so},E}$ is usually treated with a procedure called second variation (cf. Chapter 3.9.2).

Note, that the spin-orbit coupling term always contains non-vanishing off-diagonal elements in spin-space (that mix among \uparrow and \downarrow), whereas in the scalar-relativistic approximation most systems are collinear magnetic (or not magnetic at all).

3.9 Spin-orbit coupling in helical spin spirals

The previously mentioned approximation of the spin-orbit coupling cannot directly be applied to spin spirals. The generalized Bloch theorem does not hold, if atoms with different magnetization direction can be distinguished by their spin-orbit contribution. In principle, every spin spiral with fractional \mathbf{q} -vector can be calculated in a correspondingly large unit cell in which it is commensurate. But the required computer time increases quadratic with the size of the unit cell, so that the range of spirals, that can be calculated in practice, is rather restricted.

This chapter describes some tricks that decrease the computational effort and therefore allow to calculate the spin-orbit coupling corrections of spin spirals in much larger unit cells. These tricks make use of the fact that the spin-orbit coupling can be regarded as a small perturbation. The unperturbed spiral can be calculated easily (in a small unit cell by applying the generalized Bloch theorem). The explicit form of the perturbation is not relevant for the method.

At first the local force theorem is described. Then a method called second variation is introduced and referred to the special case of spin-orbit coupling in helical spin spirals. A perturbative scheme to gain further speedup is presented in Appendix D. It is a widely used approach to treat spin-orbit coupling in second variation and to estimate the anisotropy energies with the local force theorem.

3.9.1 Local force theorem

The local force theorem is first published in [66], extended to magnetic systems in [77] and further generalized in [61]. The theorem investigates the change of the total electronic energy due to a small perturbation in the framework of the Kohn-Sham equation in LDA. The remarkable result is that in 1st-order perturbation theory the change of the total energy of the selfconsistent solution coincides with the change of the single-electron eigenvalues of the Kohn-Sham equation for unperturbed V_H and V_{xc} . This means that one can approximate the changes in the total energy due to a small perturbation by comparing the single-electron eigenvalues of the Kohn-Sham equation with the unperturbed potential. It is not necessary to converge the selfconsistency cycle for the perturbed system.

For example, $\mathcal{H}_0[n]$ denotes the unperturbed Kohn-Sham Hamiltonian (2.11) with the selfconsistent solution n_0 , $\{\epsilon_{0,\nu}\}_\nu$, $\{\psi_{0,\nu}\}_\nu$ and $(\mathcal{H}_0[n] + \mathcal{H}_1)$ denotes the perturbed Kohn-Sham Hamiltonian with the selfconsistent solution n_1 , $\{\epsilon_{1,\nu}\}_\nu$, $\{\psi_{1,\nu}\}_\nu$:

$$\mathcal{H}_0[n_0] \psi_{0,\nu} = \epsilon_{0,\nu} \psi_{0,\nu} \quad , \quad (\mathcal{H}_0[n_1] + \mathcal{H}_1) \psi_{1,\nu} = \epsilon_{1,\nu} \psi_{1,\nu} \quad .$$

With Eqn. (2.13) the respective total energies have the form

$$E_{\text{tot},0} = \sum_{\nu} \epsilon_{0,\nu} + E_{\text{dc},0} \quad , \quad E_{\text{tot},1} = \sum_{\nu} \epsilon_{1,\nu} + E_{\text{dc},1} \quad .$$

If the perturbation \mathcal{H}_1 is small, then the energy difference can be approximated by

$$E_{\text{tot},1} - E_{\text{tot},0} \approx \sum_{\nu} \epsilon_{2,\nu} - \sum_{\nu} \epsilon_{0,\nu} \quad \text{where} \quad (\mathcal{H}_0[n_0] + \mathcal{H}_1) \psi_{2,\nu} = \epsilon_{2,\nu} \psi_{2,\nu} \quad .$$

A derivation of the local force theorem is given in Appendix C. In this derivation it is assumed that the changes in the potential due to the changes of the occupation numbers can be neglected, otherwise the theorem cannot be applied.

The local force theorem can be applied to a variety of perturbations, since it can be

proven without knowing the explicit form of the perturbation. But, if the perturbation introduces strong changes in the charge density $n(\mathbf{r})$ (e.g. in the case of structural relaxations) then it is usually not sufficient to treat the Hartree energy in 1st-order perturbation theory and the local force theorem cannot be applied. Changes in the magnetic structure, on the other hand, are often well described by the local force theorem. In Chapter 6.4.1 the local force theorem is used to estimate the energies of spin spirals (i.e. to estimate the energy changes due to changes of the magnetic boundary conditions), in this Chapter 3.9 the spin-orbit coupling term of the Hamiltonian is regarded as the perturbation.

3.9.2 Second variation

If the approximate (i.e. unperturbed) solution of the (perturbed) Hamiltonian is known, there is an efficient way to reduce the number of basis functions which is usually referred to as *second variation*: Instead of the LAPW functions the eigenstates $\{\psi_\nu^{(0)}\}$ of the unperturbed Hamiltonian \mathcal{H}_0 are used as basis functions when diagonalizing the perturbed Hamiltonian $\mathcal{H}_0 + \mathcal{H}_1$. Thus, the eigenstates $\{\psi_\nu\}$ of $\mathcal{H}_0 + \mathcal{H}_1$ are expanded as $\psi_\nu = \sum_{\nu'} c_{\nu,\nu'} \psi_{\nu'}^{(0)}$. This way the size of the Hamiltonian matrix (i.e. the number of basis functions) can be kept small without introducing a large error. From elementary perturbation theory it is plausible that the projection of an unperturbed on a perturbed state decreases with increasing energy difference. This is due not only to the energy denominator, but also to the fact that the \mathcal{H}_1 matrix elements are usually small if the states differ much in energy. Thus, if describing a perturbed state then it is possible to neglect not only the projection of an unperturbed state that differs much in energy but even the sum of the projections of all states that differ much in energy. Since one is interested only in the occupied states the set of basis functions can be restricted to the unperturbed states below a certain energy level. In the case of spin-orbit coupling it is in many cases sufficient to work with an incomplete basis set that contains twice (or less) the number of occupied states.

In the case of helical spin spirals it is particular useful to treat the spin-orbit coupling as a perturbation ($\mathcal{H}_1 = \mathcal{H}_{\text{so}}$), this allows to calculate the eigenstates of \mathcal{H}_0 in the chemical unit cell (with the generalized Bloch theorem as described in Chapter 3.7.3).

But, there are non-zero \mathcal{H}_{so} matrix elements between states of different \mathbf{k} -vectors:

With $\left\{ |\psi_{\mathbf{k},\nu}^{(\text{ss})}\rangle \right\}_{\mathbf{k},\nu}$ denoting the set of unperturbed states with spiral vector \mathbf{q} ,

$$|\psi_{\mathbf{k},\nu}^{(\text{ss})}\rangle = \left(|\psi_{\mathbf{k},\nu}^{(\uparrow)}\rangle \quad |\psi_{\mathbf{k},\nu}^{(\downarrow)}\rangle \right)^{\text{t}},$$

$$\mathcal{H}_{\text{so}} = \begin{pmatrix} \mathcal{H}_{\text{so}}^{(\uparrow,\uparrow)} & \mathcal{H}_{\text{so}}^{(\uparrow,\downarrow)} \\ \mathcal{H}_{\text{so}}^{(\downarrow,\uparrow)} & \mathcal{H}_{\text{so}}^{(\downarrow,\downarrow)} \end{pmatrix} \text{ denoting the perturbation,}$$

$\{\mathbf{G}\}$ denoting the set of reciprocal lattice vectors of the chemical lattice,

one can conclude for the matrix elements

$$\langle \psi_{\mathbf{k}',\nu'}^{(\text{ss})} | \mathcal{H}_{\text{so}} | \psi_{\mathbf{k},\nu}^{(\text{ss})} \rangle = \sum_{\sigma',\sigma} \langle \psi_{\mathbf{k}',\nu'}^{(\sigma')} | \mathcal{H}_{\text{so}}^{(\sigma',\sigma)} | \psi_{\mathbf{k},\nu}^{(\sigma)} \rangle$$

that

$$\begin{aligned}
\langle \psi_{\mathbf{k}',\nu'}^{(\uparrow)} | \mathcal{H}_{\text{so}}^{(\uparrow,\uparrow)} | \psi_{\mathbf{k},\nu}^{(\uparrow)} \rangle &\neq 0 \Rightarrow \mathbf{k}' - \mathbf{k} \in \{\mathbf{G}\}, \\
\langle \psi_{\mathbf{k}',\nu'}^{(\uparrow)} | \mathcal{H}_{\text{so}}^{(\uparrow,\downarrow)} | \psi_{\mathbf{k},\nu}^{(\downarrow)} \rangle &\neq 0 \Rightarrow \mathbf{k}' - \mathbf{k} - \mathbf{q} \in \{\mathbf{G}\}, \\
\langle \psi_{\mathbf{k}',\nu'}^{(\downarrow)} | \mathcal{H}_{\text{so}}^{(\downarrow,\uparrow)} | \psi_{\mathbf{k},\nu}^{(\uparrow)} \rangle &\neq 0 \Rightarrow \mathbf{k}' - \mathbf{k} + \mathbf{q} \in \{\mathbf{G}\}, \\
\langle \psi_{\mathbf{k}',\nu'}^{(\downarrow)} | \mathcal{H}_{\text{so}}^{(\downarrow,\downarrow)} | \psi_{\mathbf{k},\nu}^{(\downarrow)} \rangle &\neq 0 \Rightarrow \mathbf{k}' - \mathbf{k} \in \{\mathbf{G}\}.
\end{aligned} \tag{3.17}$$

This gets comprehensible with the following considerations:

The real-space representation of \mathcal{H}_{so} (Eqn. (2.16)) has the periodicity of the chemical lattice. Thus, for any lattice-periodic function $f(\mathbf{r}) = \sum_{\mathbf{G}} \exp(i\mathbf{G}\cdot\mathbf{r}) c_{\mathbf{G}}$ one obtains

$$\mathcal{H}_{\text{so}}^{(\sigma',\sigma)} \exp(i(\mathbf{k} \pm \frac{1}{2}\mathbf{q})\cdot\mathbf{r}) f(\mathbf{r}) = \exp(i(\mathbf{k} \pm \frac{1}{2}\mathbf{q})\cdot\mathbf{r}) f^{\text{so}}(\mathbf{r})$$

with a lattice-periodic function $f^{\text{so}}(\mathbf{r}) = \sum_{\mathbf{G}} \exp(i\mathbf{G}\cdot\mathbf{r}) c_{\mathbf{G}}^{\text{so}}$. Inserting the components of the spinor $\psi_{\mathbf{k},\nu}^{(\text{ss})}$ for f leads to the expansions

$$\begin{aligned}
\psi_{\mathbf{k},\nu}^{(\sigma)}(\mathbf{r}) &= \sum_{\mathbf{G}} \exp(i(\mathbf{k} + \mathbf{G} \pm \frac{1}{2}\mathbf{q})\cdot\mathbf{r}) c_{\mathbf{k},\nu,\mathbf{G}}^{(\sigma)}, \\
\mathcal{H}_{\text{so}}^{(\sigma',\sigma)} \psi_{\mathbf{k},\nu}^{(\sigma)}(\mathbf{r}) &= \sum_{\mathbf{G}} \exp(i(\mathbf{k} + \mathbf{G} \pm \frac{1}{2}\mathbf{q})\cdot\mathbf{r}) c_{\mathbf{k},\nu,\mathbf{G}}^{\text{so}(\sigma)}.
\end{aligned}$$

The matrix elements in (3.17) vanish if $(\mathbf{k}' \pm \frac{1}{2}\mathbf{q}) \neq (\mathbf{k} \pm \frac{1}{2}\mathbf{q})$, since $\lim_{R \rightarrow \infty} \frac{1}{R} \int_0^R dr \exp(igr) = 0$ if $g \neq 0$. There are non-vanishing \mathcal{H}_{so} matrix elements between states whose \mathbf{k} -vectors are connected by \mathbf{q} .

If the \mathbf{q} -vector is a fraction of a reciprocal lattice vector \mathbf{G} of the chemical lattice (i.e. $\mathbf{q} = \frac{1}{n}\mathbf{G}$, n integer) then the \mathcal{H}_{so} matrix can be partitioned in blocks of the form as indicated in Fig. 3.4. In this case each set of \mathbf{k} -vectors that is connected with \mathbf{q} corresponds to *one* \mathbf{k} -vector in the first Brillouin zone of the magnetic unit cell (in which the spin spirals are commensurate). \mathbf{q} is a reciprocal lattice vector of this magnetic unit cell.

$$H_{\text{so}} = H_{\text{so}}^\dagger = \begin{pmatrix}
\begin{array}{c|c|c|c|c|c}
\mathbf{k} & \mathbf{k}+\mathbf{q} & \mathbf{k}+2\mathbf{q} & \mathbf{k}+3\mathbf{q} & \dots & \mathbf{k}+(n-1)\mathbf{q} \\
\hline
\begin{array}{cc} A_1 & B_1^\dagger \end{array} & & & & & \begin{array}{c} B_n \end{array} \\
\hline
\begin{array}{c} B_1 \\ A_2 \end{array} & \begin{array}{c} B_2^\dagger \\ A_3 \end{array} & & & & \\
\hline
\begin{array}{c} B_2 \\ A_3 \\ B_3 \end{array} & & \ddots & & & \\
\hline
\begin{array}{c} 0 \\ \vdots \\ 0 \end{array} & & & & & \\
\hline
\begin{array}{c} B_n^\dagger \\ B_{n-1} \\ A_n \end{array} & & & & & \\
\hline
\mathbf{k} & \mathbf{k}+\mathbf{q} & \mathbf{k}+2\mathbf{q} & \vdots & \mathbf{k}+(n-2)\mathbf{q} & \mathbf{k}+(n-1)\mathbf{q}
\end{array}
\end{pmatrix}$$

Figure 3.4: Most \mathcal{H}_{so} matrix elements are zero. Nevertheless the shown partition, corresponding to the states whose \mathbf{k} -vectors are connected by $\mathbf{q} = \frac{1}{n}\mathbf{G}$, is not block-diagonal.

The matrix H_{so} that is sketched in Fig. 3.4 can be diagonalized, if n is not too large (i.e. on a reasonably coarse \mathbf{q} -grid). The discrete \mathbf{k} -point mesh that is used for sampling the Brillouin zone has to be chosen in accordance with the \mathbf{q} -vector. Usually, this does not present a problem since the calculation of spin-orbit interaction requires a large \mathbf{k} -point density anyhow.

Note that the sparseness of H_{so} is important in the actual calculations, for large n this reduces the time and memory required for calculating and storing the matrix elements drastically.

Explicit expressions (in terms of LAPWs) for the \mathcal{H}_{so} matrix elements of spin spiral eigenstates are presented in Appendix B.

3.9.3 Diagonalizing the sparse matrix $H_0 + H_{\text{so}}$

The choice of the unperturbed spiral functions as basis reduces the number of required basis functions and the size of the Hamiltonian matrix a lot. But further approximations are needed in order to deal with very big matrices (i.e. small \mathbf{q} -vectors).

A simple and fast procedure to find the eigenvalues of a band matrix can be found in many books on numerical linear algebra but the corners that are named B_n, B_n^\dagger in Fig. 3.4 impose a problem. Unfortunately, the common methods do not allow to treat the corners as perturbation to the band matrix: In order to represent the perturbation in the basis that diagonalizes the unperturbed band matrix one needs not only the eigenvalues but also parts of all eigenvectors of the band matrix, furthermore in this basis the perturbation is not sparse anymore and can hardly be stored in the computer memory. Subspace methods that do not need all the eigenvectors of the unperturbed problem are feasible for calculating a few energies but require much time when successively calculating the energies of all occupied states. Also it is not possible to neglect the disturbing corners completely, the error would be too large.

Therefore, the whole matrix H_{so} is treated as a perturbation to the spiral solutions of the Pauli equation. The perturbative method is in detail described in Appendix D. It is based on 2nd-order Rayleigh-Schrödinger perturbation theory, the sums that occur thereby are of moderate length if the sparseness of the matrix is taken into account. For the investigated systems this approach turned out to be accurate and fast enough to determine the sum of eigenvalues, but if one is interested in the individual energy levels (i.e. band structure) at small $|\mathbf{q}|$ a more sophisticated algorithm has to be used.

Chapter 4

Magnetic interactions

4.1 Exchange interactions

In widely used simple models the magnetic configuration of a system is described by the magnetization directions $\{\mathbf{S}_j\}_j$ of the individual atoms (or unit cells), i.e. the magnetization direction of the j th atom is described by \mathbf{S}_j with $|\mathbf{S}_j|=1$. The energies of the systems are approximated by functions of these normed vectors. In the simplest case, the energy is expressed by the *Heisenberg model*:

$$E = \frac{1}{2} \sum_{j,j'}^{\text{at}} J_{j,j'}^{\text{at}} \mathbf{S}_j \cdot \mathbf{S}_{j'} \quad \text{with} \quad J_{j,j'}^{\text{at}} = J_{j',j}^{\text{at}} . \quad (4.1)$$

The parameters $\{J_{j,j'}^{\text{at}}\}$ are called (effective) *exchange integrals*. In most systems, they decay very fast with the distance of the lattice sites.

There are several approaches that lead to the Heisenberg model as an approximation of the many-body Hamiltonian. It is beyond the scope of this thesis to give a detailed discussion of that matter, in the following only some aspects are briefly sketched. For further explanations cf. e.g. [4, 5, 103].

A possible perturbative approach, that leads to the Heisenberg model, is to split from the many-body Hamiltonian (2.1) the single-particle (and possibly on-site interaction part) and to apply the ordinary Rayleigh-Schrödinger perturbation theory to the Coulomb interaction between states of different lattice sites. Then (4.1) is obtained in first order perturbation from the direct exchange interaction (hence the name exchange integral). An expression of the same structure is obtained in second order perturbation theory, when the interaction between states of different atoms is neglected and the hopping term resulting from the single particle part of the Hamiltonian is obtained by perturbation theory.

In some approaches the states at one atom are approximated by atomic functions, in other approaches they are Wannier functions that are constructed from the eigenstates of the unperturbed Hamiltonian. In the latter case, \mathbf{S}_j is the mean magnetization direction of the Wannier functions of site j and not the mean magnetization in the j th unit cell.

In higher orders of the several perturbative approaches, there appear additional terms of the form

$$\begin{aligned} & (\mathbf{S}_{j_1} \cdot \mathbf{S}_{j_2})^2 && \text{biquadratic interaction ,} \\ & (\mathbf{S}_{j_1} \cdot \mathbf{S}_{j_2}) (\mathbf{S}_{j_3} \cdot \mathbf{S}_{j_4}) + (\mathbf{S}_{j_1} \cdot \mathbf{S}_{j_4}) (\mathbf{S}_{j_2} \cdot \mathbf{S}_{j_3}) - (\mathbf{S}_{j_1} \cdot \mathbf{S}_{j_3}) (\mathbf{S}_{j_2} \cdot \mathbf{S}_{j_4}) && \text{four-spin interaction .} \end{aligned}$$

They can be identified with electronic hopping processes between two or four lattice sites, their coefficients are called higher order exchange constants or hopping integrals. A repeated back and forth hopping between two lattice sites contributes to the biquadratic

term, a hopping between four lattice sites contributes to the four-spin interaction.

In most cases, it is not feasible to identify the exchange integrals with a distinct term of a perturbative expansion since the term $\mathbf{S}_j \cdot \mathbf{S}_{j'}$ usually results from many processes. More often, it is possible to obtain the exchange integrals from fits to the results of parameter-free calculations or experiments.

4.1.1 Dzyaloshinsky-Moriya interaction

If spin-orbit coupling is taken into account, there is the possibility of an antisymmetric interaction with an energy contribution of the form

$$E_{\text{DM}} = \mathbf{D}^{\text{at}} \cdot (\mathbf{S}_1 \times \mathbf{S}_2) . \quad (4.2)$$

This interaction is called *Dzyaloshinsky-Moriya interaction*. The possibility of an energy term with this symmetry properties was for the first time pointed out by Dzyaloshinsky in 1957 [29]. An atomistic description, that expresses \mathbf{D} in terms of exchange and hopping integrals, was derived by Moriya in 1960 [71]. In this ansatz, it is necessary to include interactions of at least three lattice sites. Of course, the accuracy of the latter approach depends on the system.

In a phenomenological picture, one can expand the energy of the pair interaction of \mathbf{S}_1 and \mathbf{S}_2 in a Fourier series of the angles between \mathbf{S}_1 and \mathbf{S}_2 , then the Heisenberg model (4.1) is the lowest-order symmetric and (4.2) is the lowest order antisymmetric term.

It is very illuminating to analyze the general symmetry conditions that allow for an interaction of the form (4.2) without referring to a detailed exchange mechanism. This is done in the following.

Such an interaction cannot be described with the non-relativistic Pauli equation, since spin-orbit coupling is essential: Without spin-orbit coupling the energy is invariant under spin reflections, whereas E_{DM} is not. E.g. if $\mathbf{D} = \mathbf{e}_z$, $\mathbf{S}_1 = \mathbf{e}_x$, $\mathbf{S}_2 = \mathbf{e}_y$ then a spin reflection on the (y, z) -plane changes the sign of E_{DM} .

If spin-orbit coupling is taken into account then the crystal field can break the chiral symmetry of the magnetic structure. This is illustrated by an example in Fig. 4.1. In that example, the symmetry is broken by a third atom with negligible magnetic moment.

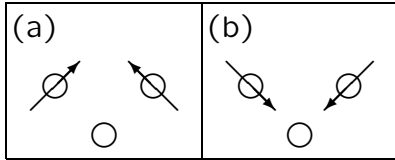


Figure 4.1: Broken chiral symmetry of the magnetic structure. The atoms are indicated with circles and the corresponding magnetic moments (with directions \mathbf{S}_1 , \mathbf{S}_2) are indicated with arrows. Between Fig. a and Fig. b the sign of the angle between \mathbf{S}_1 and \mathbf{S}_2 changes. Due to the non-magnetic atom, the configurations in Fig. a and Fig. b are not equivalent if the orientation between spin- and real-space is taken into account.

If the chiral symmetry of the magnetic structure is not broken, then the effect of the spin-orbit coupling contributes only to the symmetric exchange integral J (Eqn. (4.1)). If the symmetry is broken, it can contribute to the symmetric term (Eqn. (4.1)) and to the antisymmetric term (Eqn. (4.2)).

The \mathbf{D} -vector vanishes if the chemical lattice is invariant under real-space inversion: In Appendix E it is shown that spin-space inversion cannot change the energy. Real-space inversion plus spin-space inversion leads to an equivalent system and thus to the same energy.

For some further crystal symmetries it is straightforward to determine the direction of the \mathbf{D} -vector, the following rules are given in [71]. It is assumed that \mathbf{S}_1 and \mathbf{S}_2 are located at \mathbf{R}_1 and \mathbf{R}_2 respectively. The point in the middle is denoted with $\mathbf{R}_3 = \frac{1}{2}(\mathbf{R}_1 + \mathbf{R}_2)$. Then one gets:

- If a center of inversion is located at \mathbf{R}_3 then

$$\mathbf{D} = 0 \ .$$

- If a mirror plane perpendicular to $(\mathbf{R}_1 - \mathbf{R}_2)$ includes \mathbf{R}_3 then

$$\mathbf{D} \perp (\mathbf{R}_1 - \mathbf{R}_2) \ .$$

- If a mirror plane includes \mathbf{R}_1 and \mathbf{R}_2 then

$$\mathbf{D} \perp \text{mirror plane} \ .$$

- If a two-fold rotation axis perpendicular to $(\mathbf{R}_1 - \mathbf{R}_2)$ includes \mathbf{R}_3 then

$$\mathbf{D} \perp \text{two-fold axis} \ .$$

- If a n -fold axis ($n \geq 2$) includes \mathbf{R}_1 and \mathbf{R}_2 then

$$\mathbf{D} \parallel (\mathbf{R}_1 - \mathbf{R}_2) \ .$$

In [25] it is pointed out, that the low symmetry of surfaces also induces the Dzyaloshinsky-Moriya interaction. In this reference, the direction of the \mathbf{D} -vector is discussed for several surface crystal structures.

4.2 Magnetostatic interactions

The above considerations do not include the interactions due to the magnetic fields. The magnetostatic energy of solids can be approximated well by replacing the magnetization density with the magnetic dipolar moments of the atoms. The magnetostatic interactions can affect the preferred real-space orientation of the magnetic moments, but a further influence of these interactions on the electronic structure can be neglected.

The magnetostatic energy $E^{(\text{dip})}$ of a magnetic dipole at position \mathbf{R}_0 with moment \mathbf{M}_0 that is exposed to the fields of other dipoles at positions $\{\mathbf{R}_j\}_{j \neq 0}$ with moments $\{\mathbf{M}_j\}_{j \neq 0}$ is given by (cf. e.g. [23]):

$$E^{(\text{dip})} = \frac{\mu_B^2}{2} \sum_{j \neq 0} \frac{(\mathbf{M}_j \cdot \mathbf{M}_0)(\mathbf{R}_j - \mathbf{R}_0)^2 - 3((\mathbf{R}_j - \mathbf{R}_0) \cdot \mathbf{M}_j)((\mathbf{R}_j - \mathbf{R}_0) \cdot \mathbf{M}_0)}{|\mathbf{R}_j - \mathbf{R}_0|^5} \ . \quad (4.3)$$

In order to obtain the total magnetostatic energy of a sample the last equation has to be evaluated for each dipole.

Eqn. (4.3) gives rise to a magnetostatic *anisotropy energy* since $E^{(\text{dip})}$ depends on the orientations of the magnetic moments with respect to the chemical lattice (the lattice is given by the positions $\{\mathbf{R}_j\}$).

In bulk material $E^{(\text{dip})}$ depends on the macroscopic shape of the magnetic sample (*shape anisotropy*), whereas in magnetic films and wires $E^{(\text{dip})}$ depends only on the local

orientation of the magnetic moments. The reason for this is that the sum (4.3) converges only if the lattice of magnetic moments extends infinitely in less than 3 dimensions: Consider an infinite set of identical dipoles \mathbf{M}_j that are equally distributed in d dimensions and let $N(n)$ denote the number of lattice points \mathbf{R}_j that are localized within a shell of radius $n\Delta$ and thickness Δ that is centered at \mathbf{R}_0 , i.e. $N(n) = \#\{j \mid n\Delta < |\mathbf{R}_j - \mathbf{R}_0| \leq (n+1)\Delta\}$. Then each term of the sum (4.3) is of the order $|\mathbf{R}_j - \mathbf{R}_0|^{-3}$ and for large n the number $N(n)$ is proportional to n^{d-1} . The contribution of one shell to the sum (4.3) is of the order $(n\Delta)^{-3} N(n) \sim n^{d-4}$ and the summation over all shells leads to $E^{(\text{dip})} \sim \sum_n n^{d-4}$. This sum diverges logarithmically for $d=3$ but converges for $d \leq 2$.

4.3 Domain structure

Ferromagnets usually show a magnetic superstructure. They are divided into several uniformly magnetized *domains* that differ by their magnetization direction. The domains are separated by thin boundary regions (*domain walls*) where the magnetization orientation turns from one domain to the next. Of course, the domain walls have a larger exchange energy density than the domains. The formation of the domain structure can be explained by an interplay of magnetostatic and exchange interactions and anisotropy energy:

The microscopic magnetic structure is mainly governed by the exchange interactions. The magnetostatic interactions contribute to the anisotropy energy but are much too weak to inhibit domains with local ferromagnetic spin alignment, if the latter is favored by the exchange interactions. However, the range of the magnetostatic interactions is much larger than the range of the exchange interactions: The dipolar interaction between two atoms decays as the inverse cube of the distance whereas the exchange interactions usually decay much faster.

In a simplified picture, the division of a ferromagnetic sample in domains of opposite magnetization direction decreases the energy in the entire volume due to the long-ranged magnetostatic interactions and increases the energy in the domain boundaries due to the short-ranged exchange interactions. When a bulk domain pattern is scaled with the length r , then the domain volume grows with r^3 whereas the boundary area grows with r^2 . Therefore, a magnetic structure with sufficiently large domains has lower energy than an uniformly magnetized ferromagnet.

A gradual change of the magnetization over the entire sample also would show low exchange energy as the local structure would be almost ferromagnetic. But such a configuration is prohibited by the anisotropy energy that favors certain magnetization directions.

The domain pattern in a real sample (at low temperature) is not generally the ground state, but a metastable state. The transitions between different domain patterns involve the remagnetization of many atoms, therefore the energy barriers between the metastable patterns are relatively high. The actual domain pattern often depends on the history of the sample.

Chapter 5

Domain walls

This chapter describes the structure of the domain walls that form in the boundary region between two ferromagnetic domains. The most important quantities are the wall width and the wall energy. The width is referred to in Chapter 6 where magnetic surfaces are discussed since this quantity can be accessed directly by experiments. In some cases the wall energy can determine the size of the domains (cf. Chapter 4.3).

The following analysis is carried out on the basis of a simple model that is sufficient to explain the main effects. In particular, it is assumed that the magnetization changes only in the direction perpendicular to the walls. This reduces the analysis to the investigation of a quasi one-dimensional problem. If the shape of the walls is described just by a competition between spin stiffness and anisotropy energy, the solution of the model is simple and well known. But if the Dzyaloshinsky-Moriya (DM) interaction is included the situation is more complicated. The main aim of Chapter 5 is to describe the effects of the DM interaction on the domain wall shape. This interaction is of particular importance at magnetic surfaces, since they show large spin-orbit coupling effects and no inversion symmetry.

Some non-standard situations that require extensions to the model that is discussed here, are sketched briefly in Chapter 5.4.

5.1 Some definitions

For the following discussion of the domain walls it is important to distinguish the different directions and rotation paths that characterize the magnetic configurations. All domain walls that are considered in this thesis change their magnetization direction only along one direction in real-space. Their local magnetic structure can be described by a \mathbf{q} -vector. This is the wave vector of a frozen magnon. The direction of \mathbf{q} defines the real-space direction along which the magnetization rotates, the rotation period is given as $2\pi |\mathbf{q}|^{-1}$ unit cells (cf. Chapter 3.7.3). Even though the direction of the \mathbf{q} -vector is assumed to be constant, its absolute value $|\mathbf{q}|$ changes along the way from one domain to the other. Apart from the real-space orientations the walls can differ by their alignment in spin-space, i.e. by the direction of the spin rotation axis and the rotational direction. Of course, the last distinctions have to be made only if a coupling between real- and spin-space is taken into account. The orientations and directions are illustrated in Fig. 5.1. A wall with a spin rotation axis parallel to the \mathbf{q} -vector is called *Bloch wall*, a wall with a spin rotation axis perpendicular to the \mathbf{q} -vector is called *Néel wall* (cf. Fig. 5.2).

When the model systems are discussed x , y , z denote the magnetization direction in spin-space while r denotes the real-space coordinate parallel to \mathbf{q} . Since the discussion is restricted to domain walls that change their magnetization only in the direction of the

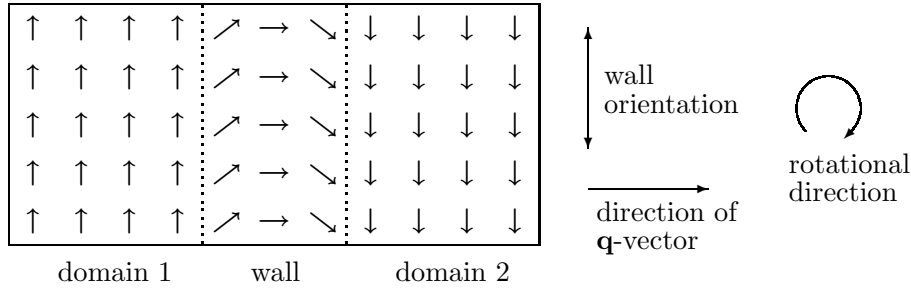


Figure 5.1: Definition of the wall orientation and rotation. In the bulk the orientation is the orientation of a plane, but in atomically thin films it is just one direction in the film plane. The \mathbf{q} -vector defines the wall orientation but not the spin rotation axis. A change of the sign of \mathbf{q} reverts the spin rotational direction.

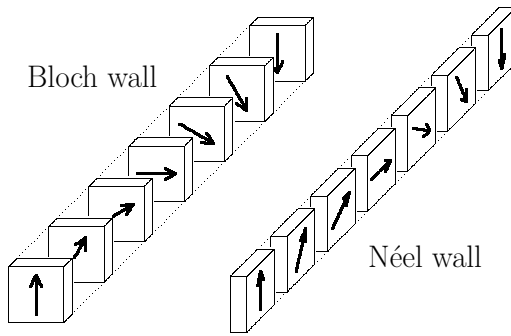


Figure 5.2: Rotation paths of the Bloch and Néel walls.

In the Bloch walls the spin rotation axis is parallel to the \mathbf{q} -vector, whereas in the Néel walls it is perpendicular to the \mathbf{q} -vector.

\mathbf{q} -vector the magnetization is described by $\mathbf{M}(r) = |\mathbf{M}(r)| \mathbf{m}(r)$ with $\mathbf{m}(r) = (x(r) \mathbf{e}_x + y(r) \mathbf{e}_y + z(r) \mathbf{e}_z)$, $x(r)^2 + y(r)^2 + z(r)^2 = 1$. The magnetization direction of a discrete atom at lattice point j is described by $\mathbf{S}_j = x_j \mathbf{e}_x + y_j \mathbf{e}_y + z_j \mathbf{e}_z$ with $x_j^2 + y_j^2 + z_j^2 = 1$. Polar coordinates are used according to the convention

$$x = \sin \vartheta \cos \varphi \quad , \quad y = \sin \vartheta \sin \varphi \quad , \quad z = \cos \vartheta \quad .$$

When it is necessary to describe all three real-space dimensions (e.g. in Chapter 5.2.2), then the corresponding real-space vector is denoted with \mathbf{r} .

The term *ferromagnetic* denotes a homogeneous ferromagnetic structure (in contrast to a domain wall between two ferromagnetic domains or to a homogeneous spin spiral).

Note that in the framework of density functional theory and LDA (Chapters 2, 3) the notation \mathbf{m} is used to describe the magnetization density with $|\mathbf{m}| \neq 1$. The nomenclature is chosen according to the usual conventions in the electronic structure calculations and micromagnetic calculations respectively, therefore it is not consistent within this thesis.

5.2 Micromagnetic model

If the magnetization in a wall changes on length scales that are large compared to the atomic distances the walls can be described with a micromagnetic model, where the discrete crystal lattice is replaced by a continuum. This is the case in most bulk systems. In the micromagnetic model used here all relevant interactions are regarded as being local (i.e. it is assumed that the magnetic structure does not change significantly on the length scale where the relevant magnetic interactions decay). The assumption of local relevant interactions is no contradiction to the requirement of long-range magnetostatic interactions for the formation of the domain structure: The energy density in the small wall

volume is much higher than in the domains and therefore the mechanisms responsible for the wall internal structure are on a different energy scale than the long-range interactions relevant for the domain pattern.

Detailed descriptions of the derivation and applications of micromagnetic models can be found in many text books [e.g. 28]. The model that is introduced in the following and is used throughout this thesis is restricted to the terms of most importance for the system discussed in Chapter 6, i.e. to the spin stiffness, the anisotropy energy and the DM interaction. The main scope of this chapter is to discuss the influence of the DM interaction on the domain wall profile as the DM interaction usually is neglected in micromagnetic calculations.

5.2.1 Ansatz

The Expressions (4.1) and (4.2) combine to a Heisenberg-like model. Usually, the higher-order terms mentioned in Chapter 4.1 are of minor relevance if the magnetization orientation does not change much from one atom to the next.

The atomic interactions that are discussed in the following are the spin stiffness, the anisotropy energy and the DM interaction. The magnetostatic dipolar interactions are mapped into the effective anisotropy energy constant (in Chapter 6.3 it is shown that this is sufficient when describing the ultrathin films that are studied in this thesis).

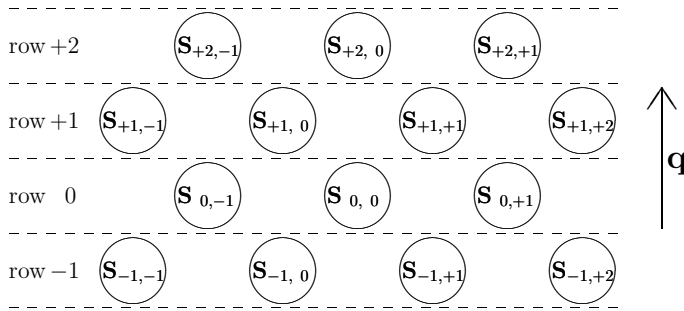


Figure 5.3: Atomic rows in two dimensions. It is assumed that all atoms in one row have the same magnetization direction (i.e. $\mathbf{S}_{j,i} = \mathbf{S}_{j,i'}$). Then it is possible to work with effective pair interactions between atomic rows instead of pair interactions between atoms.

If the \mathbf{q} -vector points along a high-symmetry line it can be assumed that the magnetic moments in the atomic rows perpendicular to \mathbf{q} are all aligned in parallel to each other (cf. Fig. 5.3). This is a reasonable assumption, which is made in this entire thesis (without testing its validity). Now the problem of finding the magnetization distribution is reduced to a quasi one-dimensional problem. The interactions within one atomic row are irrelevant since they do not depend on the rows orientation \mathbf{S}_j . The interaction $J_{j,j'}$ between row j and row j' can be written the following way:

$$J_{j,j'} = J_{|j'-j|} = \frac{1}{N} \sum_{i,i'=1}^N \overset{\text{at}}{J}_{(j,i),(j',i')} = \sum_{i=1}^N \overset{\text{at}}{J}_{(j,i),(j',0)} . \quad (5.1)$$

Here $\overset{\text{at}}{J}_{(j,i),(j',i')}$ denotes the effective exchange integral between atom i in row j and atom i' in row j' (cf. Eqn. 4.1). It is assumed that there are N equivalent atoms in each row. With the prefactor $\frac{1}{N}$ the interaction is given in energy per atom. Furthermore, it is assumed that all atomic rows are chemically equivalent. Then the exchange integral depends only on $|j' - j|$.

When the DM interaction is treated the same way, the total energy of the *discrete model* used here has the form

$$E = \sum_{j < j'} \left(J_{|j'-j|} (1 - \mathbf{S}_j \cdot \mathbf{S}_{j'}) + \mathbf{D}_{j'-j} \cdot (\mathbf{S}_j \times \mathbf{S}_{j'}) \right) + \sum_j \mathbf{S}_j^\dagger \cdot \mathbf{K} \cdot \mathbf{S}_j \quad (5.2)$$

with the anisotropy energy tensor $\mathbf{K} = \begin{pmatrix} K_x & 0 & 0 \\ 0 & K_y & 0 \\ 0 & 0 & K_z \end{pmatrix}$.

The exchange term $J_{|j'-j|}(1 - \mathbf{S}_j \cdot \mathbf{S}_{j'})$ is chosen such that it vanishes in the ferromagnetic state and for $J > 0$ any deviations from the ferromagnetic state increase the energy. It should be pointed out that J represents some effective exchange integral that can have contributions from the quantities described in Chapter 4.1 as well as from symmetric spin-orbit coupling effects that are not included in Eqn. (4.2). The term $\mathbf{S}_j^\dagger \cdot \mathbf{K} \cdot \mathbf{S}_j$ describes only local contributions. Furthermore, one should note that the structure of the anisotropy energy tensor \mathbf{K} depends on the crystal structure. The (110)-surface that is studied in Chapter 6 has 2-fold in-plane symmetry and the leading anisotropy energy terms are 2nd-order in the magnetization direction. In this case the anisotropy energy can be approximated with $\mathbf{S}_j^\dagger \cdot \mathbf{K} \cdot \mathbf{S}_j$ and \mathbf{K} is diagonal in Cartesian spin-space coordinates (cf. Appendix E).

If $J_{j'-j}$ and $\mathbf{D}_{j'-j}$ decay on a length scale where $\mathbf{S}_{j'} - \mathbf{S}_j$ is small and $\mathbf{S}_{j+1} - \mathbf{S}_j$ is approximately constant, then (5.2) can be approximated by a micromagnetic energy functional that depends on the magnetizations orientation \mathbf{m} and its first spatial derivative $\dot{\mathbf{m}} = \frac{d}{dr} \mathbf{m}$. This *micromagnetic model* has the form

$$\tilde{E} = \int dr \left(\tilde{A} \dot{\mathbf{m}}(r)^2 + \tilde{\mathbf{D}} \cdot (\mathbf{m}(r) \times \dot{\mathbf{m}}(r)) + \mathbf{m}(r)^\dagger \cdot \tilde{\mathbf{K}} \cdot \mathbf{m}(r) \right). \quad (5.3)$$

In the following the tilde ($\tilde{}$) is omitted since it is clear from the context whether a discrete or continuous ansatz is made. The micromagnetic equivalence of J is denoted by A which is a widely used convention. A detailed derivation of (5.3) from (5.2) is given in Appendix F.1, but one should keep in mind that (5.3) approximates most discrete lattice models with reasonably fast decaying interactions (not only (5.2)).

In the discrete model (5.2) E denotes the energy of a stripe of atoms that consists of one atom from each atomic row (e.g. $\{\mathbf{S}_{j,0}\}_j$ in Fig. 5.3). In the micromagnetic model (5.3) the crystal structure enters only in the parameters A , \mathbf{D} , \mathbf{K} . Therefore these parameters are scaled such that E denotes the energy per area (in bulk systems) or length (in film systems) perpendicular to \mathbf{q} .

In this Chapter 5 the coordinate system is chosen such that $\mathbf{D} \parallel \mathbf{e}_z$. This simplifies the description of the DM term in polar coordinates. The assumption $\mathbf{D} \parallel \mathbf{e}_z$ in combination with the diagonal structure of \mathbf{K} restricts \mathbf{D} to a high symmetry direction of the real-space lattice. But, the spin-space vector \mathbf{e}_z can point parallel or perpendicular to \mathbf{q} .

With $\mathbf{D} = D \mathbf{e}_z$ and the polar coordinates $\vartheta(r)$, $\varphi(r)$ the energy functional (5.3) has the form

$$\mathbf{D} = D \mathbf{e}_z \Rightarrow E = \int dr \left(A (\dot{\vartheta}^2 + \sin^2 \vartheta \dot{\varphi}^2) + D \sin^2 \vartheta \dot{\varphi} + K_x \sin^2 \vartheta \cos^2 \varphi + K_y \sin^2 \vartheta \sin^2 \varphi + K_z \cos^2 \vartheta \right). \quad (5.4)$$

The walls between ferromagnetic domains are calculated by minimizing the energy (5.3) under the boundary conditions

$$\mathbf{m}(r) \xrightarrow{r \rightarrow \pm\infty} \pm \mathbf{m}_{\text{easy}}$$

where $\pm \mathbf{m}_{\text{easy}}$ denotes the domain magnetization parallel to the easy axis, i.e. it is assumed that the size of the domains does not influence the wall profile and the interaction between different walls can be neglected.

5.2.2 Symmetry considerations to the \mathbf{D} -vector

In [25, 71] and Chapter 4.1.1 some general relations between the direction of the \mathbf{D} -vector and the crystal symmetry are given. The systems that are further investigated in Chapter 6 are domain walls in films at surfaces that have some in-plane symmetry. In this chapter some special surface symmetries are investigated in detail.

Symmetry considerations allow to identify configurations of equal energy and opposite sign of the term $\mathbf{m} \times \dot{\mathbf{m}}$, i.e. of opposite rotational direction. In such cases the \mathbf{D} -vector must be zero or orthogonal to $\mathbf{m} \times \dot{\mathbf{m}}$.

According to Appendix E two magnetic configurations ψ and $\mathcal{S}\mathcal{R}\psi$ have equal energy if $[\mathcal{H}-\mathcal{V}, \mathcal{S}\mathcal{R}] = 0$. Here \mathcal{S} denotes a spin-space operator and \mathcal{R} a real-space symmetry operator of the chemical lattice (i.e. $[V_{\text{ext}}, \mathcal{R}] = 0$). It is useful to identify the operations $\mathcal{S}\mathcal{R}$ that reverse the rotational direction for a given real-space symmetry operation \mathcal{R} .

The real-space inversion $\mathcal{R}_{\mathcal{I}}$ changes the rotational direction:

$$\mathbf{m}(\mathbf{r}) \times \dot{\mathbf{m}}(\mathbf{r}) \xrightarrow{\mathcal{R}_{\mathcal{I}}} -\mathbf{m}(-\mathbf{r}) \times \dot{\mathbf{m}}(-\mathbf{r}) ,$$

thus in systems with inversion symmetry there is $\mathbf{D} = 0$. Usually there is a non-vanishing DM interaction at the surface since a surface breaks the inversion symmetry of the system.

\mathcal{R}_2 and \mathcal{S}_2 denote 2-fold real- and spin-space rotations around the surface normal \mathbf{n} . It can be shown easily that $[\mathcal{H}-\mathcal{V}, \mathcal{S}_2\mathcal{R}_2] = 0$ if $[V_{\text{ext}}, \mathcal{R}_2] = 0$. \mathcal{R}_2 changes the sign of $\dot{\mathbf{m}}$ since the \mathbf{q} -vector is in the surface plane. \mathcal{S}_2 does not influence the component parallel to \mathbf{n} and changes the sign of the in-plane components of $\mathbf{m} \times \dot{\mathbf{m}}$. Thus, a 2-fold rotational symmetry implies $\mathbf{D} \cdot \mathbf{n} = 0$.

Similar considerations show that a mirror plane perpendicular to the \mathbf{q} -vector implies $\mathbf{D} \cdot \mathbf{q} = 0$ and a mirror plane parallel to the \mathbf{q} -vector implies that the \mathbf{D} -vector is perpendicular to the mirror plane (i.e. \mathbf{D} lies in the surface plane and perpendicular to \mathbf{q}).

The resulting consequences for the domain walls that rotate within one high-symmetry plane are summarized in the following table, an example is illustrated in Fig. 5.4

| | rotation axis | | | |
|-------------------------------------|---|--|---------------------------|--|
| | in-plane $\parallel \mathbf{q}$ Bloch wall | in-plane $\perp \mathbf{q}$ Néel wall | out-of-plane Néel wall | |
| 2-fold rotation | X | X | | X means that the DM term does not vanish generally |
| mirror plane $\parallel \mathbf{q}$ | | X | | |
| mirror plane $\perp \mathbf{q}$ | | X | X | |

Note that the Néel walls that are induced by stray fields always have an out-of-plane rotation axis.

Two systems are of opposite *chirality* if they can be brought into coincidence by inverting and rotating the (real- and spin-space) coordinates. In the following this term is always related to the magnetization given by $\mathbf{m}(\mathbf{r})$ and its properties defined by the energy functional. Thus, in this nomenclature two walls of opposite *rotational direction* are never of the same chirality but not necessarily of opposite chirality.

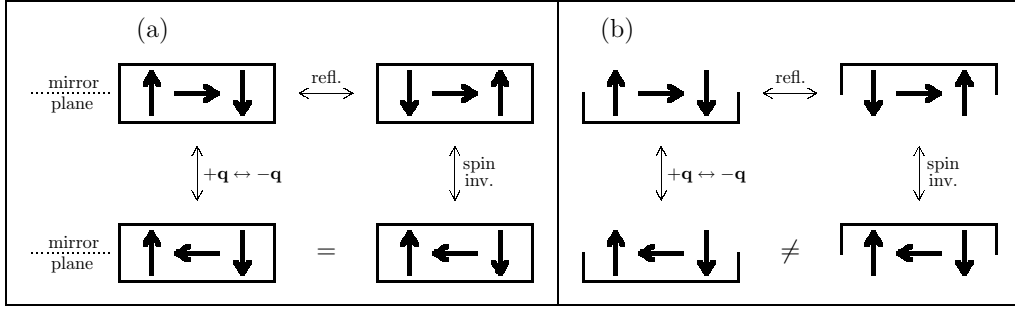


Figure 5.4: Sketch illustrating the influence of a mirror plane $\parallel \mathbf{q}$ on Néel walls. In Fig. a the chemical lattice has a mirror plane parallel to the rotation axis. In this case the system with opposite rotational direction is equivalent to the mirror image of the original system. In Fig. b the symmetry is broken (e.g. if the wall has a rotation axis parallel to a surface). In this case the system with opposite rotational direction is *not* equivalent to the mirror image of the original system, i.e. both systems cannot be brought into coincidence by any rotation or spin inversion (spin inversion is frequently referred to as time inversion).

If spin-orbit coupling (and the magnetostatic interaction) is neglected, two systems are already equivalent if they can be brought into coincidence by any spin rotation or spin reflection. In this case the systems in Fig. b are equivalent.

Reflections in real- *and* spin-space are further commented in Appendix E.

5.2.3 Analytic solution for $\mathbf{D} = 0$

At first the case $\mathbf{D} = 0$ is considered. In this case the domain-wall magnetization stays in one plane (normal to the hard axis) and can be described by one angle ϑ . If z labels the easy and y labels the hard axis then ϑ is 0 or π in the domains and the energy functional (5.4) simplifies with $K = K_x - K_z$ (and by adding an irrelevant constant to the integrand) to

$$E = \int_{-\infty}^{+\infty} dr (A \dot{\vartheta}^2 + K \sin^2 \vartheta). \quad (5.5)$$

The variation of Eqn. (5.5) has a well-known analytic solution that can be found in many text books [e.g. 58] and is first derived by Landau and Lifshitz in 1935 [57]. It is clear from the integrand that the solution of minimal energy is a monotonic function $\vartheta(r)$, this allows for some substitutions in order to simplify the calculation. With the boundary conditions $\vartheta(r \searrow -\infty) = 0$, $\vartheta(r \nearrow +\infty) = \pi$ (implying $A, K > 0$) and the choice $\vartheta(r=0) = \frac{\pi}{2}$ one gets

$$\begin{aligned} \int_{-\infty}^{+\infty} dr (A \dot{\vartheta}^2 + K \sin^2 \vartheta) &= \int_0^{\pi} d\vartheta r' \left(\frac{A}{r'^2} + K \sin^2 \vartheta \right) \quad \text{where } r' = \frac{dr}{d\vartheta}, \\ 0 &\stackrel{!}{=} \left(\frac{d}{d\vartheta} \frac{\partial}{\partial r'} - \frac{\partial}{\partial r} \right) \left(r' \left(\frac{A}{r'^2} + K \sin^2 \vartheta(r) \right) \right) = \frac{d}{d\vartheta} \left(-\frac{A}{r'^2} + K \sin^2 \vartheta \right) \stackrel{\text{bound. cond.}}{\implies} \\ -\frac{A}{r'^2} + K \sin^2 \vartheta &= 0 \quad \implies \quad \sqrt{\frac{A}{K}} \frac{1}{1 - \cos^2 \vartheta} = \frac{r'}{\sin \vartheta} = -\frac{dr}{d(\cos \vartheta)} \quad \implies \\ r &= -\int_0^{\cos \vartheta} dc \sqrt{\frac{A}{K}} \frac{1}{1 - c^2} = -\sqrt{\frac{A}{K}} \operatorname{arctanh}(\cos \vartheta) \quad \implies \\ \vartheta &= \arccos \tanh \left(-\sqrt{\frac{K}{A}} r \right). \end{aligned} \quad (5.6)$$

From the last equation it is obvious that the wall is symmetric in r and that its width scales proportionally to $\sqrt{A/K}$. In this thesis the wall width is defined as

$$w = 2\sqrt{\frac{A}{K}}. \quad (5.7)$$

The prefactor 2 is just a convention. It is constructed from the r -intercept of a straight line $f(r)$ that is tangent to $\tanh(-\sqrt{\frac{K}{A}}r)$ at $r=0$ and extends from $f(r)=+1=\cos 0$ to $f(r)=-1=\cos \pi$.

From $-\frac{A}{r'^2} + K \sin^2 \vartheta = 0$ one obtains the maximum slope as

$$\dot{\vartheta}(r) \leq \dot{\vartheta}(0) = \sqrt{\frac{K}{A}}. \quad (5.8)$$

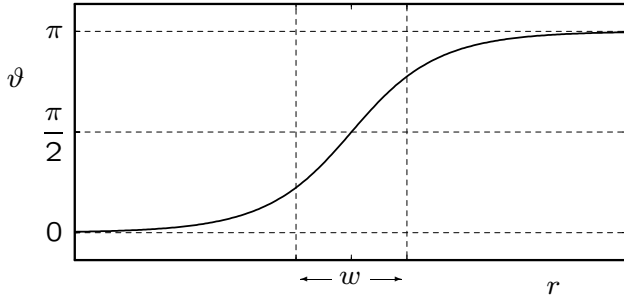


Figure 5.5: Domain wall profile derived from the micromagnetic model.

The wall width according to the convention $w = 2\sqrt{A/K}$ is indicated. Note that the shape of the wall does not depend on the parameters A, K .

Another important quantity is the wall energy. With the use of $-\frac{A}{r'^2} + K \sin^2 \vartheta = 0$ the energy integral can be simplified to

$$\begin{aligned} E &= \int_0^\pi d\vartheta r' \left(\frac{A}{r'^2} + K \sin^2 \vartheta \right) = \int_0^\pi d\vartheta \sqrt{\frac{A}{K}} \frac{2K \sin^2 \vartheta}{\sin \vartheta} = 2\sqrt{AK} \int_0^\pi d\vartheta \sin \vartheta \\ &= 4\sqrt{AK}. \end{aligned} \quad (5.9)$$

5.2.4 Influence of the Dzyaloshinsky-Moriya term

Unlike the other terms in (5.4) the DM interaction does not favor ferromagnetism. For large \mathbf{D} the system does not form ferromagnetic domains (and corresponding walls) but has a non-collinear periodic spin configuration as ground state [e.g. 7, 30–32, 46, 74].

Even if the ground state is ferromagnetic the DM interaction can be relevant for the domain wall shape. In this case the wall shape is more complicated than the one discussed above since the magnetization generally does not stay in one plane. For a fixed set of parameters ($A, \mathbf{D}, \mathbf{K}$) the domain wall configuration can be determined numerically by the method described in Appendix F.2, whereas a general analytical solution does not seem to be feasible.

In the following the \mathbf{D} -vector is assumed to be parallel to one of the (Cartesian) coordinate axes. With the ansatz made for the anisotropy energy tensor these axes correspond to the high-symmetry lines of the crystal. Therefore the analysis covers (among others) all cases where the domain walls are oriented along a high-symmetry line of the (110)-surface (as this implies $\mathbf{D} \perp \mathbf{q}$). It is important to note that in this cases the parameter space spanned by $A, \mathbf{D}, \mathbf{K}$ can be described in 2 dimensions, i.e. all points in the parameter space can be mapped into a 2-dimensional space just by exchanging the coordinate axes and rescaling the units (see below).

Ground state of the quasi one-dimensional model

Before the shape of the domain walls is studied the ground state of the model (5.4) is investigated, taking into account the non-collinear periodic spin configurations. The restriction to one dimension in real-space is reasonable for the description of walls between ferromagnetic domains (which are the main subject of investigation in this thesis), but one has to keep in mind that this might be a crude simplification if the domains are not ferromagnetic. Nevertheless, this simple model already shows a complex behavior if \mathbf{D} is large enough to compete with A, \mathbf{K} .

At first the most simple case is considered: If the \mathbf{D} -vector points parallel to the hard axis the magnetization obviously stays in the plane perpendicular to \mathbf{D} . If the easy axis is the x -axis, the hard axis is the z -axis and $K = K_y - K_x$ then the energy functional has the form:

$$E = \int dr (A \dot{\varphi}^2 + D \dot{\varphi} + K \sin^2 \varphi) . \quad (5.10)$$

This case is already analyzed in [32, 46]. The DM term can give a negative contribution to the energy of a periodic state only if the magnetization performs a full rotation and in any possible non-collinear periodic ground state $D \dot{\varphi}$ is negative over the entire period. The energy of one period with length R can be written as

$$E_R = \int_0^R dr (A \dot{\varphi}^2 + K \sin^2 \varphi) \pm 2 \pi D$$

where the sign of the last term depends on the rotational direction. A full spin rotation from $\varphi = 0$ to $\varphi = \pm 2\pi$ with a period length R cannot take less energy than two optimal domain walls, since the latter cover the same φ -intervals but are not bounded on the r -axis. With Expression (5.9) a rotating state has the energy $E_R \geq 8 \sqrt{A K} \pm 2 \pi D$. If this value is positive the ground state cannot be non-collinear, if this value is negative there exist states (e.g. a series of domain walls) that have lower energy than any ferromagnetic state. Therefore a non-collinear periodic spin-configuration is the ground state if and only if

$$|D| > \frac{4}{\pi} \sqrt{A K} . \quad (5.11)$$

Note that $|D|$ is much weaker in most real systems. The shape of the periodic ground state is shown in Fig. 5.6, the real-space period is plotted in Fig. 5.7. In the limit $|D| \searrow \frac{4}{\pi} \sqrt{A K}$ the system forms two domains of diverging length. In this limit it requires only minor energy to move the domain walls with respect to each other and the domain size calculated from (5.10) is not meaningful.

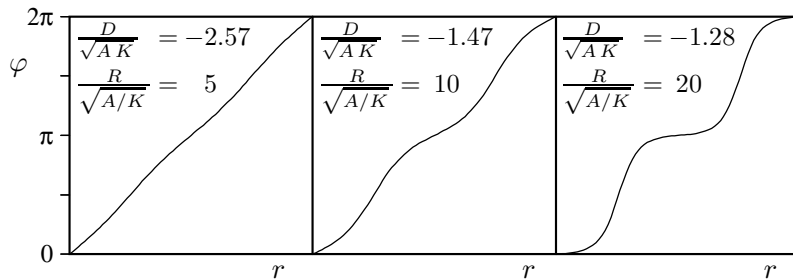


Figure 5.6: Shape of the periodic ground state for \mathbf{D} parallel to the hard axis. If the period length R is small $\dot{\varphi}$ is almost constant. For increasing R two domains of length $R/2$ emerge.

If the \mathbf{D} -vector does not point parallel to the hard axis the magnetization can deviate from the plane normal to \mathbf{D} . Depending on the size of $A, \mathbf{D}, \mathbf{K}$ the ground state can be

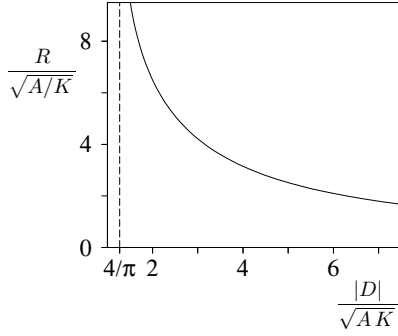


Figure 5.7: Period length R of the ground state for \mathbf{D} parallel to the hard axis. If R is considerably larger than the wall width $2\sqrt{A/K}$ then the system forms virtually ferromagnetic domains whose size in reality depend on effects not considered here (like magnetostatic interactions, further boundary conditions). For large $|D|$ the period length approaches zero very slowly.

A straightforward method to obtain this curve is presented in Appendix F.3.

ferromagnetic, rotate in the plane normal to \mathbf{D} or describe a truly 3-dimensional rotation path in spin-space. In the following an overview over the possible ground states is given.

The system can be described with just two independent nondimensional parameters \mathcal{D} , \mathcal{K} instead of A , $|\mathbf{D}|$, \mathbf{K} , this simplifies the situation a lot:

The coordinate system is chosen such that

$$\mathbf{D} = D \mathbf{e}_z \quad , \quad K_y > K_z \quad .$$

With the definitions

$$\mathcal{E} = \frac{E}{\sqrt{A(K_y - K_z)}} \quad , \quad \mathcal{K} = \frac{K_x - K_z}{K_y - K_z} \quad , \quad \mathcal{D} = \frac{-D}{\sqrt{A(K_y - K_z)}}$$

$$\bar{\vartheta}(r) = \vartheta\left(\sqrt{\frac{K_y - K_z}{A}} r\right) \quad , \quad \bar{\varphi}(r) = \varphi\left(\sqrt{\frac{K_y - K_z}{A}} r\right)$$

the energy functional (5.4) can be written as

$$\mathcal{E} = \int dr \left(\dot{\bar{\vartheta}}^2 + \sin^2 \bar{\vartheta} \left(\dot{\bar{\varphi}}^2 - \mathcal{D} \dot{\bar{\varphi}} + \mathcal{K} \cos^2 \bar{\varphi} + \sin^2 \bar{\varphi} \right) + \text{const} \right) .$$

In the following the irrelevant constant term in the integrand and the bars ($\bar{}$) on ϑ, φ are omitted:

$$\mathcal{E} = \int dr \left(\dot{\vartheta}^2 + \sin^2 \vartheta \left(\dot{\varphi}^2 - \mathcal{D} \dot{\varphi} + \mathcal{K} \cos^2 \varphi + \sin^2 \varphi \right) \right) . \quad (5.12)$$

The investigation of Eqn. (5.12) can be restricted to the parameter space $\mathcal{K} \leq 1$ and $\mathcal{D} \geq 0$: The intervals $\mathcal{K} \in (0, 1)$ and $\mathcal{K} \in (1, \infty)$ correspond to equivalent cases, just the labeling of the x - and y -axes are exchanged. Also the cases for $+\mathcal{D}$ and $-\mathcal{D}$ differ only by the rotational direction.

For $\mathcal{K} < 0$ the easy axis is perpendicular to the \mathbf{D} -vector. If the magnetization stays in the plane normal to \mathbf{D} (i.e. $\sin^2 \vartheta = 1$, $\dot{\vartheta} = 0$), the energies of the ferromagnetic and the flat rotating state can be compared with the same argument as above: By noting that $\mathcal{K} \cos^2 \varphi + \sin^2 \varphi = (1 - \mathcal{K}) \sin^2 \varphi + \text{const}$ one can conclude from (5.12) that there is a flat rotating state that has lower energy than any ferromagnetic state if and only if

$$|\mathcal{D}| > \frac{4}{\pi} \sqrt{1 - \mathcal{K}} .$$

But since \mathbf{D} now is pointing parallel to the intermediate instead of the hard axis ($\mathcal{K} < 0$, $K_y > K_z$), the rotating system can lower its anisotropy energy by deviating from the (x, y) -plane while $\sin^2 \varphi$ is large. The numerical simulations reveal that for small $|\mathcal{D}|$ the ground state is always ferromagnetic. With increasing $|\mathcal{D}|$ the system undergoes a

first-order phase transition¹ to a non-collinear ground state. For $\mathcal{K} < \mathcal{K}_c \approx -0.08$ this non-collinear ground state rotates entirely in the (x, y) -plane. For $\mathcal{K}_c < \mathcal{K} < 0$ there is an additional phase with a truly 3-dimensional rotation path that separates the ferromagnetic phase from the phase with the flat rotation path. With increasing $|\mathcal{D}|$ the 3-dimensional rotation path flattens out and at a critical point there is a continuous transition towards the flat rotation path in the (x, y) -plane. The corresponding phase diagram is given in Fig 5.8, the shapes of the ground states are plotted in Fig. 5.9.

For $\mathcal{K} > 0$ the easy axis is parallel to the \mathbf{D} -vector. In this case the system can gain energy by rotating around the \mathbf{D} -vector without deviating much from the easy axis. Thus, with increasing $|\mathcal{D}|$ the ground state changes continuously from the ferromagnetic to the flat rotating state without a first-order phase transition. In Appendix F.4.2 it is shown that the ground state is ferromagnetic if and only if

$$|\mathcal{D}| \leq \mathcal{D}_c = \sqrt{\mathcal{K}} + 1. \quad (5.13)$$

At $|\mathcal{D}| = \mathcal{D}_c$ the system undergoes a second-order phase transition, for larger $|\mathcal{D}|$ the ground state is truly 3-dimensional until a second critical point is reached beyond which the system rotates entirely in the (x, y) -plane normal to the easy axis. The phase diagram is given in Fig. 5.8, the shapes of the ground states are plotted in Fig. 5.9.

For $\mathcal{K} \nearrow 1$ the distance between the two critical points vanishes. At $\mathcal{K} = 1$ the directions normal to the \mathbf{D} -vector do not differ in anisotropy energy and (5.12) simplifies to

$$\mathcal{E} = \int dr \left(\dot{\varphi}^2 + \sin^2 \vartheta (\dot{\varphi}^2 - \mathcal{D} \dot{\varphi} + 1) \right).$$

In this case the system is ferromagnetic if $\dot{\varphi}^2 - \mathcal{D} \dot{\varphi} + 1 > 0$, otherwise the magnetization rotates in the (x, y) -plane. In the latter case the \mathcal{E} is minimal for $\dot{\varphi} = \frac{1}{2} \mathcal{D} = \text{const}$, the phase transition from ferromagnetic to rotating magnetization takes place at $|\mathcal{D}| = 2$.

A numerical procedure suitable to obtain the phase diagram (Fig. 5.8) is sketched briefly in Appendix F.4.1.

Domain walls

The discussion of the domain walls is split in the two cases where the \mathbf{D} -vector points perpendicular or parallel to the easy axis. The independent parameters are chosen differently in both cases. This might help to win the competition between simple nomenclature and simple phase diagrams.

- Easy axis perpendicular to \mathbf{D} :

In the case that \mathbf{D} is perpendicular to the easy axis, the coordinate system is chosen such that

$$\mathbf{D} = D \mathbf{e}_z \quad , \quad K_y, K_z > K_x$$

and as independent parameters are used

$$\mathcal{K}_\perp = \frac{K_z - K_x}{K_y - K_x} \quad , \quad \mathcal{D}_\perp = \frac{-D}{\sqrt{A(K_y - K_x)}}.$$

¹There are several definitions for the term *phase transition*. In this thesis it is used in a generalized sense: Here, a phase transition is a non-analytic behavior of the total energy \mathcal{E} with respect to some parameter \mathcal{P} . If $\frac{d\mathcal{E}}{d\mathcal{P}}$ is not continuous, the transition is first-order. In all other cases it is second-order. The line that describes the position of a phase transition in the parameter space is called *coexistence curve* in analogy to the corresponding curves describing chemical phase transitions.

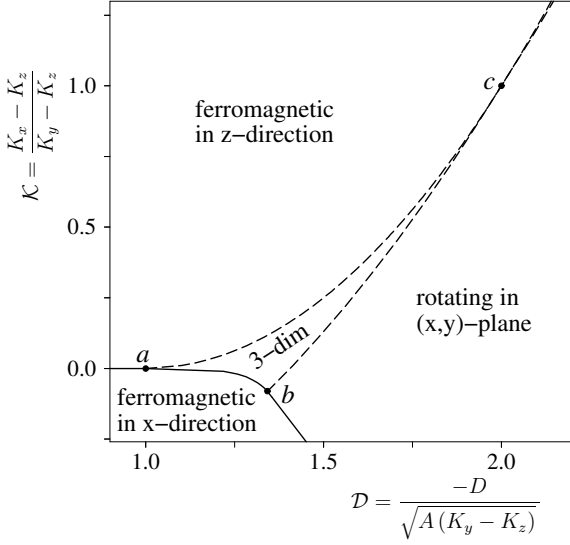


Figure 5.8: Phase diagram for the ground state of the 1-dimensional micromagnetic model. For positive \mathcal{K} the easy axis is parallel to the \mathbf{D} -vector, for negative \mathcal{K} the intermediate axis is parallel to the \mathbf{D} -vector. The case that the hard axis is parallel to the \mathbf{D} -vector cannot be described with this choice of \mathcal{K} , \mathcal{D} . The intervals $\mathcal{K} \in (1, \infty)$, $\mathcal{K} \in (0, 1)$ describe the same case in different coordinate systems, also the ground states at $+\mathcal{D}$ and $-\mathcal{D}$ differ just by chirality.

For $\mathcal{D} < 1$ the ground state is collinear. The dashed line starting at a ($\mathcal{D} = 1$, $\mathcal{K} = 0$) defines the critical points for the transition to the non-collinear ground state, the dashed line starting at b ($\mathcal{K} = \mathcal{K}_c$) defines the critical points for the transition from the truly 3-dimensional to the flat rotation path. At c ($\mathcal{D} = 2$, $\mathcal{K} = 1$) both lines touch (at this point only). The solid line defines a first-order transition. It separates ground states that are ferromagnetic perpendicular to \mathbf{D} from ground states that rotate around \mathbf{D} . For $\mathcal{K} < \mathcal{K}_c$ this line is defined by $\mathcal{D} = \frac{4}{\pi} \sqrt{1 - \mathcal{K}}$.

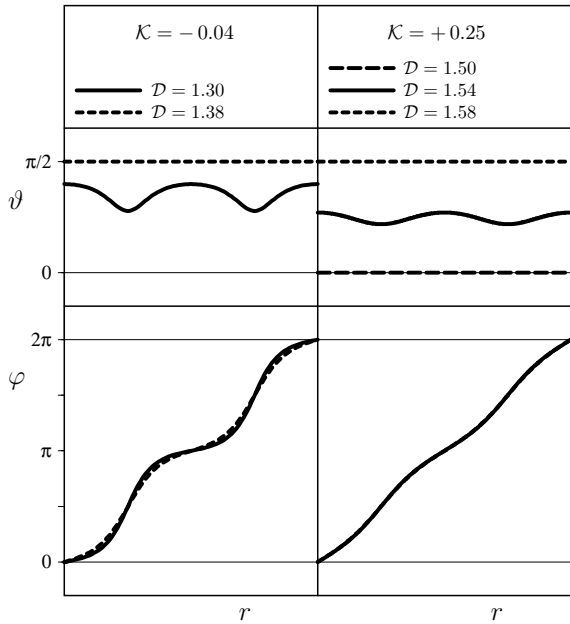


Figure 5.9: Shape of the ground state for different \mathcal{D} , \mathcal{K} . Each curve shows one period, thus the scale of r is not constant.

For $\mathcal{K} = -0.04 < 0$ (i.e. $\mathbf{D} \perp$ easy x -axis) the magnetization is plotted at the non-collinear limit of the first-order transition at $\mathcal{D} = 1.30$ and at the second-order transition at $\mathcal{D} = 1.38$. At $|\mathcal{D}| < 1.30$ the magnetization is collinear.

For $\mathcal{K} = +0.25 > 0$ (i.e. $\mathbf{D} \parallel$ easy z -axis) the magnetization is plotted at both second-order transitions at $\mathcal{D} = 1.50$ and at $\mathcal{D} = 1.58$ as well as at a truly 3-dimensional state in between. The φ -curves coincide within the resolution of this plot.

The definition of the polar angles is repeated for direct comparison with the figure:

$$\begin{pmatrix} x \\ y \\ z \end{pmatrix} = \begin{pmatrix} \sin \vartheta \cos \varphi \\ \sin \vartheta \sin \varphi \\ \cos \vartheta \end{pmatrix}.$$

\mathbf{D} perpendicular to the easy axis implies $\mathcal{K}_\perp > 0$. Then the energy functional has the form

$$\mathcal{E}_\perp = \int dr \left(\dot{\vartheta}^2 + \sin^2 \vartheta \left(\dot{\varphi}^2 - \mathcal{D}_\perp \dot{\varphi} - \mathcal{K}_\perp + \sin^2 \varphi \right) \right). \quad (5.14)$$

For \mathbf{D} parallel to the hard axis (i.e. $\mathcal{K}_\perp > 1$) the magnetization obviously stays in the (x, y) -plane normal to \mathbf{D} . In this case the domain walls between ferromagnetic domains minimize the functional

$$\begin{aligned} \mathcal{E}_\perp &= \int_{-\infty}^{+\infty} dr \left(\dot{\varphi}^2 - \mathcal{D}_\perp \dot{\varphi} + \sin^2 \varphi \right) = \int_{-\infty}^{+\infty} dr \left(\dot{\varphi}^2 + \sin^2 \varphi \right) \pm \int_0^\pi d\varphi \frac{dr}{d\varphi} \mathcal{D}_\perp \dot{\varphi} \\ &= \int_{-\infty}^{+\infty} dr \left(\dot{\varphi}^2 + \sin^2 \varphi \right) \pm \pi \mathcal{D}_\perp. \end{aligned}$$

(provided that the ground state is ferromagnetic). The sign of the last term depends on the rotational direction. The integral in the last expression is already discussed above. It leads to the domain wall profile (5.6) with the energy

$$\mathcal{E}_\perp = 4 - \pi |\mathcal{D}_\perp| \quad \Leftrightarrow \quad E = 4 \sqrt{A(K_y - K_x)} - \pi |D|. \quad (5.15)$$

It is remarkable that the size of the DM interaction in this case influences the wall energy but not the wall profile. The sign of \mathcal{D}_\perp determines the favorable rotational direction.

If the \mathbf{D} -vector points neither parallel to the hard nor easy axis but along the intermediate axis there is a competition between the DM interaction that favors a rotation in the plane normal to \mathbf{D} and the anisotropy energy that favors a rotation in the plane normal to the hard axis. For large $|\mathcal{D}_\perp|$ the magnetization stays entirely in the plane normal to \mathbf{D} but when moving along in the parameter space the system undergoes a second-order phase transition where the magnetization starts to rotate out of this plane.

For $\mathcal{D}_\perp = 0$ and $\mathcal{K}_\perp < 1$ the magnetization rotates in the (x, z) -plane where the anisotropy energy is lowest. There are two degenerate rotation paths of opposite chirality. With increasing \mathcal{D}_\perp the wall profile changes continuously, since a wall in the (x, z) -plane cannot benefit from the DM interaction. For small \mathcal{D}_\perp the magnetization rotates on a truly 3-dimensional path in spin-space and there remain two degenerate rotation paths of opposite chirality. For larger \mathcal{D}_\perp the solutions of opposite chirality both approach the same rotation path that is flat in the (x, y) -plane (cf. Fig. 5.10).

The second-order phase transition from the wall that rotates truly in 3-dimensions to the wall that rotates entirely in the (x, y) -plane is observed by analyzing the numerical solutions of Eqn. (5.14). The magnetization normal to the (x, y) -plane (i.e. $\int dr |z|$) can be chosen as an order parameter that vanishes at the critical point. The characteristic behavior of this order parameter and the derivative of the energy at the phase transition are shown in Fig. 5.11. The parameter space is sampled by performing calculations like the one shown in Fig. 5.11 for several \mathcal{K}_\perp , the resulting coexistence curve is presented in Fig. 5.12.

If \mathbf{D} is parallel to the intermediate axis, the size of the \mathbf{D} -vector can influence the width of the walls between ferromagnetic domains to a certain extent: For $\mathcal{D}=0$ the magnetization rotates in the plane normal to the hard axis and the width according to Formula (5.7) is $w = \sqrt{A/K_{i-e}}$ where K_{i-e} denotes the anisotropy energy between the intermediate and the easy axis. With increasing \mathcal{D} the rotation path moves towards the plane normal to \mathbf{D} , along this path the anisotropy energy is higher and thus the walls get thinner. If \mathcal{D} is

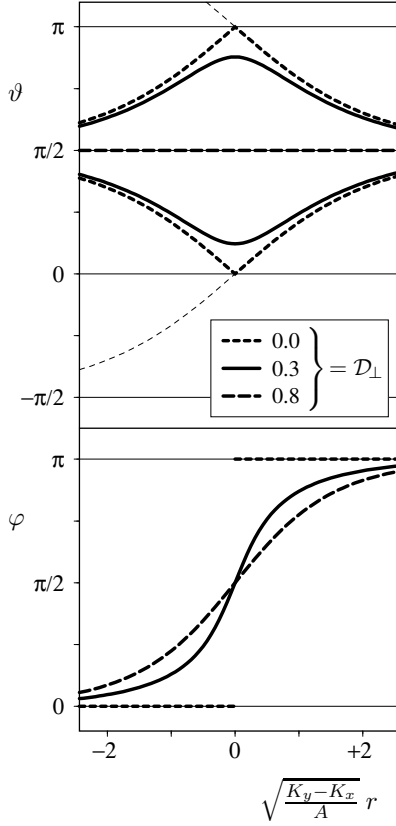


Figure 5.10: Domain wall profiles for different \mathcal{D}_\perp . The curves are calculated for $\mathcal{K}_\perp = 0.5$. For $\mathcal{D}_\perp = 0$ the wall rotates entirely in the (x, z) -plane and has the width $w = 2\sqrt{A/(K_z - K_x)}$. For \mathcal{D}_\perp beyond its critical value (0.65 at $\mathcal{K}_\perp = 0.5$) the wall rotates entirely in the (x, y) -plane and has the width $w = 2\sqrt{A/(K_y - K_x)}$. With further increasing \mathcal{D}_\perp the wall profile does not change until the periodic state shown in Fig. 5.6 appears for $\mathcal{D}_\perp > \frac{4}{\pi} = 1.27$. For $\mathcal{D}_\perp < 0.65$ there are two degenerate wall profiles of opposite chirality.

The definition of the polar angles is repeated for direct comparison with the figure:

$$\begin{pmatrix} x \\ y \\ z \end{pmatrix} = \begin{pmatrix} \sin \vartheta \cos \varphi \\ \sin \vartheta \sin \varphi \\ \cos \vartheta \end{pmatrix}.$$

Note that $\mathbf{m}(r)$ is smooth, the discontinuity in φ is introduced by the definition of the polar angles.

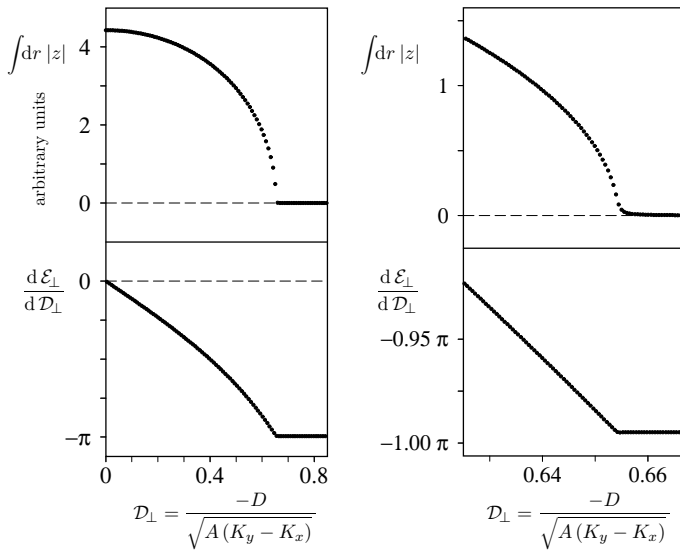


Figure 5.11: Behavior of the order parameter and $\frac{d}{d\mathcal{D}_\perp} \mathcal{E}_\perp$ when varying \mathcal{D}_\perp at fixed \mathcal{K}_\perp . The critical point can be identified easily. The magnified image shows that the kink in the order-parameter curve is slightly smeared out due to numerical effects. In this particular calculations the acuity of the kink depends primarily not on the system size but on other numerical cutoffs.

This figure is obtained for $\mathcal{K}_\perp = 0.5$.

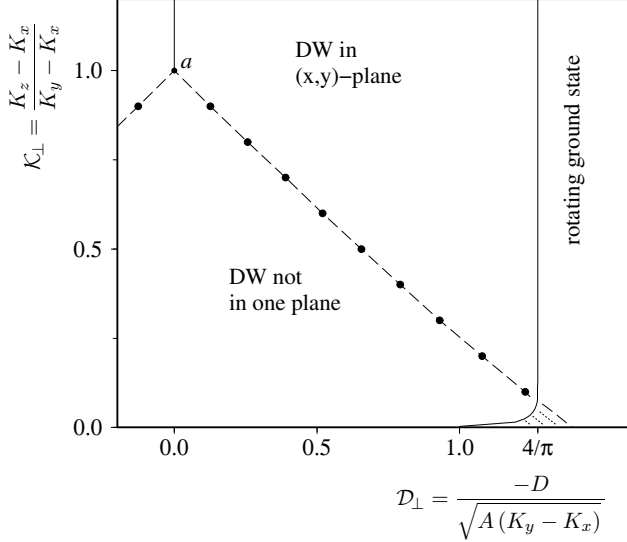


Figure 5.12: Phase diagram for \mathbf{D} perpendicular to the easy x -axis. The data points represent the second-order transition from the flat to the truly 3-dimensional domain walls (DW). The magnetic structures for $+\mathcal{D}_\perp$ and $-\mathcal{D}_\perp$ differ just by chirality, the solid line starting at a ($\mathcal{D}_\perp = 0$, $\mathcal{K}_\perp = 1$) represents a first-order transition whereas the walls on the line $\mathcal{D}_\perp = 0$, $\mathcal{K}_\perp < 1$ are flat in the (x, z) -plane.

In the regime of the truly 3-dimensional walls there are two rotation paths of opposite chirality for each $(\mathcal{D}_\perp, \mathcal{K}_\perp)$, these paths coincide at the coexistence curve towards the regime of flat walls.

The solid line on the right separates the areas of collinear and non-collinear ground states. For large \mathcal{K}_\perp the magnetization of the non-collinear ground state rotates in the (x, y) -plane and there exist no separate domains, for small \mathcal{K}_\perp (shaded area) it describes a truly 3-dimensional rotation path (cf. Fig. 5.8, note the different axes-labels).

large enough the magnetization rotates entirely in the plane normal to \mathbf{D} , Formula (5.7) can be applied again and leads to $w = \sqrt{A/K_{\text{h-e}}}$ where $K_{\text{h-e}}$ denotes the anisotropy energy between the hard and the easy axis.

- Easy axis parallel to \mathbf{D}

In the case that \mathbf{D} is parallel to the easy axis, the coordinate system is chosen such that

$$\mathbf{D} = D \mathbf{e}_z \quad , \quad K_x, K_y > K_z$$

and as independent parameters are used

$$\mathcal{K} = \frac{K_x - K_z}{K_y - K_z} \quad , \quad \mathcal{D} = \frac{-D}{\sqrt{A(K_y - K_z)}} \quad .$$

\mathbf{D} parallel to the easy axis implies $\mathcal{K} > 0$. The following discussion can be restricted to $\mathcal{K} \in (0, 1]$ since $\mathcal{K} > 1$ describes the same situation in a different coordinate system. The energy functional has the form

$$\mathcal{E} = \int dr \left(\dot{\vartheta}^2 + \sin^2 \vartheta \left(\dot{\varphi}^2 - \mathcal{D} \dot{\varphi} + \mathcal{K} \cos^2 \varphi + \sin^2 \varphi \right) \right) . \quad (5.16)$$

The domain walls are numerically investigated in the regime of the collinear ground state (i.e. $|\mathcal{D}| < \sqrt{\mathcal{K}+1}$). They show no phase transition, the magnetization rotates around the easy axis for all $\mathcal{K} > 0$, $\mathcal{D} \neq 0$. Small \mathcal{K} corresponds to a large anisotropy in the (x, y) -plane. For small \mathcal{K} the magnetization stays close to the (x, z) -plane normal to the hard axis ($\varphi \approx \pi$ if $\vartheta \approx \frac{1}{2}\pi$). For increasing $\mathcal{K} < 1$ the anisotropy between the hard and the

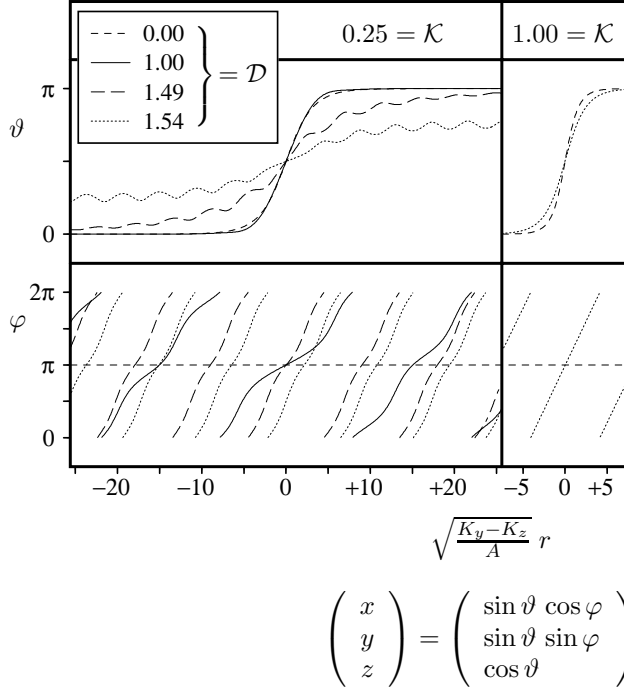


Figure 5.13: Domain wall profiles for different \mathcal{D} , \mathcal{K} . ϑ describes the deviation from the easy axis, φ the rotation around the easy axis. For \mathcal{D} well below \mathcal{D}_c ($\mathcal{D}_c = 1.5$ at $\mathcal{K} = 0.25$, cf. Eqn. (5.13)) the shape of $\vartheta(r)$ does not change much and the magnetization component in the hard y -axis is small everywhere (i.e. $\varphi \approx \pi$ while $\vartheta \approx \frac{1}{2}\pi$). In the vicinity of \mathcal{D}_c ϑ oscillates and converges slowly towards the domain magnetization. Beyond the critical point \mathcal{D}_c the domains are not ferromagnetic (cf. Eqn. 5.13). Beyond the second critical point of the ground state ($\mathcal{D} \approx 1.58$ at $\mathcal{K} = 0.25$) the magnetization rotates entirely in the (x, y) -plane and there are no diverse domains.

← The definition of the polar angles is repeated for direct comparison with the figure.

intermediate axis decreases and the rotation path moves further out of the (x, z) -plane (cf. Fig. 5.13).

In the special case $\mathcal{K} = 1$ (i.e. $K_x = K_y$) the anisotropy energy does not depend on φ and the Euler-Lagrange equations can be solved analytically:

$$\mathcal{E}_{(\mathcal{K}=1)} = \int dr L(\vartheta, \varphi, \dot{\vartheta}, \dot{\varphi}) \quad \text{with} \quad L = \dot{\vartheta}^2 + \sin^2 \vartheta (\dot{\varphi}^2 - \mathcal{D} \dot{\varphi} + 1) \quad ,$$

$$L_{\varphi} = \left(\frac{\partial}{\partial \varphi} - \frac{d}{dr} \frac{\partial}{\partial \dot{\varphi}} \right) L(\vartheta, \varphi, \dot{\vartheta}, \dot{\varphi}) = - \frac{d}{dr} (\sin^2 \vartheta (2 \dot{\varphi} - \mathcal{D})) \stackrel{!}{=} 0 \quad \lim_{|r| \rightarrow \infty} \sin^2 \vartheta = 0 \implies$$

$$\dot{\varphi} = \frac{1}{2} \mathcal{D} = \text{const} \quad ,$$

$$L_{\vartheta} \Big|_{\dot{\varphi} = \frac{1}{2} \mathcal{D}} = \left(\frac{\partial}{\partial \vartheta} - \frac{d}{dr} \frac{\partial}{\partial \dot{\vartheta}} \right) (\dot{\vartheta}^2 + \sin^2 \vartheta (-\frac{1}{4} \mathcal{D}^2 + 1)) \stackrel{!}{=} 0 \quad .$$

The last equation has the same structure as the Euler-Lagrange equation of the functional (5.5) that describes the case $\mathbf{D} = 0$. The optimal wall has the energy

$$\mathcal{E}_{(\mathcal{K}=1)} = 4 \sqrt{1 - \frac{1}{4} \mathcal{D}^2}$$

$$\Leftrightarrow E_{(K_x=K_y)} = 4 \sqrt{A(K_x - K_z) - \frac{1}{4} D^2} = 4 \sqrt{A(K_y - K_z) - \frac{1}{4} D^2} \quad .$$

and the width (that is defined with respect to the deviation from the easy axis, i.e. independently of φ) is

$$w_{(K_x=K_y)} = 2 \sqrt{\frac{A}{K - \frac{D^2}{4A}}} \geq 2 \sqrt{\frac{A}{K}} \quad .$$

This simple analytic solution can give some idea about the general behavior. One should note that $K_x \approx K_y$ might be a reasonable approximation for some real system but is not directly induced by the crystal symmetry. For example, an (100)-surface of a cubic lattice

has negligible in-plane anisotropy but the \mathbf{D} -vector cannot point out-of-plane (cf. Chapter 5.2.2).

In the regime of the truly 3-dimensional ground state the domain walls look like the one plotted in Fig. 5.13. The width of these walls obviously vanishes if the difference between the domains vanishes at the critical point towards the flat rotating ground state.

General remarks

In this chapter it has been shown that the effect of the DM interaction depends strongly on the relations between the anisotropy constants and the direction of the \mathbf{D} -vector. The direction of \mathbf{D} depends on the direction of \mathbf{q} as well as on the crystal symmetry, it is determined by the rules given in Chapters 4.1.1 and 5.2.2.

For the understanding of the domain pattern the precise shape of the walls is of minor importance, although it plays a role in the dynamics of the wall formation. In the analysis presented in Chapter 6.7.2 it is of particular importance that A , $|\mathbf{D}|$ depend on the direction of the \mathbf{q} -vector. This way the DM interaction can influence the preferable wall orientation.

The sign of $\mathbf{m} \times \dot{\mathbf{m}}$ is the only term in the energy functional (5.3) that depends on the rotational direction, thus the introduction of the DM interaction breaks the chiral symmetry.

For large $|\mathbf{D}|$ the ground state is non-collinear, but in the quasi one-dimensional model it is surely ferromagnetic if $|\mathbf{D}| < \sqrt{A (\Delta K)_{\min}}$.

If the \mathbf{D} -vector is parallel to the hard axis it does not influence the wall profile (apart from the rotational direction), although it alters the energy. If the \mathbf{D} -vector is parallel to the intermediate axis it reduces the wall width by changing the wall shape towards a rotation path with higher anisotropy energy. If the \mathbf{D} -vector is parallel to the easy axis the wall width is only subtly altered for small $|\mathbf{D}|$ but considerably enlarged in the vicinity of the non-collinear ground state (at even larger $|\mathbf{D}|$ the difference between the non-collinear domains vanishes, then the width also vanishes).

In Chapter 6 the influence of the DM interaction is discussed for domain walls oriented along high-symmetry lines of the (110)-surface. Even in that restricted symmetry there are several different cases to be distinguished.

If large values of $|\mathbf{D}|$ (or small values of A) are considered one should check whether the ansatz (5.2) is still valid, in this ansatz the exchange interactions are considered only in lowest relevant order.

5.3 Effects of the discrete lattice structure

If the magnetization direction changes on short length scales the simplifications of the micromagnetic model are questionable. In this cases the discrete model (5.2) can be employed. In the following the ground state and the domain walls of the discrete model are investigated. The interactions are restricted to nearest neighbors for simplicity:

$$E = \sum_j \left(J (1 - \mathbf{S}_j \cdot \mathbf{S}_{j+1}) + \mathbf{D} \cdot (\mathbf{S}_j \times \mathbf{S}_{j+1}) + K_x (\mathbf{e}_x \cdot \mathbf{S}_j)^2 + K_y (\mathbf{e}_y \cdot \mathbf{S}_j)^2 + K_z (\mathbf{e}_z \cdot \mathbf{S}_j)^2 \right). \quad (5.17)$$

One has to keep in mind that this model is a crude simplification of the real systems: As the magnetization is allowed to vary only along one direction in real-space all possible

two-dimensional patterns are excluded a priori. The interactions are assumed to be local (i.e. between nearest neighbors). Furthermore, if the difference in the magnetization directions of two neighboring atoms is not small then it might not be sufficient to describe the exchange processes by the lowest-order pair-interactions that enter (5.17). The aim of the following analysis is not to give an accurate description of real domain walls but to give some idea how the discrete nature of the lattice modifies the micromagnetic results.

At first the DM interaction is neglected (Chapter 5.3.1). Then the influence of the \mathbf{D} -vector is discussed briefly (Chapter 5.3.2).

5.3.1 The case $\mathbf{D} = \mathbf{0}$

If the DM term can be neglected (e.g. in systems with inversion symmetry) the spins obviously stay in the plane normal to the hard axis, with an appropriate orientation of the coordinate system (5.17) reduces to

$$\begin{aligned} E &= \sum_j \left(J(1 - \mathbf{S}_j \cdot \mathbf{S}_{j+1}) + K_x (\mathbf{e}_x \cdot \mathbf{S}_j)^2 + K_z (\mathbf{e}_z \cdot \mathbf{S}_j)^2 \right) \\ &= \sum_j \left(J(1 - \cos(\vartheta_{j+1} - \vartheta_j)) + (K_x - K_z) \sin^2 \vartheta_j + \text{const} \right). \end{aligned}$$

With $K = K_x - K_z$ (and by dropping the constant term) the discrete model can be written as

$$\frac{1}{K} E = \sum_j \left(\frac{J}{K} (1 - \cos(\vartheta_{j+1} - \vartheta_j)) + \sin^2 \vartheta_j \right). \quad (5.18)$$

The corresponding micromagnetic energy functional has the form

$$\frac{1}{K} E = \int dr \left(\frac{A}{K} \dot{\vartheta}(r)^2 + \sin^2 \vartheta(r) \right).$$

It is obvious that the discrete model has a well defined antiferromagnetic ground state for $\frac{J}{K} < 0$.

Eqn. (5.18) has been analyzed already in 1972 [40] in order to compare the domain wall shape resulting from the discrete model with the result (5.6) from micromagnetic theory. It turns out that for small $\frac{J}{K}$ the discrete ansatz leads to a sharp domain wall where the magnetization rotates by π from one lattice point to the next. At $\frac{J}{K} = \frac{3}{2}$ the system undergoes a second-order phase transition from a sharp to an asymptotically decaying wall. For increasing $\frac{J}{K}$ the spin orientations quickly approach values that are predicted from the corresponding micromagnetic ansatz (cf. Fig. 5.14).

It is not surprising that the continuum ansatz (5.5) leads to broader domain walls than the discrete ansatz (5.18): The spin stiffness A is fitted to the quadratic term of $\cos(\vartheta_{j+1} - \vartheta_j)$ at small angle differences, but for large $(\vartheta_{j+1} - \vartheta_j)$ the $(1 - \cos)$ -term is considerably smaller than the quadratic fit and thus causing less exchange energy. Furthermore, in a narrow discrete wall there are no lattice points with $\vartheta \approx \frac{\pi}{2}$ (i.e. with large anisotropy energy).

The critical $(\frac{J}{K})$ -value can be determined as the sharp domain wall is always an extremal of (5.18) but for $\frac{J}{K} > (\frac{J}{K})_{\text{crit}}$ it is not a local minimum with respect to varying $\{\vartheta_j\}_j$. Thus the Hessian matrix $(\frac{\partial^2 (E/K)}{\partial \vartheta_j \partial \vartheta_{j'}})_{j,j'}$ evaluated for the sharp walls is positive definite only for $\frac{J}{K} < (\frac{J}{K})_{\text{crit}}$ [63]. For finite systems it is straightforward to estimate $(\frac{J}{K})_{\text{crit}}$ numerically with nested intervals: In each iteration one has to diagonalize the Hessian matrix and to change the upper or lower limit of $\frac{J}{K}$ according to the sign of the lowest

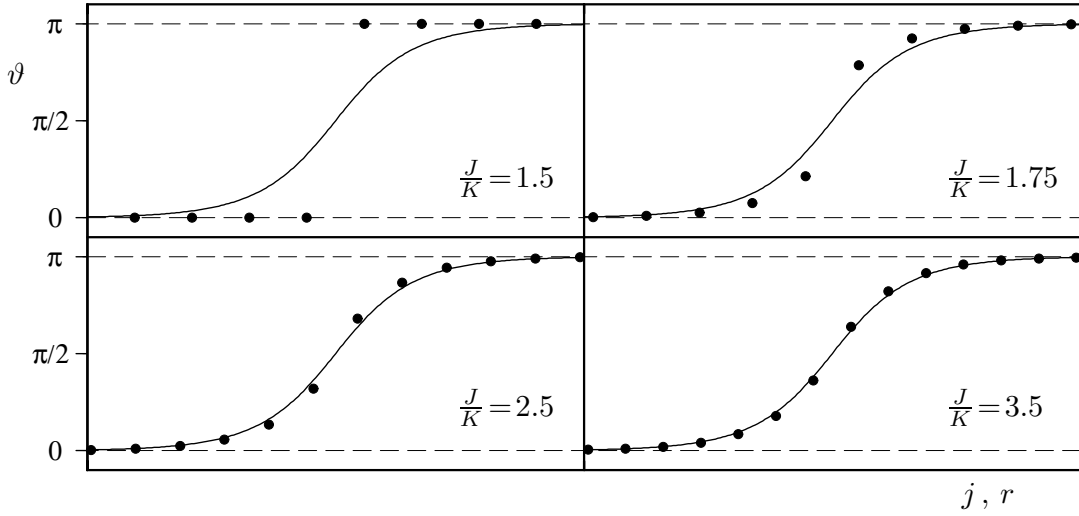


Figure 5.14: Domain wall profiles for the discrete model (\bullet) and the corresponding continuum model ($—$) with $\frac{A}{K} = \frac{J}{2K} \Delta^2$, here Δ denotes the lattice spacing. One dot represents one lattice point, i.e. the scale of the r -axis is not the same for all plots.

eigenvalue. For increasing number of lattice sites the critical value reaches the thermodynamic limit (i.e. the limit for infinite system size) very rapidly, thus the finite-size effects do not impose a problem. But it should be mentioned that the critical point $(\frac{J}{K})_{\text{crit}} = \frac{3}{2}$ is also determined analytically in [63].

5.3.2 Influence of the Dzyaloshinsky-Moriya term

The influence of the DM interaction in the discrete model (5.17) is shown in two special cases that are easy to analyze. The discussion of the general case is beyond the scope of this thesis but for a given set of parameters A , \mathbf{K} , \mathbf{D} the domain wall width, energy and shape can always be calculated with the method that is described in Appendix F.2.

- Hard axis parallel to \mathbf{D}

Like in the continuum model the magnetization obviously stays in the plane normal to the hard axis if the \mathbf{D} -vector points parallel to the hard axis. With an appropriate choice of the coordinate system Eqn. (5.17) can be simplified to

$$E = \sum_j \left(J(1 - \cos(\varphi_{j+1} - \varphi_j)) + D \sin(\varphi_{j+1} - \varphi_j) + K \sin^2 \varphi_j \right) \quad (5.19)$$

where $K = K_y - K_x$ denotes the anisotropy energy in the plane normal to the hard axis. For large $|D|$ the ground states of (5.19) is non-collinear but (in contrast to the continuum model) the period length converges for diverging D : $|\varphi_{j+1} - \varphi_j| \xrightarrow{|D| \rightarrow \infty} \frac{\pi}{2}$. For $|D| \neq 0$ the sharp domain wall that is described in the previous section is not an extremal solution of (5.19). The phase diagram is plotted in Fig. 5.15, details are given in Appendix F.5.

- Easy axis parallel to \mathbf{D} , plane normal to hard axis isotropic

The case that the \mathbf{D} -vector points parallel to the easy axis is analyzed under the assumption that there is no anisotropy in the plane normal to the easy axis. Like in the continuum case this assumption reduces the applicability of the model but simplifies the calculations

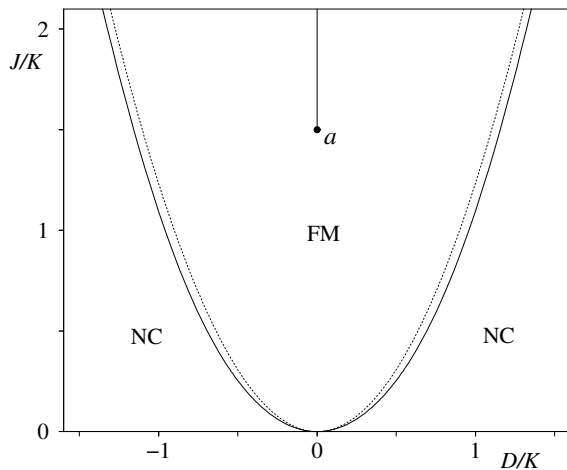


Figure 5.15: Phase diagram for \mathbf{D} parallel to the hard axis. The solid line starting at the critical point a ($\frac{D}{K} = 0$, $\frac{J}{K} = \frac{3}{2}$) indicates a first-order transition between walls of opposite rotational direction that is absent for $\frac{J}{K} < \frac{3}{2}$. The solid parabolic line is the coexistence curve between the ferromagnetic (FM) and non-collinear (NC) ground state. It does not differ much from the corresponding curve of the micromagnetic model that is defined by $\frac{D}{K} = \pm \frac{4}{\pi} \sqrt{\frac{J}{2K}}$ (dotted line).

significantly. With an appropriate choice of the coordinate system Eqn. (5.17) can be simplified to

$$E = \sum_j \left(\begin{aligned} & J (1 - \sin \vartheta_j \sin \vartheta_{j+1} \cos(\varphi_{j+1} - \varphi_j) - \cos \vartheta_j \cos \vartheta_{j+1}) \\ & + D (\sin \vartheta_j \sin \vartheta_{j+1} \sin(\varphi_{j+1} - \varphi_j)) \\ & + K \sin^2 \vartheta_j \end{aligned} \right) \quad (5.20)$$

where $K = K_x = K_y$ denotes the anisotropy energy between the easy axis and the plane normal to it. The corresponding phase diagram is plotted in Fig. 5.16, details are given in Appendix F.5.

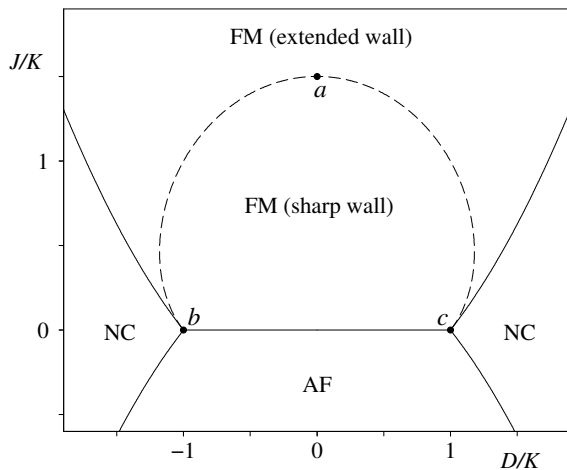


Figure 5.16: Phase diagram for \mathbf{D} parallel to the easy axis and no anisotropy energy in the plane normal to it. The solid lines indicate the first-order transitions between the ferromagnetic (FM), antiferromagnetic (AF) and helical non-collinear (NC) ground states. The dashed lines denote the second-order transition between the sharp and asymptotically decaying domain walls. The point a at ($\frac{D}{K} = 0$, $\frac{J}{K} = \frac{3}{2}$) is the critical point discussed above for $\mathbf{D} = 0$. Four coexistence curves meet in the points b and c at ($\frac{D}{K} = \mp 1$, $\frac{J}{K} = 0$) respectively.

5.4 Extension of the models

The previously described micromagnetic model is a good description for most broad domain walls. Some of the drawbacks are already mentioned: If the magnetization varies on length scales that are comparable with the atomic distance the exchange interactions have to be considered explicitly. Generally, they have a more complicated structure than the one considered in (5.2). Even if a continuous ansatz is sufficient, in some cases it

might be necessary to include more terms than it is done in (5.3). The diagonal form of the anisotropy energy tensor that is assumed in (5.2) is not appropriate for all crystal structures, obviously it is not suitable to describe hexagonal surfaces.

If the crystal symmetry allows for non-collinearity between two adjacent (ferromagnetic) domains then the length of the rotation path is not independent of the rotational direction.

Other extensions of the model are necessary if the sample geometry induces further boundary conditions. In [19] the effect of the boundary geometry of narrow magnetic stripes is discussed, if the broadness of the stripe changes on the same length scale as the magnetization then the wall length (perpendicular to \mathbf{q}) competes with the wall width. Another example for the influence of the sample geometry is the transition from Bloch to Néel walls in systems where the magnetostatic (dipolar) interactions are dominant: In thick magnetic films Bloch walls are energetically more favorable, but in thinner films (thickness on the same length scale as wall width) an in-plane Néel wall reduces the stray field energy. This is first pointed out in [75]. When the magnetostatic interactions are mapped to Eqn. (5.3) then the parameters depend on the film thickness. In the atomically thin films that are discussed in Chapter 6 the stray fields are of minor importance and the Néel walls that interact with the \mathbf{D} -vector do *not* rotate in-plane.

A good overview of different domain walls and adequate models can be found e.g. in [45].

Chapter 6

The system Fe/W(110)

The previously described concepts are used to analyze the magnetic properties of atomically thin surface Fe films that cover a (non-magnetic) W-substrate. The domain walls of these system are of particular interest as the parameters of the models discussed in Chapter 5 are in a rather different energy regime than the parameters of the well-described walls in bulk material and thicker magnetic films. Furthermore the atomic sleaziness of the magnetic layer is important for the magnetocrystalline anisotropy that in the studied case is mainly governed by surface effects.

This system is chosen for this thesis, since it is well studied experimentally. The theoretical analysis mainly focusses on the quantities that are directly accessible with the experiment, i.e. the orientation and shape of the domain walls (that can be probed in real-space experimentally).

The analysis is constricted to the static equilibrium properties, i.e. to the low-temperature regime.

The ab-initio calculations show the orders of magnitude of the different effects and therefore help to identify the relevant interactions. The theoretical prediction of the domain-wall structures is limited by the accuracy of the method.

The results are presented in this chapter, the details concerning the ab-initio calculations (computational parameters etc.) are given in Appendix H.

6.1 Structure

The system in study are atomic thin Fe films that are grown on the W(110)-surface. The geometry and the notation used for the coordinate axes is decribed in Fig. 6.1. The experimentally investigated samples are based on a vicinal W-surface. In this thesis the terraces are approximated by infintite surfaces (with constant Fe coverage and without step edges). This approach is justified by the experimental evidence that the local magnetic structure hardly depends on the shape of the terraces. (Nevertheless, the steps are crucial to support a homogeneous coverage of more than one Fe layer, the internal strain of an Fe double layer in the W lattice constant prohibits a smooth coverage on an extended plain W(110)-surface.)

Coverages of one mono-layer (ML) and one double-layer (DL) Fe are considered.

The structural relaxations are determined for the ferromagnetic surface neglecting the spin-orbit coupling. All magnetic configurations are calculated with the same interlayer relaxation.

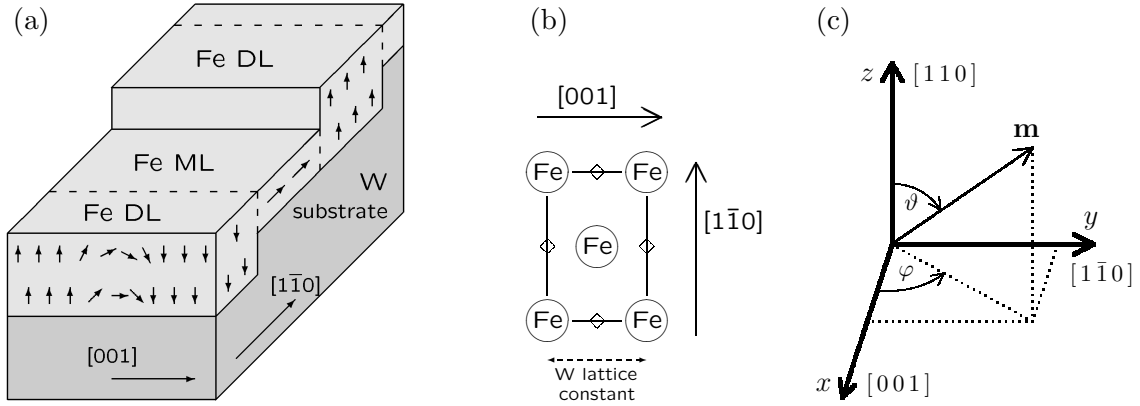


Figure 6.1: (a) The Fe films on the vicinal W(110)-surface grown with one (ML) or two (DL) layers coverage. The $[110]$ direction points perpendicular to the surface of a single step. (b) Orientation of a two-atomic surface unit-cell. In the $[1\bar{1}0]$ -direction the plotted unit cell has the length of $\sqrt{2}$ times the W lattice constant. The diamonds (\diamond) indicate the atomic positions in the next layer (W or Fe). (c) Definition of the polar angles $\vartheta \in [0, \pi]$ and $\varphi \in [0, 2\pi)$ that are used to describe the direction of the magnetic moment \mathbf{m} in spin-space. Note that $\vartheta = 0$ indicates the direction out-of-plane (i.e. perpendicular to the surface). The $[001]$ - $[1\bar{1}0]$ - and $[00\bar{1}]$ -directions are occasionally referenced as x - y - and z -directions respectively.

6.2 Experimental observations

The experimental results that are of most relevance for this thesis are obtained with spin-polarized STM. This technique allows to construct a two-dimensional map of the surface magnetic structure from the tunneling current into a ferromagnetic tip. For a review of this technique cf. e.g. [13].

Results on the system Fe/W(110) can be found in [e.g. 13, 81–83, 97], a typical image is shown in Fig. 6.2.

Several properties of the studied system can be obtained directly from the STM images. In the context of this thesis the most important observations are:

- Easy axis:

The easy axis can be identified from the contrast between the domains since the STM tip is known to have in-plane magnetization. However, the in-plane orientation of the tip is not known.

In the ML the magnetization points in-plane, in the DL it points out-of-plane.

- Domain size:

The size of the domains can be read immediately from the STM image. The irregular boundaries between the mono- and double-layers complicate the estimation of the wall energies, therefore it is not straightforward to check whether the domain size is related to the wall energy as described in Chapter 4.3.

- Domain wall orientation:

The orientation of the domain walls is analyzed for a variety of terrace width and orientations.

In the case of the ML several wall orientations are observed. The wall energy is reduced by minimizing the wall length, thus the favored orientation depends on the sample topology. But even at ≈ 15 K random deviations from the shortest path are

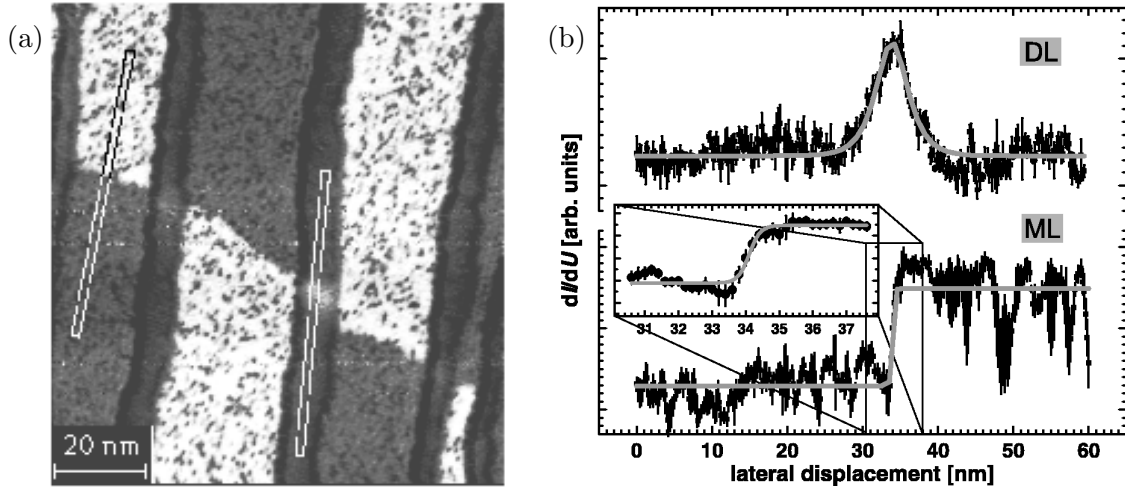


Figure 6.2: (from [83]) STM image of the magnetic structure. The tip magnetization points parallel to the surface. (a) The broad stripes represent areas with ML coverage. Here the contrast between the domains magnetized parallel and antiparallel to the tip is obvious. The narrow stripes in-between represent areas with DL coverage. Here the magnetization in both domains is perpendicular to the magnetization in the tip, but the tilted magnetization in the domain walls is represented by the small brighter areas. The dark stains (clearly visible on the bright ML domains) are caused by impurities, mainly O adatoms. (b) Linescans roughly along the $[001]$ -direction (the path of the scans is indicated in Fig. a). The data is fitted with the wall profile (5.6) that is obtained from the micromagnetic model. Note that the experimental results for the ML wall width are not very clear (see text).

observed, most likely the wall is pinned by the adatom impurities.

In the case of the DL the walls are usually oriented along the $[1\bar{1}0]$ -direction (i.e. $\mathbf{q} \parallel [001]$), independent of the sample topology (there are only a few exceptions observed in the case of very narrow constrictions).

- Domain wall width and shape:

The wall profile in the regions with constant Fe coverage can be measured directly. The Formula (5.6) is fitted to the experimental data in order to obtain a value for the width $2\sqrt{A/K}$.

For the broad DL walls the results are quite clear. The wall shape fits well to (5.6) and the observed widths are in the range of 5-10 nm, the average value is reported as 7.3 nm.

For the ML the results are less evident. The walls are very narrow, in most experiments the width reaches the resolution of the experimental setup and thus is estimated to be less than ≈ 0.8 nm. But recent measurements on very clean samples show ML walls with a width of ≈ 1.5 nm [14].

- Domain wall rotation path and rotational direction:

The magnetization direction in the middle of the wall cannot be determined without further assumptions about the tips magnetization direction (in the narrow ML walls it cannot be detected at all). But the STM images reveal that all DL walls show the same rotational direction, even if the walls are separated by several topological steps.

6.3 Magnetostatic dipolar interactions

The magnetostatic energy is described by the sum (4.3). In Chapter 4.2 it is shown that this sum converges in the two-dimensional surface layers, therefore it can be evaluated by summing over the contributions from all atoms within a certain real-space cutoff.

In the ferromagnetic domains (4.3) can be reduced to two anisotropy energy constants:

$$E^{(\text{dip})}(\varphi, \vartheta) = K_{001}^{(\text{dip})} \cos^2 \varphi \sin^2 \vartheta + K_{1\bar{1}0}^{(\text{dip})} \sin^2 \varphi \sin^2 \vartheta + \text{const} \quad (6.1)$$

$$\text{where} \quad K_{001}^{(\text{dip})} = -\frac{\mu_B^2}{2} \sum_{j,j'}^{j \neq j'} \frac{3|\mathbf{M}_j||\mathbf{M}_{j'}|}{|\mathbf{r}_j - \mathbf{r}_{j'}|^5} \frac{((\mathbf{r}_j - \mathbf{r}_{j'}) \cdot \mathbf{e}_x)^2 - ((\mathbf{r}_j - \mathbf{r}_{j'}) \cdot \mathbf{e}_z)^2}{|\mathbf{r}_j - \mathbf{r}_{j'}|^5},$$

$$K_{1\bar{1}0}^{(\text{dip})} = -\frac{\mu_B^2}{2} \sum_{j,j'}^{j \neq j'} \frac{3|\mathbf{M}_j||\mathbf{M}_{j'}|}{|\mathbf{r}_j - \mathbf{r}_{j'}|^5} \frac{((\mathbf{r}_j - \mathbf{r}_{j'}) \cdot \mathbf{e}_y)^2 - ((\mathbf{r}_j - \mathbf{r}_{j'}) \cdot \mathbf{e}_z)^2}{|\mathbf{r}_j - \mathbf{r}_{j'}|^5}.$$

Here \mathbf{r}_j and \mathbf{M}_j denote the position and magnetic moment of atom number j , in the sums j runs over all atoms and j' runs over all atoms in one unit cell. In the case of just one magnetic layer it is immediately clear from the last formulas that the anisotropy constants $K_{001}^{(\text{dip})}$, $K_{1\bar{1}0}^{(\text{dip})}$ are negative and thus in-plane magnetization is favored. In thicker films the dipolar interactions also favor in-plane magnetization.

The magnetic moment $|\mathbf{M}_j|$ of atom j is obtained from the ab-initio results by integrating the magnetization density over the muffin-tin sphere j (thus neglecting the orbital moment). Inserting these values in the last formulas leads to the anisotropy constants

$$\text{ML:} \quad K_{001}^{(\text{dip})} = -0.10 \text{ meV per surf. atom} \quad , \quad K_{1\bar{1}0}^{(\text{dip})} = -0.11 \text{ meV per surf. atom} \quad ,$$

$$\text{DL:} \quad K_{001}^{(\text{dip})} = -0.28 \text{ meV per surf. atom} \quad , \quad K_{1\bar{1}0}^{(\text{dip})} = -0.27 \text{ meV per surf. atom} \quad .$$

It is tempting to approximate the magnetostatic energies of non-collinear structures with

$$E^{(\text{dip})} = \frac{1}{N} \sum_{j=1}^N \left(K_{001}^{(\text{dip})} \sin^2 \vartheta_j \cos^2 \varphi_j + K_{1\bar{1}0}^{(\text{dip})} \sin^2 \vartheta_j \sin^2 \varphi_j \right) \quad (6.2)$$

where the sum runs over the non-equivalent atoms and the anisotropy constants $K_{001}^{(\text{dip})}$, $K_{1\bar{1}0}^{(\text{dip})}$ are defined as in (6.1). But the applicability of (6.2) implies that $|\mathbf{M}_j|$ or the continuous equivalence $|\mathbf{M}(r)|$ do not depend much on the magnetic configuration and that the sum (4.3) converges on a length scale where the spatial rotation of \mathbf{M} can be neglected.

Considerable fluctuations of $|\mathbf{M}|$ are observed in none of the ab-initio calculations that are presented in Chapter 6. For spin spirals with \mathbf{q} in [001]-direction the magnetic moments are shown in Fig. 6.3.

In this chapter the \mathbf{q} -vector is given in terms of $4\pi a^{-1}$ and $\sqrt{8}\pi a^{-1}$ respectively. Here a denotes the W bcc lattice constant, $(2a^{-1})^{-1}$ is the distance in [001]-direction and $(\sqrt{2}a^{-1})^{-1}$ is the distance in [1 $\bar{1}$ 0]-direction between two atomic rows. Thus $q_x = 0.5(4\pi a^{-1})$ and $q_y = 0.5(\sqrt{8}\pi a^{-1})$ respectively denote row-wise antiferromagnetic spin alignment.

In the following it is shown that the local ansatz (6.2) is sufficient to describe the magnetostatic energy of the broad DL domain walls. It is assumed that \mathbf{M} remains constant in the real-space direction in-plane perpendicular to \mathbf{q} . Therefore one can work with a quasi one-dimensional model (as introduced in Chapter 5.2.1) and always sum over

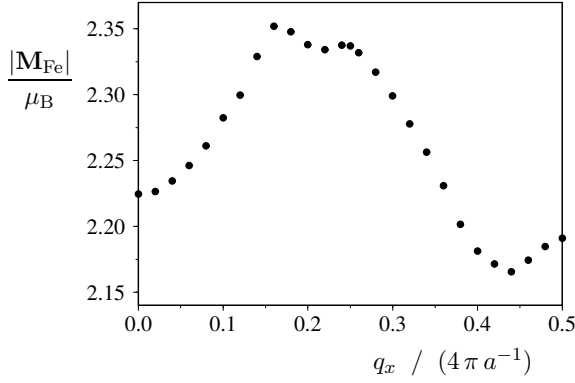


Figure 6.3: Magnetic moments of the ML Fe atoms (integrated over the muffin-tin sphere). The calculations are done for flat spin spirals with different \mathbf{q} -vectors in $[001]$ -direction.

In the DL domain walls there is $q_x < 0.01 (4 \pi a^{-1})$, on this q -scale the DL Fe moments change by less than 0.5%.

all dipoles within one atomic row perpendicular to \mathbf{q} . Thus the applicability of (6.2) means that the sum

$$E_N^{(\text{dip})} = \frac{\mu_B^2}{2} \sum_{j=-N}^N \sum_{i=-\infty}^{\infty} \sum_{i' \in \text{unit cell}}^{(j,i) \neq (0,i')} \frac{(\mathbf{M}_{j,i} \cdot \mathbf{M}_{0,i'}) (\mathbf{r}_{j,i} - \mathbf{r}_{0,i'})^2 - 3 ((\mathbf{r}_{j,i} - \mathbf{r}_{0,i'}) \cdot \mathbf{M}_{j,i}) ((\mathbf{r}_{j,i} - \mathbf{r}_{0,i'}) \cdot \mathbf{M}_{0,i'})}{|\mathbf{r}_{j,i} - \mathbf{r}_{0,i'}|^5}$$

(at $r_{j,i}$, $\mathbf{M}_{j,i}$ the index j labels the (atomic rows perp. to \mathbf{q}) and i the atoms within one row)

converges on a length scale N where the magnetization does not change considerably. In Fig. 6.4 the sum $E_N^{(\text{dip})}$ is evaluated in the ferromagnetic case. Obviously only the interactions with closely neighboring rows are important.

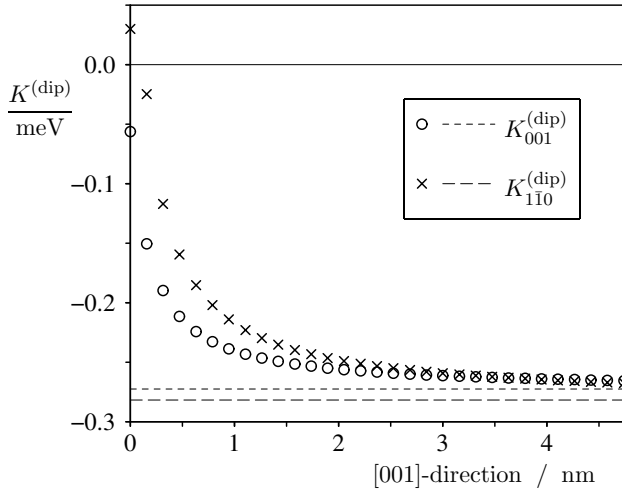


Figure 6.4: Convergence of the DL dipolar anisotropy constants. Each data point represents the sum $E_N^{(\text{dip})}$ evaluated over all atoms that in $[001]$ -direction lie within a certain range N (in $[1\bar{1}0]$ -direction the sum runs over the entire atomic row). The horizontal lines indicate the asymptotic limits (obtained by summing over (2000×2000) unit cells).

The magnetic moments are ferromagnetically aligned.

But just from Fig. 6.4 one cannot estimate the effect of the spatial rotation of \mathbf{M}_j on the magnetostatic energy. This effect is investigated for homogeneous spin spirals. Fig. 6.5 shows the difference of the total dipolar energy $E_{\text{tot}}^{(\text{dip})}$ (obtained with (4.3)) and the approximation $E^{(\text{dip})} = \frac{1}{N} \sum_j \mathbf{S}_j^\dagger \cdot \mathbf{K}^{(\text{dip})} \cdot \mathbf{S}_j$ obtained with (6.2). The energy corrections to the sum over the entire spiral are negligible (at least for $q_x < 0.01 (4 \pi a^{-1})$, i.e. for scales that are relevant for the broad DL domain walls). Fig. 6.5.c illustrates that the local energy corrections are much higher, they just cancel in the sum over the entire spiral. Even the local corrections to (6.2) are not important in the DL. In the ML the magnetization rotates with much larger q , therefore one should work with (4.3) instead of the approximation (6.2). But in Chapter 6.7.3 it is shown that the magnetostatic interactions in the ML can be neglected entirely since the magnetocrystalline anisotropy is much larger.

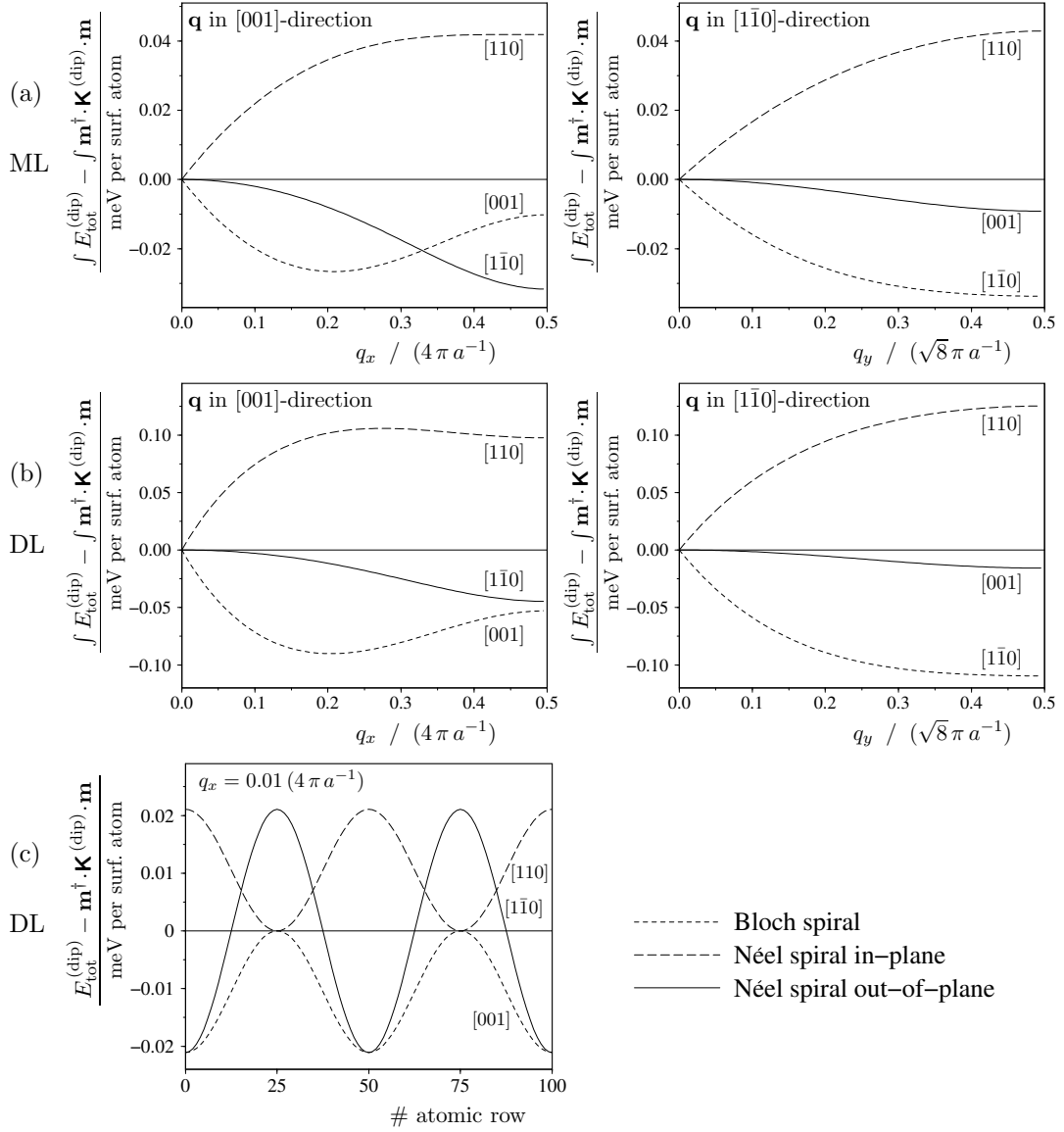


Figure 6.5: Influence of $\text{curl}(\mathbf{M})$ on the magnetostatic energy. The energies are calculated for homogeneous spin spirals. (a), (b) show the deviation of the total dipolar energy $E_{\text{tot}}^{(\text{dip})}$ from the energy evaluated by Formula (6.2). (c) shows the energy density resolved over one period of a spiral with $q_x = 0.01 (4 \pi a^{-1})$ in [001]-direction. The contribution of one pair-interaction is counted half on both lattice sites.

The curves are labeled with the directions of the rotation axes.

6.4 Effective exchange interactions

This chapter describes the calculation of the effective exchange parameters sketched in Chapter 4.1, i.e. the calculation of the parameters describing the energy changes when the spin-quantization axes of neighboring atoms rotate against each other. The Fe magnetic moments remain fairly constant in these calculations (cf. Fig. 6.3), the magnetic structure can be described just by the magnetization direction.

The effect of spin-orbit coupling is neglected in this chapter.

In the following (effective) *exchange energy* denotes the energy changes due to all exchange and correlation processes (and resulting changes in the occupation numbers) that result from a Pauli-type Hamiltonian, i.e. when spin-orbit coupling and magnetostatic interactions are neglected.

6.4.1 Spin stiffness

If the magnetization rotates on large length scales, the electronic structure can locally be approximated by spin spirals (cf. Chapter 3.7.3). In this case no attempt is made to decompose the spin stiffness energy (energy of the spirals) in terms of several exchange processes. At small spiral vectors \mathbf{q} the energy is proportional to \mathbf{q}^2 , the prefactor is the spin stiffness constant A that enters the micromagnetic equation (5.3).

The results for the ML and DL Fe are

$$\text{ML: } A_{001} = 2.0 \left(\frac{a}{4\pi}\right)^2 \text{ eV per surf. atom} \quad , \quad A_{1\bar{1}0} = 2.6 \left(\frac{a}{\sqrt{8}\pi}\right)^2 \text{ eV per surf. atom} \quad ,$$

$$\text{DL: } A_{001} = 6.3 \left(\frac{a}{4\pi}\right)^2 \text{ eV per surf. atom} \quad , \quad A_{1\bar{1}0} = 2.5 \left(\frac{a}{\sqrt{8}\pi}\right)^2 \text{ eV per surf. atom} \quad ,$$

$$\text{for comparison bcc bulk Fe: } A_{100} = 1.1 \left(\frac{a}{4\pi}\right)^2 \text{ eV per atom} \quad .$$

The corresponding data is shown in Fig. 6.6.

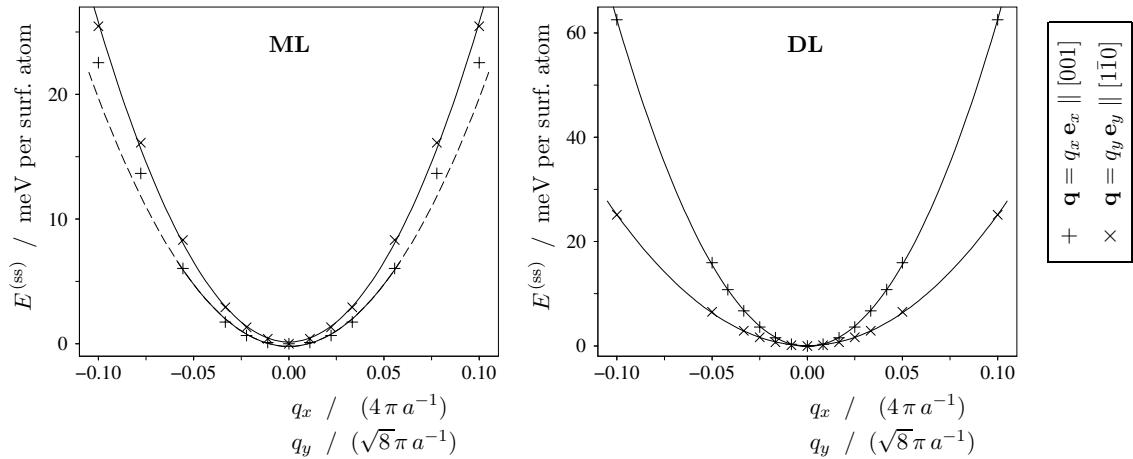


Figure 6.6: Spin-stiffness energies. The points denote the ab-initio results and the solid lines denote the fits with quadratic and constant term only.

6.4.2 Hopping parameters

In the case of one ML Fe the magnetization direction changes on very short length scales (the domain wall width is smaller than 10 atomic rows), here the validity of a continuous model is questionable. In order to find an adequate description of these magnetic structures

the attempt is made to dissolve the magnetic interaction in a sum of hopping processes between discrete atomic rows and to calculate the exchange parameters that can be fed into a model Hamiltonian.

It is assumed that all atoms within one atomic row ($\perp \mathbf{q}$) have the same magnetization direction. Therefore, it is possible to work with effective exchange integrals between atomic rows instead of exchange integrals between single atoms (cf. Chapter 5.2.1). Note that a four-atom interaction contributes to a three-row interaction, if two of the four atoms are in the same row.

Furthermore, it is assumed that all magnetic moments rotate within one plane. This reduces the degrees of freedom considerably.

The ansatz for the exchange energy, that is further investigated in the following, is the expansion

$$\begin{aligned}
E^{(\text{xc})} = & \sum_{j_1, j_1'} X_{j_1, j_1'}^{(1)} (1 - (\mathbf{S}_{j_1} \cdot \mathbf{S}_{j_1'})) \\
& + \sum_{j_1, j_1', j_2, j_2'} X_{j_1, j_1', j_2, j_2'}^{(2)} (1 - (\mathbf{S}_{j_1} \cdot \mathbf{S}_{j_1'}) (\mathbf{S}_{j_2} \cdot \mathbf{S}_{j_2'})) \\
& + \sum_{j_1, j_1', j_2, j_2', j_3, j_3'} X_{j_1, j_1', j_2, j_2', j_3, j_3'}^{(3)} (1 - (\mathbf{S}_{j_1} \cdot \mathbf{S}_{j_1'}) (\mathbf{S}_{j_2} \cdot \mathbf{S}_{j_2'}) (\mathbf{S}_{j_3} \cdot \mathbf{S}_{j_3'})) \\
& + \dots
\end{aligned} \tag{6.3}$$

where \mathbf{S}_j denotes the magnetization orientation of atomic row j .

This expansion is motivated by the description of the exchange in terms of hopping processes, as mentioned in Chapter 4.1. But, (6.3) can be mapped to *any* symmetric function $E^{(\text{xc})}(\{\mathbf{S}_j\}_j)$, provided that all magnetic moments $\{\mathbf{S}_j\}_j$ lie within one plane. No assumptions on the relevant hopping processes are made. Of course, if (6.3) cannot be reduced to just a few dominant terms (i.e. a few parameters X), then it is not useful. This can be the case, for example, if the changes in the occupation numbers cause significant changes in the energy (cf. Chapter 4.1).

Some of the parameters X coincide due to symmetry reasons, e.g. $X_{j_1, j_1'}^{(1)} = X_{j_1', j_1}^{(1)} = X_{j_1+n, j_1'+n}^{(1)}$.

The Heisenberg model (i.e. the exchange term in Eqn. (5.2)) is the leading term in (6.3) with

$$X_{j_1, j_1'}^{(1)} = \frac{1}{2} J_{|j_1 - j_1'|}.$$

Here the factor $\frac{1}{2}$ accounts for the double counting as the sum in (6.3) is understood to count $X_{j_1, j_1'}^{(1)}$ and $X_{j_1', j_1}^{(1)}$.

In Appendix G it is shown, that the Heisenberg model can describe the major changes in the exchange energy. The nearest-neighbor interaction is dominant, but in many cases the consideration of the interactions between 2nd- and 3rd-nearest neighbors improves the approximation. Thus, the exchange energy $E^{(\text{xc})}$ is approximated by

$$E^{(\text{xc})} = \sum_{j=j'+1}^{j'+N} J_{j-j'} (1 - \mathbf{S}_j \cdot \mathbf{S}_{j'}) + \text{const} \tag{6.4}$$

$$\text{with } J_1 = +54 \frac{\text{meV}}{\text{surf. atom}}, \quad J_2 = -14 \frac{\text{meV}}{\text{surf. atom}}, \quad J_3 = +14 \frac{\text{meV}}{\text{surf. atom}}.$$

For the tests presented in Appendix G the error made by (6.4) is $\lesssim 10$ meV per surface atom.

It is *not* possible to improve the approximation by including the terms next to the Heisenberg model (parameters $X_{\dots}^{(2)}$) in the expansion (6.3). In Appendix G.2 it is shown that the corrections to (6.4) cannot be described with one fixed set of parameters $\{X_{\dots}^{(2)}\}$ for a general magnetic configuration.

Note, that (6.4) is a reasonable approximation for the large energy differences between magnetic configurations of big discrepancy (e.g. between ferromagnetic alignment and an atomically sharp domain wall), whereas the approach of the previous Chapter 6.4.1 is suited well for the approximation of the (small) exchange energy in the ferromagnetic limit. The approximations in these two regimes are not necessarily governed by the same exchange integrals (cf. Appendix G.1).

6.5 Magnetocrystalline anisotropy in the ferromagnetic domains

In the ferromagnetic domains the studied surface possesses two mirror planes that are rectangular to each other. In Appendix E it is shown that the magnetocrystalline anisotropy tensor has local extrema (or saddle points) at the high-symmetry directions $[001]$, $[1\bar{1}0]$, $[110]$. With the polar angles as defined in Fig. 6.1 the magnetocrystalline anisotropy energy is approximated by

$$E^{(\text{so})}(\varphi, \vartheta) = K_{001}^{(\text{so})} \cos^2 \varphi \sin^2 \vartheta + K_{1\bar{1}0}^{(\text{so})} \sin^2 \varphi \sin^2 \vartheta + \text{const} . \quad (6.5)$$

The parameters $K_{001}^{(\text{so})}$, $K_{1\bar{1}0}^{(\text{so})}$ are calculated by comparing the energies for the magnetization along the corresponding directions:

$$K_{001}^{(\text{so})} = E^{(\text{so})}(\varphi=0, \vartheta=\frac{1}{2}\pi) - E^{(\text{so})}(\vartheta=0) , \quad K_{1\bar{1}0}^{(\text{so})} = E^{(\text{so})}(\varphi=\frac{1}{2}\pi, \vartheta=\frac{1}{2}\pi) - E^{(\text{so})}(\vartheta=0) .$$

These magnetocrystalline anisotropy constants are very sensitive to small changes in the atomic structure and to computational parameters. Fortunately the local force theorem (cf. Chapter C) can be applied. The magnetocrystalline anisotropy constants are:

$$\begin{aligned} \text{ML} : \quad & K_{001}^{(\text{so})} = 0.39 \text{ meV per surf. atom} , \quad K_{1\bar{1}0}^{(\text{so})} = -2.42 \text{ meV per surf. atom} , \\ \text{DL} : \quad & K_{001}^{(\text{so})} = 0.36 \text{ meV per surf. atom} , \quad K_{1\bar{1}0}^{(\text{so})} = 0.43 \text{ meV per surf. atom} . \end{aligned}$$

As pointed out in [76] the ML anisotropy energies are remarkably high for the ML Fe due to the high potential gradient in the vicinity of the first W-layer nuclei. The states of unbalanced magnetic moment are mainly of (Fe3d)-character and only to a small amount localized at the W-nuclei, but the SOC-term (2.15) in the Hamiltonian is proportional to ∇V and thus much larger in the vicinity of the W nuclei (that have $\frac{74}{26}$ times more protons than the Fe nuclei). The results in Fig. 6.7 show the contributions from the different atom layers to the anisotropy energies. Note that the first W atoms have an induced magnetic moment of $0.1 \mu_B$ in the case of ML or DL coverage alike. Nevertheless, in the case of ML coverage the W nuclei have a much stronger impact on the anisotropy energy.

The applicability of the ansatz (6.5) is checked by calculating the anisotropy energy not only in the three high-symmetry directions. The results are shown in Fig. 6.8, the discrepancy between the \cos^2 -ansatz and the ab-initio results is within the numerical uncertainty. In the following it is assumed that Eqn. (6.5) (with parameters fitted to the energies in the high-symmetry directions) is sufficient to describe the magnetocrystalline anisotropy in the studied system.

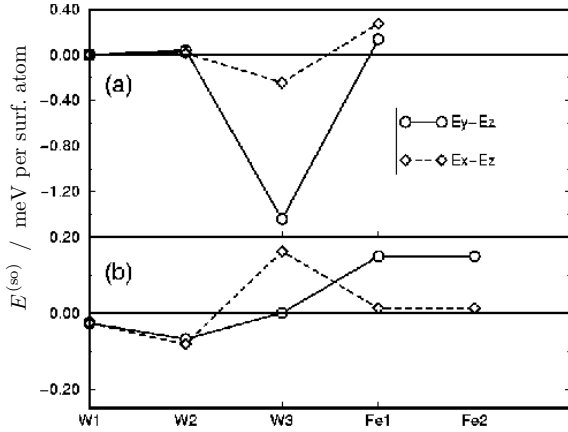


Figure 6.7: (from [76]) Contribution of the different surface layers to the anisotropy energy. The curves are obtained by including the SOC-term only in the real-space part (i.e. muffin tin) that belongs to a certain atomic layer. Fig. a shows the results for the ML, Fig. b for the DL.

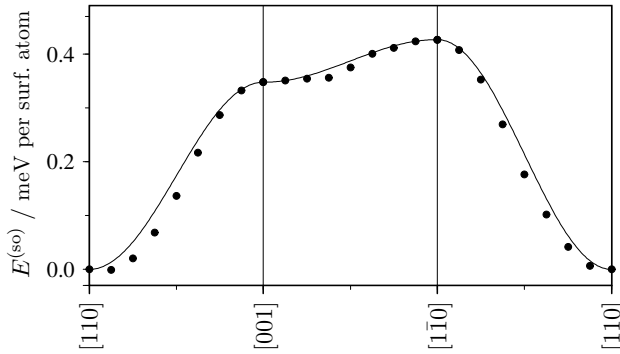


Figure 6.8: Magnetocrystalline anisotropy of the Fe DL calculated along the lines between the three high-symmetry points (with local force theorem). The dots represent the ab-initio results and the solid lines the \cos^2 -ansatz according to Eqn. (6.5) fitted to the results in the three high-symmetry points. $[110]$ denotes the direction out-of-plane.

6.6 Dzyaloshinsky-Moriya interaction in the DL domain walls

The energy corrections due to the SOC-term in the Hamiltonian depend on the size of the \mathbf{q} -vector. For spiral structures these energies can be estimated by the method presented in Chapter 3.9. In the ferromagnetic limit the energy density (averaged over an entire spiral period) corresponds to the integral of the anisotropy-energy curves presented in Fig. 6.8. If the DM interaction does not vanish, then the (averaged) SOC-induced corrections to the energy density have a term that is linear in q . Of course, for large spiral periods (i.e. small q) the SOC-induced corrections are dominated by their linear term. The size of this linear term corresponds to the size of the \mathbf{D} -vector.

In Fig. 6.9 the results for small \mathbf{q} -vectors are given for the Fe DL. The curves allow to estimate the value of the DM interaction for both wall orientations as well as the validity of some of the approximations made in the micromagnetic ansatz, namely that in the relevant $|\mathbf{q}|$ -intervals the odd part of the curves can be approximated by the linear term and the corrections due to the even part can be neglected against the spin stiffness that is calculated in Chapter 6.4.1. For the rotation axes orthogonal to the ones chosen in the figure the curves are certainly even and the DM interaction vanishes (cf. Chapter 5.2.2).

The linear fits that are indicated in Fig. 6.9 correspond to the values

$$\text{DL: } \begin{aligned} D_{001} &= (-25 \pm 10) \left(\frac{a}{4\pi}\right) \text{ meV per surf. atom} \quad ; \mathbf{q} \parallel [001] \quad , \\ D_{1\bar{1}0} &= (14.5 \pm 3) \left(\frac{a}{\sqrt{8}\pi}\right) \text{ meV per surf. atom} \quad ; \mathbf{q} \parallel [1\bar{1}0] \quad . \end{aligned}$$

In the case of the Fe ML the magnetic structure in the domain walls is far from the

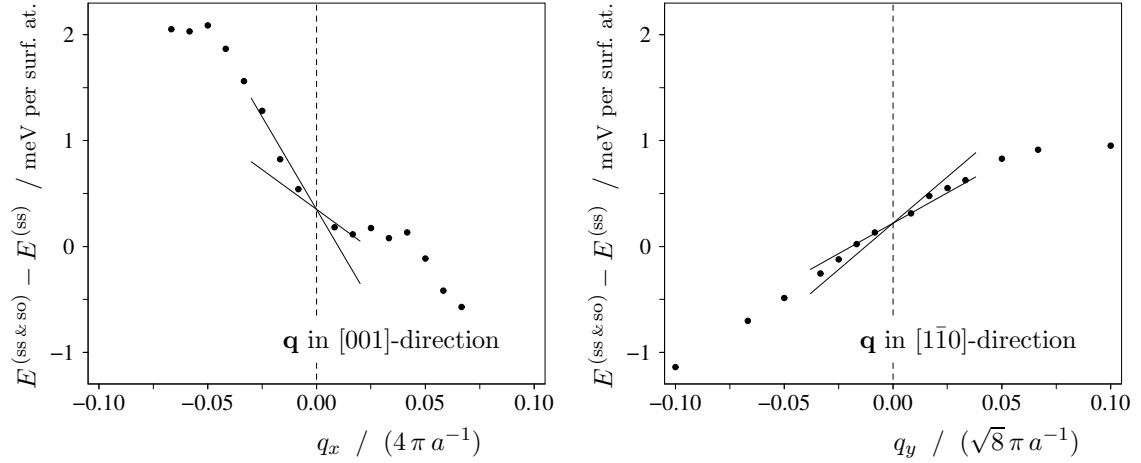


Figure 6.9: SOC corrections to the spin-spiral energies in the Fe DL. The curves show only the contribution of the spin-orbit coupling to the total energy, i.e. they show the energies of the spin spirals obtained with SOC included in the Hamiltonian minus the energies presented in Fig. 6.6 that are obtained from the pure Pauli-type Hamiltonian (i.e. with the scalar-relativistic approximation). In the left figure the spins rotate in the (x, z) -plane and in the right figure they rotate in the (y, z) -plane, in both cases the spin rotation axis is parallel to the \mathbf{D} -vector. The size of $|\mathbf{D}|$ is estimated by the slope of the curves at $\mathbf{q}=0$ (indicated with solid lines).

ferromagnetic limit. The experimental results do not rule out an atomically sharp wall. It is not clear to what extent the effects, that arise from the interplay of non-collinearity and spin-orbit coupling, can be described with the \mathbf{D} -vector (and with the spin-orbit coupling effects in homogeneous spin spirals respectively). Due to the immense computational effort and the limited significance of the result the calculation of the DM interaction is abandoned in the case of the Fe ML.

6.7 Modeling the domain-wall structure

6.7.1 Domain magnetization

In the domains the total anisotropy energy is the sum $K^{(\text{dip})} + K^{(\text{so})}$.

| | anisotropy const. / (meV per surf. atom) | | | | | |
|-----------|--|-------------------------|--------------------------|--------------------------------|-------------------------------|--------------------------------|
| | $K_{001}^{(\text{dip})}$ | $K_{001}^{(\text{so})}$ | $K_{001}^{(\text{tot})}$ | $K_{1\bar{1}0}^{(\text{dip})}$ | $K_{1\bar{1}0}^{(\text{so})}$ | $K_{1\bar{1}0}^{(\text{tot})}$ |
| ML | -0.10 | 0.39 | 0.29 | -0.11 | -2.42 | -2.53 |
| DL | -0.28 | 0.36 | 0.08 | -0.27 | 0.43 | 0.16 |

Table 6.1: Calculated anisotropy constants. Note that the error in $K^{(\text{so})}$ is of the order 0.1 meV, therefore the relative error of the DL $K^{(\text{tot})}$ is huge.

For the ML Fe the easy axis can unambiguously be identified as the $[1\bar{1}0]$ -in-plane-axis, but in case of the DL the total anisotropy energy is too small to identify the easy axis (cf. Table 6.1).

6.7.2 Micromagnetic model for the broad DL walls

The broad DL domain walls can be described within the micromagnetic model that is introduced in Chapter 5.2, recall Eqn. (5.3):

$$E = \int dr \left(A \dot{\mathbf{m}}(r)^2 + \mathbf{D} \cdot (\mathbf{m}(r) \times \dot{\mathbf{m}}(r)) + \mathbf{m}(r)^\dagger \cdot \mathbf{K} \cdot \mathbf{m}(r) \right) \quad \text{where } \mathbf{m} = \frac{\mathbf{M}}{|\mathbf{M}|}.$$

If \mathbf{q} points along a high-symmetry line (i.e. $[001]$ or $[\bar{1}\bar{1}0]$) then the \mathbf{D} -vector is in-plane perpendicular to \mathbf{q} . From experiments it is known that the magnetization in the domains points out-of-plane. As the easy axis is perpendicular to \mathbf{D} , the walls that are oriented along a high-symmetry direction correspond to Figs. 5.10, 5.12 (remember that in Chapter 5 there is $\mathbf{D} \parallel \mathbf{e}_z$).

Even if the wall magnetization rotates within one plane, there are eight different combinations of the high-symmetry wall orientations and spin rotations. They are listed in Table 6.2. The Bloch walls of opposite chirality are equivalent, but there remain six configurations with pairwise different energies.

The model parameters A , \mathbf{D} , \mathbf{K} are obtained from the ab-initio calculations. They are converted into areal densities and listed in Table 6.3. The spin stiffness A gets contributions from the exchange interactions presented in Fig. 6.6 and from the quadratic fit to the DM curves presented in Fig. 6.9, the latter is rather small and neglected here.

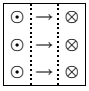
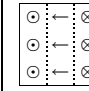
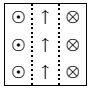
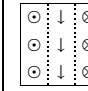
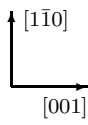
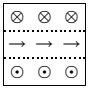
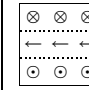
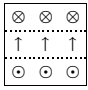
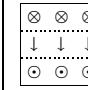
| | K_{001} | | $K_{\bar{1}\bar{1}0}$ | | |
|--|--|--|--|--|---|
| walls parallel to $[\bar{1}\bar{1}0]$ A_{001} |  $+D_{001}$ |  $-D_{001}$ |  $D=0$ |  $D=0$ |  |
| walls parallel to $[001]$ $A_{\bar{1}\bar{1}0}$ |  $D=0$ |  $D=0$ |  $+D_{\bar{1}\bar{1}0}$ |  $-D_{\bar{1}\bar{1}0}$ | |

Table 6.2: Rotation paths and corresponding model parameters for the DL domain walls. In-between the listed Bloch- and Néel-wall paths there are truly 3-dimensional rotation paths in spin-space (cf. Figs. 5.10, 5.12).

| | | 001 | $\bar{1}\bar{1}0$ |
|--|----------------------------|-------------------|-------------------|
| spin stiffness | $A / (\text{meV})$ | 56.4 | 44.8 |
| anisotropy energy | $K / (\text{meV nm}^{-2})$ | 1.1 ^{*)} | 2.3 ^{*)} |
| DM interaction | $D / (\text{meV nm}^{-1})$ | -8.9 | 7.3 |
| *) Note that the error in K is about 1.5 meV nm^{-2} . | | | |

Table 6.3: DL model parameters converted into areal densities.

If the magnetization rotates within one plane the wall energy can be calculated by Eqn. (5.15):

$$E = 4\sqrt{AK} - \pi D.$$

The error margins of the calculated model parameters leave some space for interpretations.

All walls that are observed in the broad DL stripes are oriented in $[\bar{1}\bar{1}0]$ -direction. The experiments show that the rotational direction is the same in all these walls. It is most likely that they are Néel walls, otherwise one would observe both of the two degenerate rotation paths that are shown in Fig. 5.10. In the Néel walls the width is described by

$w = 2\sqrt{A/K} \Rightarrow K = 4A/w^2$. The calculated spin stiffness and the measured wall width are both of reasonable accuracy. This allows to estimate the anisotropy energy as

$$K_{001} = 4 \frac{A_{001}}{w^2} \approx 4 \frac{56.4}{7.3^2} \text{ meV nm}^{-2} = 4.2 \text{ meV nm}^{-2}.$$

If this value is inserted in Eqn. (5.15) then one gets (with the error bars of D_{001} that are indicated in Fig. 6.9):

$$E_{1\bar{1}0}^{(\text{Néel})} = 4\sqrt{A_{001}K_{001}} - \pi|D_{001}| \approx 62 \text{ meV nm}^{-1} - \pi|D_{001}| \approx (34 \pm 11) \text{ meV nm}^{-1}.$$

The contribution from the DM interaction is large enough to lower the wall energy considerably. A hypothetical Bloch wall oriented in $[1\bar{1}0]$ -direction has the energy

$$E_{1\bar{1}0}^{(\text{Bloch})} = 4\sqrt{A_{001}K_{1\bar{1}0}} \approx 30\sqrt{K_{1\bar{1}0}} \text{ meV}.$$

It is energetically more favorable than the Néel wall if $K_{1\bar{1}0} \lesssim 1 \text{ meV nm}^{-2}$. Of course, the truly 3-dimensional walls that are described in Chapter 5.2.4 have lower energy than pure Néel or Bloch walls. The coexistence curve in Fig. 5.12 can be approximated with $\mathcal{K}_\perp = 1 - 0.75|D_\perp|$, the domain walls are truly 3-dimensional if $K_{1\bar{1}0} < K_{001} - 0.75|D_{001}|\sqrt{K_{001}/A_{001}} \approx (2.4 \pm 0.7) \text{ meV nm}^{-2}$. But, \mathcal{K}_\perp must be considerably smaller than $0.75|D_\perp|$ if the deviation from the Néel-wall rotation path is detectable with STM.

The next step is to compare $E_{1\bar{1}0}^{(\text{Néel})}$ with the energies E_{001} of the hypothetical walls that are oriented in $[001]$ -direction. The energy (per length) E_{001} is expected to be *much* higher than $E_{1\bar{1}0}^{(\text{Néel})}$ since walls oriented in $[001]$ -direction are observed only in very narrow constrictions (i.e. only in cases where the wall length ($\perp \mathbf{q}$) gets much shorter if the wall is oriented in $[001]$ -direction). A Néel wall that is oriented in the $[001]$ -direction has the energy

$$E_{001}^{(\text{Néel})} = 4\sqrt{A_{1\bar{1}0}K_{1\bar{1}0}} - \pi|D_{1\bar{1}0}| \approx 27\sqrt{K_{1\bar{1}0}} \text{ meV} - (23 \pm 5) \text{ meV nm}^{-1}.$$

(The error bars of $D_{1\bar{1}0}$ refer to the ones indicated in Fig. 6.9.) Thus, a Néel wall in $[001]$ -direction has higher energy per length than a Néel wall in $[1\bar{1}0]$ -direction if $K_{1\bar{1}0} \gtrsim (4.7 \pm 3.2) \text{ meV nm}^{-2}$. A Bloch wall that is oriented in the $[001]$ -direction has the energy

$$E_{001}^{(\text{Bloch})} = 4\sqrt{A_{1\bar{1}0}K_{001}} \approx 55 \text{ meV nm}^{-1}.$$

Again, if a truly 3-dimensional wall exists it has even lower energy than a pure Néel or Bloch wall.

The terms of the magnetostatic energy that depend on the spatial rotation of \mathbf{M} , are not included in Eqn. (5.3). They are calculated with the procedure that is presented in Appendix F.2.3. Their contribution to the wall energy is less than 5 meV nm^{-1} .

Obviously, the calculated parameters and specified error margins (in particular of K) do not quite match with the interpretation given above.

But one should be aware of the meaning of these error margins. The error margin that is given for D corresponds to the fits that are indicated in Fig. 6.9. The error margin of D_{001} is very sensitive to the fitting procedure, over and above the accuracy of the computed data points is not known (cf. Appendix H.4). The accuracy of $K^{(\text{so})}$ is known better. The convergence is estimated with respect to important computational parameters and with respect to the number of W-layers (cf. Appendix H.3). But, this convergence tests do not tell anything about the discrepancy between the perfect LDA

result (for the interlayer relaxations as given in Appendix H.1) and the real system. The relevant energy differences reach the limit of the computational method (note that $1 \text{ meV nm}^{-2} \cong 0.035 \text{ meV per Fe atom}$).

Furthermore, one should keep in mind that the micromagnetic model (5.3) is not exact, though it is sufficient to describe the essential effects (cf. e.g. Fig. 6.8).

Some of the qualitative experimental results are quite distinct. One has to use them as a basis for the interpretation. On the relevant energy scale one cannot expect that the DFT results definitely confirm the proposed explanation. The merit of the ab-initio calculations is to estimate the order of magnitude of the interactions and thus to identify the relevant effects. In particular, the calculations show that the DM interaction is large enough to compete with \sqrt{AK} and dominates the $\text{curl}(\mathbf{M})$ -dependent terms of the magnetostatic interaction. Furthermore, the ab-initio calculations show that the preferred wall orientation cannot be explained just by the anisotropy of the spin stiffness: The DFT calculations that do not include SOC are relatively stable and precise, moreover the large uncertainties in K and E result from the partial cancellation of different quantities. Without the DM term the magnetization rotation path would not depend on the wall orientation and the energy of walls oriented in $[1\bar{1}0]$ - and $[001]$ -direction would be just proportional to $\sqrt{A_{001}}$ and $\sqrt{A_{1\bar{1}0}}$ respectively.

All walls show the same rotational direction. Therefore, it is most likely that they are Néel walls and

$$E_{1\bar{1}0}^{(\text{Neel})} = 4\sqrt{A_{001}K_{001}} - \pi|D_{001}| < E_{1\bar{1}0}^{(\text{Bloch})} = 4\sqrt{A_{001}K_{1\bar{1}0}}.$$

All walls are oriented in $[1\bar{1}0]$ -direction. The terms $4\sqrt{AK}$ and $\pi|D|$ are of the same order of magnitude. Therefore, it is most likely that

$$E_{1\bar{1}0}^{(\text{Neel})} = 4\sqrt{A_{001}K_{001}} - \pi|D_{001}| \ll \begin{cases} E_{001}^{(\text{Neel})} = 4\sqrt{A_{1\bar{1}0}K_{1\bar{1}0}} - \pi|D_{1\bar{1}0}| \\ E_{001}^{(\text{Bloch})} = 4\sqrt{A_{1\bar{1}0}K_{001}} \end{cases}.$$

In the studied system the magnetostatic interactions decay fast. It is questionable, whether the average domain size is determined by the interplay of magnetostatic energy and domain-wall energies. Another explanation for a limited domain size in the ground state is discussed in Chapter 5.2.4: According to Eqn. (5.11) the DM interaction (that favors non-collinearity) wins against the exchange and anisotropy terms if

$$E_{1\bar{1}0}^{(\text{Neel})} = 4\sqrt{A_{001}K_{001}} - \pi|D_{001}| < 0.$$

The values obtained by the ab-initio calculations do not support this scenario (see above), but due to the large uncertainties it cannot be ruled out completely. One should be aware, that the experimentally observed domain pattern is not necessarily the ground state. It can depend on the dynamics during the domain formation (i.e. during the cooling of the sample) which metastable state evolves.

6.7.3 Micromagnetic and discrete model for the narrow ML walls

In the case of the narrow ML domain walls the application of the micromagnetic model is questionable. But it is a good starting point to calculate the ML wall width w with Eqn. (5.7). With the results from Chapters 6.4.1, 6.5 one obtains

$$w_{1\bar{1}0} = 2\sqrt{\frac{A_{001}}{-K_{1\bar{1}0}}} = 1.4 \text{ nm} \quad , \quad w_{001} = 2\sqrt{\frac{A_{1\bar{1}0}}{-K_{1\bar{1}0}}} = 2.3 \text{ nm}$$

where $w_{1\bar{1}0}$ and w_{001} denote the width of the walls that are oriented in $[1\bar{1}0]$ - and $[001]$ -direction respectively. These values are in contradiction to most experimental results, a width below the experimental resolution ($w \lesssim 0.8$ nm) is reported in [e.g. 13, 81, 83]. In some recent experiments on very clean samples, however, a width of $w_{1\bar{1}0} \approx 1.5$ nm is measured [14].

In the following it is investigated, whether the formation of very narrow walls can be understood on the basis of the ab-initio results. This investigation goes beyond the micromagnetic model, it is restricted to walls oriented in the $[1\bar{1}0]$ -direction and ideally clean samples.

The discrete model (5.2) with the exchange integrals J_1, J_2, J_3 given in (6.4), the anisotropy constants given in Table 6.1 and $\mathbf{D} = 0$ is investigated with the method presented in Appendix F.2. For the actual values of the parameters, the discrete model exhibits virtually the same domain wall profile as the continuous micromagnetic model: The simulation of the discrete model do not show any (meta)stable solution of (5.2) but the domain wall plotted in Fig. 6.10. In Fig. 6.10, this wall profile is compared with the wall profile (5.6) from the corresponding micromagnetic model. In the micromagnetic model the three exchange integrals (6.4) are approximated by a spin stiffness $A = 2.4 \left(\frac{a}{4\pi}\right)^2$ eV per surf. atom, resulting in a wall width $w = \sqrt{A/K} = 1.6$ nm (cf. Eqn. (F.1), note that in Appendix F.1 the exchange integrals J_j have the dimensions of energy and (eV per surf. atom) is an areal energy density).

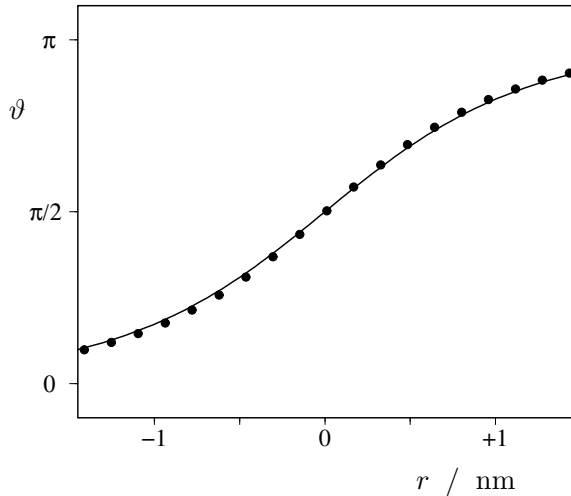


Figure 6.10: ML domain wall profile obtained from the discrete model with 3 exchange integrals. The dots (\bullet) represent the magnetization orientation at the discrete lattice points, the solid line represents the wall profile obtained with the corresponding micromagnetic model.

As the next step, the influence of the magnetostatic interaction is investigated. So far, this interaction is considered only in the anisotropy tensor $\mathbf{K}^{(\text{tot})} = \mathbf{K}^{(\text{so})} + \mathbf{K}^{(\text{dip})}$. The neglect of $\mathbf{K}^{(\text{dip})}$ introduces only a minor error in the wall width $w \sim 1/\sqrt{K}$ since $\sqrt{K_{1\bar{1}0}^{(\text{tot})}/K_{1\bar{1}0}^{(\text{so})}} = 1.02$.

$\mathbf{K}^{(\text{dip})}$ is calculated for a ferromagnetic system. But, if the magnetization rotates on small length scales the contribution of the magnetostatic energy can be much larger than in the ferromagnetic limit (for the DL this is already illustrated in Fig. 6.5.c). Therefore, the dipolar interactions are explicitly included in the discrete model with the use of Formula (4.3) (cf. Appendix F.2.3). The wall profile resulting from this extended model does not show a significant deviation from the result presented in Fig. 6.10.

The inclusion of the DM interaction in the models cannot result in a smaller wall width: In

Chapter 5.2.4 it is shown, that the neglect of the \mathbf{D} -vector in the micromagnetic model does not lead to a significantly larger wall width (there is an exception if the anisotropy difference between the easy and intermediate axis is large, this does not apply here). In the numerical investigations of the discrete model (5.17) a significant decrease of the wall width with increasing $|\mathbf{D}|$ has not been observed. For \mathbf{q} parallel to the [001]-direction the anisotropy energy between the easy and intermediate axis is very small (cf. Table 6.1). In this case Fig. 5.16 applies for Eqn. (5.17). This figure shows that a wall cannot be sharp for a certain J/K and $\mathbf{D} \neq 0$ if it is not sharp for the same J/K and $\mathbf{D} = 0$.

Of course, if the domain walls are very narrow, it might be necessary to extend Eqn. (5.17) not only by higher-order exchange-terms but also by higher-order terms that depend on the spin-orbit coupling. The identification of these terms by ab-initio calculations requires further calculations in large supercells. These calculations reach the limit of the currently available computing resources and are omitted in this thesis.

6.8 Summary

The purpose of this theoretical analysis is to show which effects are relevant for the description of the domain walls in the atomically thin Fe films on the W(110)-surface.

The formation of domain walls in these ultrathin surface-films is significantly different to those observed in bulk systems.

In Fe bulk the domain walls have a width of ≈ 40 nm [24]. The spin stiffness in the bulk and in the studied surface films is of the same order of magnitude, but the anisotropy energy in the bulk is much smaller. In cubic symmetry the leading term of the magnetocrystalline anisotropy is $K_{\text{bulk}}^{(\text{so})}(x^2 y^2 + y^2 z^2 + z^2 x^2)$, for Fe it has the value $K_{\text{bulk}}^{(\text{so})} \approx 0.004$ meV per atom [35]. But the magnetostatic interactions are very important in bulk materials: the stray fields inhibit the formation of Néel walls and the anisotropy energy depends on the mesoscopic domain structure. In the atomically thin surface films, however, the magnetocrystalline anisotropy is large and from magnetostatic interactions only the short-ranged contributions are relevant.

Furthermore, the DM interaction is an important quantity for the studied surface, but irrelevant in most bulk systems. In particular, it vanishes in systems with inversion symmetry and thus is absent in many bulk geometries.

Fe DL

The domain walls in the Fe DL can be described with the micromagnetic ansatz (5.3). They are Néel walls with an in-plane rotation axis. On this rotation path the walls can benefit most from the DM interaction. The observed walls are oriented in $[1\bar{1}0]$ -direction, their energy per length is

$$E_{1\bar{1}0}^{(\text{Néel})} = 4 \sqrt{A_{001} K_{001}} - \pi |D_{001}| .$$

It is expected that this difference is much smaller than

$$E_{001}^{(\text{Néel})} = 4 \sqrt{A_{1\bar{1}0} K_{1\bar{1}0}} - \pi |D_{1\bar{1}0}| \quad \text{and} \quad E_{001}^{(\text{Bloch})} = 4 \sqrt{A_{1\bar{1}0} K_{001}} \quad ,$$

either because $|D_{001}| > |D_{1\bar{1}0}|$ or because $K_{001} < K_{1\bar{1}0}$. This can explain that all walls are oriented in the same direction, although the single model parameters are for both directions of the same order of magnitude.

The Fe DL fits well to the micromagnetic model that is discussed in Chapter 5. The magnetization rotates on a length scale where the discrete lattice structure is not relevant and all interactions can be regarded as local. A linear term like the DM term in the energy functional is of particular importance if the \mathbf{q} -vector is small. On the other hand, a small \mathbf{q} -vector is connected with small K and thus with small spin-orbit coupling effects. In the studied system \mathbf{q} is smaller than it would be expected just from $\sqrt{A/K^{(so)}}$, since the magnetostatic anisotropy energy constant $K^{(\text{dip})}$ happens to cancel a considerable part of $K^{(so)}$.

Fe ML

The domain walls in the Fe ML are very narrow. This is mainly due to the large magnetocrystalline anisotropy, with the ab-initio calculations it is estimated as $K^{(so)} \approx 2.4 \text{ meV}$ per surface atom. The theoretical results suggest a domain wall width $w_{1\bar{1}0} \approx 1.4 \text{ nm}$. On this length scale the micromagnetic model that is discussed in Chapter 5 is sufficient to describe the magnetic structure. The experiments, that report significantly narrower walls, cannot be understood with the models that are discussed in this thesis.

The effect of the DM interaction is not investigated with ab-initio calculations, but with the ansatz made in Chapter 5.2.1 the inclusion of the \mathbf{D} -vector cannot explain the sharp domain walls.

The magnetostatic interactions have only negligible influence on the magnetic structure in the Fe ML.

Chapter 7

Summary

In this thesis the shape and size of magnetic domain walls in surface films is investigated. The main focus is on the Dzyaloshinsky-Moriya (DM) interaction, since the influence of this interaction on domain-wall structures is sparsely discussed in literature.

The best known magnetic domain walls are the ones, that form the boundary between two ferromagnetic domains with opposite magnetization direction. Domain walls can be described by a competition between spin stiffness and anisotropy energy. If the magnetization rotates on long length scales, then a micromagnetic model can be applied. In the simplest case, the solution of this model is very elementary and known for 70 years. In certain crystal symmetries, however, the energy functional can be extended by the DM term that is linear in q (i.e. that favors a certain rotational direction). The inclusion of this term in the micromagnetic model significantly increases the complexity of the domain walls: The magnetization can rotate on a 3-dimensional path in spin-space, the different rotation paths can be classified by several distinct phases. This thesis presents a systematic overview of the resulting domain wall profiles and phase diagrams.

The effect of the discrete lattice structure is discussed within a Heisenberg-like model. The DM interaction is included in this model and the solutions are analysed for some exemplary cases.

The DM interaction vanishes if the crystal possesses inversion symmetry and, thus, is absent in most bulk materials. Of course, the inversion symmetry is broken on every surface. The DM interaction is expected to be particularly relevant for atomically thin magnetic films on non-magnetic substrates: Usually, these systems are not governed by stray fields. Furthermore, in ultrathin films the reduced symmetry (surface) is relevant in the local environment and for the short range interactions of all magnetic atoms. Thus, the DM interaction can play a considerable role in a class of materials whose importance has increased over the last decade. Atomically thin films and other magnetic nanostructures attract some attention since it is possible to resolve their magnetic properties with advanced experimental techniques (like spin-polarized STM). The variety of magnetic properties makes these systems interesting from a purely scientific point of view as well as for future spintronic devices.

The simple models are a very useful to understand the main mechanisms and to gain an overview of the possible scenarios. But, the actual results depend on the values of the model parameters, i.e. on A , \mathbf{D} , \mathbf{K} . In order to estimate the effects on real systems it is important to know the size of these parameters. In this thesis the model parameters are determined with electronic structure calculations. The calculation of the spin stiffness A and magnetocrystalline anisotropy $\mathbf{K}^{(\text{so})}$ in the framework of the FLAPW method has been established over the last years. The \mathbf{D} -vector can be obtained from the magnetocrystalline anisotropy of homogeneous spin spirals. It requires some extensions of the usual ab-initio

methods to calculate these spin spirals, since they consist of very many non-equivalent atoms. In this thesis a perturbative approach is developed, that allows to estimate the magnetocrystalline anisotropy of spin spirals with long periods and thus allows to estimate the size of the \mathbf{D} -vector with parameter-free calculations.

The theoretical model and the computational method are applied on the system Fe/W(110), i.e. one or two mono-layer Fe coverage on the W(110)-surface. The range of the model parameters depends significantly on the Fe coverage. Furthermore, the easy axis depends on the coverage. Thus, the rotation paths differ qualitatively from the mono- to the double-layer Fe.

The double-layer Fe shows a large (A/K) -ratio. This implies broad domain walls that are well suited for the description with a micromagnetic model (remember that this model is justified for the limit of small q). It is shown, that the magnetic structure can be explained by an interplay of spin stiffness, magnetocrystalline and magnetostatic anisotropy and DM interaction. The magnetostatic interactions can be treated as a local anisotropy. The DM interaction is strong enough to determine the rotational direction and, strikingly, the orientation of the domain walls. The description of the magnetic domain boundaries in the mono-layer Fe is more problematic. Due to the large anisotropy energy they are much sharper than in the double-layer, but the precise magnetic structure is revealed neither experimentally nor theoretically. The magnetization changes on a length scale, where the discrete crystal structure might be relevant. Thus, one has to find a description beyond the micromagnetic model. But, far from the small- q -limit and under consideration of the discrete lattice structure there are many effects of possible importance. The ab-initio calculations indicate that the exchange interaction can be approximated by a Heisenberg model with three parameters. But further and more-accurate parameter-free calculations are limited by the size of the supercells.

In summary, this thesis gives an overview of the magnetic structure of domain walls under consideration of the Dzyaloshinsky-Moriya interaction. Simple models are presented as well as computational methods for parameter-free calculations, thus a link is made between the fields of micromagnetism and electronic-structure calculations. The relevant effects are identified for the exemplary system Fe/W(110).

Appendix A

Applying GGA to non-collinear magnetism

A.1 Construction of V_{xc}

Most of the LDA functions $f_{\text{xc}}(n, |\mathbf{m}|)$ are constructed for general non-collinear configurations [e.g. 98], but so far all GGA functions $f_{\text{xc}}(n, |m|, |\nabla n|, |\nabla m|)$ have been constructed only for collinear configurations. Nevertheless one can try to approximate the exchange-correlation energy of a non-collinear configuration by $\int d^3\mathbf{r} f_{\text{xc}}$ using the function $f_{\text{xc}}(n, |m|, |\nabla n|, |\nabla m|)$ that is known for the collinear configurations. In this case the gradient of the scalar magnetization m is not well-defined. When choosing a local z -axis parallel to the magnetization direction a straightforward generalization of f_{xc} is to interpret m and ∇m as m_z and ∇m_z (note that a pure rotation of the magnetization does not give any additional energy contribution if $\nabla m_x, \nabla m_y$ are neglected). This procedure is equivalent to the replacement of m and ∇m with $|\mathbf{m}|$ and $\nabla|\mathbf{m}|$ in global coordinates.

Most of the advantages of GGA over LDA are already produced by functions of the form $f_{\text{xc}}(n, |m|, |\nabla n|)$, not depending on the gradient of the magnetization [e.g. 79]. The generalization of this functions to non-collinear configurations is clear. Nevertheless non-collinearity is not regarded in the construction of this functions and it is as doubtful whether they describe the non-collinear configurations well as it is for the previously mentioned GGA functions that depend on $|\nabla m|$.

More sophisticated (but not necessarily more successful) ways of generalizing the standard GGA functionals to non-collinear magnetism are investigated in [20, 21, 49].

It is possible to construct an *density-dependent* exchange-correlation *potential* V_{xc} from the energy functional $E_{\text{xc}} = \int d^3\mathbf{r} f_{\text{xc}}(n, |\mathbf{m}|, |\nabla n|, |\nabla|\mathbf{m}||)$. Furthermore, the potential can be written in the form $V_{\text{xc}} = V_{\text{xc}}\mathbb{1} + B_{\text{xc}} \boldsymbol{\sigma} \cdot \frac{\mathbf{m}}{|\mathbf{m}|}$ where V_{xc} and $B_{\text{xc}} = |\mathbf{B}_{\text{xc}}|$ have the same functional dependence on the densities $n, |\mathbf{m}|$ and their derivatives as they have on n and m in the collinear case. The last point is of big practical advantage, since the variation of the energy functional does not have to be recalculated and reprogrammed when extending the computer code in order to deal with non-collinear magnetism.

To prove the last statements one has to show that the variation of E_{xc} with respect to $\uparrow_{\nu}^*, \downarrow_{\nu}^*$ can be written in the form

$$\begin{aligned}\frac{\delta F_{\text{xc}}}{\delta \uparrow_{\nu}^*} &= \frac{\partial f_{\text{xc}}(\Phi)}{\partial \uparrow_{\nu}^*} - \sum_{s \in \{x,y,z\}} \frac{d}{dr_s} \frac{\partial f_{\text{xc}}(\Phi)}{\partial \left(\frac{d \uparrow_{\nu}^*}{dr_s}\right)} \\ &= V_{\text{xc}}(\mathcal{N}) \uparrow_{\nu}(\mathbf{r}) + B_{\text{xc}}(\mathcal{N}) \left(\frac{m_z(\mathbf{r})}{|\mathbf{m}(\mathbf{r})|} \uparrow_{\nu}(\mathbf{r}) + \frac{m_x(\mathbf{r}) - i m_y(\mathbf{r})}{|\mathbf{m}(\mathbf{r})|} \downarrow_{\nu}(\mathbf{r}) \right),\end{aligned}$$

$$\begin{aligned}\frac{\delta F_{\text{xc}}}{\delta \downarrow_{\nu}^*} &= \frac{\partial f_{\text{xc}}(\Phi)}{\partial \downarrow_{\nu}^*} - \sum_{s \in \{x,y,z\}} \frac{d}{dr_s} \frac{\partial f_{\text{xc}}(\Phi)}{\partial \left(\frac{d \downarrow_{\nu}^*}{dr_s}\right)} \\ &= V_{\text{xc}}(\mathcal{N}) \downarrow_{\nu}(\mathbf{r}) + B_{\text{xc}}(\mathcal{N}) \left(\frac{-m_z(\mathbf{r})}{|\mathbf{m}(\mathbf{r})|} \downarrow_{\nu}(\mathbf{r}) + \frac{m_x(\mathbf{r}) + i m_y(\mathbf{r})}{|\mathbf{m}(\mathbf{r})|} \uparrow_{\nu}(\mathbf{r}) \right)\end{aligned}$$

with

$$\begin{aligned}\Phi &= \left\{ \uparrow_{\nu'}^*(\mathbf{r}), \downarrow_{\nu'}^*(\mathbf{r}), \uparrow_{\nu'}(\mathbf{r}), \downarrow_{\nu'}(\mathbf{r}), \frac{d}{dr_s} \uparrow_{\nu'}^*(\mathbf{r}), \frac{d}{dr_s} \downarrow_{\nu'}^*(\mathbf{r}), \frac{d}{dr_s} \uparrow_{\nu'}(\mathbf{r}), \frac{d}{dr_s} \downarrow_{\nu'}(\mathbf{r}) \right\}_{\substack{s \in \{x,y,z\}, \\ \nu' \in [1,N]}}, \\ \mathcal{N} &= \left\{ n(\mathbf{r}), |\mathbf{m}(\mathbf{r})|, \frac{d}{dr_s} n(\mathbf{r}), \frac{d}{dr_s} |\mathbf{m}(\mathbf{r})|, \frac{d^2}{dr_s dr_{s'}} n(\mathbf{r}), \frac{d^2}{dr_s dr_{s'}} |\mathbf{m}(\mathbf{r})| \right\}_{s,s' \in \{x,y,z\}}.\end{aligned}$$

These formulas reduce to the ones used in the collinear case with the quantization axis in z -direction and $m \geq 0$. (Negative magnetization does not impose a problem since E_{xc} is isotropic.)

In the following the last formulas are verified by evaluating the variations explicitly. The real-space derivatives will be indicated by upper indices, e.g. $\frac{d}{dr_s} n = n^{(s)} = \sum_{\nu'} \left(\uparrow_{\nu'}^{*(s)} \uparrow_{\nu'} + \uparrow_{\nu'}^* \uparrow_{\nu'}^{(s)} + \downarrow_{\nu'}^{*(s)} \downarrow_{\nu'} + \downarrow_{\nu'}^* \downarrow_{\nu'}^{(s)} \right)$.

$$\begin{aligned}\frac{\delta F_{\text{xc}}}{\delta \uparrow_{\nu}^*} &= \frac{\partial f_{\text{xc}}}{\partial n} \frac{\partial n}{\partial \uparrow_{\nu}^*} + \sum_s \left(\frac{\partial f_{\text{xc}}}{\partial n^{(s)}} \frac{\partial n^{(s)}}{\partial \uparrow_{\nu}^*} - \frac{d}{dr_s} \left(\frac{\partial f_{\text{xc}}}{\partial n^{(s)}} \frac{\partial n^{(s)}}{\partial \uparrow_{\nu}^{*(s)}} \right) \right) \\ &+ \frac{\partial f_{\text{xc}}}{\partial |\mathbf{m}|} \frac{\partial |\mathbf{m}|}{\partial \uparrow_{\nu}^*} + \sum_s \left(\frac{\partial f_{\text{xc}}}{\partial |\mathbf{m}|^{(s)}} \frac{\partial |\mathbf{m}|^{(s)}}{\partial \uparrow_{\nu}^*} - \frac{d}{dr_s} \left(\frac{\partial f_{\text{xc}}}{\partial |\mathbf{m}|^{(s)}} \frac{\partial |\mathbf{m}|^{(s)}}{\partial \uparrow_{\nu}^{*(s)}} \right) \right) \\ &= \left(\underbrace{\frac{\partial f_{\text{xc}}}{\partial n} - \sum_s \left(\frac{d}{dr_s} \frac{\partial f_{\text{xc}}}{\partial n^{(s)}} \right)}_{= V_{\text{xc}}(\mathcal{N})} \right) \uparrow_{\nu} + \underbrace{\frac{\partial f_{\text{xc}}}{\partial |\mathbf{m}|} \frac{\partial |\mathbf{m}|}{\partial \uparrow_{\nu}^*}}_{= B'_{\text{xc}}(\mathcal{N})} \\ &+ \sum_s \frac{\partial f_{\text{xc}}}{\partial |\mathbf{m}|^{(s)}} \left(\underbrace{\frac{\partial |\mathbf{m}|^{(s)}}{\partial \uparrow_{\nu}^*} - \frac{d}{dr_s} \frac{\partial |\mathbf{m}|^{(s)}}{\partial \uparrow_{\nu}^{*(s)}}}_{= C} \right) - \sum_s \left(\underbrace{\frac{d}{dr_s} \frac{\partial f_{\text{xc}}}{\partial |\mathbf{m}|^{(s)}}}_{= B''_{\text{xc},s}(\mathcal{N})} \right) \frac{\partial |\mathbf{m}|^{(s)}}{\partial \uparrow_{\nu}^{*(s)}}.\end{aligned}$$

The forms V_{xc} , B'_{xc} , $B''_{\text{xc},s}$ as a functions of \mathcal{N} do not depend on the particular choice of the function $m(\{\uparrow_{\nu'}(\mathbf{r}), \downarrow_{\nu'}(\mathbf{r})\}_{\nu'})$.

It is $C = 0$, that can be seen by evaluating the derivatives and by noting that

$$m_{s'} = \sum_{\nu'} \begin{pmatrix} \uparrow_{\nu'} \\ \downarrow_{\nu'} \end{pmatrix}^{\dagger} \sigma_{s'} \begin{pmatrix} \uparrow_{\nu'} \\ \downarrow_{\nu'} \end{pmatrix} \Rightarrow \left(\frac{\partial m_{s'}(\Phi)}{\partial \uparrow_{\nu}^*} = \frac{\partial m_{s'}^{(s)}(\Phi)}{\partial \uparrow_{\nu}^{*(s)}}; \frac{\partial m_{s'}^{(s)}(\Phi)}{\partial \uparrow_{\nu}^*} = \frac{d}{dr_s} \frac{\partial m_{s'}^{(s)}(\Phi)}{\partial \uparrow_{\nu}^{*(s)}} \right)$$

and

$$\begin{aligned}\frac{\partial |\mathbf{m}|^{(s)}}{\partial \uparrow_{\nu}^*} &= \frac{\partial}{\partial \uparrow_{\nu}^*} \sum_{s'} \frac{m_{s'} m_{s'}^{(s)}}{|\mathbf{m}|} = \\ &\sum_{s'} \frac{1}{|\mathbf{m}|^2} \left(|\mathbf{m}| m_{s'}^{(s)} \frac{\partial m_{s'}}{\partial \uparrow_{\nu}^*} + |\mathbf{m}| m_{s'} \frac{\partial m_{s'}^{(s)}}{\partial \uparrow_{\nu}^*} - m_{s'} m_{s'}^{(s)} \sum_{s''} \frac{m_{s''}}{|\mathbf{m}|} \frac{\partial m_{s''}}{\partial \uparrow_{\nu}^*} \right) =\end{aligned}$$

$$\begin{aligned}
& \sum_{s'} \frac{1}{|\mathbf{m}|^2} |\mathbf{m}| m_{s'}^{(s)} \frac{\partial m_{s'}}{\partial \uparrow_\nu^*} - \sum_{s', s''} \frac{1}{|\mathbf{m}|^2} m_{s'} m_{s'}^{(s)} \frac{m_{s''}}{|\mathbf{m}|} \frac{\partial m_{s''}}{\partial \uparrow_\nu^*} + \sum_{s'} \frac{m_{s'}}{|\mathbf{m}|} \frac{\partial m_{s'}^{(s)}}{\partial \uparrow_\nu^*} = \\
& \sum_{s'} \frac{1}{|\mathbf{m}|^2} \left(|\mathbf{m}| m_{s'}^{(s)} - m_{s'} \sum_{s''} \frac{m_{s''} m_{s''}^{(s)}}{|\mathbf{m}|} \right) \frac{\partial m_{s'}^{(s)}}{\partial \uparrow_\nu^*} + \sum_{s'} \frac{m_{s'}}{|\mathbf{m}|} \left(\frac{d}{d r_s} \frac{\partial m_{s'}^{(s)}}{\partial \uparrow_\nu^*} \right) = \\
& \frac{d}{d r_s} \sum_{s'} \frac{m_{s'}}{|\mathbf{m}|} \frac{\partial m_{s'}^{(s)}}{\partial \uparrow_\nu^*} = \frac{d}{d r_s} \frac{\partial |\mathbf{m}|^{(s)}}{\partial \uparrow_\nu^*}.
\end{aligned}$$

The remaining terms reduce to

$$\begin{aligned}
\frac{\partial |\mathbf{m}|}{\partial \uparrow_\nu^*} &= \frac{1}{|\mathbf{m}|} \left(m_z \frac{\partial m_z(\Phi)}{\partial \uparrow_\nu^*} + m_x \frac{\partial m_x(\Phi)}{\partial \uparrow_\nu^*} + m_y \frac{\partial m_y(\Phi)}{\partial \uparrow_\nu^*} \right) \\
&= \frac{1}{|\mathbf{m}|} (m_z \uparrow_\nu + (m_x - i m_y) \downarrow_\nu) , \\
\frac{\partial |\mathbf{m}|^{(s)}}{\partial \uparrow_\nu^{*(s)}} &= \frac{1}{|\mathbf{m}|} \left(m_z \frac{\partial m_z^{(s)}(\Phi)}{\partial \uparrow_\nu^{*(s)}} + m_x \frac{\partial m_x^{(s)}(\Phi)}{\partial \uparrow_\nu^{*(s)}} + m_y \frac{\partial m_y^{(s)}(\Phi)}{\partial \uparrow_\nu^{*(s)}} \right) \\
&= \frac{1}{|\mathbf{m}|} (m_z \uparrow_\nu + (m_x - i m_y) \downarrow_\nu) .
\end{aligned}$$

The variations with respect to \uparrow_ν^* can be calculated in the same way and the exchange-correlation potential can be written in the desired form

$$V_{\text{xc}}(\mathcal{N}) = V_{\text{xc}}(\mathcal{N}) \mathbb{1} + \left(B'_{\text{xc}}(\mathcal{N}) - \sum_s B''_{\text{xc},s}(\mathcal{N}) \right) \boldsymbol{\sigma} \cdot \frac{\mathbf{m}}{|\mathbf{m}|} .$$

A.2 Technical aspects

This chapter discusses numerical instabilities that are strongly connected with the actual implementation, the following discussion is surely not relevant for every DFT-based computer code.

In the code that is used in this thesis, the interstitial densities n and \mathbf{m} are calculated and stored on a discrete mesh in reciprocal space (i.e. by their Fourier coefficients), but the function $V_{\text{xc}}(\mathcal{N})$ is parameterized in real space (where it is local). In the collinear case the method of choice is to calculate the real-space derivatives $\frac{d}{d r_s} n$, $\frac{d}{d r_s} m$, $\frac{d^2}{d r_s d r_{s'}} n$, $\frac{d^2}{d r_s d r_{s'}} m$ in reciprocal space analytically before transforming them to real space via FFT.

In the non-collinear case the derivatives of $|\mathbf{m}(\mathbf{r})| = \sqrt{m_x(\mathbf{r})^2 + m_y(\mathbf{r})^2 + m_z(\mathbf{r})^2}$ have to be calculated. It would be a major task to calculate the absolute value in reciprocal space, therefore each component of \mathbf{m} is transformed to real space before $|\mathbf{m}|$ is calculated. A straightforward and practicable way to obtain $\frac{d}{d r_s} |\mathbf{m}|$, $\frac{d^2}{d r_s d r_{s'}} |\mathbf{m}|$ is to calculate the derivatives in real space numerically. But it should be noted that it is not recommended to transform $|\mathbf{m}|$ back to reciprocal space via FFT in order to calculate the required derivatives analytically from the Fourier coefficients.

In reciprocal space the eigenfunctions ψ_ν of the discrete Hamiltonian matrix (that is used in actual calculations) are described on the mesh points within the k_{max} -sphere (i.e. $\psi_\nu(\mathbf{r}) = \sum_{\mathbf{k}}^{|\mathbf{k}| < k_{\text{max}}} \begin{pmatrix} c_{\uparrow, \mathbf{k}} \\ c_{\downarrow, \mathbf{k}} \end{pmatrix} e^{2\pi i \mathbf{k} \cdot \mathbf{r}}$, cf. Chapter 3.4), each component of the magnetization $\mathbf{m} = \sum_\nu \psi_\nu^\dagger \boldsymbol{\sigma} \psi_\nu$ is described within the $(2k_{\text{max}})$ -sphere and m_z^2 is described within the $(4k_{\text{max}})$ -sphere. But the Fourier expansion of the square-root shows a considerably slow (asymptotic) decay (Fig. A.1). $|\mathbf{m}(\mathbf{r})|$ is described well when this series gets truncated

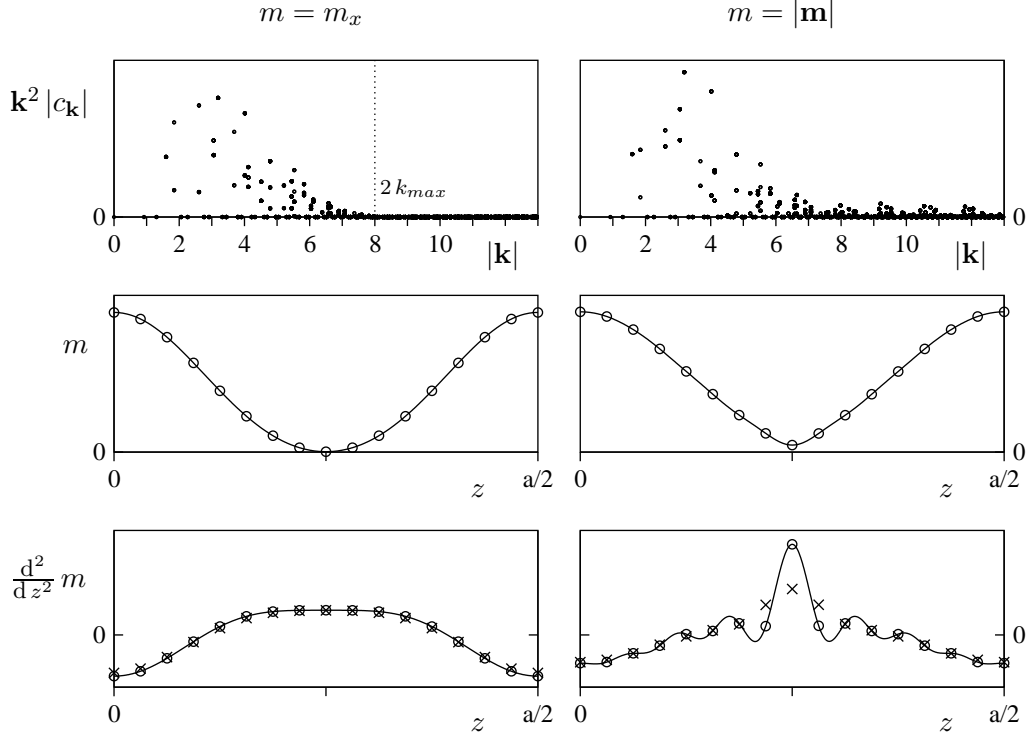


Figure A.1: Test calculations of γ -Fe show the numerical problems concerning the evaluation of $\frac{d^2}{dz^2} |\mathbf{m}|$. The first row shows the decay of the Fourier coefficients of $m = \sum_{\mathbf{k}} c_{\mathbf{k}} \exp(2\pi i \mathbf{k} \mathbf{r})$, the weighting factor \mathbf{k}^2 is introduced to take into account the size of each $|\mathbf{k}|$ -shell. The Fourier expansion of m_x decays completely at $8 (\text{a.u.})^{-1} = 2 k_{\max}$. The second row shows m along the z -direction (i.e. along the line $[\frac{1}{4}, 0, 0]$, $[\frac{1}{4}, 0, \frac{1}{2}]$). The solid line (—) represents the evaluation of the Fourier sum, the values that are on the discrete real-space mesh used by the code are marked with (o). The third row compares the 2nd order derivative of the Fourier sum (\ominus) and the 2nd order derivative obtained numerically on the discrete real-space mesh (\times) (note that the largest mismatch between (o) and (\times) is outside the muffin tins).

at the usual cutoff (typically between $2 k_{\max}$ and $4 k_{\max}$), but for the real-space derivatives $\frac{d}{dr_s} |\mathbf{m}(\mathbf{r})|$ and $\frac{d^2}{dr_s dr_{s'}} |\mathbf{m}(\mathbf{r})|$ the Fourier coefficients are multiplied with $2\pi i k_s$ and $-4\pi^2 k_s k_{s'}$, thus giving more weight to the coefficients with higher $|\mathbf{k}|$.

One should note that the (slowly varying) derivatives of $|\mathbf{m}|$ can be approximated well by a Fourier expansion truncated at $2 k_{\max}$, the problem is to evaluate these expansion from the Fourier sum of $|\mathbf{m}|$:

If a smooth and periodic function $m(r)$ is evaluated on a discrete mesh $\{r_j\}_j$ and FFT is applied to the set $\{m(r_j)\}_j$ in order to calculate the Fourier coefficients $\{c_{\mathbf{k}}\}_{\mathbf{k}}$, then the resulting function $\tilde{m}(r) = \sum_{\mathbf{k}} c_{\mathbf{k}} \exp(2\pi i \mathbf{k} \mathbf{r})$ is usually *not* the best approximation of $m(r)$ in the sense that the calculated set $\{c_{\mathbf{k}}\}_{\mathbf{k}}$ minimizes $\|m - \tilde{m}\|$ according to some reasonable norm (like e.g. $\int dr (m(r) - \tilde{m}(r))^2$), instead the function \tilde{m} coincides with m exactly on the mesh points $\{r_j\}_j$ while it might deviate between the mesh points. Usually the Fourier-transformed function still is a reasonable approximation to the original one (there is e.g. no problem when transforming V_{xc} back to reciprocal space), but it shows small oscillations and the derivatives $\frac{d}{dr_s} \tilde{m}(\mathbf{r})$ and especially $\frac{d^2}{dr_s dr_{s'}} \tilde{m}(\mathbf{r})$ at the points $\{r_j\}_j$ do not coincide well with the derivatives of the smoother function $m(r)$.

Since these numerically induced oscillations are very sensitive to small changes in $\{m(r_j)\}_j$ the above described procedure in many cases leads to a very bad convergence of the self-consistency cycle.

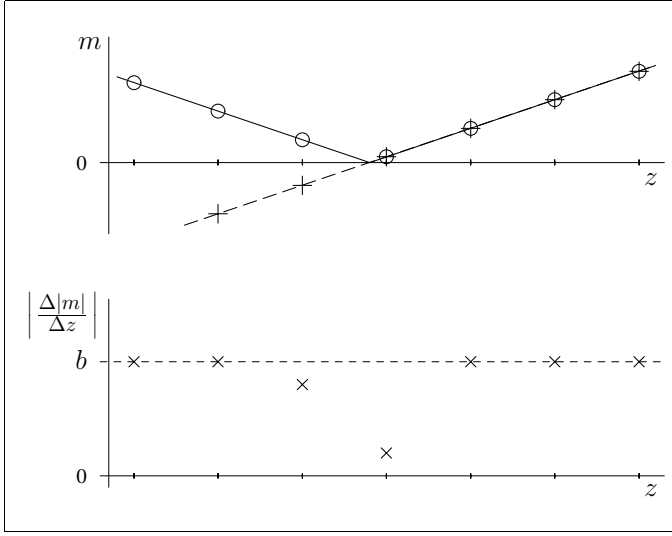


Figure A.2: m can locally be described as $\mathbf{m}(x, y, z) = \mathbf{e}_z b z$. At each grid point z_j the magnetization $m_j = b z_j$ (+) and $|m_j|$ (o) are evaluated. $\left| \frac{d|m|}{dz} \right| = b$ is constant in the shown interval, but its numerical approximation $\left| \frac{|m_{j+1}| - |m_{j-1}|}{z_{j+1} - z_{j-1}} \right|$ (x) decreases where m changes sign.

Unfortunately other inaccuracies can occur, when the derivatives of $|\mathbf{m}(\mathbf{r})|$ are evaluated numerically in real space. The standard numerical differentiation techniques are disturbed by discontinuities in $\frac{d}{dz} |\mathbf{m}|$ although $\left| \frac{d}{dz} |\mathbf{m}| \right|$ (what actually needs to be calculated) might be smooth. The problem is further illustrated in Fig. A.2. In most real situations the error is rather small, in practical use I did not encounter a situation where it is relevant.

In order to avoid these inaccuracies it is possible, first to calculate the derivatives of each component m_x, m_y, m_z analytically in reciprocal space, then to apply FFT and to calculate the derivatives (in the notation of the previous Chapter A.1) as:

$$|\mathbf{m}|^{(s)} = \frac{\sum_{s'} m_{s'} m_{s'}^{(s)}}{|\mathbf{m}|},$$

$$|\mathbf{m}|^{(s_1, s_2)} = \frac{\sum_{s'} (m_{s'}^{(s_1)} m_{s'}^{(s_2)} + m_{s'} m_{s'}^{(s_1, s_2)})}{|\mathbf{m}|} - \frac{\left(\sum_{s'} m_{s'} m_{s'}^{(s_1)} \right) \left(\sum_{s'} m_{s'} m_{s'}^{(s_2)} \right)}{|\mathbf{m}|^3}.$$

This procedure requires special care at in the implementation to avoid errors at mesh points \mathbf{r}_j with $|\mathbf{m}(\mathbf{r}_j)| \approx 0$.

Appendix B

SOC matrix elements described with the LAPW basis

This appendix shows an explicit expression for the matrix elements of the spin-orbit coupling operator \mathcal{H}_{so} with spin-spiral states (i.e. for the elements of the matrix H_{so} as shown in Fig. 3.4) in the framework of LAPW basis functions.

The spin-orbit coupling operator \mathcal{H}_{so} is approximated according to Eqn. (2.16):

$$\mathcal{H}_{\text{so}} = \sum_{\mu} \Theta^{(\mu)}(\mathbf{r}) v^{(\mu)}(|\mathbf{r} - \mathbf{R}^{(\mu)}|) \boldsymbol{\sigma} \cdot \hat{\mathbf{L}}^{(\mu)} \quad \text{with} \quad \Theta^{(\mu)}(\mathbf{r}) = \begin{cases} 1 & \text{if } |\mathbf{r} - \mathbf{R}^{(\mu)}| < R_{\text{MT}}^{(\mu)} \\ 0 & \text{else} \end{cases}$$

($\mathbf{R}^{(\mu)}$ denotes the center of the μ th muffin-tin sphere, $R_{\text{MT}}^{(\mu)}$ the muffin-tin radius).

The calculation of the \mathcal{H}_{so} matrix elements is described within the LAPW basis functions. The equations are written for one muffin-tin sphere, the summation over all atoms as well as the atom index μ is dropped in the following. \mathbf{r} is described in polar coordinates with respect to the muffin-tin center: $\mathbf{r} - \mathbf{R}^{(\mu)} = r (\sin \vartheta \cos \varphi \mathbf{e}_x + \sin \vartheta \sin \varphi \mathbf{e}_y + \cos \vartheta \mathbf{e}_z)$ with $r = |\mathbf{r} - \mathbf{R}^{(\mu)}|$. Thus, the spin-orbit coupling operator can be written as

$$\mathcal{H}_{\text{so}} = v(r) \boldsymbol{\sigma} \cdot \hat{\mathbf{L}} = v(r) \begin{pmatrix} +\hat{L}_z & \hat{L}_- \\ \hat{L}_+ & -\hat{L}_z \end{pmatrix}.$$

The LAPW basis functions are described in Eqns. (3.5), (3.7). They are labeled with the \mathbf{k} -vector, the reciprocal lattice vector \mathbf{G} and the spin index $\tilde{\sigma}$. The LAPW basis functions in the muffin-tin sphere are written as

$$\phi_{\mathbf{k},\mathbf{G}}^{(\tilde{\sigma})}(\mathbf{r}) = \sum_{\ell,m} Y_{\ell,m}(\vartheta, \varphi) \left(A_{\mathbf{k},\mathbf{G},\ell,m}^{(\tilde{\sigma})} u_{\ell}^{(\tilde{\sigma})}(r) + B_{\mathbf{k},\mathbf{G},\ell,m}^{(\tilde{\sigma})} \dot{u}_{\ell}^{(\tilde{\sigma})}(r) \right)$$

and the expansion of the wave function $\tilde{\psi}_j$ (with $j = (\mathbf{k}_j, \nu_j)$) has the form

$$\tilde{\psi}_j(\mathbf{r}) = \sum_{\mathbf{G}} \begin{pmatrix} c_{j,\mathbf{G}}^{(\tilde{\sigma})} \phi_{\mathbf{k}_j,\mathbf{G}}^{(\tilde{\sigma})}(\mathbf{r}) \\ c_{j,\mathbf{G}}^{(\tilde{\sigma})} \phi_{\mathbf{k}_j,\mathbf{G}}^{(\tilde{\sigma})}(\mathbf{r}) \end{pmatrix} = \sum_{\ell,m} Y_{\ell,m}(\vartheta, \varphi) \begin{pmatrix} a_{j,\ell,m}^{(\tilde{\sigma})} u_{\ell}^{(\tilde{\sigma})}(r) + b_{j,\ell,m}^{(\tilde{\sigma})} \dot{u}_{\ell}^{(\tilde{\sigma})}(r) \\ a_{j,\ell,m}^{(\tilde{\sigma})} u_{\ell}^{(\tilde{\sigma})}(r) + b_{j,\ell,m}^{(\tilde{\sigma})} \dot{u}_{\ell}^{(\tilde{\sigma})}(r) \end{pmatrix}$$

$$\text{with} \quad a_{j,\ell,m}^{(\tilde{\sigma})} = \sum_{\mathbf{G}} c_{j,\mathbf{G}}^{(\tilde{\sigma})} A_{\mathbf{k},\mathbf{G},\ell,m}^{(\tilde{\sigma})} \quad , \quad b_{j,\ell,m}^{(\tilde{\sigma})} = \sum_{\mathbf{G}} c_{j,\mathbf{G}}^{(\tilde{\sigma})} B_{\mathbf{k},\mathbf{G},\ell,m}^{(\tilde{\sigma})} .$$

In the last equation the spinor is given with respect to the local spin coordinate frame of the specific muffin tin (cf. Chapter 3.7.1). In this appendix the spin indices of the local spin coordinate frame are marked with tildes ($\tilde{}$) in order to distinguish them from indices of the global spin coordinate frame that is the same for all muffin tins. In the case of spin spirals the global spin coordinate frame is chosen such that the spiral rotation axis coincides with the z -axis, this simplifies the expressions for the wave functions and the \mathcal{H}_{so} matrix elements (cf. Chapter 3.9.2).

In order to identify the up- and down-components of $\tilde{\psi}_j$ in the global frame the spinor is rotated by the spin rotation matrix U_{MT} that transforms from the local to the global frame:

$$\begin{aligned} \psi_j(\mathbf{r}) &= U_{\text{MT}} \tilde{\psi}_j(\mathbf{r}) = \begin{pmatrix} U_{\text{MT}}^{(\uparrow, \tilde{\uparrow})} & U_{\text{MT}}^{(\uparrow, \tilde{\downarrow})} \\ U_{\text{MT}}^{(\downarrow, \tilde{\uparrow})} & U_{\text{MT}}^{(\downarrow, \tilde{\downarrow})} \end{pmatrix} \sum_{\ell, m} Y_{\ell, m}(\vartheta, \varphi) \begin{pmatrix} a_{j, \ell, m}^{(\tilde{\uparrow})} u_{\ell}^{(\tilde{\uparrow})}(r) + b_{j, \ell, m}^{(\tilde{\uparrow})} \dot{u}_{\ell}^{(\tilde{\uparrow})}(r) \\ a_{j, \ell, m}^{(\tilde{\downarrow})} u_{\ell}^{(\tilde{\downarrow})}(r) + b_{j, \ell, m}^{(\tilde{\downarrow})} \dot{u}_{\ell}^{(\tilde{\downarrow})}(r) \end{pmatrix} \\ &= \sum_{\ell, m} Y_{\ell, m}(\vartheta, \varphi) \begin{pmatrix} a_{j, \ell, m}^{(\uparrow, \tilde{\uparrow})} u_{\ell}^{(\tilde{\uparrow})}(r) + a_{j, \ell, m}^{(\uparrow, \tilde{\downarrow})} u_{\ell}^{(\tilde{\downarrow})}(r) + b_{j, \ell, m}^{(\uparrow, \tilde{\uparrow})} \dot{u}_{\ell}^{(\tilde{\uparrow})}(r) + b_{j, \ell, m}^{(\uparrow, \tilde{\downarrow})} \dot{u}_{\ell}^{(\tilde{\downarrow})}(r) \\ a_{j, \ell, m}^{(\downarrow, \tilde{\uparrow})} u_{\ell}^{(\tilde{\uparrow})}(r) + a_{j, \ell, m}^{(\downarrow, \tilde{\downarrow})} u_{\ell}^{(\tilde{\downarrow})}(r) + b_{j, \ell, m}^{(\downarrow, \tilde{\uparrow})} \dot{u}_{\ell}^{(\tilde{\uparrow})}(r) + b_{j, \ell, m}^{(\downarrow, \tilde{\downarrow})} \dot{u}_{\ell}^{(\tilde{\downarrow})}(r) \end{pmatrix} \end{aligned}$$

$$\text{with } a_{j, \ell, m}^{(\sigma', \tilde{\sigma})} = U_{\text{MT}}^{(\sigma', \tilde{\sigma})} a_{j, \ell, m}^{(\tilde{\sigma})} \quad , \quad b_{j, \ell, m}^{(\sigma', \tilde{\sigma})} = U_{\text{MT}}^{(\sigma', \tilde{\sigma})} b_{j, \ell, m}^{(\tilde{\sigma})} \quad .$$

In the computer code that is used for this thesis the real-space z -axis is fixed normal to the film plane. Therefore, further rotations are necessary in order to rotate the global spin coordinate frame (with the spiral rotation axis in z -direction) with respect to the real-space coordinate frame. The corresponding spin rotation matrix is denoted with $U_{\text{r-s}}$, the \mathcal{H}_{so} matrix elements have the form

$$\langle \psi_{j'} | U_{\text{r-s}}^\dagger \mathcal{H}_{\text{so}} U_{\text{r-s}} | \psi_j \rangle = \int_{\text{muffin tin}} d^3\mathbf{r} \psi_{j'}(\mathbf{r})^\dagger U_{\text{r-s}}^\dagger \mathcal{H}_{\text{so}} U_{\text{r-s}} \psi_j(\mathbf{r}) \quad .$$

The angular-momentum operator $\hat{\mathbf{L}}$ commutes with the r -dependent (spherically symmetric) functions. Therefore, the real-space integration of the matrix elements can be split in angular and radial integrations:

With the abbreviation

$$U_{\text{r-s}}^\dagger (\boldsymbol{\sigma} \cdot \hat{\mathbf{L}}) U_{\text{r-s}} = \begin{pmatrix} \hat{L}^{(\uparrow, \uparrow)} & \hat{L}^{(\uparrow, \downarrow)} \\ \hat{L}^{(\downarrow, \uparrow)} & \hat{L}^{(\downarrow, \downarrow)} \end{pmatrix}$$

the angular integrals are denoted with

$$\mathcal{A}_{\ell, m', m}^{(\sigma', \sigma)} = \int_0^\pi d\vartheta \int_0^{2\pi} d\varphi (-\sin \vartheta) Y_{\ell, m'}(\vartheta, \varphi)^* \hat{L}^{(\sigma', \sigma)} Y_{\ell, m}(\vartheta, \varphi) \quad .$$

These integrals are evaluated analytically with the use of

$$\begin{aligned} \int_0^\pi d\vartheta \int_0^{2\pi} d\varphi (-\sin \vartheta) Y_{\ell', m'}(\vartheta, \varphi)^* \hat{L}_z Y_{\ell, m}(\vartheta, \varphi) &= \delta_{\ell', \ell} \delta_{m', m} \quad m \quad , \\ \int_0^\pi d\vartheta \int_0^{2\pi} d\varphi (-\sin \vartheta) Y_{\ell', m'}(\vartheta, \varphi)^* \hat{L}_\pm Y_{\ell, m}(\vartheta, \varphi) &= \delta_{\ell', \ell} \delta_{m', \pm 1, m} \sqrt{\ell(\ell+1) - m(m\pm 1)} \quad . \end{aligned}$$

Note that $\mathcal{A}_{\ell,m',m}^{(\sigma',\sigma)}$ needs only one ℓ -label.

The radial integrals are denoted with

$$\begin{aligned} \mathcal{R}_{\ell,u,u}^{(\bar{\sigma}',\bar{\sigma})} &= \int_0^{R_{\text{MT}}} dr r^2 v(r) u_{\ell}^{(\bar{\sigma}')} (r) u_{\ell}^{(\bar{\sigma})} (r) \quad , \quad \mathcal{R}_{\ell,u,\dot{u}}^{(\bar{\sigma}',\bar{\sigma})} = \int_0^{R_{\text{MT}}} dr r^2 v(r) u_{\ell}^{(\bar{\sigma}')} (r) \dot{u}_{\ell}^{(\bar{\sigma})} (r) \quad , \\ \mathcal{R}_{\ell,\dot{u},u}^{(\bar{\sigma}',\bar{\sigma})} &= \int_0^{R_{\text{MT}}} dr r^2 v(r) \dot{u}_{\ell}^{(\bar{\sigma}')} (r) u_{\ell}^{(\bar{\sigma})} (r) \quad , \quad \mathcal{R}_{\ell,\dot{u},\dot{u}}^{(\bar{\sigma}',\bar{\sigma})} = \int_0^{R_{\text{MT}}} dr r^2 v(r) \dot{u}_{\ell}^{(\bar{\sigma}')} (r) \dot{u}_{\ell}^{(\bar{\sigma})} (r) \quad . \end{aligned}$$

A further abbreviation is introduced:

$$\begin{aligned} \mathcal{I}^{(\sigma',\sigma)} &= \sum_{\substack{\ell,m',m \\ \bar{\sigma}',\bar{\sigma}}} \mathcal{A}_{\ell,m',m}^{(\sigma',\sigma)} \left(\begin{aligned} &a_{j',\ell,m'}^{(\sigma',\bar{\sigma}')*} a_{j,\ell,m}^{(\sigma,\bar{\sigma})} \mathcal{R}_{\ell,u,u}^{(\bar{\sigma}',\bar{\sigma})} + a_{j',\ell,m'}^{(\sigma',\bar{\sigma}')*} b_{j,\ell,m}^{(\sigma,\bar{\sigma})} \mathcal{R}_{\ell,u,\dot{u}}^{(\bar{\sigma}',\bar{\sigma})} \\ &+ b_{j',\ell,m'}^{(\sigma',\bar{\sigma}')*} a_{j,\ell,m}^{(\sigma,\bar{\sigma})} \mathcal{R}_{\ell,\dot{u},u}^{(\bar{\sigma}',\bar{\sigma})} + b_{j',\ell,m'}^{(\sigma',\bar{\sigma}')*} b_{j,\ell,m}^{(\sigma,\bar{\sigma})} \mathcal{R}_{\ell,\dot{u},\dot{u}}^{(\bar{\sigma}',\bar{\sigma})} \end{aligned} \right) . \end{aligned}$$

With these definitions a \mathcal{H}_{so} matrix element of two spin-spiral eigenstates $|\psi_{j'}\rangle, |\psi_j\rangle$ can be written as

$$\langle \psi_{j'} | \mathbf{U}_{\text{r-s}}^\dagger \mathcal{H}_{\text{so}} \mathbf{U}_{\text{r-s}} | \psi_j \rangle = \begin{cases} \mathcal{I}^{(\uparrow,\uparrow)} + \mathcal{I}^{(\downarrow,\downarrow)} & \text{if } \mathbf{k}_{j'} = \mathbf{k}_j \\ \mathcal{I}^{(\uparrow,\downarrow)} & \text{if } \mathbf{k}_{j'} = \mathbf{k}_j + \mathbf{q} \\ \mathcal{I}^{(\downarrow,\uparrow)} & \text{if } \mathbf{k}_{j'} = \mathbf{k}_j - \mathbf{q} \\ 0 & \text{else} \end{cases} .$$

The calculation of the SOC matrix elements of spin spirals with long real-space periods is very time consuming. In many cases, it has to be done for thousands of \mathbf{k} -points in order to achieve reliable results. Thus, it might be of high value for future applications to analyse and exploit the symmetries of these matrix elements.

Appendix C

Local force theorem

In this appendix a derivation of the local force theorem is given. This derivation is mainly oriented on [68].

Recall Eqn. (2.13) :

$$E_{\text{tot}} = \sum_{\nu} \epsilon_{\nu} w_{\nu} + E_{\text{dc}} .$$

Here the sum runs over all states and $\{w_{\nu}\}$ denote the occupation numbers. The Kohn-Sham equation (2.11) that determines the single-particle energies (and occupation numbers) depends on the perturbation explicitly and implicitly (the latter as the potential depends on the density, the selfconsistent solution for the density depends on the perturbation). The double-counting term E_{dc} depends on the perturbation only implicitly. When the perturbation is parameterized by X the functional of the total electronic energy can be written as

$$E_{\text{tot}}[X, n(X), \mathbf{m}(X), \mathbf{V}[n(X), \mathbf{m}(X)]] = \sum_{\nu} \epsilon_{\nu}[X, \mathbf{V}[n(X), \mathbf{m}(X)]] w_{\nu}(X) + E_{\text{dc}}[n(X), \mathbf{m}(X), \mathbf{V}[n(X), \mathbf{m}(X)]]$$

where $\epsilon_{\nu}[X]$ denotes the dependency of ϵ_{ν} on the explicit change of the Kohn-Sham equation due to X at fixed n, \mathbf{m} . Here \mathbf{V} labels only the density-dependent part of the potential while the external potential might depend explicitly on X . The energies and occupation numbers as well as $n, \mathbf{m}, \mathbf{V}$ at fixed \mathbf{r} are functions of the parameter X . With F denoting one of these quantities one can introduce the nomenclature

$$F_0 = F|_{X=X_0}$$

for the unperturbed function and

$$\delta_X F = F|_{X=X_0+\delta X} - F_0 = \left. \frac{dF}{dX} \right|_{X=X_0} \delta X + \mathcal{O}((\delta X)^2)$$

for the response to the perturbation. Then one gets by elementary differential calculus

$$\begin{aligned} \delta_X E_{\text{tot}} &= E_{\text{tot}}[X_0 + \delta X, n_0 + \delta_X n, \mathbf{m}_0 + \delta_X \mathbf{m}, \mathbf{V}_0 + \delta_X \mathbf{V}] - E_{\text{tot},0} \\ &= (E_{\text{tot}}[X_0 + \delta X, n_0, \mathbf{m}_0, \mathbf{V}_0] - E_{\text{tot},0}) \\ &\quad + (E_{\text{tot}}[X_0, n_0 + \delta_X n, \mathbf{m}_0 + \delta_X \mathbf{m}, \mathbf{V}_0 + \delta_X \mathbf{V}] - E_{\text{tot},0}) \\ &\quad + \mathcal{O}((\delta X)^2) . \end{aligned}$$

The first bracket on the right hand side simplifies to

$$\sum_{\nu} \epsilon_{\nu}[X_0 + \delta X, \mathbf{V}_0] w_{\nu}(X_0 + \delta X) - \sum_{\nu} \epsilon_{\nu}[X_0, \mathbf{V}_0] w_{\nu}(X_0) ,$$

i.e. the difference in the sum of eigenvalues of the occupied single-electron states calculated with the *unperturbed* potential. The last expression has to be calculated when the local force theorem is applied while the remaining terms almost cancel each other if the perturbation is small.

In order to see this the remaining terms are divided in the single-electron and the double-counting part:

$$\begin{aligned} E_{\text{tot}}[X_0, n_0 + \delta_X n, \mathbf{m}_0 + \delta_X \mathbf{m}, \mathbf{V}_0 + \delta_X \mathbf{V}] - E_{\text{tot},0} = \\ \sum_{\nu} w_{\nu}(X_0) (\epsilon_{\nu}[X_0, \mathbf{V}_0 + \delta_X \mathbf{V}] - \epsilon_{\nu}[X_0, \mathbf{V}_0]) + \delta_X E_{\text{dc}} . \end{aligned}$$

The single-electron term can be approximated by first order standard perturbation theory:

$$\epsilon_{\nu}[X_0, \mathbf{V}_0 + \delta_X \mathbf{V}] - \epsilon_{\nu}[X_0, \mathbf{V}_0] = \int d^3 \mathbf{r} \psi_{\nu}^{\dagger} \delta_X \mathbf{V} \psi_{\nu} + \mathcal{O}((\delta_X \mathbf{V})^2) . \quad (\text{C.1})$$

With this expression and the notation

$$B_s = |\mathbf{B}_{\text{xc}}| \frac{m_s}{|\mathbf{m}|} = \mathbf{B}_{\text{xc}} \cdot \mathbf{e}_s \quad , \quad \mathbf{V} = V_{\text{H}} \mathbf{1} + \mathbf{V}_{\text{xc}} = (V_{\text{H}} + V_{\text{xc}}) \mathbf{1} + \sum_{s \in \{x,y,z\}} B_s \sigma_s$$

for the density-dependent potential the sum over the (occupied) single-electron states can be written as

$$\begin{aligned} \int d^3 \mathbf{r} \sum_{\nu} w_{\nu} \left(\psi_{\nu}^{\dagger} \mathbf{1} \psi_{\nu} \delta_X (V_{\text{H}} + V_{\text{xc}}) + \sum_s \psi_{\nu}^{\dagger} \sigma_s \psi_{\nu} \delta_X B_s \right) \\ = \int d^3 \mathbf{r} \left(n \delta_X (V_{\text{H}} + V_{\text{xc}}) + \sum_s m_s \delta_X B_s \right) . \end{aligned}$$

With Eqn. (2.13) the response of the double-counting part can be written as

$$\begin{aligned} \delta_X E_{\text{dc}} &= \delta X \frac{d}{dX} E_{\text{dc}} + \mathcal{O}((\delta X)^2) \\ &= -\delta X \frac{d}{dX} \int d^3 \mathbf{r} \frac{1}{2} V_{\text{H}} n - \delta X \frac{d}{dX} \int d^3 \mathbf{r} (V_{\text{xc}} n + \mathbf{B}_{\text{xc}} \cdot \mathbf{m} - f_{\text{lda}}(n, |\mathbf{m}|)) \\ &\quad + \mathcal{O}((\delta X)^2) . \end{aligned}$$

The Hartree term can be simplified by renaming the integration variables:

$$\begin{aligned} \frac{d}{dX} \int d^3 \mathbf{r} \frac{1}{2} V_{\text{H}} n &= \frac{1}{2} \frac{d}{dX} \int d^3 \mathbf{r} d^3 \mathbf{r}' \frac{n(\mathbf{r}') n(\mathbf{r})}{|\mathbf{r}' - \mathbf{r}|} \\ &= \frac{1}{2} \int d^3 \mathbf{r} d^3 \mathbf{r}' \left(\frac{n(\mathbf{r})}{|\mathbf{r}' - \mathbf{r}|} \frac{d}{dX} n(\mathbf{r}') + \frac{n(\mathbf{r}')}{|\mathbf{r}' - \mathbf{r}|} \frac{d}{dX} n(\mathbf{r}) \right) = \int d^3 \mathbf{r} n \frac{d}{dX} V_{\text{H}} . \end{aligned}$$

After recalling the definitions of \mathbf{V}_{xc} (cf. Chapter 2.3)

$$V_{\text{xc}} = \frac{\partial}{\partial n} f_{\text{lda}}(n, \mathbf{m}) \quad , \quad \mathbf{B}_{\text{xc}} \cdot \mathbf{e}_s = \frac{\partial}{\partial m_s} f_{\text{lda}}(n, \mathbf{m}) \quad , \quad s \in \{x, y, z\}$$

the exchange-correlation term can easily be simplified:

$$\begin{aligned}
& \frac{d}{dX} \int d^3\mathbf{r} (V_{\text{xc}} n + \mathbf{B}_{\text{xc}} \cdot \mathbf{m} - f_{\text{lda}}(n, |\mathbf{m}|)) \\
&= \int d^3\mathbf{r} \left(n \frac{d}{dX} V_{\text{xc}} + V_{\text{xc}} \frac{d}{dX} n + \mathbf{m} \cdot \left(\frac{d}{dX} \mathbf{B}_{\text{xc}} \right) + \mathbf{B}_{\text{xc}} \cdot \left(\frac{d}{dX} \mathbf{m} \right) \right. \\
&\quad \left. - \left(\frac{\partial}{\partial n} f_{\text{lda}}(n, \mathbf{m}) \right) \frac{d}{dX} n - \sum_s \left(\frac{\partial}{\partial m_s} f_{\text{lda}}(n, \mathbf{m}) \right) \frac{d}{dX} m_s \right) \\
&= \int d^3\mathbf{r} \left(n \frac{d}{dX} V_{\text{xc}} + \mathbf{m} \cdot \left(\frac{d}{dX} \mathbf{B}_{\text{xc}} \right) \right) = \int d^3\mathbf{r} \left(n \frac{d}{dX} V_{\text{xc}} + \sum_s m_s \frac{d}{dX} B_s \right).
\end{aligned}$$

Now the response of the double-counting part becomes

$$\begin{aligned}
\delta_X E_{\text{dc}} &= - \int d^3\mathbf{r} \delta X \left(n \frac{d}{dX} V_{\text{H}} + n \frac{d}{dX} V_{\text{xc}} + \sum_s m_s \frac{d}{dX} B_s \right) + \mathcal{O}((\delta X)^2) \\
&= - \int d^3\mathbf{r} \left(n \delta_X (V_{\text{H}} + V_{\text{xc}}) + \sum_s m_s \delta_X B_s \right) + \mathcal{O}((\delta X)^2). \tag{C.2}
\end{aligned}$$

This term (C.2) obviously cancels with the sum of the single-electron energies (C.1). For a smooth function $V(X)$ (that is required by the perturbative approach anyway) one gets $\mathcal{O}((\delta_X V)^2) = \mathcal{O}((\delta X)^2)$ and the response of the total energy to the perturbation can be written as

$$\begin{aligned}
\delta_X E_{\text{tot}} &= \\
&\sum_{\nu} \epsilon_{\nu}[X_0 + \delta X, \mathbf{V}_0] w_{\nu}(X_0 + \delta X) - \sum_{\nu} \epsilon_{\nu}[X_0, \mathbf{V}_0] w_{\nu}(X_0) + \mathcal{O}((\delta X)^2).
\end{aligned}$$

Note that the changes in the occupation numbers lead to discontinuities in $n(X)$ and thus to discontinuities in $V(X)$. If these discontinuities cannot be neglected, then $V(X)$ cannot be regarded as smooth and the local force theorem is very inaccurate.

As pointed out in [68] the local force theorem does not hold if the perturbation changes the size or shape of the unit cell, in this case not all 1st-order terms cancel.

Appendix D

Perturbation theory for the sum of eigenvalues

This appendix describes a perturbative approach that allows to estimate the changes in the spectrum around the Fermi energy and in the sum of eigenvalues of the occupied states due to a small perturbation of the Hamiltonian. The method is a simple extension of the Rayleigh-Schrödinger perturbation theory of quasi-degenerate levels as it is discussed in many text books [e.g. 9]. The perturbation is assumed to be small, but its particular form is not exploited. Only the sparseness of the perturbation matrix decreases the computational effort further since the below described sums do not have to include the terms with zero-valued matrix-elements.

H_0 denotes the unperturbed Hamiltonian (with known eigenstates and eigenvalues), $H_0 + H_{\text{so}}$ denotes the perturbed Hamiltonian.

It is assumed that the quantity $\lambda = \frac{1}{\Delta} \langle m | H_{\text{so}} | n \rangle$ is small and terms in $\mathcal{O}(\lambda^2)$ can be neglected in the Hamiltonian and in the eigenvalue spectrum for a fixed energy difference Δ and for all relevant states $|m\rangle, |n\rangle$ (if the perturbation is not small, Δ has to be large and the method is not efficient).

The perturbation is split in four terms

$$H_{\text{so}} = H_1 + H_2 + H_3 + H_4 ,$$

each term can be treated in a different way:

- H_1 has to be treated with exact diagonalization, but the corresponding matrix is relatively small since H_1 mixes only between the states close to the Fermi energy.
- H_2 can be treated with the standard perturbation approach since its matrix elements are exactly zero if the distance between the energy levels of the corresponding states is small.
- H_3 mixes only between states well below the Fermi energy that remain occupied after the perturbation. Therefore the sum of the energy corrections of these states is simply the trace of H_3 .
- H_4 mixes only between the states well above the Fermi energy. The energy shifts among these unoccupied states are irrelevant.

Although these basic ideas are not complicated, it is quite cumbersome to formulate them rigorously.

In the following derivation the four terms of H_{so} are applied successively, i.e. at first the eigenstates of $H_0 + H_1$ are determined, then $H_0 + H_1$ is perturbed by H_2 , etc. .

In order to define the different terms of H_{so} the following notation is used:

ϵ_F denotes the Fermi energy.

$|n_0\rangle, |n_1\rangle, |n_2\rangle$ and $\epsilon_{n,0}, \epsilon_{n,1}, \epsilon_{n,2}$ denote the n th eigenstate and corresponding eigenvalue of $H_0, H_0 + H_1, H_0 + H_1 + H_2$.

The set of eigenstates of H_0 is divided according to the energy $e_0 > 0$:

$$|n_0\rangle \in A \Leftrightarrow \epsilon_{n,0} - \epsilon_F > +e_0 ,$$

$$|n_0\rangle \in M \Leftrightarrow +e_0 \geq \epsilon_{n,0} - \epsilon_F \geq -e_0 ,$$

$$|n_0\rangle \in B \Leftrightarrow -e_0 > \epsilon_{n,0} - \epsilon_F .$$

H_1 is constructed such that the eigenstates of $H_0 + H_1$ are either a linear combination of or orthogonal to all elements of M . The subset of eigenstates of $H_0 + H_1$ that consists of elements of $\text{Span } M$ is divided according to the energies $e_0 > e_1 > e_2 > 0$:

$$|n_1\rangle \in M_{aa} \Leftrightarrow \epsilon_{n,1} - \epsilon_F > +e_1 ,$$

$$|n_1\rangle \in M_{ab} \Leftrightarrow +e_1 \geq \epsilon_{n,1} - \epsilon_F > +e_2 ,$$

$$|n_1\rangle \in M_m \Leftrightarrow +e_2 \geq \epsilon_{n,1} - \epsilon_F \geq -e_2 ,$$

$$|n_1\rangle \in M_{ba} \Leftrightarrow -e_2 > \epsilon_{n,1} - \epsilon_F \geq -e_1 ,$$

$$|n_1\rangle \in M_{bb} \Leftrightarrow -e_1 > \epsilon_{n,1} - \epsilon_F .$$

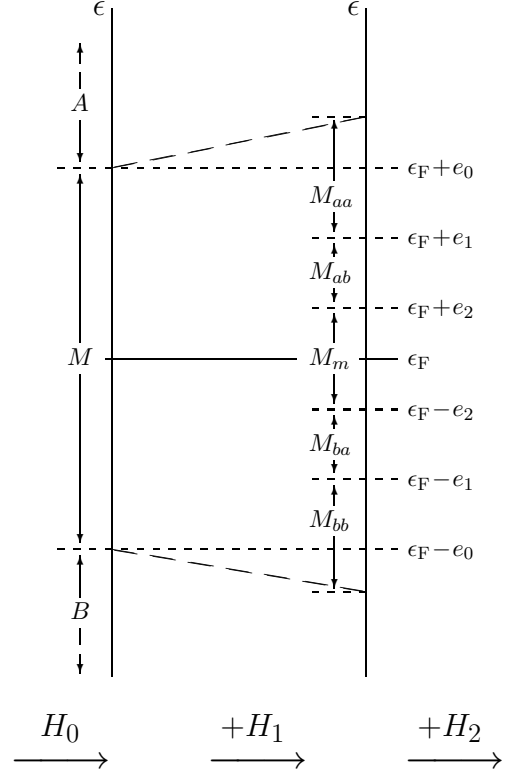


Figure D.1: Sketch illustrating the definitions of e_0, e_1, e_2 and $A, M, B, M_{aa}, M_{ab}, M_m, M_{ba}, M_{bb}$.

In the following it is not distinguished between the Fermi energy of the unperturbed and of the perturbed system. This inaccuracy can be compensated by choosing the relevant intervals around ϵ_F a bit larger.

At first H_1 is applied. It mixes only between the states close to ϵ_F :

$$H_1 = \sum_{\substack{n, m \\ |m_0\rangle \in M \\ |n_0\rangle \in M}} |m_0\rangle \langle m_0 | H_{\text{so}} | n_0 \rangle \langle n_0 | .$$

The exact solutions of $H_0 + H_1$ are obtained by diagonalizing the matrix $(\langle m_0 | H_{\text{so}} | n_0 \rangle + \delta_{m,n} \epsilon_{n,0})_{m,n}$. Since the matrix elements of H_1 with states $\notin M$ are zero only a block of size $(\#M \times \#M)$ has to be considered. Certainly the elements of A, B are solutions of $H_0 + H_1$ as well. It is desired to choose e_0 as small as possible as the exact diagonalization usually is the most time consuming part of the calculations (especially if most matrix elements of H_{so} are zero).

H_2 has non-zero matrix elements only between states whose energy levels are separated at least by $e_0 - e_1$:

$$\begin{aligned}
H_2 = & \sum_{\substack{n,m \\ |m_1\rangle \in A \\ |n_1\rangle \in B}} |m_1\rangle \langle m_1| H_{\text{so}} |n_1\rangle \langle n_1| \\
& + \sum_{\substack{n,m \\ |m_1\rangle \in M \setminus M_{bb} \\ |n_1\rangle \in B}} \left(|m_1\rangle \langle m_1| H_{\text{so}} |n_1\rangle \langle n_1| + |n_1\rangle \langle n_1| H_{\text{so}} |m_1\rangle \langle m_1| \right) \\
& + \sum_{\substack{n,m \\ |m_1\rangle \in M \setminus M_{aa} \\ |n_1\rangle \in A}} \left(|m_1\rangle \langle m_1| H_{\text{so}} |n_1\rangle \langle n_1| + |n_1\rangle \langle n_1| H_{\text{so}} |m_1\rangle \langle m_1| \right) .
\end{aligned}$$

For $e_0 - e_1 > \Delta$ the corrections to the solutions of $H_0 + H_1$ can be estimated with the standard 2nd-order perturbation theory:

$$\begin{aligned}
|n_2\rangle &= |n_1\rangle + \sum_{\substack{m \\ |m_1\rangle \in X}} |m_1\rangle \frac{\langle m_1| H_{\text{so}} |n_1\rangle}{\underbrace{\epsilon_{n,1} - \epsilon_{m,1}}_{\mathcal{O}(\lambda)}} + \mathcal{O}(\lambda^2) , \quad (\text{D.1}) \\
\epsilon_{n,2} &= \epsilon_{n,1} + \sum_{\substack{m \\ |m_1\rangle \in X}} \frac{|\langle m_1| H_{\text{so}} |n_1\rangle|^2}{\epsilon_{n,1} - \epsilon_{m,1}} + \mathcal{O}(\lambda^2)
\end{aligned}$$

$$\begin{aligned}
\text{with} \quad X = & B \cup M \setminus M_{aa} \quad \text{if } |n_1\rangle \in A , \\
& B \quad \text{if } |n_1\rangle \in M_{aa} , \\
& A \cup B \quad \text{if } |n_1\rangle \in M_{ab} \cup M_m \cup M_{ba} , \\
& A \quad \text{if } |n_1\rangle \in M_{bb} , \\
& A \cup M \setminus M_{bb} \quad \text{if } |n_1\rangle \in B .
\end{aligned}$$

The remaining terms of H_{so} are:

$$\begin{aligned}
H_3 = & \sum_{\substack{n,m \\ |m_1\rangle \in B \\ |n_1\rangle \in B}} |m_1\rangle \langle m_1| H_{\text{so}} |n_1\rangle \langle n_1| \\
& + \sum_{\substack{n,m \\ |m_1\rangle \in B \\ |n_1\rangle \in M_{bb}}} \left(|m_1\rangle \langle m_1| H_{\text{so}} |n_1\rangle \langle n_1| + |n_1\rangle \langle n_1| H_{\text{so}} |m_1\rangle \langle m_1| \right) , \\
H_4 = & \sum_{\substack{n,m \\ |m_1\rangle \in A \\ |n_1\rangle \in A}} |m_1\rangle \langle m_1| H_{\text{so}} |n_1\rangle \langle n_1| \\
& + \sum_{\substack{n,m \\ |m_1\rangle \in A \\ |n_1\rangle \in M_{aa}}} \left(|m_1\rangle \langle m_1| H_{\text{so}} |n_1\rangle \langle n_1| + |n_1\rangle \langle n_1| H_{\text{so}} |m_1\rangle \langle m_1| \right) .
\end{aligned}$$

The Expression (D.1) defines an one-to-one mapping from the eigenstates of $H_0 + H_1$ to the eigenstates of $H_0 + H_1 + H_2$. This allows the use of $|n_1\rangle, |m_1\rangle$ and $|n_2\rangle, |m_2\rangle$ in the following definitions:

$$H_{3,1} = \sum_{\substack{n,m \\ |m_1\rangle \in B \cup M_{bb} \\ |n_1\rangle \in M_m}} \left(|m_2\rangle \langle m_2| H_3 |n_2\rangle \langle n_2| + |n_2\rangle \langle n_2| H_3 |m_2\rangle \langle m_2| \right) ,$$

$$H_{3,2} = H_3 - H_{3,1} ,$$

$$H_{4,1} = \sum_{\substack{n,m \\ |m_1\rangle \in A \cup M_{aa} \\ |n_1\rangle \in M_m}} \left(|m_2\rangle \langle m_2| H_4 |n_2\rangle \langle n_2| + |n_2\rangle \langle n_2| H_4 |m_2\rangle \langle m_2| \right) ,$$

$$H_{4,2} = H_4 - H_{4,1} .$$

Again, the idea of this decomposition is to separate a term like $H_{3,1} + H_{4,1}$ that can be treated with the standard perturbation theory. If $|n_1\rangle \in M_{bb}$ then the 2nd-order correction of $|n_2\rangle$ leads to

$$|n_{3,1}\rangle = |n_2\rangle + \sum_{\substack{m \\ |m_1\rangle \in M_m}} |m_2\rangle \frac{\langle m_2| H_3 |n_2\rangle}{\epsilon_{n,2} - \epsilon_{m,2}} + \dots$$

$$\text{where } \frac{\langle m_2| H_3 |n_2\rangle}{\epsilon_{n,2} - \epsilon_{m,2}} = \sum_{\substack{m' \\ |m'_1\rangle \in B}} \frac{\langle m'_1| H_{so} |m_1\rangle}{\underbrace{\epsilon_{m',1} - \epsilon_{m,1}}_{\mathcal{O}(\lambda)}} \frac{\langle m'_1| H_{so} |n_1\rangle}{\epsilon_{n,2} - \epsilon_{m,2}} .$$

For sufficiently large $e_2 - e_1 \gtrsim \Delta$ the last term is in $\mathcal{O}(\lambda^2)$. If $|n_1\rangle \in M_m$ or $|n_1\rangle \in M_{aa}$ the situation is analogous. Hence the eigenstates of $H_0 + H_1 + H_2 + H_{3,1} + H_{4,1}$ can be expressed as $|n_2\rangle + \mathcal{O}(\lambda^2)$, an according expression holds for the eigenvalues.

Therefore the matrix elements of $H_{3,2} + H_{4,2}$ with the eigenstates of $H_0 + H_1 + H_2 + H_{3,1} + H_{4,1}$ can be written as $\langle m_2| H_{3,2} + H_{4,2} |n_2\rangle + \mathcal{O}(\lambda^2)$, inserting the expressions for $|m_2\rangle$, $|n_2\rangle$ one gets

$$\langle m_2| H_{3,2} + H_{4,2} |n_2\rangle = \begin{cases} \langle m_2| H_4 |n_2\rangle + \mathcal{O}(\lambda^2) & \text{if } |m_1\rangle, |n_1\rangle \in A \cup M_{aa} \cup M_{ab} \\ \langle m_2| H_3 |n_2\rangle + \mathcal{O}(\lambda^2) & \text{if } |m_1\rangle, |n_1\rangle \in B \cup M_{bb} \cup M_{ba} \\ 0 + \mathcal{O}(\lambda^2) & \text{else} \end{cases} .$$

As the terms in $\mathcal{O}(\lambda^2)$ are neglected, $H_{3,2} + H_{4,2}$ separates in two blocks, one of them mixes only states of the energy below $\epsilon_F - e_2$, the other mixes only states of the energy above $\epsilon_F + e_2$. Under the assumption that these states do not change their occupation numbers when they are perturbed by $H_{3,2} + H_{4,2}$, the sum of eigenvalues of these occupied states is

$$\begin{aligned} & \text{Tr} \left\{ \langle m_2| H_3 |n_2\rangle + \delta_{m,n} \epsilon_{n,2} \right\}_{m,n} \\ & \quad \quad \quad \uparrow \\ & \quad \quad \quad \underbrace{|m_1\rangle, |n_1\rangle \in B \cup M_{bb} \cup M_{ba}} \\ & = \sum_{\substack{n \\ |n_1\rangle \in B}} \langle n_1| H_{so} |n_1\rangle + \sum_{\substack{n \\ |n_1\rangle \in B \cup M_{bb} \cup M_{ba}}} \epsilon_{n,2} + \mathcal{O}(\lambda^2) . \end{aligned}$$

Of course, the shifts of the unoccupied levels due to $H_{4,2}$ are not important.

Now the influence of the total perturbation $H_{so} = H_1 + H_2 + H_3 + H_4$ has been calculated in $\mathcal{O}(\lambda)$. In the following the steps that have to be done in the calculation are summarized (note that e_2 does not have to be defined explicitly):

- Calculate the eigenstates $\{|n_0\rangle\}_n$ and eigenvalues $\{\epsilon_{n,0}\}_n$ and the Fermi energy ϵ_F of the unperturbed Hamiltonian H_0 .
- Choose the intervals $[\epsilon_F - e_0, \epsilon_F + e_0]$ and $[\epsilon_F - e_1, \epsilon_F + e_1]$ such that
 - the eigenstates of H_0 with $\epsilon_{n,0} \notin [\epsilon_F - e_0, \epsilon_F + e_0]$ do not change their occupation numbers when H_{so} is applied,
 - the eigenstates of $H_0 + H_1$ with $\epsilon_{n,1} \notin [\epsilon_F - e_1 + \Delta, \epsilon_F + e_1 - \Delta]$ do not change their occupation numbers when $H_{\text{so}} - H_1$ is applied,
 - $e_0 - e_1$ is large compared to the relevant matrix elements of H_{so} .

Note that the computational effort is determined mainly by e_0 .

- Calculate the eigenstates $\{|n_1\rangle\}_n$ and eigenvalues $\{\epsilon_{n,1}\}_n$ of $H_0 + H_1$ in the subspace $\text{Span } M$ by exact diagonalization.
- Estimate the eigenvalues $\{\epsilon_n\}_n$ of $H_0 + H_{\text{so}}$ around the Fermi energy:

$$\epsilon_{n,1} \in [\epsilon_F - e_1, \epsilon_F + e_1] \quad \Rightarrow \quad \epsilon_n = \epsilon_{n,1} + \sum_{\substack{m \\ |\epsilon_{m,0} - \epsilon_F| > e_0}} \frac{|\langle m_0 | H_{\text{so}} | n_1 \rangle|^2}{\epsilon_{n,1} - \epsilon_{m,0}} + \dots$$

Determine the Fermi energy $e_F^{(\text{so})}$ of the perturbed system.

- Calculate the sum of the energies of the occupied eigenstates of $H_0 + H_{\text{so}}$:

$$\begin{aligned} E = & \sum_{\substack{n \\ |n_0\rangle \in B}} \langle n_0 | H_{\text{so}} | n_0 \rangle \\ & + \sum_{|n_0\rangle \in B} \left(\epsilon_{n,0} + \sum_{\substack{m \\ |m_0\rangle \in A}} \frac{|\langle m_0 | H_{\text{so}} | n_0 \rangle|^2}{\epsilon_{n,1} - \epsilon_{m,0}} + \sum_{\substack{m \\ |m_1\rangle \in M \\ \epsilon_{m,0} - \epsilon_F > -e_1}} \frac{|\langle m_1 | H_{\text{so}} | n_0 \rangle|^2}{\epsilon_{n,0} - \epsilon_{m,1}} \right) \\ & + \sum_{\substack{n \\ |n_1\rangle \in M \\ \epsilon_{n,1} - \epsilon_F < -e_1}} \left(\epsilon_{n,1} + \sum_{\substack{m \\ |m_0\rangle \in A}} \frac{|\langle m_0 | H_{\text{so}} | n_1 \rangle|^2}{\epsilon_{n,1} - \epsilon_{m,0}} \right) \\ & + \sum_{\substack{n \\ |n_1\rangle \in M \\ |\epsilon_{n,1} - \epsilon_F| \leq e_1 \\ \epsilon_n < e_F^{(\text{so})}}} \left(\epsilon_{n,1} + \sum_{\substack{m \\ |m_0\rangle \in A \cup B}} \frac{|\langle m_0 | H_{\text{so}} | n_1 \rangle|^2}{\epsilon_{n,1} - \epsilon_{m,0}} \right) \\ & + \mathcal{O}(\lambda^2) . \end{aligned}$$

Appendix E

Relations between real- and spin-space symmetries

E.1 Transformations in real- and spin-space

In this chapter it is shown, that for every real-space rotation or reflection \mathcal{R} there is a corresponding rotation or reflection \mathcal{S} in spin space. When \mathcal{R} and \mathcal{S} are both applied, then the orientation between real- and magnetic structure does not change and the energy of the system stays the same. Furthermore, it is shown that the energy does not change under spin inversion.

The analysis is done in the framework of the Kohn-Sham Dirac equation (2.14). The same results can be obtained when using the Pauli equation extended by the spin-orbit coupling operator \mathcal{H}_{so} .

The Hamiltonian (in absence of an external magnetic field) can be written as

$$\mathcal{H} = \mathcal{T} + V_{\text{ext}} + V_{\text{el}} \quad \text{with} \quad V_{\text{el}} = V_{\text{H}}[\{\psi_\nu\}] + V_{\text{xc}}[\{\psi_\nu\}] \quad , \quad \mathcal{T} = c \boldsymbol{\sigma} \cdot \hat{\mathbf{p}} \begin{pmatrix} 0 & \mathbb{1} \\ \mathbb{1} & 0 \end{pmatrix} .$$

\mathcal{R} , \mathcal{R}_V denote operators that transform the real-space coordinates and \mathcal{S} denotes an operator that transform only the spin orientation. When all (occupied) eigenstates ψ_ν of the single-particle Hamiltonian \mathcal{H} are transformed by the symmetry operation $\mathcal{S}\mathcal{R}$ then the charge and magnetization densities are transformed as well. In the usual DFT approach the transformation of the non-external potential V_{el} (that might include constraining fields) can be described by

$$V_{\text{el}}[\{\mathcal{S}\mathcal{R} \psi_\nu\}] = (\mathcal{S}\mathcal{R}) V_{\text{el}}[\{\psi_\nu\}] (\mathcal{S}\mathcal{R})^{-1} .$$

In the following V_{el} denotes the selfconsistent potential that corresponds to the eigenfunctions $\{\psi_\nu\}$ of \mathcal{H} . It is investigated, which transformations $\mathcal{S}\mathcal{R}$ leave the energy invariant, if the external potential is transformed by \mathcal{R}_V , i.e. which transformations $\mathcal{S}\mathcal{R}$ fulfill the following condition:

$$\forall \nu : \quad \begin{aligned} & (\mathcal{T} + V_{\text{ext}} + V_{\text{el}}) \psi_\nu = \epsilon_\nu \psi_\nu \\ \Leftrightarrow & (\mathcal{T} + \mathcal{R}_V V_{\text{ext}} \mathcal{R}_V^{-1} + (\mathcal{S}\mathcal{R}) V_{\text{el}} (\mathcal{S}\mathcal{R})^{-1}) \mathcal{S}\mathcal{R} \psi_\nu = \epsilon_\nu \mathcal{S}\mathcal{R} \psi_\nu \end{aligned} \quad . \quad (\text{E.1})$$

If $[V_{\text{ext}}, \mathcal{R}_V] = 0$ then (E.1) defines the symmetry operations $\mathcal{S}\mathcal{R}$ that leave the energy invariant for a given potential V_{ext} . If $[V_{\text{ext}}, \mathcal{R}_V] \neq 0$ then (E.1) defines the transformations $\mathcal{S}\mathcal{R}$ of the wavefunctions $\{\psi_\nu\}$ that are induced by the transformation of V_{ext} .

The condition (E.1) can be simplified since

$$\begin{aligned} & (\mathcal{T} + \mathcal{R}_V V_{\text{ext}} \mathcal{R}_V^{-1} + (\mathcal{S}\mathcal{R}) V_{\text{el}} (\mathcal{S}\mathcal{R})^{-1}) \mathcal{S}\mathcal{R} \psi_\nu \\ &= (\mathcal{S}\mathcal{R} (\mathcal{T} + V_{\text{ext}} + V_{\text{el}}) + [\mathcal{T}, \mathcal{S}\mathcal{R}] + \mathcal{R}_V [V_{\text{ext}}, \mathcal{R}_V^{-1} \mathcal{R}]) \psi_\nu \\ &= \epsilon_\nu \mathcal{S}\mathcal{R} \psi_\nu + ([\mathcal{T}, \mathcal{S}\mathcal{R}] + \mathcal{R}_V [V_{\text{ext}}, \mathcal{R}_V^{-1} \mathcal{R}]) \psi_\nu . \end{aligned}$$

Apart from accidental cancelations, (E.1) is fulfilled if

$$[\mathcal{T}, \mathcal{S}\mathcal{R}] = 0 \quad , \quad [V_{\text{ext}}, \mathcal{R}_V^{-1} \mathcal{R}] = 0 . \quad (\text{E.2})$$

The last condition is surely fulfilled, if $\mathcal{R} = \mathcal{R}_V$. The condition $[\mathcal{T}, \mathcal{S}\mathcal{R}] = 0$ is further analyzed for some special transformations $\mathcal{S}\mathcal{R}$, namely rotations, reflections and spin inversion:

Spin inversion

The spin-inversion operator \mathcal{S}_I changes the sign of the magnetization, i.e. $\mathcal{S}_I^\dagger \boldsymbol{\sigma} \mathcal{S}_I = -\boldsymbol{\sigma}$. If \mathcal{S}_I is applied to all states, the sign of the magnetization changes, i.e. $\mathbf{m}(\mathbf{r}) \rightarrow -\mathbf{m}(\mathbf{r})$.

\mathcal{S}_I can be represented by $\mathcal{S}_I = i \sigma_y \mathcal{K}$, where \mathcal{K} denotes the operator of complex conjugation.

Straightforward calculations show, that

$$[\boldsymbol{\sigma} \cdot \hat{\mathbf{p}}, i \sigma_y \mathcal{K}] = 0 .$$

Thus, (E.2) is fulfilled for $\mathcal{S} = i \sigma_y \mathcal{K}$ and $\mathcal{R}_V = \mathcal{R} = 1$. This means, that a Hamiltonian (in absence of an external magnetic field) always has two equivalent solutions with opposite magnetization directions.

Rotations

The eigenenergies do not change if the same rotations are performed in real- and spin-space. This is trivial, since the rotated system can be described equivalently as the original system, just with a rotated coordinate frame.

Mirror-plane reflections

In time-independent systems, the eigenenergies do not change if the same mirror-plane reflections are performed in real- and spin-space. But this is not as trivial as in the case of rotations, since a mirror-plane reflection changes the chirality of the system.

The choice of the coordinate system is arbitrary, therefore it is sufficient to study the reflections on the (x, z) -plane. \mathcal{R}_y and \mathcal{S}_y denote the corresponding real- and spin-space operator respectively.

With $\hat{\mathbf{p}}_w = i \frac{d}{dw}$, $w \in \{x, y, z\}$ it is obvious, that

$$[\mathcal{R}_y, \hat{p}_x] = [\mathcal{R}_y, \hat{p}_z] = 0 \quad , \quad \mathcal{R}_y \hat{p}_y = -\hat{p}_y \mathcal{R}_y .$$

\mathcal{S}_y can be represented by

$$\mathcal{S}_y = \begin{pmatrix} \mathcal{K} \mathbb{1} & 0 \\ 0 & -\mathcal{K} \mathbb{1} \end{pmatrix} .$$

This can be seen easily when inserting $\psi_\nu = (\varphi_\nu, \chi_\nu)^\dagger$ and $\mathcal{S}_y \psi_\nu$ in the expression for \mathbf{m} that is given in Chapter 2.5.

Now, straightforward calculations show that

$$[\mathcal{T}, \mathcal{S}_y \mathcal{R}_y] = \left[\begin{pmatrix} 0 & c \boldsymbol{\sigma} \cdot \hat{\mathbf{p}} \\ c \boldsymbol{\sigma} \cdot \hat{\mathbf{p}} & 0 \end{pmatrix}, \mathcal{S}_y \mathcal{R}_y \right] = 0.$$

E.2 Anisotropy energy tensor

In the micromagnetic model, the anisotropy energy tensor $E^{(\text{so})}(\mathbf{m})$ describes the energy depending on the local magnetization direction (cf. Chapter 5.2.1).

Usually, $E^{(\text{so})}$ represents the crystal symmetry but does not show much further oscillations. Therefore the energy can be approximated by an expansion in the polar angles and neglecting the terms that do not reflect the crystal symmetry. The local extrema of these expansions are possible orientations of the easy axis. The general expansion (as first proposed in [1]) has the form

$$\begin{aligned} E^{(\text{so})} = & \sum_j k_j m_j + \sum_{j,j'} k_{j,j'} m_j m_{j'} + \sum_{j,j',j''} k_{j,j',j''} m_j m_{j'} m_{j''} \\ & + \sum_{j,j',j'',j'''} k_{j,j',j'',j'''} m_j m_{j'} m_{j''} m_{j'''} + \dots \\ & \text{with } j = x, y, z. \end{aligned}$$

Spin inversion symmetry requires that the coefficients with an odd number of indices are zero.

The existence of one mirror plane already results in 2-dimensional spin-inversion symmetry in the mirror plane:

$E^{(\text{so})}(m_x, m_y, m_z) \stackrel{z\text{-refl.}}{=} E^{(\text{so})}(m_x, m_y, -m_z) \stackrel{\text{spin inv.}}{=} E^{(\text{so})}(-m_x, -m_y, m_z)$. This indicates a local extrema (or saddle point) of $E^{(\text{so})}(\mathbf{m})$ in the spin orientation normal to the mirror plane.

The surfaces that are further investigated in this thesis possess two orthogonal mirror axes (e.g. x, y). Then the coefficients of $m_x m_y$, $m_y m_z$, $m_z m_x$ must be zero and the first relevant terms of the expansion are $K_x = k_{x,x}$, $K_y = k_{y,y}$, $K_z = k_{z,z}$:

$$E^{(\text{so})} \approx K_x m_x^2 + K_y m_y^2 + K_z m_z^2 = \mathbf{m}^\dagger \cdot \mathbf{K} \cdot \mathbf{m} \quad \text{with} \quad \mathbf{K} = \begin{pmatrix} K_x & 0 & 0 \\ 0 & K_y & 0 \\ 0 & 0 & K_z \end{pmatrix}.$$

Appendix F

Details concerning the domain wall models

F.1 Derivation of the micromagnetic model

In this chapter the micromagnetic approximation

$$\tilde{E} = \int dr \left(\tilde{A} \dot{\mathbf{m}}(r)^2 + \tilde{\mathbf{D}} \cdot (\mathbf{m}(r) \times \dot{\mathbf{m}}(r)) + \mathbf{m}(r)^\dagger \cdot \tilde{\mathbf{K}} \cdot \mathbf{m}(r) \right) \quad (5.3, \text{Page 42})$$

is deduced from the discrete model

$$E = \sum_{j < j'} \left(J_{|j'-j|} (1 - \mathbf{S}_j \cdot \mathbf{S}_{j'}) + \mathbf{D}_{j'-j} \cdot (\mathbf{S}_j \times \mathbf{S}_{j'}) \right) + \sum_j \mathbf{S}_j^\dagger \cdot \mathbf{K} \cdot \mathbf{S}_j . \quad (5.2, \text{Page 41})$$

In the discrete model E denotes the energy of one stripe of atoms. In film systems b denotes the broadness ($\perp \mathbf{q}$) of this stripe (cf. Fig. F.1), in bulk systems b denotes the cross-sectional area ($\perp \mathbf{q}$) of this stripe. In the micromagnetic model \tilde{E} denotes the energy per length (in film systems) or per area (in bulk systems). Thus, if (5.2) can be approximated by (5.3) then $E \approx b \tilde{E}$.

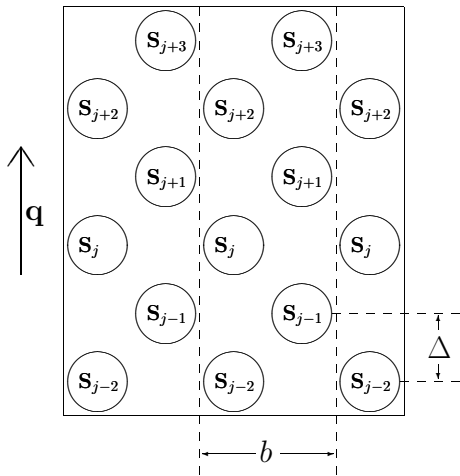


Figure F.1: Definition of Δ and b in two dimensions. In Eqn. (5.2) E denotes the energy of one line of atoms, i.e. of a stripe of broadness b .

It is certainly possible to choose the continuous function $\mathbf{m}(r)$ such that

$$\mathbf{m}(j \Delta) = \mathbf{S}_j$$

where Δ denotes the spacing between the lattice points on the r -axis (cf. Fig. F.1).

All interactions in (5.3) are local, thus one needs to assume that \mathbf{m} does not vary much on a length scale where the interactions J, \mathbf{D} are relevant. In the following all terms in (5.2) are treated within the lowest relevant order of the Taylor expansion of $\mathbf{m}(r)$:

$$\begin{aligned} 1 - \mathbf{S}_j \cdot \mathbf{S}_{j'} &\approx 1 - \mathbf{m}(j \Delta)^2 - (j' - j) \Delta \mathbf{m}(j \Delta) \cdot \dot{\mathbf{m}}(j \Delta) - ((j' - j) \Delta)^2 \frac{1}{2} \mathbf{m}(j \Delta) \cdot \ddot{\mathbf{m}}(j \Delta) \\ &= ((j' - j) \Delta)^2 \frac{1}{2} \ddot{\mathbf{m}}(j \Delta)^2, \\ \mathbf{S}_j \times \mathbf{S}_{j'} &\approx (j' - j) \Delta \mathbf{m}(j \Delta) \times \dot{\mathbf{m}}(j \Delta). \end{aligned}$$

For the exchange term it is used that $|\mathbf{m}(r)|=1$ and therefore

$$1 = \mathbf{m}(r)^2, \quad 0 = \frac{d}{dr} \mathbf{m}(r)^2 = 2 \mathbf{m}(r) \cdot \dot{\mathbf{m}}(r), \quad 0 = \frac{d^2}{dr^2} \mathbf{m}(r)^2 = 2 \mathbf{m}(r) \cdot \ddot{\mathbf{m}}(r) + 2 \dot{\mathbf{m}}(r)^2.$$

With this expressions (5.2) can be written as

$$\begin{aligned} E &= \sum_j \Delta \left(\sum_{j' > j}^{j' > j} \left(\frac{1}{2} (j' - j)^2 \Delta J_{j'-j} \dot{\mathbf{m}}(j \Delta)^2 + (j' - j) \mathbf{D}_{j'-j} \cdot (\mathbf{m}(j \Delta) \times \dot{\mathbf{m}}(j \Delta)) \right) \right. \\ &\quad \left. + \Delta^{-1} \mathbf{m}(j \Delta)^\dagger \cdot \mathbf{K} \cdot \mathbf{m}(j \Delta) \right) \\ &\approx \int dr \left(b \tilde{A} \dot{\mathbf{m}}(r)^2 + b \tilde{\mathbf{D}} \cdot (\mathbf{m}(r) \times \dot{\mathbf{m}}(r)) + b \mathbf{m}(r)^\dagger \cdot \tilde{\mathbf{K}} \cdot \mathbf{m}(r) \right) = b \tilde{E} \end{aligned}$$

$$\text{where} \quad \tilde{A} = \frac{\Delta}{2b} \sum_{j>0} j^2 J_j, \quad \tilde{\mathbf{D}} = \frac{1}{b} \sum_{j>0} j \mathbf{D}_j, \quad \tilde{\mathbf{K}} = \frac{1}{b\Delta} \mathbf{K}. \quad (\text{F.1})$$

The first sum in (5.2) runs over all pairs (j, j') once. In (F.1) the summation over $j > 0$ avoids double counting.

F.2 Optimizing the magnetization numerically

This chapter introduces a procedure for the numerical solution of the discrete lattice model that is described in Chapter 5.2.1 and is characterized by

$$\begin{aligned} E &= \sum_{j < j'} \left(J_{|j'-j|} (1 - \mathbf{S}_j \cdot \mathbf{S}_{j'}) + \mathbf{D}_{j'-j} \cdot (\mathbf{S}_j \times \mathbf{S}_{j'}) \right) \\ &\quad + \sum_j \left(K_x (\mathbf{e}_x \cdot \mathbf{S}_j)^2 + K_y (\mathbf{e}_y \cdot \mathbf{S}_j)^2 + K_z (\mathbf{e}_z \cdot \mathbf{S}_j)^2 \right). \end{aligned} \quad (\text{5.2, Page 41})$$

It is straightforward to solve this model in the case $\mathbf{D} = 0$, but if the DM interaction is relevant the magnetization of one atomic row j may take any direction in spin-space and cannot be parameterized by a single angle.

In Chapter F.2.3 it is shown how the numerical procedure can be extended in order to include magnetostatic dipolar interactions in magnetic films.

This procedure can also be used to solve the micromagnetic equations, if the lattice spacing is small with respect to the change of magnetization. In this case it is certainly possible to limit the row interactions to nearest neighbors.

F.2.1 Outline

In Formula (5.2) each lattice point j corresponds to one atomic row and its magnetization \mathbf{S}_j can be described with two polar angles. The numerical calculations are restricted to a finite lattice (and a finite range of pair-interactions $J_{j'-j}, \mathbf{D}_{j'-j}$ between the atomic rows). The numerical procedure allows to vary the N spin orientations $\{\mathbf{S}_j\}_{1 \leq j \leq N}$ while for $j \notin [1, N]$ the orientation \mathbf{S}_j is replaced with its boundary value at $j \rightarrow \pm\infty$.

The energy E is minimized by an iterative process: In each iteration each spin is rotated into the orientation that minimizes E for the current configuration of the other spins. After all spins have been modified once the next iteration starts. The process stops when each spin is virtually in an optimal orientation for the current configuration of the other spins, here “virtually” means that the angle needed to rotate to the optimum is smaller than the desired accuracy. It turned out to be useful in most cases to update the spin orientations not simultaneously at the end of the iteration. Instead, the spins are rotated in the succession of the atomic rows and each lattice point is updated before the optimal orientation of the one is calculated.

It is obvious that a local minimum is reached when the process converges. But, one has to check whether the resulting spin configuration depends on the starting configuration.

For the investigation of common domain walls the number of lattice points (in the calculation) does not need to match the number of atomic rows. The discrete lattice structure is important only for narrow walls where the magnetization converges reasonably fast towards its bulk orientation. Broader walls can be described with a continuum model. In this case, the lattice points can be regarded just as numerical grid points. The model parameters $J, \mathbf{D}, \mathbf{K}$ can be rescaled in such a way that the wall fits on the available number of lattice points.

F.2.2 Optimizing the spin orientation at one lattice point

During the iteration process the spin orientation \mathbf{S}_n at the lattice point n has to be chosen such that the energy E is minimized for a fixed set $\{\mathbf{S}_j\}_{j \neq n}$. According to Formula (5.2) the energy contribution that depends on \mathbf{S}_n can be written as

$$\begin{aligned} E_n &= \sum_{j \neq n} \left(J_j \mathbf{S}_n \cdot \mathbf{S}_j + \mathbf{D}_j \cdot (\mathbf{S}_n \times \mathbf{S}_j) \right) + K_x (\mathbf{e}_x \cdot \mathbf{S}_n)^2 + K_y (\mathbf{e}_y \cdot \mathbf{S}_n)^2 + K_z (\mathbf{e}_z \cdot \mathbf{S}_n)^2 \\ &= c_x x_n + c_y y_n + c_z z_n + k_x x_n^2 + k_y y_n^2 + \text{const} \quad , \end{aligned}$$

$$\mathbf{S}_j = x_j \mathbf{e}_x + y_j \mathbf{e}_y + z_j \mathbf{e}_z \quad ,$$

$$c_x = \sum_{j \neq n} \left(J_j x_j + \mathbf{D}_j \cdot (y_j \mathbf{e}_z - z_j \mathbf{e}_y) \right) \quad (c_y, c_z \text{ are calculated analogously}) \quad ,$$

$$k_x = K_x - K_z \quad , \quad k_y = K_y - K_z \quad .$$

The relation $z_n^2 = 1 - x_n^2 - y_n^2$ has been used to eliminate the third anisotropy constant.

In the following the index n is dropped from x, y, z, E , i.e. $E = c_x x + c_y y + c_z z + k_x x^2 + k_y y^2 + \text{const}$.

With an appropriate choice of the coordinate system $k_x, k_y \geq 0$ and $c_x, c_y, c_z \leq 0$. In this case E surely is minimal for $x, y, z \geq 0$. The system has 2 degrees of freedom. The energy E can be parameterized by x, y with $0 \leq x, 0 \leq y, x^2 + y^2 < 1$ and $z = \sqrt{1 - x^2 - y^2}$. The reason to work with the parameters x, y and the additional condition $x^2 + y^2 < 1$ instead of the polar angles is, that the numerical procedure gets particularly simple in this

approach (see below). A necessary condition for a local minimum is that the derivatives with respect to x, y vanish:

$$\begin{aligned} \frac{d}{dx}E(x, y) &= c_x + c_z \frac{dz}{dx} + 2k_x x = c_x - c_z \frac{x}{z} + 2k_x x \quad , \\ \frac{d}{dx}E(x, y) = 0 &\Rightarrow x = \frac{c_x z}{c_z - 2k_x z} \quad , \quad \frac{d}{dy}E(x, y) = 0 \Rightarrow y = \frac{c_y z}{c_z - 2k_y z} \quad . \end{aligned}$$

For $k_x, k_y \geq 0$ and $c_z, c_y, c_x < 0$ the last expressions for x, y are zero for $z=0$ and increase monotonic with increasing z . Therefore the vector-length $(x^2 + y^2 + z^2)$ also increases monotonic with increasing z and coincides with 1 exactly once for $0 < z \leq 1$. Thus, it is straightforward numerical iteration to solve the conditions

$$\frac{d}{dx}E(x, y) = 0 \quad , \quad \frac{d}{dy}E(x, y) = 0 \quad , \quad x^2 + y^2 + z^2 = 1 \quad .$$

Since the energy can be parameterized as $E(x, y)$ only for $z > 0$ it is necessary to check the limiting case separately. But for $c_z < 0$ there exists no local minimum at $z = 0$ since $\frac{d}{dz}E(x, z) = -(c_y y^{-1} + 2k_y)z + c_z \xrightarrow{z \searrow 0} c_z$.

The case $c_z = 0$ has to be analyzed separately. In this case E does not depend on z . The minimal E under the constraint $x^2 + y^2 = 1$ can be determined with a procedure analogous to the one described above. This value has to be compared with the local extremum of E at $(x = \frac{-c_x}{2k_x}, y = \frac{-c_y}{2k_y})$. Furthermore, it has to be checked whether the local extremum is in the area $x^2 + y^2 \leq 1$.

F.2.3 Including the dipolar interactions

In an ultrathin film the magnetostatic (dipolar) energy can be calculated easily by summing over the dipoles as the interactions decay reasonably fast (cf. Chapter 4.2). In the system studied in Chapter 6 every atom lies on a mirror plane parallel to the \mathbf{q} -vector. Using this symmetry it is straightforward to include the magnetostatic energy in the formalism shown above.

In the next expressions the index j denotes the atomic rows and i, i' denotes the atoms within one row. The magnetic dipole moment of atom i in row j is

$$\mathbf{M}_{j,i} = M_i \mathbf{S}_j = M_i (x_j \mathbf{e}_x + y_j \mathbf{e}_y + z_j \mathbf{e}_z) \quad .$$

With the well-known formula for the dipolar energy the energy resulting from all interactions between row n and all other rows can be written in a form that is suitable for the procedure described in the previous chapter:

$$\begin{aligned} E_n^{(\text{dip})} &= \sum_{\substack{(j,i) \neq (n,i') \\ j,i,i'}} \frac{(\mathbf{M}_{j,i} \cdot \mathbf{M}_{n,i'}) (\mathbf{r}_{j,i} - \mathbf{r}_{n,i'})^2 - 3 ((\mathbf{r}_{j,i} - \mathbf{r}_{n,i'}) \cdot \mathbf{M}_{j,i}) ((\mathbf{r}_{j,i} - \mathbf{r}_{n,i'}) \cdot \mathbf{M}_{n,i'})}{|\mathbf{r}_{j,i} - \mathbf{r}_{n,i'}|^5} \\ &= c_x^{(\text{dip})} x_n + c_y^{(\text{dip})} y_n + c_z^{(\text{dip})} z_n + k_x^{(\text{dip})} x_n^2 + k_y^{(\text{dip})} y_n^2 + \text{const} \quad , \end{aligned}$$

$$c_x^{(\text{dip})} = \sum_j^{j \neq n} \left(x_j \sum_{i,i'} \frac{M_i M_{i'}}{|\mathbf{r}_{j,i} - \mathbf{r}_{n,i'}|^3} + \sum_{s \in \{x,y,z\}} s_j \sum_{i,i'} \frac{-3 M_i M_{i'} (\mathbf{r}_{j,i} \cdot \mathbf{e}_s - \mathbf{r}_{n,i'} \cdot \mathbf{e}_s) (\mathbf{r}_{j,i} \cdot \mathbf{e}_x - \mathbf{r}_{n,i'} \cdot \mathbf{e}_x)}{|\mathbf{r}_{j,i} - \mathbf{r}_{n,i'}|^5} \right),$$

$$k_x^{(\text{dip})} = \sum_{i,i'}^{i \neq i'} \frac{-3 M_i M_{i'} ((\mathbf{r}_{n,i} \cdot \mathbf{e}_x - \mathbf{r}_{n,i'} \cdot \mathbf{e}_x)^2 - (\mathbf{r}_{n,i} \cdot \mathbf{e}_z - \mathbf{r}_{n,i'} \cdot \mathbf{e}_z)^2)}{|\mathbf{r}_{j,i} - \mathbf{r}_{n,i'}|^5}$$

($c_y^{(\text{dip})}$, $c_z^{(\text{dip})}$, $k_y^{(\text{dip})}$ are calculated analogously).

The coefficient of each mixed product $x_n y_n$, $y_n z_n$, $z_n x_n$ is zero. With an appropriate choice of the coordinate system two coefficients are zero as one real-space coordinate is constant within one atomic row, for the third coefficient the mirror symmetry is important. This symmetry can be exploited further when evaluating the sum $\sum_{s \in \{x,y,z\}} (\dots)$. In systems without this mirror plane the algorithm of Chapter F.2.2 needs to be extended.

As one is interested in the (finite) energy per two-dimensional unit cell the sum over i' runs over the atoms in one unit cell whereas the sum over i runs over the entire atomic row (i.e. up to a numerical cutoff).

$c_x^{(\text{dip})}$ has to be calculated for each lattice point and each iteration. But the sums over (i, i') have to be calculated only once (for each distance $|j-n|$). In each iteration the calculation of $c_x^{(\text{dip})}$ is done by a single sum over the atomic rows (and x, y, z). One should note that the magnetostatic interactions require a significantly larger cutoff (for the number of rows) than the effective exchange interactions.

F.3 Period length of the rotating ground state

This chapter describes a simple procedure to determine the period length of the periodic solutions of Eqn. (5.10). With the period length R the energy per period has the form

$$E_R = \int_{-R/2}^{+R/2} dr (A \dot{\varphi}^2 + K \sin^2 \varphi + D \dot{\varphi}).$$

In the following it is assumed that $D < 0$, this implies that $\dot{\varphi}$ is positive throughout the entire rotation path. This allows to work with $r(\varphi)$ instead of $\varphi(r)$, which will help to simplify the expressions considerably. Further simplifications are obtained by rescaling the parameters:

$$\mathcal{E} = \sqrt{\frac{1}{AK}} E_R \quad , \quad \mathcal{R} = \sqrt{\frac{K}{A}} R \quad , \quad \mathcal{D} = \pi \sqrt{\frac{1}{AK}} D < -4 \quad .$$

$\mathcal{D} < -4$ follows from the condition $D < -\frac{4}{\pi} \sqrt{AK}$ (5.11) for the existence of a periodic ground state. Now the energy per period has the form

$$\begin{aligned} \mathcal{E} &= \int_{-\mathcal{R}/2}^{+\mathcal{R}/2} dr (\dot{\varphi}^2 + \sin^2 \varphi + \frac{1}{\pi} \mathcal{D} \dot{\varphi}) = \int_0^{2\pi} d\varphi (r'^{-1} + r' \sin^2 \varphi + \frac{1}{\pi} \mathcal{D}) \\ &= \int_0^{2\pi} d\varphi (r'^{-1} + r' \sin^2 \varphi) + 2\mathcal{D} \quad \text{with} \quad r' = \frac{d}{d\varphi} r \quad . \end{aligned}$$

The last integral must be minimal if \mathcal{R} is fixed to its optimal value. This leads to the Euler-Lagrange equation

$$\frac{d}{d\varphi} (-r'^{-2} + \sin^2 \varphi) \stackrel{!}{=} 0 \quad \Rightarrow \quad -r'^{-2} + \sin^2 \varphi = -c \quad \Rightarrow \quad r' = (\sin^2 \varphi + c)^{-\frac{1}{2}} .$$

Negative values of c can be ruled out since the Euler-Lagrange equation must be valid for all φ . Unlike in Chapter 5.2.3 the constant c cannot be set to zero since the boundary conditions for $r \rightarrow \pm\infty$ cannot be applied for periodic solutions. Instead one has the condition $r|_{\varphi=0} + \mathcal{R} = r|_{\varphi=2\pi}$. Therefore the period length can be parameterized by c by using $r' = (\sin^2 \varphi + c)^{-1/2}$:

$$\mathcal{R}(c) = \int_0^{2\pi} d\varphi (\sin^2 \varphi + c)^{-\frac{1}{2}} .$$

The energy functional can be parameterized by c as well if the last expression for r' is inserted:

$$\mathcal{E}(c) = \int_0^{2\pi} d\varphi \left((\sin^2 \varphi + c)^{+1/2} + \sin^2 \varphi (\sin^2 \varphi + c)^{-1/2} \right) + 2\mathcal{D} .$$

Now c can be determined from the condition that the (average) energy per length $\mathcal{F} = \mathcal{E}/\mathcal{R}$ has to be minimal in the ground state.

$$\frac{d\mathcal{F}(c)}{dc} = \frac{d}{dc} \frac{\mathcal{E}(c)}{\mathcal{R}(c)} \stackrel{!}{=} 0 \quad \Rightarrow \quad \mathcal{R}(c) \frac{d\mathcal{E}(c)}{dc} - \mathcal{E}(c) \frac{d\mathcal{R}(c)}{dc} = 0 .$$

The last derivatives can be evaluated

$$\begin{aligned} \frac{d\mathcal{E}(c)}{dc} &= \frac{1}{2} \int_0^{2\pi} d\varphi \left((\sin^2 \varphi + c)^{-\frac{1}{2}} - \sin^2 \varphi (\sin^2 \varphi + c)^{-\frac{3}{2}} \right) = \frac{c}{2} \int_0^{2\pi} d\varphi (\sin^2 \varphi + c)^{-\frac{3}{2}} , \\ \frac{d\mathcal{R}(c)}{dc} &= -\frac{1}{2} \int_0^{2\pi} d\varphi (\sin^2 \varphi + c)^{-\frac{3}{2}} = -\frac{1}{c} \frac{d\mathcal{E}(c)}{dc} . \end{aligned}$$

Therefore one gets

$$\begin{aligned} \mathcal{R}(c) \frac{d\mathcal{E}(c)}{dc} - \mathcal{E}(c) \frac{d\mathcal{R}(c)}{dc} &= 0 \quad \Rightarrow \\ \mathcal{E}(c) + c\mathcal{R}(c) &= \int_0^{2\pi} d\varphi \left((\sin^2 \varphi + c)^{+\frac{1}{2}} + (\sin^2 \varphi + c) (\sin^2 \varphi + c)^{-\frac{1}{2}} \right) + 2\mathcal{D} = 0 \quad \Rightarrow \\ \mathcal{D}(c) &= -\int_0^{2\pi} d\varphi (\sin^2 \varphi + c)^{+\frac{1}{2}} . \end{aligned}$$

Thus \mathcal{R} and \mathcal{D} are both expressed as monotonic functions of c . The range of c is known as $(0, \infty)$. This reduces the problem of obtaining $\mathcal{R}(\mathcal{D})$ (Fig. 5.7) to the problem of accurate numerical evaluation of the integrals. In practice this is not a difficult task since these integrals are supported by most mathematical software. In the form

$$\int_0^{2\pi} d\varphi (\sin^2 \varphi + c)^{\pm\frac{1}{2}} = 4 \int_0^{\pi/2} d\varphi (\cos^2 \varphi + c)^{\pm\frac{1}{2}} = 4(c+1)^{\pm\frac{1}{2}} \int_0^{\pi/2} d\varphi \left(1 - \sqrt{\frac{1}{c+1}} \sin^2 \varphi \right)^{\pm\frac{1}{2}}$$

they are known as the *complete elliptic integrals*

$$\mathbf{E}(\epsilon) = \int_0^{\pi/2} d\varphi (1 - \epsilon^2 \sin^2 \varphi)^{+\frac{1}{2}} \quad , \quad \mathbf{K}(\epsilon) = \int_0^{\pi/2} d\varphi (1 - \epsilon^2 \sin^2 \varphi)^{-\frac{1}{2}}$$

and \mathcal{D} , \mathcal{R} can be parameterized by

$$\mathcal{D}(\epsilon) = -\frac{4}{\epsilon} \mathbf{E}(\epsilon) \quad , \quad \mathcal{R}(\epsilon) = 4\epsilon \mathbf{K}(\epsilon) \quad , \quad \epsilon \in (0, 1) \quad .$$

F.4 Phase transitions of the micromagnetic ground state

F.4.1 Numerical procedure

The procedure that is explained in F.2 can be used to identify the phase transitions of the micromagnetic model that are described in Chapter 5.2.4. In order to obtain Fig. 5.8 the magnetization is optimized and the energy \mathcal{E} is calculated on a dense \mathcal{D} -grid for each \mathcal{K} -point. The critical points of the second-order transitions are detected by evaluating $\frac{d}{d\mathcal{D}} \mathcal{E}$ for fixed \mathcal{K} and identifying the kinks in these curves (cf. Fig. F.2). In the vicinity of the first-order phase transitions it depends on the starting configuration whether the procedure of Chapter F.2 converges towards the global or just a local energy minimum, but the transition point can be identified by comparing the energies.

It is not advisable to localize the phase transitions by calculating order parameters like $\int dr |z|$ instead of $\frac{d}{d\mathcal{D}} \mathcal{E}$, it requires very large numerical cutoffs to calculate these order parameters with sufficient accuracy.

The periodic states are calculated with periodic boundary conditions. The period length of the non-collinear states depends on \mathcal{K}, \mathcal{D} . Therefore, it is necessary to find the optimal period length for every fixed pair of \mathcal{K}, \mathcal{D} . In order to do this the energy is calculated in unit cells of different sizes and the optimal period length is determined in an iterative process. The size of the unit cell is varied by rescaling the parameters while the number of real-space lattice points is kept constant for better numerical stability.

F.4.2 Second-order transition from ferromagnetism to non-collinearity

For large $|D|$ the ground state of the quasi one-dimensional micromagnetic model undergoes a phase-transition from the ferromagnetic to a non-collinear configuration. If the \mathbf{D} -vector points parallel to the easy axis, this transition is second-order. An analytic expression for the corresponding critical point is deduced in this chapter.

In the vicinity of the critical point it is possible to describe the magnetization of the non-collinear state by its lowest order Taylor expansion around the ferromagnetic state. In this approximation it is straightforward to solve the Euler-Lagrange equations.

As in Chapter 5.2.4 the coordinate system is chosen such that

$$\mathbf{D} = D \mathbf{e}_z \quad , \quad K_x, K_y > K_z$$

and as independent parameters are used

$$\mathcal{K} = \frac{K_x - K_z}{K_y - K_z} \quad , \quad \mathcal{D} = \frac{-D}{\sqrt{A(K_y - K_z)}} \quad .$$

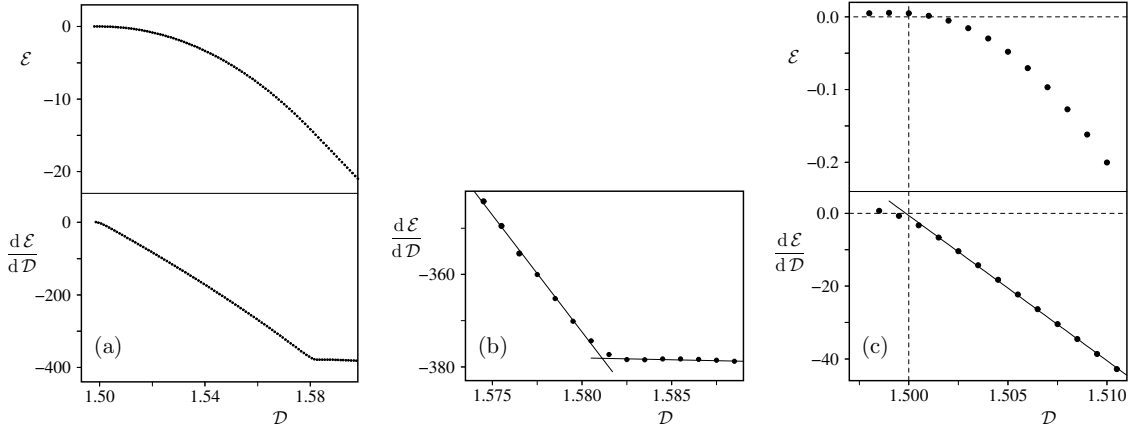


Figure F.2: Behavior of \mathcal{E} and $\frac{d}{d\mathcal{D}} \mathcal{E}$ when \mathcal{D} is varied at fixed \mathcal{K} . The zero point of the energy scale corresponds to collinear magnetization parallel to the easy axis. The critical points are defined by the kinks in the $(\frac{d\mathcal{E}}{d\mathcal{D}})$ -curve. The transition from the truly 3-dimensional to the flat rotating state can be localized easily (Fig. b). The transition from the collinear to the truly 3-dimensional state is less convenient from a numerical point of view: The period length of the non-collinear state depends on \mathcal{D} and needs to be optimized for each data point. In this thesis this is done with an algorithm that is unstable in the ferromagnetic regime (where the period length is arbitrary), therefore there are no data points calculated for small \mathcal{D} (Fig. a). But for every \mathcal{D} there is a collinear solution of the Euler-Lagrange equations with $\mathcal{E} = \frac{d\mathcal{E}}{d\mathcal{D}} = 0$ and Fig. c shows that \mathcal{E} and $\frac{d\mathcal{E}}{d\mathcal{D}}$ at the same point connect continuously to this solution.

This figure is obtained for $\mathcal{K} = 0.25$. In Chapter F.4.2 it is shown that the critical point for the transition from the collinear to the non-collinear state is at $\mathcal{D} = \sqrt{\mathcal{K}} + 1 = 1.5$.

The range of \mathcal{K} can be restricted to $\mathcal{K} \in (0, 1]$, (cf. Chapter 5.2.4). In Cartesian coordinates the energy functional (5.3) has the form

$$\mathcal{E} = \int dr (\dot{x}^2 + \dot{y}^2 + \dot{z}^2 - \mathcal{D}(x\dot{y} - y\dot{x}) + \mathcal{K}x^2 + y^2)$$

where the condition $x^2 + y^2 + z^2 = 1$ reduces the degrees of freedom.

For $\mathcal{K} > 0$ the \mathbf{D} -vector points parallel to the easy axis and in the ferromagnetic state there holds $x = y = 0$, $z = 1$. In the ferromagnetic limit x, y can be used as independent variables. With

$$z = \sqrt{1 - x^2 - y^2} \quad , \quad \dot{z} = \frac{-x\dot{x} - y\dot{y}}{\sqrt{1 - x^2 - y^2}}$$

the integrand of the energy functional can be written and expanded around $x = y = 0$ as

$$\begin{aligned} L(x, y, \dot{x}, \dot{y}) &= \dot{x}^2 + \dot{y}^2 + \frac{(x\dot{x} + y\dot{y})^2}{1 - x^2 - y^2} - \mathcal{D}(x\dot{y} - y\dot{x}) + \mathcal{K}x^2 + y^2 \\ &= \dot{x}^2 + \dot{y}^2 - \mathcal{D}(x\dot{y} - y\dot{x}) + \mathcal{K}x^2 + y^2 + \mathcal{O}\left((x + y + \dot{x} + \dot{y})^4\right) \end{aligned}$$

and the Euler-Lagrange equations become

$$\begin{aligned} \frac{1}{2} L_x &= -\mathcal{D}\dot{y} + \mathcal{K}x - \ddot{x} + \mathcal{O}\left((x + y + \dot{x} + \dot{y})^3\right) \stackrel{!}{=} 0 \quad , \\ \frac{1}{2} L_y &= +\mathcal{D}\dot{x} + y - \ddot{y} + \mathcal{O}\left((x + y + \dot{x} + \dot{y})^3\right) \stackrel{!}{=} 0 \quad . \end{aligned}$$

If the higher-order terms are neglected these equations have the general periodic solution

$$x = \alpha_x \cos(\omega r + p_x) \quad , \quad y = \alpha_y \cos(\omega r + p_y)$$

where the phases can be chosen such that

$$x = \alpha_x \cos(\omega r) \quad , \quad y = \alpha_y \sin(\omega r) \quad .$$

In order to determine $\alpha = \frac{\alpha_y}{\alpha_x}$ and ω these expressions can be inserted into the Euler-Lagrange equations

$$\left. \begin{aligned} \frac{1}{2} x^{-1} L_x = -\omega \alpha \mathcal{D} + \mathcal{K} + \omega^2 = 0 \\ \frac{1}{2} y^{-1} L_y = -\omega \alpha^{-1} \mathcal{D} + 1 + \omega^2 = 0 \end{aligned} \right\} \Rightarrow \begin{cases} \alpha = \frac{\omega^2 + \mathcal{K}}{\omega \mathcal{D}} \\ 2\omega^2 = \mathcal{D}^2 - \mathcal{K} - 1 \pm \sqrt{(\mathcal{D}^2 - \mathcal{K} - 1)^2 - 4\mathcal{K}} \end{cases} .$$

The next step is to find the area in the $(\mathcal{D}, \mathcal{K})$ -space where the last expression has a real solution for ω . This area is defined by the conditions that the radicand is positive and that $2\omega^2$ is positive. It is useful to split this analysis in the cases $\mathcal{D}^2 > \mathcal{K} + 1$ and $\mathcal{D}^2 < \mathcal{K} + 1$.

- case $\mathcal{D}^2 > \mathcal{K} + 1$:

At first the sign of the radicand is examined:

$$(\mathcal{D}^2 - \mathcal{K} - 1)^2 - 4\mathcal{K} > 0 \quad \Leftrightarrow \quad \mathcal{D}^2 > \mathcal{K} + 2\sqrt{\mathcal{K}} + 1 = (\sqrt{\mathcal{K}} + 1)^2 .$$

Under the assumption that the radicand is positive the last expression for $2\omega^2$ is positive as well, i.e.

$$\mathcal{D}^2 - \mathcal{K} - 1 \pm \sqrt{(\mathcal{D}^2 - \mathcal{K} - 1)^2 - 4\mathcal{K}} > 0$$

is fulfilled for all $\mathcal{K} > 0$, $\mathcal{D}^2 > \mathcal{K} + 1$.

- case $\mathcal{D}^2 < \mathcal{K} + 1$:

If the radicand is positive and $\mathcal{D}^2 < \mathcal{K} + 1$ then the condition

$$\mathcal{D}^2 - \mathcal{K} - 1 \pm \sqrt{(\mathcal{D}^2 - \mathcal{K} - 1)^2 - 4\mathcal{K}} > 0$$

cannot be fulfilled if “ \pm ” is replaced with “ $-$ ”, if “ \pm ” is replaced with “ $+$ ” then one gets

$$\mathcal{D}^2 - \mathcal{K} - 1 > -\sqrt{(\mathcal{D}^2 - \mathcal{K} - 1)^2 - 4\mathcal{K}} \quad \Leftrightarrow \quad (\mathcal{D}^2 - \mathcal{K} - 1)^2 < (\mathcal{D}^2 - \mathcal{K} - 1)^2 - 4\mathcal{K} .$$

The last equation cannot be fulfilled for $\mathcal{K} > 0$.

Thus it turns out that the lowest-order expansion of the Euler-Lagrange equations has a non-collinear solution in the case $\mathcal{K} > 0$ if and only if

$$|\mathcal{D}| > \mathcal{D}_c = \sqrt{\mathcal{K}} + 1 .$$

This inequality defines the critical point for the transition from the ferromagnetic to the non-collinear state, if the non-collinear state is lower in energy than the ferromagnetic state: If $|\mathcal{D}|$ is smaller than $\mathcal{D}_c = \sqrt{\mathcal{K}} + 1$ there cannot be any continuous transition into a non-collinear state, if $|\mathcal{D}|$ is just larger than \mathcal{D}_c the system can lower its energy by changing to the non-collinear solution. The lengthy analytical evaluation of the sign of $\mathcal{E} = \int dr L$ in the limit $|\mathcal{D}| \searrow \mathcal{D}_c$ is skipped since the numerical analysis shows that the non-collinear state lowers the energy. Of course one cannot completely rule out the possibility of a first-order phase transition at $|\mathcal{D}| \leq \mathcal{D}_c$ that would prevent the system from reaching the critical point, but this has not been observed in the numerical simulations.

F.5 DM interaction in the discrete model

- Hard axis parallel to \mathbf{D}

The coordinate system is chosen such that $\mathbf{D} = D \mathbf{e}_z$ and $K_x < K_y < K_z$. Then the magnetization stays in the (x, y) -plane. By dropping a constant term in the integrand the model ansatz (5.17) can be simplified to

$$\frac{1}{K}E = \sum_j \frac{J}{K} (1 - \cos(\varphi_{j+1} - \varphi_j)) + \frac{D}{K} \sin(\varphi_{j+1} - \varphi_j) + \sin^2 \varphi_j \quad (5.19, \text{Page 56})$$

where $K = K_y - K_x$.

For $\frac{D}{K} = 0$ the sharp domain wall that is discussed in Chapter 5.3.1 is always an extremal solution of (5.19), although it is a minimum only for $\frac{J}{K} < \frac{3}{2}$. But for $\frac{D}{K} \neq 0$ it is not an extremal solution, that can be seen from the derivative with respect to one angle φ_j :

$$\begin{aligned} \frac{\partial(\frac{1}{K}E)}{\partial \varphi_j} &= \frac{J}{K} \left(\sin(\varphi_j - \varphi_{j-1}) - \sin(\varphi_{j+1} - \varphi_j) \right) \\ &+ \frac{D}{K} \left(\cos(\varphi_j - \varphi_{j-1}) - \cos(\varphi_{j+1} - \varphi_j) \right) \\ &+ 2 \sin \varphi_j \cos \varphi_j, \end{aligned}$$

at the sharp wall there is $\sin(\varphi_j - \varphi_{j-1}) = \sin(\varphi_{j+1} - \varphi_j) = \sin \varphi_j \cos \varphi_j = 0$.

This suggests that the domain wall profile changes smoothly from a solution of left-handed to right-handed rotation when moving in the $(\frac{D}{K}, \frac{J}{K})$ -parameter space and crossing the $(\frac{D}{K}=0)$ -line at $\frac{J}{K} < \frac{3}{2}$. For $\frac{J}{K} > \frac{3}{2}$ one can assume a first-order transition since the walls of opposite rotational direction are degenerate at $\frac{D}{K} = 0$. These assumptions are confirmed by numerical simulation of the system described by (5.19) and plotting $\left. \frac{d(E/K)}{d(D/K)} \right|_{J/K=\text{const}}$ for several $\frac{J}{K}$: For $\frac{J}{K} < \frac{3}{2}$ these curves are smooth, for $\frac{J}{K} > \frac{3}{2}$ they show a discontinuity and for $\frac{J}{K} = \frac{3}{2}$ the curve shows the typical λ -point behavior at $\frac{D}{K} = 0$.

The coexistence curve for the ferromagnetic and the rotating ground state that is plotted in Fig. 5.15 is estimated by numerically determining the points in the $(\frac{D}{K}, \frac{J}{K})$ -space where the energy of the domain walls is zero.

- Easy axis parallel to \mathbf{D} , plane normal to hard axis isotropic

The coordinate system is chosen such that $\mathbf{D} = D \mathbf{e}_z$. Then the model ansatz (5.17) becomes

$$E = \sum_j \left(\begin{aligned} &J (1 - \sin \vartheta_j \sin \vartheta_{j+1} \cos(\varphi_{j+1} - \varphi_j) - \cos \vartheta_j \cos \vartheta_{j+1}) \\ &+ D (\sin \vartheta_j \sin \vartheta_{j+1} \sin(\varphi_{j+1} - \varphi_j)) \\ &+ ((K_x - K_z) \cos^2 \varphi_j + (K_y - K_z) \sin^2 \varphi_j) \sin^2 \vartheta_j + \text{const} \end{aligned} \right).$$

The model is examined only for the case $K = K_x - K_z = K_y - K_z$. By dropping the constant term the last equation simplifies to

$$\begin{aligned} \frac{1}{K}E &= \sum_j \left(\begin{aligned} &\frac{J}{K} (1 - \sin \vartheta_j \sin \vartheta_{j+1} \cos(\varphi_{j+1} - \varphi_j) - \cos \vartheta_j \cos \vartheta_{j+1}) \\ &+ \frac{D}{K} (\sin \vartheta_j \sin \vartheta_{j+1} \sin(\varphi_{j+1} - \varphi_j)) \\ &+ \sin^2 \vartheta_j \end{aligned} \right). \end{aligned} \quad (5.20, \text{Page 57})$$

In analogy to the continuum case $(\varphi_{j+1} - \varphi_j)$ remains constant for all j if $\frac{1}{K}E$ is minimal:

$$\frac{\partial(\frac{1}{K}E)}{\partial(\varphi_{j+1} - \varphi_j)} = \sin \vartheta_j \sin \vartheta_{j+1} \left(\frac{J}{K} \sin(\varphi_{j+1} - \varphi_j) + \frac{D}{K} \cos(\varphi_{j+1} - \varphi_j) \right) \stackrel{!}{=} 0 \quad \Rightarrow$$

$$\tan(\varphi_{j+1} - \varphi_j) = -\frac{D}{J} = \text{const} \quad (\text{if } \sin \vartheta_{j'} = 0 \text{ then } \varphi_{j'} \text{ may take arbitrary value}).$$

From Eqn. (5.20) it is obvious which branch of $\arctan(-\frac{D}{J})$ defines $(\varphi_{j+1} - \varphi_j)$: At minimal $\frac{1}{K}E$ there holds

$$\left. \begin{aligned} \text{sign } \cos(\varphi_{j+1} - \varphi_j) &= \text{sign } J \quad , \quad \text{sign } \sin(\varphi_{j+1} - \varphi_j) = -\text{sign } D \\ \tan(\varphi_{j+1} - \varphi_j) &= -\frac{D}{J} \end{aligned} \right\} \Rightarrow$$

$$\cos(\varphi_{j+1} - \varphi_j) = \frac{J}{\sqrt{J^2 + D^2}} \quad , \quad \sin(\varphi_{j+1} - \varphi_j) = \frac{-D}{\sqrt{J^2 + D^2}} .$$

Inserting the last expressions in Eqn. (5.20) yields

$$\frac{1}{K}E = \sum_j \left(\frac{J}{K} (1 - \cos \vartheta_j \cos \vartheta_{j+1}) - \sqrt{\left(\frac{J}{K}\right)^2 + \left(\frac{D}{K}\right)^2} \sin \vartheta_j \sin \vartheta_{j+1} + \sin^2 \vartheta_j \right), \quad (\text{F.2})$$

$$\frac{\partial(\frac{1}{K}E)}{\partial \vartheta_j} = \frac{J}{K} \sin \vartheta_j (\cos \vartheta_{j-1} + \cos \vartheta_{j+1}) - \sqrt{\left(\frac{J}{K}\right)^2 + \left(\frac{D}{K}\right)^2} \cos \vartheta_j (\sin \vartheta_{j-1} + \sin \vartheta_{j+1})$$

$$+ 2 \sin \vartheta_j \cos \vartheta_j .$$

The last expression is zero for all j if $\sin \vartheta_j = 0$ or $\cos \vartheta_j = 0$ for all j . The first case corresponds to a collinear state oriented along the easy axis, the second case to a spin spiral (rotating around the angle φ). The numerical analysis of Eqn. (5.20) does not show any further possible ground state. The next step is to compare the cases $\sin \vartheta_j = 0$ and $\cos \vartheta_j = 0$ in order to identify the ground state of (5.20) depending on $\frac{J}{K}, \frac{D}{K}$.

For $\sin \vartheta_j = 0$ Expression (F.2) simplifies to

$$\frac{1}{K}E_{\text{col}} = \sum_j \frac{J}{K} (1 - \cos \vartheta_j \cos \vartheta_{j+1}) .$$

For $\frac{J}{K} > 0$ the possible ground state is the ferromagnetic and for $\frac{J}{K} < 0$ the antiferromagnetic state oriented along the easy axis. For the ferromagnetic state $\frac{1}{K}E_{\text{col}} = 0$, for the antiferromagnetic state $\frac{1}{K}E_{\text{col}} = \sum_j 2 \frac{J}{K}$.

For $\cos \vartheta_j = 0$ Expression (F.2) simplifies to

$$\frac{1}{K}E_{\text{ss}} = \sum_j \left(\frac{J}{K} - \sqrt{\left(\frac{J}{K}\right)^2 + \left(\frac{D}{K}\right)^2} + 1 \right) .$$

This expression describes the energy of a spin spiral that is circling in the plane normal to the easy axis. It is the ground state if the energy-loss due to the DM interaction can compete with the exchange and anisotropy energy, i.e. if

$$J > 0 : \quad \frac{J}{K} - \sqrt{\left(\frac{J}{K}\right)^2 + \left(\frac{D}{K}\right)^2} + 1 < 0 \quad \Rightarrow \quad \frac{J}{K} < +\frac{1}{2} \left(\left(\frac{D}{K}\right)^2 - 1 \right) ,$$

$$J < 0 : \quad \frac{J}{K} - \sqrt{\left(\frac{J}{K}\right)^2 + \left(\frac{D}{K}\right)^2} + 1 < 2 \frac{J}{K} \quad \Rightarrow \quad \frac{J}{K} > -\frac{1}{2} \left(\left(\frac{D}{K}\right)^2 - 1 \right) .$$

In the micromagnetic limit this condition reduces to the one that is discussed in Chapter 5.2.4 (cf. Appendix F.1 for the definition of \tilde{A} , \tilde{K}):

$$\begin{aligned} \frac{J}{K} < +\frac{1}{2} \left(\left(\frac{D}{K} \right)^2 - 1 \right) &\Rightarrow \\ |D| = |\tilde{D}| > 2\sqrt{\frac{1}{2}JK + K} = 2\sqrt{\tilde{A}\tilde{K} + \tilde{K}\Delta} \xrightarrow{\Delta \rightarrow 0} 2\sqrt{\tilde{A}\tilde{K}} . \end{aligned}$$

For $\frac{J}{K} > 0$ the ground state can be ferromagnetic. In this case the domain wall configurations are considered. They show a second-order phase transition that is absent in the continuum model and has been discussed already for the case $D=0$.

The size of the Hessian matrix can be reduced by exploiting the real-space symmetry $\vartheta(r) = \pi - \vartheta(-r)$. There is no lattice point at $(r=0, \vartheta=\frac{\pi}{2})$ but there is one at $\pm\frac{1}{2}\Delta$ (Δ denotes the lattice spacing) since the anisotropy energy is maximal at $\frac{\pi}{2}$. Therefore the Expression (F.2) can be written as

$$\begin{aligned} \frac{1}{K} E = & \frac{J}{K} (1 - \cos \vartheta_1 \cos(\pi - \vartheta_1)) - \sqrt{\left(\frac{J}{K}\right)^2 + \left(\frac{D}{K}\right)^2} \sin \vartheta_1 \sin(\pi - \vartheta_1) \\ & + 2 \sum_{j>0} \left(\frac{J}{K} (1 - \cos \vartheta_j \cos \vartheta_{j+1}) - \sqrt{\left(\frac{J}{K}\right)^2 + \left(\frac{D}{K}\right)^2} \sin \vartheta_j \sin \vartheta_{j+1} + \sin^2 \vartheta_j \right) . \end{aligned}$$

For a finite system with N independent spin orientations ϑ_j (and the boundary condition $\vartheta_{N+1} = \pi$) the Hessian matrix becomes

$$\left(\frac{\partial^2 (E/K)}{\partial \vartheta_j \partial \vartheta_{j'}} \Big|_{\substack{\vartheta_n = \pi \\ n=1 \dots N+1}} \right)_{j,j'} = \begin{pmatrix} b+4 & b & & & 0 \\ b & a & b & & \\ & b & \ddots & \ddots & \\ & & \ddots & \ddots & b \\ 0 & & & b & a \end{pmatrix}$$

$$\text{where } a = 4\frac{J}{K} + 4 \quad , \quad b = -2\sqrt{\left(\frac{J}{K}\right)^2 + \left(\frac{D}{K}\right)^2} .$$

The conditions for this matrix being positive definite is analyzed numerically with the method described in Chapter 5.3.1. The results converge quickly with the number of lattice sites N . Thus, the numerical results represent the thermodynamic limit to high accuracy.

The locations of the different ground states and domain walls in the $(\frac{J}{K}, \frac{D}{K})$ -parameter-space are plotted in Fig. 5.16.

Appendix G

Calculation of the ML exchange parameters

In this appendix the magnitude of the parameters of the expansion (6.3) is estimated. The calculations are restricted to 1 ML Fe coverage and \mathbf{q} pointing in [001]-direction. It is assumed that all magnetic moments stay within one plane. Spin-orbit coupling is neglected.

G.1 Heisenberg exchange integrals

The leading terms in the expansion (6.3) are the pair interactions of the form $(X_{j,j'}^{(1)} + X_{j',j}^{(1)})(1 - \mathbf{S}_j \cdot \mathbf{S}_{j'}) = J_{|j-j'|}(1 - \mathbf{S}_j \cdot \mathbf{S}_{j'})$. If these pair interactions are sufficient to approximate the energy, i.e. if the system can be described with the Heisenberg model

$$E^{(\text{xc})} = \sum_{j=j'+1}^{j'+N} J_{j-j'} (1 - \mathbf{S}_j \cdot \mathbf{S}_{j'}) . \quad (6.4, \text{Page } 66)$$

then there is a simple way to estimate the exchange integrals J_j and the cutoff N .

With Δ denoting the distance between two neighboring rows (i.e. $\Delta = \frac{1}{2}a$ if $\mathbf{q} \parallel [001]$) the exchange energy of a homogeneous flat spin spiral can be written as (cf. e.g. [103])

$$\begin{aligned} \mathbf{S}_{j'+j} \cdot \mathbf{S}_{j'} = \cos(qj\Delta) &\stackrel{(6.4)}{\Rightarrow} E^{(\text{ss})}(q) = \sum_{j>0} J_j (1 - \cos(qj\Delta)) \\ \Rightarrow J_j &= -\frac{\Delta}{\pi} \int_0^{2\pi/\Delta} dq E^{(\text{ss})}(q) \cos(qj\Delta) . \quad (\text{G.1}) \end{aligned}$$

Thus, the exchange integrals can be calculated as the Fourier coefficients of $E^{(\text{ss})}(q)$. The number of relevant parameters $\{J_j\}_j$ (and thus the required density of the q -grid) can be estimated from the convergence of J_N with respect to N . One should note that the long-range pair interactions can be neglected if the sum $\sum_{j=N}^{\infty} J_j (1 - \mathbf{S}_j \cdot \mathbf{S}_0)$ converges fast, this is certainly the case if the sequence J_j converges in $\mathcal{O}(\frac{1}{j^2})$.

The Ansatz (F.1) requires the convergence of the sum $\sum_j^N j^2 J_j$ with respect to N . This more stringent condition is introduced by the 2nd-order Taylor approximation: In Chapter F.1 it is assumed that J_j decays on the length scale where $\mathbf{S}_j = \mathbf{m}(r_0 + j\Delta)$ can be approximated by $\mathbf{m}(r_0) + j\Delta \dot{\mathbf{m}}(r_0) + \frac{1}{2}(j\Delta)^2 \ddot{\mathbf{m}}(r_0)$. In this regime the energy contributions of the exchange terms are proportional to $j^2 \Delta J_j$ and $1 - \mathbf{S}_j \cdot \mathbf{S}_0$ is very small for small j . Thus, if the magnetization rotates on large length scales then the

exchange integrals between distant atomic rows are more important than they are if the magnetization rotates rapidly. It is not recommended to calculate the spin stiffness A with the approach presented here and Eqn. (F.1); the aim of this appendix is to determine parameters for a model that can be applied in the regime of rapidly rotating magnetization where the micromagnetic model is questionable and the interactions between nearby rows are dominant.

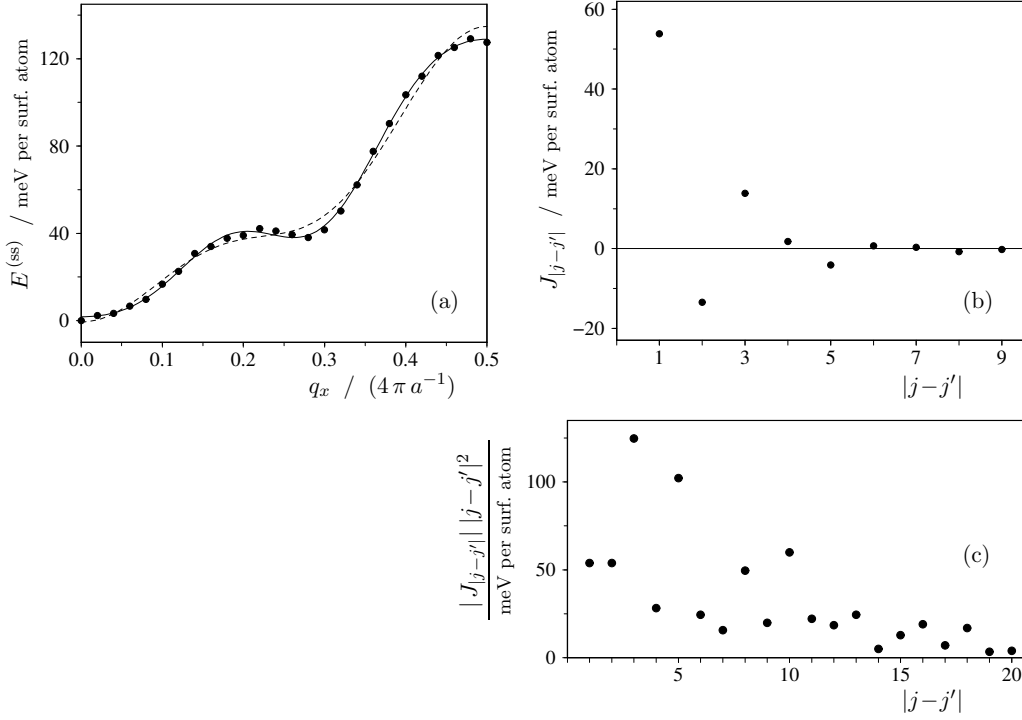


Figure G.1: Spin-spiral energies and Heisenberg exchange integrals for 1 ML Fe and $\mathbf{q}||[001]$. The data points (\bullet) in Fig. a represent the results of selfconsistent calculations of flat spin spirals. Fig. b shows the exchange integrals that are obtained from the spin-spiral energies by the Fourier transform (G.1). The dashed and solid line in Fig. a represent the approximation (6.4) for $N=3$ and $N=5$ respectively. Fig. c illustrates the convergence of (6.4): The exchange integrals J_j converge in $\mathcal{O}(j^{-2})$, hence the sum $\sum_j J_j f_j$ converges for $\{|f_j| \leq 2\}_j$. Note that the data in Fig. c reaches the numerical accuracy, therefore no points are shown for $|j-j'| > 20$.

The results of the Fourier transform (G.1) are shown in Fig. G.1. It has already been mentioned, that the above approach implies the applicability of the Heisenberg model (6.4). It is not possible to justify the ansatz (6.4) just from the spin-spiral calculations that are presented in Fig. G.1.a.

G.2 Higher-order terms

In this chapter the applicability of the Heisenberg model (6.4) and the importance of higher-order exchange parameters is investigated. This is done by comparing the energies of several magnetic configurations that are degenerate within (6.4).

G.2.1 Setup

In the following the energies of different magnetic configurations are presented. The energies are obtained from selfconsistent calculations with constrained magnetic moments

(cf. Chapter 3.7.2). The magnetic moments are rotated along special pathes that keep the energy contributions of certain low-order terms constant. This allows to break down the total energy into the contributions of the various parameters of (6.3).

Due to the structure of the (110)-surface the unit cell has to contain an even number of atomic rows. An unit cell with just 2 rows does not have enough degrees of freedom. Thus, most calculations are performed in a 4-row unit-cell (cf. Fig. G.2). It is possible to describe the magnetic consiguration with 3 angles ($\varphi_1, \varphi_2, \varphi_3$), since the magnetization direction is kept within one plane. The angles are defined according to Fig. G.2.

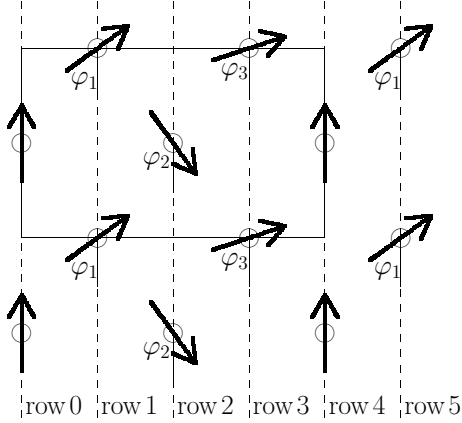


Figure G.2: Setup for the calculation of higher-order interactions.

The magnetic moments stay in one plane and do not turn along the rows in $[1\bar{1}0]$ -direction $\perp \mathbf{q}$. The solid lines denote the surface unit-cell, the angles are given with respect to the spin orientation in row 0.

Obviously, this setup allows neither to separate the interactions of 1st-, 3rd- and other $(2j+1)$ th-nearest neighbors nor to separate the interactions of 2nd-, 4th- and other $(2j)$ th-nearest neighbors.

Calculations with a 4-row unit-cell (with periodic boundary conditions) do not allow to separate all parameters of (6.3). Therefore, a reduced set of parameters is introduced that is sufficient to describe the energy in this unit cell:

$$\begin{aligned}
E_{4\text{at}}^{(\text{xc})} = & - Y_1^{(1)} \left((\mathbf{S}_0 \cdot \mathbf{S}_1) + (\mathbf{S}_1 \cdot \mathbf{S}_2) + (\mathbf{S}_2 \cdot \mathbf{S}_3) + (\mathbf{S}_3 \cdot \mathbf{S}_0) \right) \\
& - Y_2^{(1)} 2 \left((\mathbf{S}_0 \cdot \mathbf{S}_2) + (\mathbf{S}_1 \cdot \mathbf{S}_3) \right) \\
& - Y_1^{(2)} \left((\mathbf{S}_0 \cdot \mathbf{S}_1)^2 + (\mathbf{S}_1 \cdot \mathbf{S}_2)^2 + (\mathbf{S}_2 \cdot \mathbf{S}_3)^2 + (\mathbf{S}_3 \cdot \mathbf{S}_0)^2 \right) \\
& - Y_2^{(2)} 2 \left((\mathbf{S}_0 \cdot \mathbf{S}_2)^2 + (\mathbf{S}_1 \cdot \mathbf{S}_3)^2 \right) \\
& - Y_3^{(2)} \left((\mathbf{S}_0 \cdot \mathbf{S}_1) (\mathbf{S}_1 \cdot \mathbf{S}_2) + (\mathbf{S}_1 \cdot \mathbf{S}_2) (\mathbf{S}_2 \cdot \mathbf{S}_3) + (\mathbf{S}_2 \cdot \mathbf{S}_3) (\mathbf{S}_3 \cdot \mathbf{S}_0) + (\mathbf{S}_3 \cdot \mathbf{S}_0) (\mathbf{S}_0 \cdot \mathbf{S}_1) \right) \\
& - Y_4^{(2)} 2 \left((\mathbf{S}_0 \cdot \mathbf{S}_1) (\mathbf{S}_2 \cdot \mathbf{S}_3) + (\mathbf{S}_1 \cdot \mathbf{S}_2) (\mathbf{S}_3 \cdot \mathbf{S}_0) \right) \\
& - Y_5^{(2)} \frac{1}{2} \left((\mathbf{S}_0 \cdot \mathbf{S}_1) (\mathbf{S}_0 \cdot \mathbf{S}_2) + (\mathbf{S}_1 \cdot \mathbf{S}_2) (\mathbf{S}_1 \cdot \mathbf{S}_3) + (\mathbf{S}_2 \cdot \mathbf{S}_3) (\mathbf{S}_2 \cdot \mathbf{S}_0) + (\mathbf{S}_3 \cdot \mathbf{S}_0) (\mathbf{S}_3 \cdot \mathbf{S}_1) \right. \\
& \quad \left. + (\mathbf{S}_0 \cdot \mathbf{S}_1) (\mathbf{S}_3 \cdot \mathbf{S}_1) + (\mathbf{S}_1 \cdot \mathbf{S}_2) (\mathbf{S}_0 \cdot \mathbf{S}_2) + (\mathbf{S}_2 \cdot \mathbf{S}_3) (\mathbf{S}_1 \cdot \mathbf{S}_3) + (\mathbf{S}_3 \cdot \mathbf{S}_0) (\mathbf{S}_2 \cdot \mathbf{S}_0) \right) \\
& - Y_6^{(2)} 4 \left((\mathbf{S}_0 \cdot \mathbf{S}_2) (\mathbf{S}_1 \cdot \mathbf{S}_3) \right) \\
& - \mathcal{O}(Y^{(3)}) + \text{const} .
\end{aligned} \tag{G.2}$$

In the following the *order* of these terms denotes the number of factors $(\mathbf{S}_j \cdot \mathbf{S}_{j'})$, i.e. the coefficients of the n th-order terms are the parameters $\{Y_i^{(n)}\}_i$.

$\mathcal{O}(Y^{(n)})$ denotes terms of n th- and higher order.

Of course, the parameters of the 1st-order terms can be expressed with the Heisenberg exchange integrals:

$$Y_1^{(1)} = \sum_{j=1}^{\infty} J_{2j-1} \quad , \quad Y_2^{(1)} = \sum_{j=1}^{\infty} J_{4j-2} . \tag{G.3}$$

G.2.2 Three-row interactions

The ansatz (G.2) can be simplified considerably if one can restrict the relevant interactions to pair interactions $(Y_1^{(1)}, Y_2^{(1)}, Y_1^{(2)}, Y_2^{(2)}, Y_1^{(3)}, \dots)$. The importance of the other terms

(that depend on the magnetization direction of more than two atomic rows) is estimated by varying the magnetization along path 1 in the above described 4-row unit-cell. Path 1 can be parameterized by ϕ as shown in the following:

path 1 :

$$\left. \begin{array}{l} \varphi_1 = \phi \\ \varphi_2 = \pi \\ \varphi_3 = \phi + \frac{1}{2}\pi \end{array} \right\} \Rightarrow E_{4\text{at}}^{(\text{xc})} = (+Y_3^{(2)} - 2Y_4^{(2)} - Y_{4\text{row}}^{(3)}) \sin(2\phi) + \mathcal{O}(Y^{(4)}) + \text{const} ,$$

along $\phi \in \left[\frac{1}{4}\pi, \frac{3}{4}\pi \right]$ all configurations are different .

$Y_{4\text{row}}^{(3)}$ denotes a sum of exchange parameters, where the corresponding terms are of 3rd-order and depend on the magnetization direction of 4 different atomic rows.

In 4th-order there are several non-constant terms with diverse dependence on ϕ . The pair interactions have the form

$$(\mathbf{S}_0 \cdot \mathbf{S}_1)^4 + (\mathbf{S}_1 \cdot \mathbf{S}_2)^4 + (\mathbf{S}_2 \cdot \mathbf{S}_3)^4 + (\mathbf{S}_3 \cdot \mathbf{S}_0)^4 = \frac{1}{2} \cos(4\phi) + \text{const} \quad , \quad (\mathbf{S}_0 \cdot \mathbf{S}_2)^4 + (\mathbf{S}_1 \cdot \mathbf{S}_3)^4 = \text{const} .$$

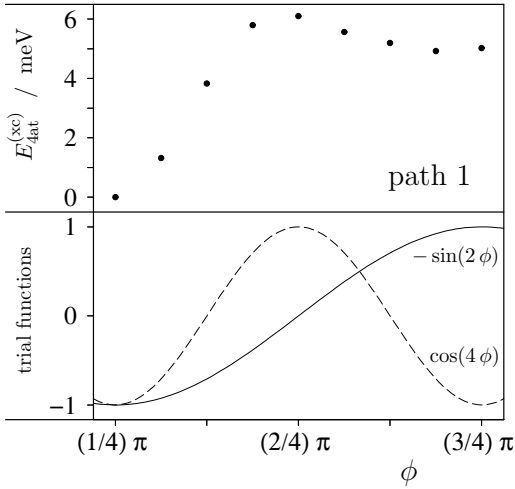


Figure G.3: Energy changes when the magnetic configuration changes along path 1. It is obvious that the data can be fitted neither with $\sin(2\phi)$ only nor with $\cos(4\phi)$ only.

Fig. G.3 presents $E_{4\text{at}}^{(\text{xc})}$ obtained from selfconsistent calculations of the magnetic configurations of path 1. The relevant energy scale of $(\frac{1}{4}6 = 1.5)$ meV per surface atom is small compared to the one shown in Figs. G.1.a, G.1.b. Thus, the three-row interactions that do not vanish in path 1 give only a minor contribution to the exchange energy.

The shape of the curve in Fig. G.3 cannot be explained with the 2nd-order terms ($\sim \sin(2\phi)$). If one wants to use the expansion (G.2) in order to describe the exchange energy on the scale relevant in Fig. G.3, then one has to take into account terms up to 4th- (or higher) order. Also, it is not sufficient to consider just the pair-interaction terms up to 4th-order ($\sim \cos(4\phi)$ along path 1).

G.2.3 Pair interactions

In the following it is assumed that the three-row interactions can be neglected in the expansions (6.3), (G.2). The influence of the higher-order pair-interactions beyond the Heisenberg exchange integrals is investigated.

With the restriction to pair interactions (6.3) simplifies to

$$E^{(\text{xc})} = \sum_{n>0} \sum_{j>j'} P_{|j-j'|}^{(n)} (1 - (\mathbf{S}_j \cdot \mathbf{S}_{j'})^n) \quad (\text{G.4})$$

$$\text{with } P_{|j-j'|}^{(1)} = J_{|j-j'|} = 2X_{j,j'}^{(1)} \quad , \quad P_{|j-j'|}^{(n)} = 2^n X_{j,j',j,j',\dots}^{(n)} \quad .$$

For $n > 1$ these terms are neglected in (G.1). The interpretation of the data shown in Fig. G.1 has to be altered if these terms are taken into account. For example, if one allows for $n > 1$ in (G.4) and neglects interactions beyond the next-nearest neighbors ($|j-j'| > 2 \Rightarrow P_{|j-j'|}^{(n)} = 0$) then the exchange energy of a homogeneous flat spin spiral can be written as

$$\begin{aligned} E^{(\text{ss})}(q) = & (P_1^{(1)} + \frac{3}{4}P_1^{(3)} + \dots) (1 - \cos(2\pi q \Delta)) \\ & + (P_2^{(1)} + \frac{1}{2}P_1^{(2)} + \frac{3}{4}P_2^{(3)} + \frac{1}{2}P_1^{(4)} + \dots) (1 - \cos(4\pi q \Delta)) \\ & + (\frac{1}{4}P_1^{(3)} + \dots) (1 - \cos(6\pi q \Delta)) \\ & + (\frac{1}{2}P_2^{(2)} + \frac{1}{8}P_1^{(4)} + \frac{1}{2}P_2^{(4)} + \dots) (1 - \cos(8\pi q \Delta)) \\ & + \dots \quad . \end{aligned}$$

The data points in Fig. G.1.b correspond to the coefficients of this expansion.

In the expansion (G.2) the leading pair-interaction terms next to the Heisenberg model are the biquadratic terms

$$-Y_1^{(2)} ((\mathbf{S}_0 \cdot \mathbf{S}_1)^2 + (\mathbf{S}_1 \cdot \mathbf{S}_2)^2 + (\mathbf{S}_2 \cdot \mathbf{S}_3)^2 + (\mathbf{S}_3 \cdot \mathbf{S}_0)^2) \quad , \quad -Y_2^{(2)} 2((\mathbf{S}_0 \cdot \mathbf{S}_2)^2 + (\mathbf{S}_1 \cdot \mathbf{S}_3)^2) \quad .$$

(If the interactions can be restricted to next-nearest neighbors then $Y_1^{(2)} = P_1^{(2)}$, $Y_2^{(2)} = P_2^{(2)}$.)

In the following it is shown that the biquadratic terms do not dominate the terms of 2nd- and higher order.

In order to estimate the magnitude of $Y_1^{(2)}$ the magnetic moments are rotated along path 2 in the 4-row unit-cell. Path 2 can be parameterized by ϕ as shown in the following:

path 2 :

$$\left. \begin{aligned} \varphi_1 &= \phi \\ \varphi_2 &= \pi \\ \varphi_3 &= \phi \end{aligned} \right\} \Rightarrow E_{4\text{at}}^{(\text{xc})} = (-Y_1^{(2)} + Y_4^{(2)} - Y_{3\text{row}}^{(3)}) 4 \cos^2 \phi + \mathcal{O}(Y^{(4)}) + \text{const} \quad ,$$

along $\phi \in [0, \frac{1}{2}\pi]$ all configurations are different .

$Y_{3\text{row}}^{(3)}$ denotes a sum of exchange parameters, where the corresponding terms depend on the magnetization direction of at least 3 different atomic rows.

In 4th-order all non-constant terms are proportional to $\cos^4 \phi$ or $\cos^2 \phi$. The pair interactions have the form

$$(\mathbf{S}_0 \cdot \mathbf{S}_1)^4 + (\mathbf{S}_1 \cdot \mathbf{S}_2)^4 + (\mathbf{S}_2 \cdot \mathbf{S}_3)^4 + (\mathbf{S}_3 \cdot \mathbf{S}_0)^4 = 4 \cos^4 \phi \quad , \quad (\mathbf{S}_0 \cdot \mathbf{S}_2)^4 + (\mathbf{S}_1 \cdot \mathbf{S}_3)^4 = \text{const} \quad .$$

The results of these calculations are shown in Fig. G.4.

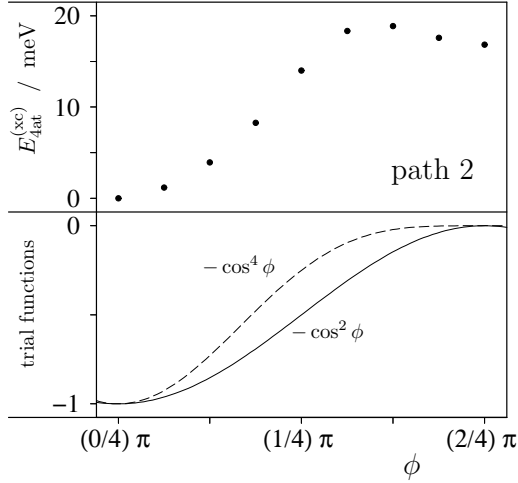


Figure G.4: Energy changes when the magnetic configuration changes along path 2.

The data points do not match well with the 2nd-order terms. Apparently the energy contributions of the 4th-order pair interactions (or other higher-order terms) are larger. From least-square fits one obtains:

$$\begin{aligned}
 E_{4at} &\approx a_2 4 \cos^2 \phi \quad \Rightarrow \\
 a_2 &= -4.6 \text{ meV} \quad , \\
 E_{4at} &\approx a_2 4 \cos^2 \phi + a_4 4 \cos^4 \phi \quad \Rightarrow \\
 a_2 &= +1.0 \text{ meV} \quad , \quad a_4 = -5.6 \text{ meV} \quad .
 \end{aligned}$$

In order to estimate the magnitude of $Y_2^{(2)}$ the energies of two different configurations (α , β) are added. This way the contributions from the 1st-order terms and from $Y_1^{(2)}$ are kept constant:

path 3 :

$$\left. \begin{aligned}
 \varphi_{\alpha,1} &= \phi \\
 \varphi_{\alpha,2} &= \phi - \arctan \frac{\cos \phi}{\sqrt{2} - \sin \phi} \\
 \varphi_{\alpha,3} &= \arctan \frac{\cos \phi}{\sqrt{2} - \sin \phi} + \pi \\
 \varphi_{\beta,1} &= \arccos(\cos(\varphi_{\alpha,1}) - \cos(\varphi_{\alpha,1} - 2\varphi_{\alpha,3})) \\
 \varphi_{\beta,2} &= 0 \\
 \varphi_{\beta,3} &= \arccos(\cos(\varphi_{\alpha,1}) - \cos(\varphi_{\alpha,1} - 2\varphi_{\alpha,3}))
 \end{aligned} \right\} \Rightarrow$$

$$\begin{aligned}
 E_{\alpha\beta}^{(xc)} &= E_{\alpha,4at}^{(xc)} - \frac{1}{4} E_{\beta,4at}^{(xc)} \\
 &= -Y_2^{(2)} 4 \cos^2 \left(\phi - \arctan \frac{\cos \phi}{\sqrt{2} - \sin \phi} \right) - Y_{3row}^{(2)} (\dots) + \mathcal{O}(Y^{(3)}) + \text{const} \quad ,
 \end{aligned}$$

along $\phi \in \left[\frac{1}{4}\pi, \frac{3}{4}\pi \right)$ all configurations are different .

The results of these calculations are shown in Fig. G.5. Note that the configuration β can be calculated with a 2-row unit-cell.

The energy curves of path 2 and path 3 show that the contribution of the biquadratic terms is small compared with the energy changes given in Fig. G.1.a.

Fig. G.4 shows that the nearest-neighbor biquadratic interaction (coefficient $Y_1^{(2)}$) is not dominant at path 2: Fits to the energy curve show that the higher-order terms $\sim \cos^4 \phi$ are more important (cf. Figure Caption G.4). The energy changes along path 3 (Fig. G.5) are relatively high. The influence of the biquadratic interaction (coefficient $Y_2^{(2)}$) on the energy curve of path 3 is not clear, a fit to the energy curve of path 3 with the biquadratic term only gives $Y_2^{(2)} \approx 8 \text{ meV}$. But, the energy curve of path 4 (presented below) shows that the biquadratic terms with of $Y_2^{(2)} \approx 8 \text{ meV}$ are no reasonable correction to the Heisenberg model (6.4).

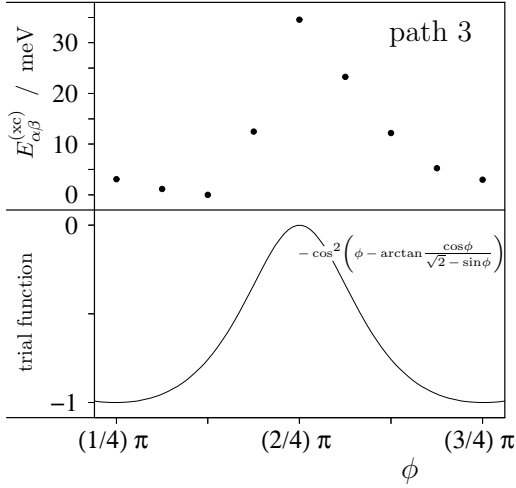


Figure G.5: Energy changes when the magnetic configuration changes along path 3.

The above calculations indicate that the Heisenberg exchange integrals (i.e. 1st-order coefficients) are dominant: The energy changes of the flat spin spirals (Fig. G.1.a) are large compared to the energy changes of the configurations that are degenerate in the Heisenberg model (Figs. G.3, G.4, G.5; remember that these curves show the energy per 4 surface atoms).

Further tests are necessary to see whether the dominant parameters $\{J_j\}$ are independent of the particular magnetic configurations. This is checked by calculations with the 4-row unit-cell, path 4 allows to separate the contributions of $Y_1^{(1)} = \sum_{j=1}^{\infty} J_{2j-1}$ and $Y_2^{(1)} = \sum_{j=1}^{\infty} J_{4j-2}$:

path 4 :

$$\left. \begin{array}{l} \varphi_{\alpha,1} = 0 \\ \varphi_{\alpha,2} = \phi \\ \varphi_{\alpha,3} = \phi \\ \varphi_{\beta,1} = \phi \\ \varphi_{\beta,2} = 0 \\ \varphi_{\beta,3} = \phi \end{array} \right\} \Rightarrow \left\{ \begin{array}{l} E_{\beta,4\text{at}}^{(\text{xc})} = (-Y_1^{(1)} + Y_{3\text{row}}^{(2)}) 4 \cos \phi + (-Y_1^{(2)} + Y_{3\text{row}}^{(2)}) 4 \cos^2 \phi \\ \quad + \mathcal{O}(Y^{(3)}) + \text{const} \\ E_{\alpha\beta}^{(\text{xc})} = E_{\alpha,4\text{at}}^{(\text{xc})} - \frac{1}{2} E_{\beta,4\text{at}}^{(\text{xc})} \\ \quad = (-Y_2^{(1)} + Y_{3\text{row}}^{(2)}) 4 \cos \phi + (-Y_2^{(2)} + Y_{3\text{row}}^{(2)}) 4 \cos^2 \phi \\ \quad + \mathcal{O}(Y^{(3)}) + \text{const} \end{array} \right. ,$$

along $\phi \in [0, \pi]$ all configurations are different .

The results of these calculations are shown in Fig. G.6. The energy curves are approximated by the Heisenberg model (6.4) with the exchange integrals $\{J_j\}$ that are obtained from the spin-spiral calculations and shown in Fig. G.1.b. The calculations show that the dominant part of the exchange-energy differences can be described by the Heisenberg model. Only a few exchange integrals need to be considered.

The curve for $E_{\alpha\beta}^{(\text{xc})}$ is “corrected” by the term $-Y_2^{(2)} 4 \cos^2 \phi$ with $Y_2^{(2)} = 8$ meV as estimated from path 3. The resulting graph illustrates that the derivations from the Heisenberg model cannot be described by the 2nd-order pair interactions (cf. right panel of Fig. G.6, compare with Fig. G.5).

A further test of the Heisenberg model is made on a less regular path. The exchange energy of configuration α of path 3 can be written as

$$E_{\alpha,4\text{at}}^{(\text{xc})} = Y_1^{(1)} \left(\cos \left(\phi - 2 \arctan \frac{\cos \phi}{\sqrt{2} - \sin \phi} \right) - \cos \phi \right) + \mathcal{O}(Y^{(2)}) + \text{const} .$$

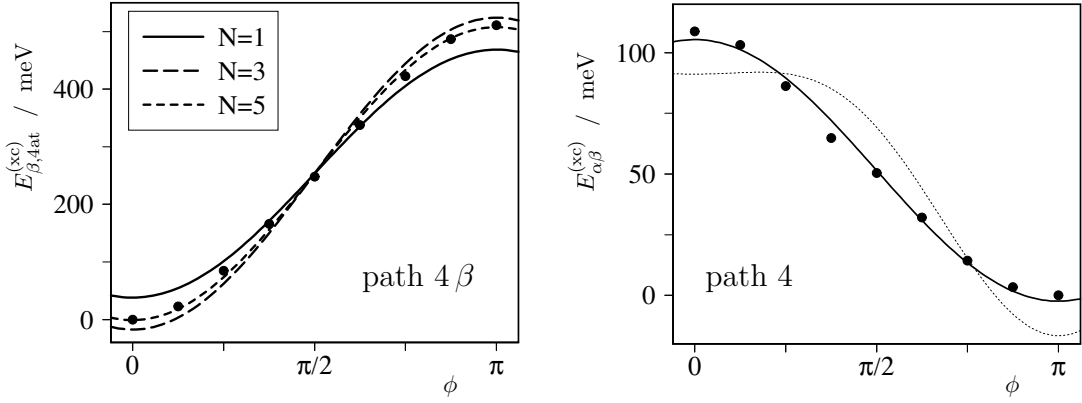


Figure G.6: Energy changes when the magnetic configuration changes along path 4. The data points (\bullet) represent the results of the ab-initio calculations. The lines represent the approximations with the leading terms of the expansion (G.2).

The left figure shows $E_{\beta,4at}^{(xc)}$ and its approximation by the Heisenberg model $E_{\beta,4at}^{(xc)} = -Y_1^{(1)} 4 \cos \phi + \text{const}$. The parameter $Y_1^{(1)}$ is obtained from the spin-spiral calculations (cf. Fig. G.1) with the Eqns. (G.1) and (G.3). In (G.3) the exchange integrals J_j are taken into account for $j \leq N$, the maximal neighbor distance N is given in the legend.

The right figure shows $E_{\alpha\beta}^{(xc)}$. The thick line represents the approximation by the Heisenberg model $E_{\alpha\beta}^{(xc)} = -Y_2^{(1)} 4 \cos \phi + \text{const}$. Likewise, the parameter $Y_2^{(1)}$ is obtained from the spin-spiral calculations. Here only the exchange integral J_2 is taken into account, according to (G.3) there is no contribution from J_1, J_3, J_4, J_5 . The thin line represents the approximation $E_{\alpha\beta}^{(xc)} = -Y_2^{(1)} 4 \cos \phi - Y_2^{(2)} 4 \cos^2 \phi + \text{const}$ with $Y_2^{(1)} = J_2, Y_2^{(2)} = 8 \text{ meV}$.

The ab-initio results of $E_{\alpha,4at}^{(xc)}$ and the approximations by the Heisenberg model are shown in Fig. G.7.

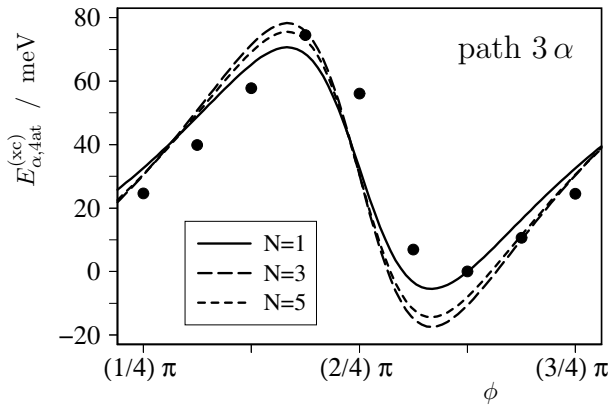


Figure G.7: Energy changes of configuration α along path 3. The data points represent the results of the ab-initio calculations, the lines represent the approximation

$$E_{\alpha,4at}^{(xc)} = Y_1^{(1)} \left(\cos \left(\phi - 2 \arctan \frac{\cos \phi}{\sqrt{2} - \sin \phi} \right) - \cos \phi \right) + \text{const} .$$

The calculation of $Y_1^{(1)}$ and the meaning of N is identical as in Fig. G.6.

Fig. G.7 shows that the nearest-neighbor interaction dominates the exchange energy and can be described by the Heisenberg model. But, contrary to path 4, the approximation does not improve considerably if the interactions beyond the nearest neighbor are taken into account. Note that the 2nd-nearest neighbor interaction vanishes when path 3α is described by the Heisenberg model.

G.3 Conclusion

In this Appendix G the applicability of the expansion (6.3) is checked and the relevant model parameters are estimated. The choice of the magnetic configurations, that are

compared with the model, introduces some arbitrariness. With the current computing resources it is not feasible to calculate many more configurations with the required accuracy. Nevertheless, the above results indicate that the Heisenberg model (6.4) describes the dominant part of the exchange energy with

$$J_1 = +53.8 \text{ meV} \quad , \quad J_2 = -13.5 \text{ meV} \quad , \quad J_3 = +13.8 \text{ meV} \\ (\quad J_4 = +1.8 \text{ meV} \quad , \quad J_5 = -4.1 \text{ meV} \quad) \quad .$$

In the above calculations the error made with this ansatz is $\lesssim 10 \text{ meV}$ per surface atom. With this inaccuracy J_4, J_5 are irrelevant.

It is not possible to improve the model by including the terms of next higher order in (6.3) while using one fixed set of model parameters for arbitrary magnetic configurations.

Appendix H

Computational details

All ab-initio calculations apart the structure relaxations are performed within the local density approximation in the parameterization of Moruzzi, Janak, Williams [72]. All results that are presented in Chapter 6 are done for the same surface geometry, i.e. the interlayer distances and the in-plane lattice constant are not changed.

The most critical computational parameters describe the range of the basis functions. They are specified in terms of K_{\max} and k_{dens} . The basis functions are set up according to Eqn. (3.7) with $\mathbf{K} < |K_{\max}|$. k_{dens} denotes the number of \mathbf{k}_{\parallel} -points that are used to sample the surface Brillouin zone. k_{dens} is given in terms of pbz, this denotes the number of mesh points per reciprocal chemical unit cell (if symmetry allows to restrict the \mathbf{k} -point mesh to $\frac{1}{n}$ th of the Brillouin zone then the number of actually used \mathbf{k} -points is $\frac{1}{n} k_{\text{dens}}$).

The muffin-tin radii are chosen as $R_{\text{MT}} = 2.1$ a.u. for the Fe atoms and $R_{\text{MT}} = 2.5$ a.u. for the W atoms.¹

H.1 Structure relaxation

The in-plane lattice constant is set according the experimental value of $a_{\text{exp}} = 0.316$ nm for the bulk bcc W lattice constant. The out-of-plane interlayer relaxations are determined from ab-initio calculations of the ferromagnetic system. These calculations are performed with an one-atomic surface unit cell, thus the possibility of surface buckling is not taken into account.

The local density approximation gives only poor description of the structural relaxations of the 3d transition metals [e.g. 6], therefore the structure is determined with a GGA approximation as described in [78, 80]. The interlayer relaxations are calculated with the GGA in-plane lattice constant a_{GGA} that is determined from calculations of W-bulk.

The final structure is obtained by keeping the relative distances constant and scaling the whole structure by a constant factor of $(a_{\text{exp}}/a_{\text{GGA}})$. The results are given in Table H.1.

The structural optimizations are calculated with a slab of 7 layers of W sandwiched between one or two layers of Fe on each side. A plane-wave cutoff of $K_{\max} = 4.0$ a.u.⁻¹ and a \mathbf{k} -point density of $k_{\text{dens}} = 100$ pbz are used.

¹ 1 a.u. = 1 Bohr radius = $5.29 \cdot 10^{-11}$ m

| | ML Fe | | | DL Fe | | |
|----|-------------------------------|---|---------------------------------|-------------------------------|---|---------------------------------|
| | $\frac{r_z}{\text{nm}}$ (GGA) | $\frac{r_z}{\text{nm}} \cdot \frac{a_{\text{exp}}}{a_{\text{GGA}}}$ | $\frac{\text{mag.mom.}}{\mu_B}$ | $\frac{r_z}{\text{nm}}$ (GGA) | $\frac{r_z}{\text{nm}} \cdot \frac{a_{\text{exp}}}{a_{\text{GGA}}}$ | $\frac{\text{mag.mom.}}{\mu_B}$ |
| Fe | — | — | — | 0.3752 | 0.3715 | 2.860 |
| Fe | 0.1938 | 0.1919 | 2.452 | 0.2024 | 0.2003 | 2.244 |
| W | 0.0 | 0.0 | -0.108 | 0.0 | 0.0 | -0.111 |
| W | -0.2256 | -0.2235 | 0.005 | -0.2256 | -0.2235 | 0.004 |

Table H.1: Interlayer distances calculated with an in-plane lattice constant of $a_{\text{GGA}} = 0.3191$ nm and scaled to the experimental lattice constant of $a_{\text{exp}} = 0.316$ nm. The distances r_z are given with respect to the top W atom, the spin magnetic moments are given for the GGA calculations with the GGA relaxations.

H.2 Exchange interactions

DL geometry

The spin-stiffness energies (Fig. 6.6, right panel) are calculated for a structure with 2 layers of Fe on one side of 7 layers of W. The local force theorem is applied, i.e. only the ferromagnetic potential is calculated selfconsistently. The basis functions are confined by $K_{\text{max}} = 4.0$ a.u.⁻¹ and $k_{\text{dens}} = 484$ pbz for the calculation of the potential and $k_{\text{dens}} = 7200$ pbz for the calculation of the spin spirals. The results for the spin-stiffness energies are a byproduct of the calculation of the DM-interaction (Fig. 6.9), the latter required 7 layers of W and the high numerical cutoffs.

ML geometry

The spin-stiffness energies (Fig. 6.6, left panel) are calculated for a structure with 1 layer of Fe on one side of 4 layers of W. The local force theorem is applied, i.e. only the ferromagnetic potential is calculated selfconsistently. The basis functions are confined by $K_{\text{max}} = 3.6$ a.u.⁻¹ and $k_{\text{dens}} = 576$ pbz for the calculation of the potential and $k_{\text{dens}} = 2700$ pbz for the calculation of the spin spirals.

The hopping parameters are calculated selfconsistently for a structure with 1 layer of Fe on one side of 2 layers of W. The influence of the number of W-layers on the results is estimated (cf. Fig. H.1).

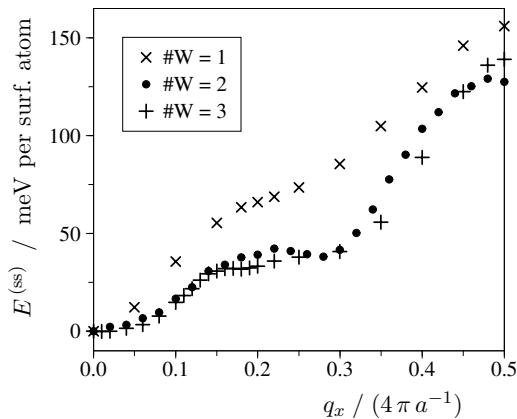


Figure H.1: Spin-spiral energies for one ML Fe on a W slab. The number of W-layers is given in the legend.

The convergence with respect to K_{max} and k_{dens} is tested carefully for the spin-spiral calculations. The plane-wave cutoff is $K_{\text{max}} = 3.6$ a.u.⁻¹. The \mathbf{k} -point density is $k_{\text{dens}} =$

576 pbz. But, the points are not isotropically distributed. In $[1\bar{1}0]$ -direction ($\perp \mathbf{q}$) the distance between the \mathbf{k} -points is $\sqrt{2}$ -times larger than in $[001]$ -direction (measured in a.u. $^{-1}$, not per length of the Brillouin zone).

The 4-row unit-cell that is introduced in Appendix G is calculated with the same K_{\max} and an equivalent set of \mathbf{k} -points (i.e. the basis functions in both unit cells are labeled with the same wave vectors $\{\mathbf{k} + \mathbf{G}\}$; the unit cell for the spin-spiral calculations (with 1 surface atom) is calculated with 4 times more \mathbf{k} -points than the 4-row unit-cell (with 4 surface atoms)).

The exchange integrals presented in Fig. G.1.b are calculated from the data presented in Fig. G.1.a. The spin-spiral energy curve $E^{(\text{ss})}(q_x)$ is approximated by connecting the data points with straight lines. For each of these linear curve segments the Fourier integral (G.1) is integrated analytically and the results for all curve segments are added.

H.3 Magnetocrystalline anisotropy

It requires a major computational effort to calculate the magnetocrystalline anisotropy constants with sufficient accuracy. In a surface film the symmetry is low and thus the relevant anisotropy constants are higher than in most bulk systems. Nevertheless, in the DL system they are well below 1 meV per surface atom.

A large amount of the energy differences results from the bands close to the Fermi energy, whose occupation numbers change with the magnetization direction. It requires a dense \mathbf{k} -point mesh to count eigenvalues of the occupied states correctly. Fortunately these small changes in the occupation numbers do not influence the potential too much, it is still possible to apply the local force theorem.

Besides the purely numerical difficulties one also has to take care how to model the structure properly. The semi-infinite W substrate is modeled with a two-dimensional slab that is covered with Fe on one side. The thickness of the slab is quite important. Even though the induced moments and the direct contribution to the anisotropy energy from the deeper W-layers can be neglected, the potential of these layers is necessary to generate wave functions that close to the surface approximate the wave functions of the semi-infinite crystal.

In the case of a DL Fe coverage the dependence of the anisotropy constants on the slab thickness is studied systematically. The results are shown in Fig. H.2. Note that these calculations are performed with a W slab that is covered with Fe on *one* side, the W atoms on the other surface are far from their bulk environment. It is necessary to choose such a setup for the calculation of the DM interaction.

In the case of one ML Fe coverage there is an energy difference of more than 2 meV per surface atom between the configurations magnetized perpendicular and along the easy $[1\bar{1}0]$ -axis. The anisotropy constants vary less than 1 meV between slabs of 3, 4 and 10 W-layers, therefore the surface can be modeled with a slab of 3 W-layers in order to get a rough estimation of the energy necessary to rotate the magnetization into the plane perpendicular to the easy axis, but for more accuracy (e.g. for a reliable sign of K_{001}) it is necessary to use a thicker slab in the calculations. It is not as important as in the case of the DL to reduce the absolute error of $K^{(\text{so})}$, therefore the convergence of $K_{001}^{(\text{so})}$, $K_{1\bar{1}0}^{(\text{so})}$ with respect to the slab thickness is not examined as careful as in the case of the DL. From Table H.2 it can be seen that three layers of W are sufficient to predict the easy axis but thicker slabs are needed to resolve the energies by less than 1 meV.

The magnetocrystalline anisotropy energies are calculated with $K_{\max} = 3.6 \text{ a.u.}^{-1}$. The

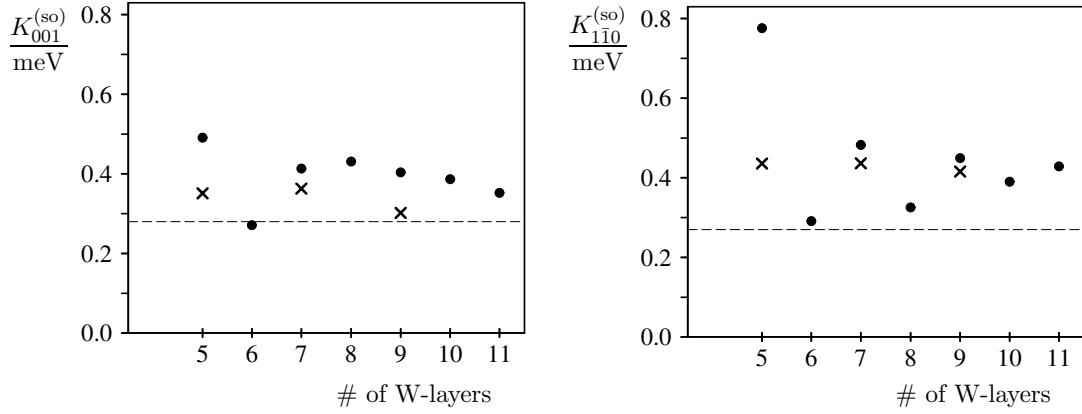


Figure H.2: Anisotropy constants for a DL Fe on a W slab. The dots (●) represent calculations of $K^{(so)}$ for slabs of different thickness, the crosses (×) represent calculations done with a slab of 11 W-layers but with no spin-orbit coupling in the last W-layers. The dashed lines indicate $-K^{(\text{dip})}$ (calculated from the moments of the Fe- and 1st W-layers), note that the major parts of dipolar and magnetocrystalline anisotropy cancel. The energies are given per surface atom.

| # W-layers | $\frac{K_{001}^{(so)}}{\text{meV}}$ | $\frac{K_{110}^{(so)}}{\text{meV}}$ | mag.mom. | | |
|------------|-------------------------------------|-------------------------------------|----------|-------|-------|
| | | | μ_B | | |
| | | | Fe | 1st W | 2nd W |
| 2 | 1.39 | -6.46 | 2.20 | -0.12 | -0.01 |
| 3 | 0.35 | -2.23 | 2.32 | -0.09 | -0.01 |
| 4 | -0.27 | -2.52 | 2.30 | -0.11 | -0.00 |
| 10 | 0.39 | -2.42 | 2.35 | -0.10 | -0.01 |

Table H.2: Anisotropy constants and spin moments for a ML Fe on a W slab. The energies are given per surface atom. Note that the drastic changes in the anisotropy constants cannot be predicted from the spin moments.

potential is determined selfconsistently under the neglect of spin-orbit coupling with $k_{\text{dens}} = 576 \text{ pbz}$ for the ML coverage and $k_{\text{dens}} = 100 \text{ pbz}$ for each of the slabs with DL coverage that are shown in Fig. H.2. From these potentials the anisotropy energies are calculated via the force theorem. In the case of the ML coverage the convergence with respect to k_{dens} is tested by calculations up to 10 000 pbz, the energies remain stable above $\approx 4000 \text{ pbz}$. But, due to the high ML anisotropy energy qualitative results can already be obtained with much lower k_{dens} , Fig. 6.7 is obtained with $k_{\text{dens}} = 404 \text{ pbz}$ [76]. The DL coverage is calculated with $k_{\text{dens}} = 4900 \text{ pbz}$.

The applicability of the local force theorem is checked by performing selfconsistent calculations for a slab with DL Fe and 7 W-layers. The anisotropy constants that are obtained from this calculations show only minor difference to the ones obtained with the local force theorem.

H.4 DM interaction

For the DL Fe the size of the **D**-vector is calculated with the method that is introduced in Chapter 3.9.

The surface is modeled with a slab of 2 Fe-layers on 7 W-layers. The contribution of the outermost W-layer (opposite to the Fe) to the SOC term is unaccounted for.

The potential is determined selfconsistently for the ferromagnetic case with $k_{\text{dens}} = 484 \text{ pbz}$ and $K_{\text{max}} = 4.0 \text{ a.u.}^{-1}$. The spin-spiral eigenstates are constructed from this potential with the generalized Bloch theorem. There are no further selfconsistent calculations

necessary since there are only small \mathbf{q} -vectors considered.

The curves in Fig. 6.9 are obtained with $k_{\text{dens}} = 7200$ pbz and $K_{\text{max}} = 4.0 \text{ a.u.}^{-1}$. Some data points (in particular in the vicinity of the kink at $q_x = 0.04 (4\pi a^{-1})$) are recalculated with $K_{\text{max}} = 3.6 \text{ a.u.}^{-1}$ and $K_{\text{max}} = 4.2 \text{ a.u.}^{-1}$ in order to estimate the effect of the basis size on the curve. There are no considerable differences in the results for $K_{\text{max}} = 4.0 \text{ a.u.}^{-1}$ and $K_{\text{max}} = 4.2 \text{ a.u.}^{-1}$. If K_{max} is reduced to 3.6 a.u.^{-1} the curves are less smooth but the positions of the main kinks at $\mathbf{q} \parallel [001]$ remain the same.

For the perturbative procedure that is presented in Appendix D the size of the energy intervals are chosen as $e_0 = 100$ mhtr and $e_1 = 50$ mhtr. For $q_x > 0.05 (4\pi a^{-1})$ and $q_y > 0.05 (\sqrt{8}\pi a^{-1})$ tests with larger energy intervals are done. These tests do not show a considerable deviation from the results that are presented in Fig. 6.9.

There is no experience with these calculations, therefore the accuracy of the method is not known. With the currently available computing resources it is not feasible to test the stability of the result with respect to changes in the geometry (e.g. number of W-layers).

Note that the calculation of the data presented in Fig. 6.9 requires an immense amount of computing time. The method presented in Appendix D reduces the time needed to apply the SOC perturbation drastically. Most time is spend in the calculation of the spin-spiral eigenstates, since this has to be done for many \mathbf{k} -points.

Bibliography

- [1] N. S. Akulov, *Z. Physik* **69**, 78 (1931)
- [2] R. Allenspach, *IBM J. Res. Develop.* **44**, 553 (2000)
- [3] O. K. Andersen, *Phys. Rev. B* **12**, 3060 (1975)
- [4] P. W. Anderson, *Phys. Rev.* **115**, 2 (1959)
- [5] T. Arai, *Phys. Rev.* **126**, 471 (1962)
- [6] T. Asada, K. Terakura, *Phys. Rev. B* **46**, 13599 (1992)
- [7] P. Bak, M. H. Jensen, *J. phys. C: Solid State Phys.* **13**, L881 (1980)
- [8] M. Barthelmess, C. Pels, A. Thieme, G. Meier, *J. Appl. Phys.* **95**, 5641 (2004)
- [9] G. Baym, *Lectures on quantum mechanics*, Benjamin Reading Mass. (1974)
- [10] D. V. Berkov, K. Ramstöck, A. Hubert, *phys. stat. sol. (a)* **137**, 207 (1993)
- [11] S. Blügel, *First Principles Calculations of the Electronic Structure of Magnetic Overlayers on Transition Metal Surfaces*, PhD thesis RWTH Aachen (1988)
- [12] S. Blügel, H. Akai, R. Zeller, P. H. Dederichs, *Phys. Rev. B* **35**, 3271 (1987)
- [13] M. Bode, *Rep. Prog. Phys.* **66**, 523 (2003)
- [14] M. Bode, private communication
- [15] A. Bogdanov, A. Hubert, *J. Magn. Magn. Mater.* **138**, 255 (1994)
- [16] A. Bogdanov, A. Hubert, *phys. stat. sol. (b)* **186**, 527 (1994)
- [17] A. N. Bogdanov, U. K. Rößler, *Phys. Rev. Lett.* **87**, 037203 (2001)
- [18] A. N. Bogdanov, D. A. Yablonskiĭ, *Sov. Phys. JETP* **69**, 142 (1989) ; *Zh. Eksp. Teor. Fiz.* **96**, 253 (1989)
- [19] P. Bruno, *Phys. Rev. Lett.* **83**, 2425 (1999)
- [20] D. M. Bylander, L. Kleinman, *Phys. Rev. B* **58**, 9207 (1998)
- [21] D. M. Bylander, L. Kleinman, *Phys. Rev. B* **59**, 6278 (1999)
- [22] D. M. Ceperley, B. J. Alder, *Phys. Rev. Lett.* **45**, 566 (1980)
- [23] S. Chikazumi, *Physics of Ferromagnetism*, University Press Oxford (1997)

- [24] J. Crangle, *The Magnetic Properties of Solids*, Edward Arnold London (1977)
- [25] C. Crépieux, C. Lacroix, *J. Magn. Magn. Mater.* **182**, 341 (1998)
- [26] P. H. Dederichs, S. Blügel, R. Zeller, H. Akai, *Phys. Rev. Lett.* **56**, 2512 (1984)
- [27] P. H. Dederichs, R. Zeller, *Phys. Rev. B* **28**, 5462, (1983)
- [28] W. Döring, *Mikromagnetismus, Handbuch der Physik XVIII/2*, ed. S. Flügge, H. P. J. Wijn, Springer-Verlag Berlin (1966)
- [29] I. E. Dzialoshinskii, *Sov. Phys. JETP* **5**, 1259 (1957) ; *Zh. Eksp. Teor. Fiz.* **32**, 1547 (1957)
- [30] I. E. Dzyaloshinskii, *Sov. Phys. JETP* **19**, 960 (1964) ; *Zh. Eksp. Teor. Fiz.* **46**, 1420 (1964)
- [31] I. E. Dzyaloshinskii, *Sov. Phys. JETP* **20**, 223 (1965) ; *Zh. Eksp. Teor. Fiz.* **47**, 336 (1964)
- [32] I. E. Dzyaloshinskii, *Sov. Phys. JETP* **20**, 665 (1965) ; *Zh. Eksp. Teor. Fiz.* **47**, 992 (1964)
- [33] H. Eschrig, *The fundamentals of density functional theory*, Teubner-Verlag Stuttgart (1996)
- [34] H. Eschrig, G. Seifert, P. Ziesche, *Solid State Communications* **56**, 777 (1985)
- [35] P. Escudier, *Ann. Phys. (Paris)* **9**, 125 (1975)
- [36] <http://www.flapw.de>
- [37] E. Fuchs, *Z. angew. Phys.* **14**, 203 (1962)
- [38] H. W. Fuller, M. E. Hale, *J. Appl. Phys.* **31**, 238 (1960)
- [39] U. Hartmann, T. Göddenhenrich, H. Lemke, C. Heiden, *IEEE Trans. Magn.* **26**, 1512 (1990)
- [40] H. R. Hilzinger, H. Kronmüller, *phys. stat. sol. (b)* **54**, 593 (1972)
- [41] P. Hohenberg, W. Kohn, *Phys. Rev.* **136**, B864 (1964)
- [42] A. Holz, A. Hubert, *Z. angew. Phys.* **26**, 145 (1969)
- [43] E. E. Huber Jr., D. O. Smith, J. B. Goodenough, *J. Appl. Phys.* **29**, 294 (1958)
- [44] A. Hubert, *phys. stat. sol.* **32**, 519 (1969)
- [45] A. Hubert, R. Schäfer, *Magnetic Domains*, Springer-Verlag Berlin (1998)
- [46] Yu. A. Izyumov, *Sov. Phys. Usp.* **27**, 845 (1984) ; *Usp. Fiz. Nauk* **144**, 439 (1984)
- [47] J. Kaczér, *J. Phys. Rad.* **20**, 120 (1959)
- [48] R. Kirchner, W. Döring, *J. Appl. Phys.* **39**, 855 (1968)
- [49] L. Kleinman, *Phys. Rev. B* **59**, 3314 (1999)

- [50] D. D. Koelling, B. N. Harmon, *J. Phys. C: Solid State Phys.* **10**, 3107 (1977)
- [51] W. Kohn, *Proceedings of the International School of Physics "Enrico Fermi", Course LXXXIX*, (1985)
- [52] W. Kohn, L. J. Sham, *Phys. Rev.* **140**, A1133 (1965)
- [53] H. Krakauer, M. Posternak, A. J. Freeman, *Phys. Rev. B* **19**, 1706 (1979)
- [54] P. Kurz, *Non-Collinear Magnetism at Surfaces and in Ultrathin Films*, PhD thesis RWTH Aachen (2000)
- [55] P. Kurz, F. Förster, L. Nordström, G. Bihlmayer, S. Blügel, *Phys. Rev. B* **69**, 024415 (2004)
- [56] A. E. LaBonte, *J. Appl. Phys.* **40**, 2450 (1969)
- [57] L. Landau, E. Lifshitz, *Phys. Z. Sowjetunion* **8**, 153 (1935)
- [58] L. D. Landau, E. M. Lifshitz, *Elektrodynamik der Kontinua (Elektrodinamika splosnych sred)*, *Lehrbuch der Theoretischen Physik*, Akademie-Verlag Berlin (1985)
- [59] L. D. Landau, E. M. Lifshitz, W. B. Berestetzki, L. P. Pitajewski, *Relativistische Quantentheorie (Reljativistskaja kvantovaja teorija)*, *Lehrbuch der Theoretischen Physik*, Akademie-Verlag Berlin (1980)
- [60] M. Levy, *Proc. Natl. Acad. Sci. USA* **76**, 6062 (1979)
- [61] A. I. Liechtenstein, M. I. Katnelson, V. P. Antropov, V. A. Gubanov, *J. Magn. Magn. Mater.* **67**, 65 (1987)
- [62] B. A. Lilley, *Phil. Mag. (7)* **41**, 792 (1950)
- [63] M. A. Lippert, H. J. Elmers, P. G. J. van Dongen, unpublished
- [64] A. H. MacDonald, W. E. Pickett, D. D. Koelling, *J. Phys. C: Solid State Phys.* **13**, 2675 (1980)
- [65] A. H. MacDonald, S. H. Vosko, *J. Phys. C: Solid State Phys.* **12**, 2977 (1979)
- [66] A. R. Mackintosh, O. K. Andersen, *Electrons at the Fermi Surface*, ed. M. Springfield (1980)
- [67] H. Matsuyama, K. Koike, *J. Electron. Microsc.* **43**, 157 (1994)
- [68] M. Methfessel, J. Kübler, *J. Phys. F: Met. Phys.* **12**, 141 (1982)
- [69] S. Methfessel, S. Middelhoek, H. Thomas, *IBM J. Res. Develop.* **4**, 96 (1960)
- [70] S. Middelhoek, *J. Appl. Phys.* **34**, 1054 (1963)
- [71] T. Moriya, *Phys. Rev.* **120**, 91 (1960)
- [72] V. L. Moruzzi, J. F. Janak, A. R. Williams, *Calculated Electronic Properties of Metals*, Pergamon Press New York (1978)
- [73] K. Nakamura, T. Ito, A. J. Freeman, L. Zhong, J. Fernandez-de-Castro, *J. Appl. Phys.* **93**, 6879 (2003)

- [74] O. Nakanishi, A. Yanase, A. Hasegawa, M. Kataoka, *Solid State Communications* **35**, 995 (1980)
- [75] L. Néel, *C. R. Acad. Sci. (Paris)*, **241**, 533 (1955)
- [76] X. Nie, G. Bihlmayer, S. Blügel, unpublished
- [77] A. Oswald, R. Zeller, P. J. Braspenning, P. H. Dederichs, *J. Phys. F: Met. Phys.* **15**, 193 (1985)
- [78] J. P. Perdew, *Electronic Structure of Solids '91*, ed. P. Ziesche, H. Eschrig, Akademie-Verlag Berlin (1991)
- [79] J. P. Perdew, K. Burke, M. Ernzerhof, *Phys. Rev. Lett.* **77**, 3865 (1996)
- [80] J. P. Perdew, J. A. Chevary, S. H. Vosko, K. A. Jackson, M. R. Pederson, D. J. Singh, C. Fiolhais, *Phys. Rev. B* **46**, 6671 (1992) ; erratum: *Phys. Rev. B* **48**, 4978 (1993)
- [81] O. Pietzsch, *Magnetic Imaging by Spin-Polarized Scanning Tunneling Spectroscopy Applied to Ultrathin Fe/W(110) Films*, PhD thesis Universität Hamburg (2001)
- [82] O. Pietzsch, A. Kubetzka, M. Bode, R. Wiesendanger, *Science* **292**, 2053 (2001)
- [83] M. Pratzner, H. J. Elmers, M. Bode, O. Pietzsch, A. Kubetzka, R. Wiesendanger, *Phys. Rev. Lett.* **87**, 127201 (2001)
- [84] R. Proksch, S. Foss, E. D. Dahlberg, G. Prinz, *J. Appl. Phys.* **75**, 5776 (1994)
- [85] A. K. Rajagopal, J. Callaway, *Phys. Rev. B* **7**, 1912 (1973)
- [86] K. Ramstöck, W. Hartung, A. Hubert, *phys. stat. sol. (a)* **155**, 505 (1996)
- [87] W. Rave, A. Hubert, *J. Magn. Magn. Mater.* **184**, 179 (1998)
- [88] H. Riedel, A. Seeger, *phys. stat. sol. (b)* **46**, 377 (1971)
- [89] L. M. Sandratskii, *phys. stat. sol. (b)* **135**, 167 (1986)
- [90] L. M. Sandratskii, *J. Phys.: Condens. Matter* **3**, 8565 (1991)
- [91] J. Schwitalla, B. L. Györfy, L. Szunyogh, *Phys. Rev. B* **63**, 104423 (2001)
- [92] V. S. Semenov, *Phys. Met. Metall.* **71.2**, 61 (1991) ; *Fiz. metal. metalloved* **71.2**, 64 (1991)
- [93] S. Senoussi, *Phys. Rev. Lett.* **26**, 2314 (1986)
- [94] D. J. Singh, *Planewaves, pseudopotentials and the LAPW method*, Kluwer Academic Publishers (1994)
- [95] J. C. Slater, *Phys. Rev.* **51**, 846 (1937)
- [96] R. Takeda, S. Yamanaka, K. Yamaguchi, *Int. J. Quantum Chem.* **102**, 80 (2005)
- [97] E. Y. Vedmedenko, A. Kubetzka, K. von Bergmann, O. Pietzsch, M. Bode, J. Kirschner, H. P. Oepen, R. Wiesendanger, *Phys. Rev. Lett.* **92**, 077207 (2004)
- [98] U. von Barth, L. Hedin, *J. Phys. C* **5**, 1629 (1972)

-
- [99] M. Weinert, *J. Math. Phys.* **22**, 2433 (1981)
- [100] R. Wiesendanger, H.-J. Güntherodt, G. Güntherodt, R. J. Gambino, R. Ruf, *Phys. Rev. Lett.* **65**, 247 (1990)
- [101] B. E. Wong, D. E. Laughlin, *J. Appl. Phys.* **79**, 6455 (1996)
- [102] B. Y. Yavorsky, I. Mertig, A. Y. Perlov, A. N. Yaresko, V. N. Antonov, *Phys. Rev. B* **66**, 174422 (2002)
- [103] K. Yoshida, *Theory of magnetism (Jisei)*, Springer-Verlag Berlin (1996)
- [104] R. Zurmühl, S. Falk, *Matrizen und ihre Anwendungen, Teil 1*, Springer-Verlag Berlin (1984)

Acknowledgments

During the process of writing this thesis, I received a lot of support from several people.

I will follow the old tradition and address the first acknowledgment to my supervisor, since he is going to evaluate this thesis later on. I want to express my gratitude to Stefan Blügel for his guidance and time he spend for discussions. Also, I am honestly thankful that he gave me the possibility to start my PhD work in his group despite the initial troubles with my employment at the Forschungszentrum.

Next I want to express my thanks to Peter-Heinz Dederichs for his willingness to become the second evaluator. Also, he proof-read a considerable part of the manuscript very thoroughly.

It would have been impossible for me to write this thesis without the great help of Gustav Bihlmayer. His knowledge seems to cover everything from the Dirac equation to the vi editor, and he was always willing to answer my questions. But I must admit, for most of my questions his patience was more important than his knowledge.

Most parts of the manuscript have been proof-read by either Peter-Heinz Dederichs, Riccardo Hertel or Christoph Friedrich. I am very thankful for that, since they pointed out some factual errors and many muddled passages.

Further, I want to thank Arno, Daniel, Erik, Jussi, Manfred, Marjana, Phivos, Samir, Yuriy and all the other members of the institute for useful discussions as well as for funny conversations. Manni was also very helpful in solving computer problems.

Matthias Bode spend some time explaining me the results of his STM experiments.

More than three years ago Ulrich Rößler came to my poster at the DPG meeting and mentioned the importance of the Dzyaloshinsky-Moriya interaction in such systems. Unfortunately I almost forgot about that until my calculation showed a linear q -dependence two years later. Otherwise, we might have saved a lot of time.

Of course, I am thankful to my parents. Their financial support enabled my undergraduate studies, but further more, they are surely responsible for my interest in science.

Academic education

| | |
|-------------------|---|
| April, 8th 1973 | Born in Düsseldorf (FRG) |
| 1979 - 1993 | Primary and high school in Erkrath, one year exchange student in Opunake (New Zealand) |
| 06/1993 | Abitur |
| 10/1994 - 07/2000 | Studies of physics at Heinrich-Heine-Universität Düsseldorf |
| 07/1999 - 07/2000 | Diploma thesis “Benetzung linienförmiger Objekte in binären Systemen” at the Institut für theoretische Physik IV, Heinrich-Heine-Universität Düsseldorf |
| 07/2000 | Diploma |
| 01/2001 - 09/2005 | Ph.D. thesis at the Institut für Festkörperforschung, Forschungszentrum Jülich |
| 02/2006 | Ph.D. exam at RWTH Aachen |

